HAL
open science

Magnetic configurations in Co-based nanowires explored by electron holography and micromagnetic calculations

David Fernando Reyes Vasquez

To cite this version:

David Fernando Reyes Vasquez. Magnetic configurations in Co-based nanowires explored by electron holography and micromagnetic calculations. Micro and nanotechnologies/Microelectronics. Université Paul Sabatier - Toulouse III, 2016. English. NNT : 2016TOU30356 . tel-01701926v2

HAL Id: tel-01701926

https://theses.hal.science/tel-01701926v2

Submitted on 14 May 2018

HAL is a multi-disciplinary open access archive for the deposit and dissemination of scientific research documents, whether they are published or not. The documents may come from teaching and research institutions in France or abroad, or from public or private research centers.

L'archive ouverte pluridisciplinaire **HAL**, est destinée au dépôt et à la diffusion de documents scientifiques de niveau recherche, publiés ou non, émanant des établissements d'enseignement et de recherche français ou étrangers, des laboratoires publics ou privés.

THÈSE

En vue de l'obtention du

DOCTORAT DE L'UNIVERSITÉ DE TOULOUSE

Délivré par :

Université Toulouse 3 Paul Sabatier (UT3 Paul Sabatier)

Présentée et soutenue par :
David Fernando Reyes Vasquez

Le jeudi 13 octobre 2016

Titre :

Magnetic configurations in Co-based nanowires explored by electron holography and micromagnetic calculations

---

ED SDM : Nano-physique, nano-composants, nano-mesures - COP 00

Unité de recherche :

Centre d'Élaboration de Matériaux et d'Études Structurales (CEMES-CNRS)

Directeur(s) de Thèse :

Dr. Bénédicte Warot-Fonrose, CR CNRS-HdR, CEMES, (France)
Dr. Christophe Gatel, MdC, Université Paul Sabatier, CEMES, (France)

Rapporteurs :

Dr. Martha R McCartney, FAPS, FMSA, Professor, Arizona State University, (USA)
Dr. Olivier Fruchart, DR CNRS, SPINTEC laboratory (CEA/CNRS/Univ. Grenoble Alpes), (France)

Autre(s) membre(s) du jury :

Dr. Jean-Philippe Ansermet, Professor, EPFL SB IPHYS LPMN, (Suisse)
Dr. Michel Goiran, Professeur, LNCMI, (France)
Dr. Nicolas Biziere, CR CNRS, (France)

THÈSE

En vue de l'obtention du

DOCTORAT DE L'UNIVERSITÉ DE TOULOUSE

Délivré par :

Université Toulouse 3 Paul Sabatier (UT3 Paul Sabatier)

Présentée et soutenue par :
David Fernando Reyes Vasquez

Le jeudi 13 octobre 2016

Titre :

Magnetic configurations in Co-based nanowires explored by electron holography and micromagnetic calculations

---

ED SDM : Nano-physique, nano-composants, nano-mesures - COP 00

Unité de recherche :

Centre d'Élaboration de Matériaux et d'Études Structurales (CEMES-CNRS)

Directeur(s) de Thèse :

Dr. Bénédicte Warot-Fonrose, CR CNRS-HdR, CEMES, (France)
Dr. Christophe Gatel, MdC, Université Paul Sabatier, CEMES, (France)

Rapporteurs :

Dr. Martha R McCartney, FAPS, FMSA, Professor, Arizona State University, (USA)
Dr. Olivier Fruchart, DR CNRS, SPINTEC laboratory (CEA/CNRS/Univ. Grenoble Alpes), (France)

Autre(s) membre(s) du jury :

Dr. Jean-Philippe Ansermet, Professor, EPFL SB IPHYS LPMN, (Suisse)
Dr. Michel Goiran, Professeur, LNCMI, (France)
Dr. Nicolas Biziere, CR CNRS, (France)

To my parents,

especially to my Mother María,

my lovely Luci

and my grandmother Ana

"I am not sure that I exist, actually. I am all the writers that I have read, all the people that I have met, all the women that I have loved; all the cities I have visited"

Jorge Luis Borges

Acknowledgements

I would like to begin saying that this work is the result of the effort of several people. First, I want to thanks to my supervisors, Bénédicte and Christophe for their advice, guidance, help and patience during this process. I'm very grateful to them for this invaluable opportunity (I admire you so much). Also, I would like to thanks to Nicolas for being a kind of 3rd supervisor and help me with the production of the samples and the simulations, it is always good to have another point of view and this one was always useful and wise. I want to say thanks to Etienne for letting me be part of the groups and be aware of my things, even if he wasn't my supervisor, it is always nice to find people who work well and also you can talk with them (you are a great leader). Thanks to Luis Alfredo which I regard as a good friend and scientist for all his advice and help during the whole process. Special thanks to Travis who show me part of the "art" of the electrodeposition, and was patient with me during the process.

I feel so lucky to have worked in the CEMES where I found people who are a specialist in the TEM and also are great human beings. In this place, during my three years, I found many people who helped me in one way or another. My friends Xiao Xiao, Luis, Lucho, Lama, Iman, Ines, Ricardo, Lluís, Nuria, Celia, Mathieu, Marion, Zofia, Roberta, Rémi, Marie, Victor, Benoît, Peter, Alessandro, Giuseppe and Delphine!!!. All of them made my life easier and colourful. Really, thanks guys.

I want to say thanks to my Colombian friends in Toulouse and Europe. Thanks to you I could feel like in Colombia in some days. I really enjoyed to meet you and share those special moments with you: Nathaly, Pacho, Angie, Diana, Pablo, Mario, Las Yuris, Edwin, Martha, Julio, James, Claudia, Roque, Jacke, Lore and Luis.

Thanks to my lovely Luci for her unconditional support, to keep my heart happy, in love and my mind clear. Really thanks for being the great human being that you are and to travel to the other side of the world to live this adventure with me. Thanks for all the discussions during our friendship and our relationship, for all these walks and more…Thanks to our lovely neighbour Doushka who has been a source of light and love.

Thanks to my family, my mother who are one of the most important people for me, for her sacrifice during all these years. You deserve the best and even more. To my grandmother and my aunt Merce who are as my second mothers and for teaching me that nothing is impossible and that you always can be positive to defeat all the difficulties, for their invaluable love and to show me the sweet scent of the matriarchy (in a good way). Special thanks to Sakura for their love and softness.

Special thanks to my dear friends Lorena and Luis, because they started a butterfly effect in my life which resulted in this work, thanks for trusting me. Thanks Lore for all the support and the advice, for all the talks about the physics and the life during our friendship.

Finally, I want to thanks to the reporters of my thesis work Marta McCartney and Olivier Fruchart to accept to read my manuscript and do a very professional report. Thanks to the other members of the jury: Jean-Philippe Ansermet and Michel Goiran, for their valuables advice, their words and the analysis my work, I really enjoyed reading your comments and listening to your words during the defence of the thesis.

Abstract

Magnetic nanowires have raised significant interest in the last 15 years due to their potential use for spintronics. Technical achievements require a detailed description of the local magnetic states inside the nanowires at the remnant state. In this thesis, I performed quantitative and qualitative studies of the remnant magnetic states on magnetic nanowires by Electron Holography (EH) experiments and micromagnetic simulations. A detailed investigation was carried out on two types of nanowires: multilayered Co/Cu and diameter-modulated FeCoCu nanowires. Both systems were grown by template-based synthesis using electrodeposition process. The combination of local magnetic, structural and chemical characterizations obtained in a TEM with micromagnetic simulations brought a complete description of the systems.

In the multilayered Co/Cu nanowires, I analysed how different factors such as the Co and Cu thicknesses or the Co crystal structure define the remnant magnetic configuration into isolated nanowires. After applying saturation fields along directions either parallel or perpendicular to the NW axis, I studied multilayered Co/Cu nanowires with the following relative Co/Cu thickness layers: 25nm/15nm, 25nm/45nm, 50nm/50nm, and 100nm/100nm. Three main remnant configurations were found: (i) antiparallel coupling between Co layers, (ii) mono-domain-like state and (iii) vortex state. In the Co(25 nm)/Cu(15 nm) nanowires, depending on the direction of the saturation field, the Co layers can present either an antiparallel coupling (perpendicular saturation field) or vortex coupling (parallel saturation field) with their core aligned parallel to the wire axis. However, 10% of the nanowires studied present a mono-domain-like state that remains for both parallel and perpendicular saturation fields. In

the Co(50 nm)/Cu(50 nm) and Co(25 nm)/Cu(45 nm) nanowires, a larger Cu thickness separating the ferromagnetic layers reduces the magnetic interaction between neighbouring Co layers. The remnant state is hence formed by the combination of monodomain Co layers oriented perpendicularly to the wire axis and some tilted vortex states. Finally for the Co(100 nm)/Cu(100 nm) nanowires a monodomain-like state is found no matters the direction of the saturation field. All these magnetic configurations were determined and simulated using micromagnetic calculations until a quantitative agreement with experimental results has been obtained. I was able to explain the appearance and stability of these configurations according to the main magnetic parameters such as exchange, value and direction of the anisotropy and magnetization. The comparison between simulations and experimental results were used to precisely determine the value of these parameters.

In the diameter-modulated cylindrical FeCoCu nanowires, a detailed description of the geometry-induced effect on the local spin configuration was performed. EH experiments seem to reveal that the wires present a remnant single-domain magnetic state with the spins longitudinally aligned. However, we found through micromagnetic simulations that such apparent single-domain state is strongly affected by the local variation of the diameter.

The study of the leakage field and the demagnetizing field inside the nanowire highlighted the leading role of magnetic charges in modulated areas. The magnetization presents a more complicated structure than a simple alignment along the wire axis. Finally my results have led to a new interpretation of previous MFM experiments.

Résumé

Les nanofils magnétiques suscitent un intérêt considérable depuis une quinzaine d'années en raison de leur utilisation potentielle pour la spintronique. Leur utilisation potentielle dans des dispositifs exige une description détaillée des états magnétiques locaux des nanofils. Dans cette thèse, j'ai étudié qualitativement et quantitativement les états magnétiques à l'état rémanent de nanofils magnétiques par holographie électronique (EH) et simulations micromagnétiques. Une analyse détaillée a été réalisée sur deux types de nanofils: multicouches Co/Cu et nanofils FeCoCu à diamètre modulé. Les deux systèmes ont été synthétisés par électrodéposition dans des membranes. La combinaison des caractérisations magnétiques, structurales et chimiques locales obtenues dans un TEM avec des simulations micromagnétiques ont permis une description complète de ces systèmes.

Pour les nanofils multicouches Co / Cu, j'ai analysé l'influence des épaisseurs de cobalt et de cuivre ou de la structure cristalline de Co sur la configuration magnétique de nanofils isolés. Après l'application d'un champs de saturation dans des directions parallèle et perpendiculaire à l'axe des nanofils, j'ai étudié les configurations magnétiques pour les épaisseurs de Co / Cu suivantes: 25nm / 15nm, 25nm / 45nm, 50nm / 50nm et 100nm / 100nm. Trois configurations principales à la rémanence ont été trouvées: (i) un couplage antiparallèle entre les couches Co, (ii) une structure mono-domaine et (iii) un état vortex. Dans les nanofils Co (25 nm) / Cu (15 nm), en fonction de la direction du champ de saturation, les couches de Co peuvent présenter soit un couplage antiparallèle (champ de saturation perpendiculaire) ou un couplage de type vortex (champ de saturation en parallèle) avec un coeur aligné parallèlement à l'axe du fil.

Cependant, 10% des nanofils étudié présente un état mono-domaine quel que soit le champ de saturation parallèle et perpendiculaire. Dans le cas Co (50 nm) / Cu (50 nm) et Co (25 nm) / Cu (45 nm), l'épaisseur plus grande de Cu séparant les couches ferromagnétiques réduit l'interaction magnétique entre des couches de Co voisines. L'état rémanent est donc formé de la combinaison de couches de Co monodomaines orientés perpendiculairement à l'axe du fil et de certains états vortex. Enfin pour la configuration Co (100 nm) / Cu (100 nm), un état monodomaine est observé quel que soit la direction du champ appliqué lors de la saturation. Toutes ces configurations magnétiques ont été déterminées et simulées à l'aide des calculs micromagnétiques jusqu'à ce qu'un accord quantitatif avec les résultats expérimentaux aient été obtenus. J'ai ainsi pu expliquer l'apparition et la stabilité de ces configurations en fonction des principaux paramètres magnétiques tels que l'échange, la valeur et la direction de l'anisotropie et l'aimantation. La comparaison entre les simulations et les résultats expérimentaux ont ainsi servi à déterminer précisément la valeur de ces paramètres.

Dans les nanofils FeCoCu à diamètre modulé, une description détaillée de l'influence de la géométrie sur la configuration locale de spins a été réalisée. Les expériences d'holographie électronique montrent une structure magnétique monodomaines avec l'aimantation alignée longitudinalement. Cependant, nous avons trouvé grâce à des simulations micromagnétiques que cette configuration monodomaine est fortement affectée par la variation locale du diamètre. L'étude en particulier du champ de fuite mais aussi du champ démagnétisant à l'intérieur des nanofils a mis en évidence le rôle prépondérant des charges magnétiques aux zones de variation de diamètre. De plus l'aimantation présente une structure plus compliquée qu'un simple alignement le long de l'axe du fil. Enfin les résultats que j'ai obtenus ont abouti à une interprétation différente d'expériences précédentes en MFM

Index

Introduction 1

Single element nanowires 2

Multilayered nanowires 4

New prospects in magnetic devices based on nanowires 6

Objectives and outline of the Thesis 10

References 13

Chapter 1: Magnetic properties 19

1.1 Introduction 19

1.2 Microscopic origin of magnetism 19

1.3 Ferromagnetic properties 22

1.4 Micromagnetic energy 23

1.4.1 Exchange energy 23

1.4.2 Zeeman energy 24

1.4.3 Magnetocrystalline energy 24

1.4.4 Demagnetizing energy (or magnetostatic energy) 25

1.4.5 Magnetostriction and stress energy 26

1.4.6 Comparison of different energies 27

1.5 Magnetic domains 28

1.6 Magnetic states in magnetic nanowires 30

1.7 Micromagnetic simulations 35

References 38

Chapter 2: Experimental techniques 41

2.1 Introduction 41

2.2 Growth of nanowires 41

2.2.1 Vapour-liquid-solid (VLS) technique 42

2.2.2 Laser-assisted growth 43

2.2.3 Thermal evaporation 44

2.2.4 Lithography from thin films and other modern methods 45

2.2.5 Solution methods 45

2.2.6 Template-based synthesis 46

2.3 Electrodeposition 47

2.3.1 Faraday laws 50

2.3.2 Electron transfer 50

2.3.3 Parameters involved during the electrodeposition 52

2.4 Imaging magnetic domains 53

2.5 TEM imaging 56

2.5.1 Image formation in TEM 58

2.5.2 Electron beam phase shift measurements: recording the magnetism 63

2.5.3 The objective lens 65

2.6 Electron holography 68

2.6.1 Off-axis electron holography 68

2.6.2 Phase reconstruction 71

2.6.3 Separation of the phase shift contributions 73

References 79

Chapter 3: Methodology 89

3.1 Introduction 89

3.2 Growth of nanowires 89

3.2.1 Growth of Co/Cu nanowires in the template 89

3.2.2 Growth of Ni nanowires in the template 93

3.2.3 Dissolution of the membrane 96

3.2.4 Observations of Co/Cu and Ni isolated nanowires 97

3.2.4.1 Ni nanowires 98

3.3 Magnetic configurations in Co/Cu nanowires 99

3.3.1 Electron holography 100

3.3.2 Hologram reconstruction 104

3.3.3 Important facts to consider in phase shift maps 110

3.3.4 Measurement of the Co magnetization 114

3.3.5 Micromagnetic simulations 115

References 119

Chapter 4: Co/Cu multilayered nanowires 121

4.1 Introduction 121

4.2 Nanowires growth 132

4.3 Structural and morphological properties 133

4.3.1 TEM analyses of the Co/Cu nanowires 133

4.3.2 Pore size and nanowires diameters 137

4.4 Local chemical analysis 141

4.5 Magnetic configurations in Co/Cu nanowires 148

4.5.1 Co/Cu = 25nm/15nm 148

4.5.2 Co/Cu = 25nm/45nm 157

4.5.3 Co/Cu = 50nm/50nm 163

4.5.4 Co/Cu = 100nm/100nm 169

4.5.5 Summary of magnetic states 176

4.6 Magnetic properties of Co nanocylinders 178

4.7 Relation between magnetic states in Co/Cu NWs and Co nanocylinders phase diagrams 186

4.7.1 Co/Cu = 25nm/15nm 186

4.7.2 Co/Cu = 25nm/45nm 187

4.7.3 Co/Cu = 50nm/50nm 187

4.7.4 Co/Cu = 100nm/100nm 188

4.8 Aspect ratio and influence of the diameter and thickness on the magnetic states 189

References 193

Chapter 5: FeCoCu diameter-modulated nanowires 199

5.1 Introduction 199

5.2 Growth of nanowires 204

5.3 Isolated FeCoCu nanowires, structural and morphological properties 206

5.4 Magnetic remnant configuration of FeCoCu NWs 209

5.4.1 Micromagnetic simulations in FeCoCu NWs 213

References 225

Conclusions and outlooks 229

Résumé étendu de la thèse 237

Introduction

The achievement of the deposition of thin films in the middle of the 20th century gave access to new properties in the field of material science. These 2D-materials could be synthetized thanks to rapid advances in vacuum technology. In thin films, deviations from the properties of the corresponding bulk materials arise because of their small thickness, large surface-to-volume ratio, and dimensions comparable to characteristic length (electronic, magnetic…). 1D (nanowires) and 0D (nanodots) materials have been synthetized since then and open access to new device architectures.

Carbon nanotubes are the most famous example of one-dimensional materials. But the development of synthesis methods allowed for the nanowire growth with others various materials (semiconductors [1], [2], metal [3], [4], oxides [5]–[7]…). These nanowires can be either single-element or include several materials. They can be grown by physical and chemical methods as vapour-liquid-solid (VLS) technique [8], [9], thermal evaporation [10], lift-off process and e-beam lithography [11]–[14], focused ion beam (FIB) [15], solution [16]–[18] and template-based synthesis [19]–[21] among others.

Beyond carbon nanotubes, known for the mechanical and electrical peculiar properties [22]–[24], nanowire applications are wide and can be found in many fields like optics [25], field emission transistors[26] designs and magnetic memories based on phenomena like magnetoresistance [27], spin-torque [28], spin accumulation [29], and domain walls movement [30].

In the next sections, we are going to discuss about the single element and multilayered magnetic nanowires and show some of their most important and recent

applications. The possible magnetic states in single and multilayer magnetic nanowires are also presented.

Single element nanowires

Applications for mono element nanowires are found in various fields, and only two of them will be detailed hereafter. Let's cite nanophotonics or medicine.

The imminent limitations of electronic integrated circuits are stimulating intense activity in the area of nanophotonics for the development of on-chip optical components [31]. Optical processing of data at the nanometre scale is promising for overcome these limitations, but requires the development of a toolbox of components including emitters, detectors, modulators, wave guides and switches. Piccione et al. [25] have demonstrated on-chip all-optical switching using individual CdS nanowires (NWs) and leveraged the concept into a working all-optical, semiconductor nanowire NAND logic gate. Another example of nanowires used for nanophotonics field are the nanolasers. These nanolasers have emerged as a new class of miniaturized semiconductor lasers that are potentially cost-effective and easier to integrate [32].

Ni nanowires were used to probe the cellular traction forces [33]. They also work as a tool for the cell manipulation [34] and outperform the commercial magnetic beads. M. Contreras and her team [35] also used Ni nanowires to kill cancer cells. The idea is to exploit a magneto-mechanical effect, where nanowires cause cell death through vibrating in a low power magnetic field. Specifically, magnetic nanowires were combined with an alternating magnetic field, with variable intensity and frequency. After the magnetic field application, cell activity was measured at the mitochondrial scale to know the level of damage produced inside the cells. Considering all these applications, nanowires are a versatile structure with a very promising present and future.

Single element nanowires have also found various applications in magnetism and are explored for storage applications. The problem of storage limit has evolved with technology. A first report in 1997 on the thermal stability problem of magnetically stored information [36] introduced a projected upper limit of about 36 Gbit/in^2. But the recent technology has already achieved densities over one order of magnitude over this value. The difference between the projected and the real values for the upper limit reside in the advances on the non-magnetic aspects of the recording technology as the mechanical actuator systems used to position the read and write sensors. A more recent study suggests that the main limitation is essentially determined by the maximum tolerable bit error rate and certain materials parameters, which include the saturation magnetization of the recording medium. They show that storage densities will be limited to 15 to 20 Tbit/in^2 unless technology can move beyond the currently available write field magnitudes [37]. Actually, some companies like Sony and Fujifilm have developed data storage on tape of 185 and 154 Tb/in^2 [38], [39].

Magnetic nanowire arrays from a single element could be used in ultra-high density magnetic storage devices. In this case, each nanowire can store one or more bit of information and, thanks to their inherent anisotropy, they can lower the limit where each bit size is limited by the size of the single magnetic domain. The fundamental study of domain wall pinning is thus of great interest. Micromagnetic simulations were used to investigate the propagation of a domain wall in magnetic nanowires[40], [41] Forster et al. [40] showed that for a wire diameter $d < 20\ nm$ just transverse walls are formed and for $d > 20\ nm$ vortex walls are formed. For $d = 20\ nm$ the energy of the transverse and the vortex walls is rather similar. The velocity of a vortex wall is about 1.3 times higher than the wall velocity of the transverse wall. Between the vortex walls a Bloch point wall can be observed in the middle of the wire for the simulations. This Bloch point was observed experimentally by combining surface and transmission x-ray

magnetic circular dichroism photoemission electron microscopy by Da Col and co-workers [42]. He et al. [43] used notched permalloy nanowires to pin transversal domain walls (TDW). In recent reports Da Col et al. implemented two methods for the controlled nucleation of domain walls in cylindrical permalloy nanowires [44]. Fast magnetic domain wall motion has been reached in ring-shaped nanowires of CoFeB showing the higher average velocity up to 550 m/s that has been reported [45].

Multilayered nanowires

Multilayered nanowires gained special attention with the study of GMR phenomena [46]–[48] which consist in a large modification of the electrical resistance in a structure composed of alternating magnetic/non-magnetic (metal) layers when a magnetic field is applied to this. The changes can be as large as 150% [46], [47] from the original resistance (measured at the remnant state) when a magnetic field is applied at low temperature and 15% for Co/Cu nanowires at room temperature [49]. Similar results were obtained by several authors [50]–[53]. The GMR was first observed in films consisting of a magnetic/non-magnetic multilayer films: these first observations were made in the current in-plane geometry (CIP), where the current flows in the same direction as the layers planes (Figure 1a)). The current perpendicular to plane (CPP) configuration was also investigated [54], [55]. This last configuration is especially attractive because of the higher GMR values that can reach 3 to 10 times the values obtained with the CIP configuration in thin films. In addition micron thick multilayers can be used [27]. Later the fundamental study of the CPP configuration on GMR has revealed the spin accumulation effect [29] which governs the propagation of a spin-polarized current (spin injection) through a succession of magnetic and nonmagnetic materials and plays an important role in all the actual developments of spintronics [48]. The multilayered nanowires combining magnetic/non-magnetic materials appear as the

best structures for the study of the temperature dependence of CPP-GMR, as the high aspect ratio leads to large signals and precise measurements on GMR, spin accumulation and injection [27]. Figure 1b) presents a multi-layered nanowire used for the CPP configuration.

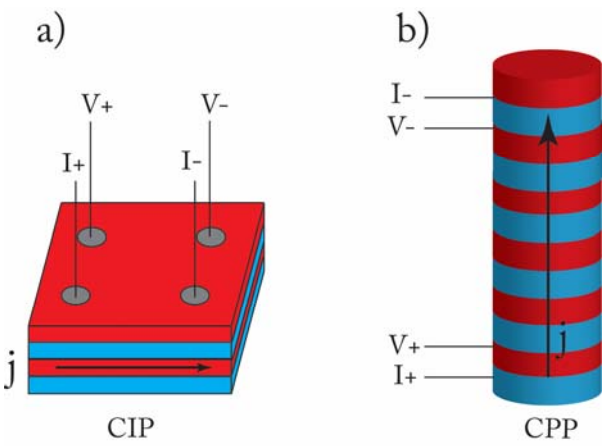

Figure 1. Scheme of disposition for a measure of magnetoresistance in: a) CIP configuration in thin films and b) CPP configuration in NW.

Magnetic multilayered nanowires composed of magnetic/magnetic materials also present others interesting properties and applications. Using Co/Ni NW , Ivanov et al. [56] have created a periodic potential for domain wall pinning: the pinning sites are generated by the interfaces between the materials of different magnetic anisotropies (hcp for Co and fcc for Ni). These magnetic nanowires are attractive materials for the next generation data storage devices owing to the theoretically achievable high domain wall velocity and their efficient fabrication. Other authors have reported magnetic nanowires composed of two kinds of segments of CoNi alloys [57] and also modulations in the shape of Co and FeCoCu NWs [58], [59] for similar application making use of the domain wall control.

New prospects in magnetic devices based on nanowires

The new non-volatile memory concepts include phase change memory [61], [62], ferroelectric memory [63] and resistive random access memory (ReRAM) or memristor. These memories are promising as an alternative to flash memory due to the structural simplicity and the memory performance, including high switching speed and endurance [64]. Alternatively, domain wall memories or racetrack memory concept as a universal data storage device has stimulated much research. In these devices domain walls in magnetic nanowires are used as bits of information which can be shifted to locate them at the position of the read or write head, without the need to move physically any part of the device. The research in materials for promising properties of domain walls and domain wall motions has increased in the last years. However two critical parameters need to be optimized: the first one is the lateral size of the domain wall which directly governs the possible information density, and the second one is the domain wall movement which is related to the pinning/depinning process. This last parameter will determine the access time and energy consumption [65]. Figure 2 shows the horizontal magnetic domain-wall racetrack memory model proposed by S. S. P. Parkin [66] based on magnetic nanowires in which magnetic domains act as the bits. Here the nanowire where the domain walls are located as well as the read and write heads are fixed, leading to much faster achievable access time and, in particular, eliminating all mechanical motion. This kind of memories present velocities of domain walls about 110m/s but recently velocities of 550m/s has been achieved in ring-shaped, rough-edged magnetic nanowire on top of a piezoelectric disk, by strain-mediated voltage-driven (i.e. application of a static and dynamic voltage to the piezoelectric disk). This velocity is comparable to current-driven wall velocity [44].

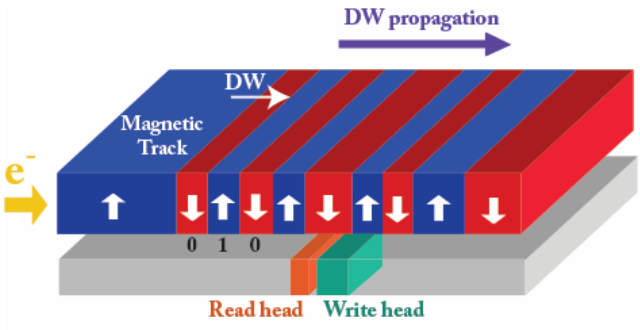

Figure 2. Racetrack memory proposed by S.S. Parkin et al. [66].

Magnetic nanowires also promise an alternate route to traditional semiconductor electronics. A complete logic architecture can be constructed using planar magnetic nanowires with simple geometric designs. They can be integrated together into one circuit [67]. Devices made of hybrid systems of piezoelectric/spin-valve nanowires can generate sizeable anisotropy changes, through induced strains driven by applied electric fields, creating magnetic domain wall gates. The same principle can be used for the racetrack memory. Figure 3 shows a design of a multi-input *NOR* logic function by using voltage control of elementary domain wall gates. Control A is used for current-driven DW motion, and the writing line is used to generate a domain wall. Inputs B_0 and B_1 are piezoelectric-controlled DW gates, and output C serves as read out for the magnetization direction in the wire through the tunnelling magnetoresistance effect [68].

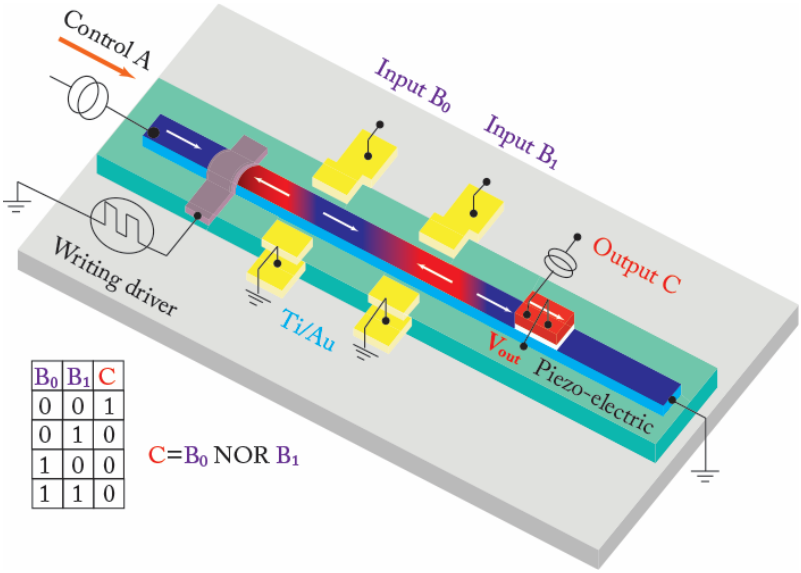

Figure 3. Scheme of a multi-input NOR logic gate with current-drive DW motion [67].

The working process of this circuit is detailed hereafter. First, a DW is nucleated inside the wire with the Oersted field generated by current flowing through the write line. If either or both gate voltages B_0 and B_1 are applied (that is the *1* state), then a local stress is induced due to the piezo-electric layer, followed by the DW blockade (due to the local stress ≈ 43 MPa), which leaves the output *C* in the *0* state. However, if both gate voltages are off (inputs B_0 and B_1 set to *0*), then the generated DW can propagate freely along the wire, driven by the spin-polarized currents controlled by *A*, leading to magnetization reversal at the output *C* and thereby switching this state to *1*.

Magnetic and particularly multilayered nanowires are also promising candidates to produce spin-torque nano-oscillators (STO) for on-chip microwave signal sources. For application purposes, they are expected to have a broad working frequency, narrow spectral linewidth, high output power and low power consumption. Zhang et al. [68] have proposed a new kind of spin transfer nano-oscillators on nanocylinders composed of three layers, a magnetically fixed layer, a non-magnetic spacer and a magnetically free

layer. They showed by simulations that a magnetic skyrmion or a group of them can be excited into oscillation by a spin-polarized current. The working frequency of this oscillators can range from nearly 0Hz to GHz with a linewidth about 1MHz. Furthermore, this device can work at current density magnitude as small as 10^8 A.m^{-2}.

Spin current applied to a nanoscale region of a ferromagnet can act as negative magnetic damping factor and thereby excite self-oscillations of its magnetization. In contrast, spin torque uniformly applied to the magnetization of an extended ferromagnetic film does not generate self-oscillatory magnetic dynamics but leads to the reduction of the saturation magnetization. Duan et al. [70] have worked on a system with a ferromagnetic nanowire of Pt(5nm)/Py(5nm) such as that shown in Figure 4. They have reported the coherent self-oscillations of magnetization in the ferromagnetic layer of the nanowire serving as the active region of a spin torque oscillator driven by spin-orbit torques. The system shows microwave emission around 6GHz.

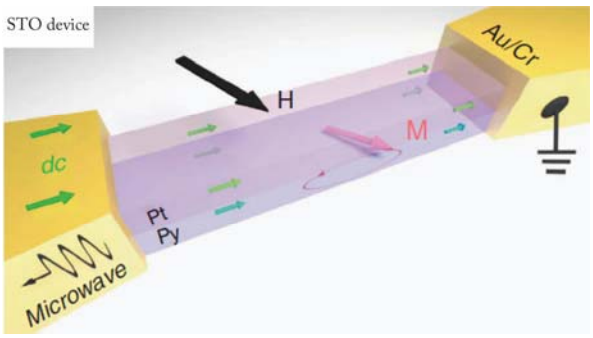

Figure 4. Scheme of a Pt/Py nanowire STO device: external magnetic field is shown as a black arrow, precessing Py magnetization is shown as a red arrow, green arrows indicate the flow of the direct electric current applied to the nanowire, microwave voltage generated by the sample is depicted as a wave with an arrow [69].

Mourik et al. [71] have proposed a model of STO using magnetic nanowires. This model has been demonstrated by simulations; they designed a scheme to use magnetic nanowire with a rectangular section as it is shown in Figure 5.

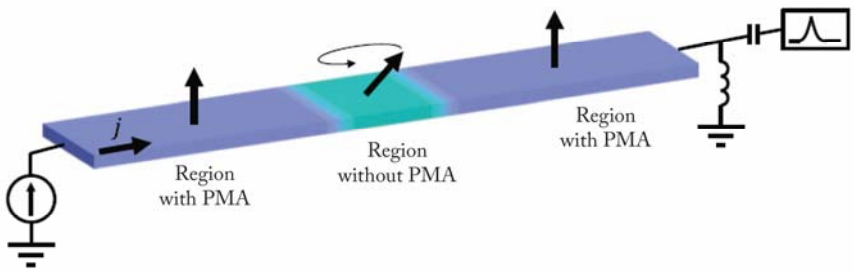

Figure 5. Schematic of the in-line spin-torque nano-oscillator proposed by Mourik et al. [70]

These thin nanowires should have perpendicular magnetic anisotropy (PMA) so that the magnetization points out-of-plane, except for a small region without PMA. Under these conditions, the competition between the in-plane shape anisotropy and the exchange energy leaves the magnetization canted between the in-plane and out-plane directions. Simply sourcing a current through the nanowire introduces the necessary spin-torque-transfer (STT) and induces a spin wave traveling along the nanowire length, composed of spins precessing around the out-of-plane directions. If there are several regions of no-PMA, the nanowire will present multiple STO, that will be coupled between them retaining the phase and this leads to amplified signal and reduces the linewidth of emission. Mourik et al. [70] also proposed the way to implement the scheme in practice. Nanowires are patterned from a PMA material such as Co/Ni bilayers [71] that are few nm thick and a few tens of nm wide. Some regions can be stripped of their PMA using ion irradiation [72].

Objectives and outline of the Thesis

Magnetic nanowires are also particularly interesting for fundamental studies of magnetic interactions at the nanoscale and very good candidates to produce non-volatile magnetic memory devices or spin-torque nano-oscillators connected in series to increase radio frequency (RF) output power [28], [73], [74]. However the technical

achievements in spintronic require a detailed description of the magnetic states in each layer at the remnant state.

The aim of this thesis is the development of qualitative and quantitative studies of local magnetic states of Co-based nanowires such as Co/Cu multilayered nanowires, and $Fe_{28}Co_{67}Cu_5$ (FeCoCu) diameter modulated nanowires by Electron Holography (EH). For the system of Co/Cu nanowires, a magnetic field is applied perpendicular and parallel to the axis of the wire and the remnant state is quantitatively mapped. Different thicknesses of Co and Cu layers are proposed in order to study the magnetic configurations and the effect of the dipolar coupling between the layers. The remnant state has been also studied in FeCoCu modulated nanowires for observing the internal and external magnetic induction. In order to reveal the 3D magnetic state in both systems, micromagnetic simulations are performed and compared qualitatively and quantitatively.

This thesis work has been structured in 5 chapters, conclusions and outlooks after the present introduction:

In *Chapter 1*: "*Magnetic properties*", the basic concepts in magnetism are described. The microscopic origin of the magnetism and the ferromagnetic properties of the materials are discussed. An overview of the micromagnetic energies that contribute to the ferromagnetic system is followed by a discussion about the magnetic states in magnetic nanowires. Finally, I will present the importance to perform micromagnetic simulations and the code used during this work.

In *Chapter 2*: "*Experimental Techniques*", I will give a description of a wide range of techniques to elaborate nanowires, with a special emphasis on the template-based synthesis by the electrodeposition process used to fabricate the nanowires studied in this

work. Then the chapter is dedicated for introducing the image formation in a TEM and how the magnetic properties can be observed by the Electron Holography technique.

The *Chapter 3*: *"Methodology*", explains the procedures and the experimental methodology followed. Along the first part, a detailed description of the elaboration process of nanowires, then the procedure to perform electro holography and the treatment of the data is shown. Also the procedure to perform micromagnetic simulations is discussed.

The *Chapter 4*: *"Co/Cu multilayered nanowires*", will show the qualitative and quantitative study of Co/Cu multilayered nanowires at the remnant state after applying a magnetic field perpendicular/parallel to the axis of the wire. This study performed by EH is supported by micromagnetic simulations. Different magnetic states are revealed which depend strongly on Co and Cu thicknesses balanced by the diameter of the NW.

For the *Chapter 5*: "*FeCoCu diameter-modulated nanowires*", a detailed description by EH and micromagnetic simulations of the magnetic state inside and outside the nanowires are performed. The importance of the stray field generated by this segments is shown and the interesting features of the magnetic states in the larger and smaller diameter segments are discussed.

Conclusions and outlooks

References

[1] C. M. Lieber, "Semiconductor nanowires: A platform for nanoscience and nanotechnology," *MRS Bull.*, vol. 36, no. 12, pp. 1052–1063, Dec. 2011.

[2] L. Chen, W. Lu, and C. M. Lieber, "Chapter 1. Semiconductor Nanowire Growth and Integration," in *RSC Smart Materials*, W. Lu and J. Xiang, Eds. Cambridge: Royal Society of Chemistry, 2014, pp. 1–53.

[3] P.-C. Hsu *et al.*, "Performance enhancement of metal nanowire transparent conducting electrodes by mesoscale metal wires," *Nat. Commun.*, vol. 4, Sep. 2013.

[4] J.-Y. Lee, S. T. Connor, Y. Cui, and P. Peumans, "Solution-Processed Metal Nanowire Mesh Transparent Electrodes," *Nano Lett.*, vol. 8, no. 2, pp. 689–692, Feb. 2008.

[5] E. Comini and G. Sberveglieri, "Metal oxide nanowires as chemical sensors," *Mater. Today*, vol. 13, no. 7, pp. 36–44, 2010.

[6] J. Cui, "Zinc oxide nanowires," *Mater. Charact.*, vol. 64, pp. 43–52, Feb. 2012.

[7] D. Han, X. Zhang, Z. Wu, Z. Hua, Z. Wang, and S. Yang, "Synthesis and magnetic properties of complex oxides La0.67Sr0.33MnO3 nanowire arrays," *Ceram. Int.*, Jul. 2016.

[8] R. S. Wagner and W. C. Ellis, "VAPOR-LIQUID-SOLID MECHANISM OF SINGLE CRYSTAL GROWTH," *Appl. Phys. Lett.*, vol. 4, no. 5, p. 89, 1964.

[9] Y. Li, Y. Wang, S. Ryu, A. F. Marshall, W. Cai, and P. C. McIntyre, "Spontaneous, Defect-Free Kinking via Capillary Instability during Vapor–Liquid–Solid Nanowire Growth," *Nano Lett.*, vol. 16, no. 3, pp. 1713–1718, Mar. 2016.

[10] Z. R. Dai, Z. W. Pan, and Z. L. Wang, "Novel nanostructures of functional oxides synthesized by thermal evaporation," *Adv. Funct. Mater.*, vol. 13, no. 1, pp. 9–24, 2003.

[11] A. Pierret *et al.*, "Generic nano-imprint process for fabrication of nanowire arrays," *Nanotechnology*, vol. 21, no. 6, p. 65305, Feb. 2010.

[12] R.-H. Horng, H.-I. Lin, and D.-S. Wuu, "ZnO nanowires lift-off from silicon substrate embedded in flexible films," in *Nanoelectronics Conference (INEC), 2013 IEEE 5th International*, 2013, pp. 1–3.

[13] P. Mohan, J. Motohisa, and T. Fukui, "Controlled growth of highly uniform, axial/radial direction-defined, individually addressable InP nanowire arrays," *Nanotechnology*, vol. 16, no. 12, pp. 2903–2907, Dec. 2005.

[14] S. F. A. Rahman *et al.*, "Nanowire Formation Using Electron Beam Lithography," 2009, pp. 504–508.

[15] A. Fernández-Pacheco *et al.*, "Three dimensional magnetic nanowires grown by focused electron-beam induced deposition," *Sci. Rep.*, vol. 3, Mar. 2013.

[16] L.-M. Lacroix, R. Arenal, and G. Viau, "Dynamic HAADF-STEM Observation of a Single-Atom Chain as the Transient State of Gold Ultrathin Nanowire Breakdown," *J. Am. Chem. Soc.*, vol. 136, no. 38, pp. 13075–13077, Sep. 2014.

[17] A. Loubat *et al.*, "Ultrathin Gold Nanowires: Soft-Templating versus Liquid Phase Synthesis, a Quantitative Study," *J. Phys. Chem. C*, vol. 119, no. 8, pp. 4422–4430, Feb. 2015.

[18] F. Ott *et al.*, "Soft chemistry nanowires for permanent magnet fabrication," in *Magnetic Nano- and Microwires*, Elsevier, 2015, pp. 629–651.

[19] T. L. Wade and J.-E. Wegrowe, "Template synthesis of nanomaterials," *Eur. Phys. J. Appl. Phys.*, vol. 29, no. 1, pp. 3–22, Jan. 2005.

[20] M. Vázquez *et al.*, "Arrays of Ni nanowires in alumina membranes: magnetic properties and spatial ordering," *Eur. Phys. J. B*, vol. 40, no. 4, pp. 489–497, Aug. 2004.

[21] D. L. Zagorskiy *et al.*, "Track Pore Matrixes for the Preparation of Co, Ni and Fe Nanowires: Electrodeposition and their Properties," *Phys. Procedia*, vol. 80, pp. 144–147, 2015.

[22] H. Dai, "Carbon Nanotubes: Synthesis, Integration, and Properties," *Acc. Chem. Res.*, vol. 35, no. 12, pp. 1035–1044, Dec. 2002.

[23] M. M. J. Treacy, T. W. Ebbesen, and J. M. Gibson, "Exceptionally high Young's modulus observed for individual carbon nanotubes," *Nature*, vol. 381, no. 6584, pp. 678–680, Jun. 1996.

[24] P. R. Bandaru, "Electrical Properties and Applications of Carbon Nanotube Structures," *J. Nanosci. Nanotechnol.*, vol. 7, no. 4, pp. 1239–1267, Apr. 2007.

[25] B. Piccione, C.-H. Cho, L. K. van Vugt, and R. Agarwal, "All-optical active switching in individual semiconductor nanowires," *Nat. Nanotechnol.*, vol. 7, no. 10, pp. 640–645, Sep. 2012.

[26] G.-C. Yi, Ed., *Semiconductor Nanostructures for Optoelectronic Devices*. Berlin, Heidelberg: Springer Berlin Heidelberg, 2012.

[27] A. Fert and L. Piraux, "Magnetic nanowires," *J. Magn. Magn. Mater.*, vol. 200, no. 1, pp. 338–358, 1999.

[28] J.-V. Kim, "Spin-Torque Oscillators," in *Solid State Physics*, vol. 63, Elsevier, 2012, pp. 217–294.

[29] T. Valet and A. Fert, "Theory of the perpendicular magnetoresistance in magnetic multilayers," *Phys. Rev. B*, vol. 48, no. 10, p. 7099, 1993.

[30] L. O'Brien *et al.*, "Tunable Remote Pinning of Domain Walls in Magnetic Nanowires," *Phys. Rev. Lett.*, vol. 106, no. 8, Feb. 2011.

[31] R. Kirchain and L. Kimerling, "A roadmap for nanophotonics," *Nat Photon*, vol. 1, no. 6, pp. 303–305, Jun. 2007.

[32] C. Couteau, A. Larrue, C. Wilhelm, and C. Soci, "Nanowire Lasers," *Nanophotonics*, vol. 4, no. 1, Jan. 2015.

[33] Y.-C. Lin, C. M. Kramer, C. S. Chen, and D. H. Reich, "Probing cellular traction forces with magnetic nanowires and microfabricated force sensor arrays," *Nanotechnology*, vol. 23, no. 7, p. 75101, Feb. 2012.

[34] A. Hultgren, M. Tanase, C. S. Chen, G. J. Meyer, and D. H. Reich, "Cell manipulation using magnetic nanowires," *J. Appl. Phys.*, vol. 93, no. 10, p. 7554, 2003.

[35] M. Contreras, R. Sougrat, A. Zaher, T. Ravasi, and J. Kosel, "Non-chemotoxic induction of cancer cell death using magnetic nanowires," *Int. J. Nanomedicine*, p. 2141, Mar. 2015.

[36] S. H. Charap, P.-L. Lu, and Y. He, "Thermal stability of recorded information at high densities," *Magn. IEEE Trans. On*, vol. 33, no. 1, pp. 978–983, 1997.

[37] R. F. L. Evans, R. W. Chantrell, U. Nowak, A. Lyberatos, and H.-J. Richter, "Thermally induced error: Density limit for magnetic data storage," *Appl. Phys. Lett.*, vol. 100, no. 10, p. 102402, 2012.

[38] "FujiFilm achieves 154TB data storage record on Tape," *StorageServers*, 20-May-2014. .

[39] "Sony creates an 185TB tape cartridge!," *StorageServers*, 01-May-2014. .

[40] H. Forster *et al.*, "Domain wall motion in nanowires using moving grids (invited)," *J. Appl. Phys.*, vol. 91, no. 10, p. 6914, 2002.

[41] R. Hertel, "Computational micromagnetism of magnetization processes in nickel nanowires," *J. Magn. Magn. Mater.*, vol. 249, no. 1, pp. 251–256, 2002.

[42] S. Da Col *et al.*, "Observation of Bloch-point domain walls in cylindrical magnetic nanowires," *Phys. Rev. B*, vol. 89, no. 18, May 2014.

[43] K. He, D. J. Smith, and M. R. McCartney, "Observation of asymmetrical pinning of domain walls in notched Permalloy nanowires using electron holography," *Appl. Phys. Lett.*, vol. 95, no. 18, p. 182507, 2009.

[44] S. Da Col *et al.*, "Nucleation, imaging and motion of magnetic domain walls in cylindrical nanowires," *ArXiv Prepr. ArXiv160307240*, 2016.

[45] J.-M. Hu *et al.*, "Fast Magnetic Domain-Wall Motion in a Ring-Shaped Nanowire Driven by a Voltage," *Nano Lett.*, Mar. 2016.

[46] M. N. Baibich *et al.*, "Giant Magnetoresistance of (001)Fe/(001)Cr Magnetic Superlattices," *Phys. Rev. Lett.*, vol. 61, no. 21, pp. 2472–2475, Nov. 1988.

[47] G. Binasch, P. Grünberg, F. Saurenbach, and W. Zinn, "Enhanced magnetoresistance in layered magnetic structures with antiferromagnetic interlayer exchange," *Phys. Rev. B*, vol. 39, no. 7, p. 4828, 1989.

[48] A. Fert, "Nobel Lecture: Origin, development, and future of spintronics," *Rev. Mod. Phys.*, vol. 80, no. 4, pp. 1517–1530, Dec. 2008.

[49] L. Piraux *et al.*, "Giant magnetoresistance in magnetic multilayered nanowires," *Appl. Phys. Lett.*, vol. 65, no. 19, p. 2484, 1994.

[50] A. Blondel, J. P. Meier, B. Doudin, and J.-P. Ansermet, "Giant magnetoresistance of nanowires of multilayers," *Appl. Phys. Lett.*, vol. 65, no. 23, p. 3019, 1994.

[51] T. Ohgai, N. Goya, Y. Zenimoto, K. Takao, M. Nakai, and S. Hasuo, "CPP-GMR of Co/Cu Multilayered Nanowires Electrodeposited into Anodized Aluminum Oxide Nanochannels with Large Aspect Ratio," *ECS Trans.*, vol. 50, no. 10, pp. 201–206, Mar. 2013.

[52] F. Nasirpouri, P. Southern, M. Ghorbani, A. Iraji zad, and W. Schwarzacher, "GMR in multilayered nanowires electrodeposited in track-etched polyester and polycarbonate membranes," *J. Magn. Magn. Mater.*, vol. 308, no. 1, pp. 35–39, Jan. 2007.

[53] D. Pullini, D. Busquets, A. Ruotolo, G. Innocenti, and V. Amigó, "Insights into pulsed electrodeposition of GMR multilayered nanowires," *J. Magn. Magn. Mater.*, vol. 316, no. 2, pp. e242–e245, Sep. 2007.

[54] W. P. Pratt Jr, S.-F. Lee, J. M. Slaughter, R. Loloee, P. A. Schroeder, and J. Bass, "Perpendicular giant magnetoresistances of Ag/Co multilayers," *Phys. Rev. Lett.*, vol. 66, no. 23, p. 3060, 1991.

[55] J. Bass and W. P. P. Jr, "Current-perpendicular (CPP) magnetoresistance in magnetic metallic multilayers," *J. Magn. Magn. Mater.*, vol. 200, no. 1–3, pp. 274–289, 1999.

[56] Y. P. Ivanov, A. Chuvilin, S. Lopatin, and J. Kosel, "Modulated Magnetic Nanowires for Controlling Domain Wall Motion: Toward 3D Magnetic Memories," *ACS Nano*, vol. 10, no. 5, pp. 5326–5332, May 2016.

[57] J. Cantu-Valle *et al.*, "Quantitative magnetometry analysis and structural characterization of multisegmented cobalt–nickel nanowires," *J. Magn. Magn. Mater.*, vol. 379, pp. 294–299, Apr. 2015.

[58] I. Minguez-Bacho, S. Rodriguez-López, M. Vázquez, M. Hernández-Vélez, and K. Nielsch, "Electrochemical synthesis and magnetic characterization of periodically modulated Co nanowires," *Nanotechnology*, vol. 25, no. 14, p. 145301, Apr. 2014.

[59] C. Bran *et al.*, "Spin configuration of cylindrical bamboo-like magnetic nanowires," *J Mater Chem C*, vol. 4, no. 5, pp. 978–984, 2016.

[60] G. W. Burr *et al.*, "Phase change memory technology," *J. Vac. Sci. Technol. B*, vol. 28, no. 2, pp. 223–262, 2010.

[61] W. W. Koelmans, A. Sebastian, V. P. Jonnalagadda, D. Krebs, L. Dellmann, and E. Eleftheriou, "Projected phase-change memory devices," *Nat. Commun.*, vol. 6, p. 8181, Sep. 2015.

[62] S. K. Hwang *et al.*, "Non-Volatile Ferroelectric Memory with Position-Addressable Polymer Semiconducting Nanowire," *Small*, vol. 10, no. 10, pp. 1976–1984, May 2014.

[63] J. J. Yang, D. B. Strukov, and D. R. Stewart, "Memristive devices for computing," *Nat. Nanotechnol.*, vol. 8, no. 1, pp. 13–24, Dec. 2012.

[64] M. Foerster, O. Boulle, S. Esefelder, R. Mattheis, and M. Kläui, "Domain Wall Memory Device," in *Handbook of Spintronics*, Y. Xu, D. D. Awschalom, and J. Nitta, Eds. Dordrecht: Springer Netherlands, 2015, pp. 1–46.

[65] S. S. Parkin, M. Hayashi, and L. Thomas, "Magnetic domain-wall racetrack memory," *Science*, vol. 320, no. 5873, pp. 190–194, 2008.

[66] D. A. Allwood, G. Xiong, C. C. Faulkner, D. Atkinson, D. Petit, and R. P. Cowburn, "Magnetic domain-wall logic," *Science*, vol. 309, no. 5741, pp. 1688–1692, 2005.

[67] N. Lei *et al.*, "Strain-controlled magnetic domain wall propagation in hybrid piezoelectric/ferromagnetic structures," *Nat. Commun.*, vol. 4, p. 1378, Jan. 2013.

[68] S. Zhang *et al.*, "Current-induced magnetic skyrmions oscillator," *New J. Phys.*, vol. 17, no. 2, p. 23061, Feb. 2015.

[69] Z. Duan *et al.*, "Nanowire spin torque oscillator driven by spin orbit torques," *Nat. Commun.*, vol. 5, p. 5616, Dec. 2014.

[70] R. A. van Mourik, T. Phung, S. S. P. Parkin, and B. Koopmans, "In-line spin-torque nano-oscillators in perpendicularly magnetized nanowires," *Phys. Rev. B*, vol. 93, no. 1, Jan. 2016.

[71] M. Haertinger, C. H. Back, S.-H. Yang, S. S. P. Parkin, and G. Woltersdorf, "Properties of Ni/Co multilayers as a function of the number of multilayer repetitions," *J. Phys. Appl. Phys.*, vol. 46, no. 17, p. 175001, May 2013.

[72] R. Hyndman *et al.*, "Modification of Co/Pt multilayers by gallium irradiation—Part 1: The effect on structural and magnetic properties," *J. Appl. Phys.*, vol. 90, no. 8, p. 3843, 2001.

[73] W. Rippard, M. Pufall, S. Kaka, T. Silva, S. Russek, and J. Katine, "Injection Locking and Phase Control of Spin Transfer Nano-oscillators," *Phys. Rev. Lett.*, vol. 95, no. 6, Aug. 2005.

[74] M. D. Stiles and J. Miltat, "Spin-transfer torque and dynamics," in *Spin dynamics in confined magnetic structures III*, Springer, 2006, pp. 225–308.

Chapter 1

Magnetic properties

1.1 Introduction

In this chapter, some basic schemes and concepts in magnetism are described, as well as the microscopic origin of the magnetism and the definition of magnetic domains. The importance of the energy minimization in the ferromagnetic systems is discussed and the different terms of energy are introduced. Finally I present the particular code of micromagnetic simulations used to obtain simulated magnetic phase images during this work.

1.2 Microscopic origin of magnetism

The magnetism has its origin in the magnetic moment of the atoms produced by the angular momenta of its constituent electrons. Each atomic electron presents two types of angular momenta: an *orbital moment* $\boldsymbol{l}_i$ associated with its orbital motion around the nucleus, and a *spin momentum* $\boldsymbol{s}_i$, intrinsic to its nature (see Figure 1.2.1. a). Most of the atoms are composed of several electrons, and their individual orbital angular moments $\boldsymbol{l}_i$ couple to produce a total orbital angular momentum $\boldsymbol{L} = \sum_i \boldsymbol{l}_i$. The same effect occurs with the spin angular moment $\boldsymbol{s}_i$ giving $\boldsymbol{S} = \sum_i \boldsymbol{s}_i$. Thus, the magnetic moment μ associated with each total atomic angular momentum can be expressed as:

$$\boldsymbol{m}_L = -\mu_B \boldsymbol{L} \qquad \textit{Eq. 1.2.1}$$

$$\boldsymbol{m}_S = -2\mu_B \boldsymbol{S} \qquad \textit{Eq. 1.2.2}$$

where μ_B is the *Bohr magneton*, a physical constant depending on the electron charge e, electron rest mass m, and reduced Planck constant $\hbar$: $\mu_B = e\hbar/2m = 9.274 \times 10^{-24} J/T$.

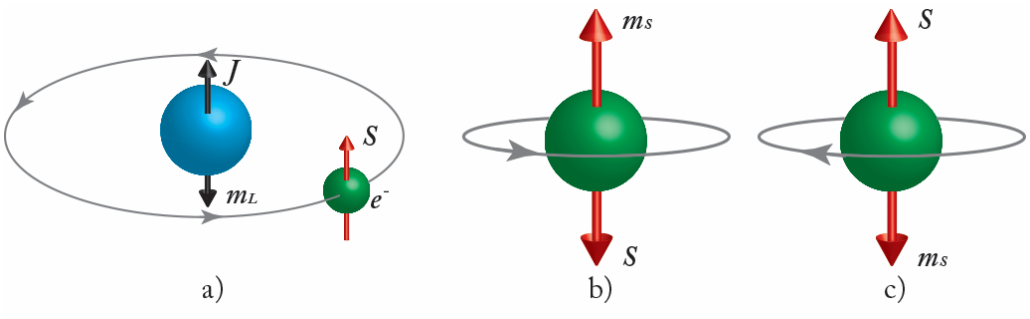

Figure 1.2.1. Schematic representation of the electron motion in an atom. a) Orbital motion around the nucleus, b) and c) spin motion around its own axis, two orientations are possible.

The total magnetic moment in the atom is then given by:

$$\boldsymbol{m} = -\mu_B(\boldsymbol{L} + 2\boldsymbol{S}) \qquad \text{Eq. 1.2.3}$$

According to the Pauli exclusion principle and the Hund's rules [1], [2], atoms with "close electronic shells" (their orbitals fully occupied) have a net magnetic moment equal to zero because, in each shell, the electrons are paired: there are as many electrons orbiting or spinning in one direction as in the opposite direction. Atoms with "partially filled electronic shells" have however unpaired electrons, usually in the outermost shell, that contribute producing a net *atomic magnetic moment* different to zero. Thus, unpaired electrons in the atomic shells produce the magnetic response of the materials. This atomic magnetic moment will be equal to:

$$\boldsymbol{m}_J = -g_J \mu_B \boldsymbol{J}$$
$$\boldsymbol{J} = \boldsymbol{L} + \boldsymbol{S} \qquad \text{Eq. 1.2.4}$$

where $\boldsymbol{J}$ is the total electronic angular momentum of the unpaired electrons and g_J is called the Landé g-factor, which is related to the different total quantum numbers *L, S,* and *J*

$$g = 1 + \frac{J(J+1) + S(S+1) - L(L+1)}{2J(J+1)} \qquad \textit{Eq. 1.2.5}$$

Even if Eq. 1.2.4 considers both orbital and spin angular momenta of the atom, the largest contribution to the total magnetic moment is due to the spin, which is for instance 10 times stronger that the orbital angular momentum, for instance, in the ferromagnetic elements Fe, Co and Ni elements [3]. In an arrangement of atoms (e.g., a crystal lattice), the atomic magnetic moments of neighbouring atoms interact with each other through a quantum phenomenon known as the *exchange interaction*. Proposed for the first time by Heisenberg in 1928 [2], [4], [5], two atoms with unpaired electrons of spins $\boldsymbol{S}_i$ and $\boldsymbol{S}_j$ interact with an energy ε:

$$\varepsilon = -2J_{ij}\boldsymbol{S}_i \cdot \boldsymbol{S}_j \qquad \textit{Eq. 1.2.6}$$

where J_{ij} is the exchange constant. If $J_{ij} > 0$, the energy is lowest when $\boldsymbol{S}_i$ is parallel to $\boldsymbol{S}_j$, while an antiparallel alignment of the spins will minimize the energy if $J_{ij} < 0$. Thus, the type of exchange interaction defines the type of magnetism: in the absence of an external magnetic field, a parallel alignment of spins produces a long-range *ferromagnetic* (*FM*) order, while an antiparallel alignment of neighbouring spins induces an *antiferromagnetic* (*AFM*) order.

1.3 Ferromagnetic properties

From a macroscopic point of view, a microscopic *ferromagnetic* order induces a *spontaneous magnetization* $\boldsymbol{M}$ at zero applied magnetic field, the magnetization being defined as the magnetic moment density per volume unit. The existence of a net magnetization produces a magnetic induction field inside and around the material, which results in the strong attractive or repulsive force that magnetic materials exert on other magnetic materials. The first theory explaining such spontaneous magnetization was postulated by P. Weiss in 1907 [2], [4], [6]. He considered that, in the site of each spin, there is an effective field produced by the interaction with the neighbouring spins. Thus, the effective induction field, $\boldsymbol{B}$, associate with the total magnetization of the system $\boldsymbol{M}$ is:

$$\boldsymbol{B} = \lambda_W \boldsymbol{M} \qquad \text{Eq. 1.3.1}$$

where λ_W is the mean field parameter that represents the strength of the interaction (*Weiss constant*). These ordered spins states could be altered by the temperature. When the temperature of the system increases, the thermal agitation decreases such long-range spin order. Above a critical temperature, called Curie temperature (T_C), the thermal excitation dominates and their magnetic moments are randomly oriented producing a *paramagnetic* state. Thus, Curie temperature and spontaneous magnetization are two characteristic parameters of ferromagnetic materials.

Another important feature of ferromagnetic materials is the fact that, even if the exchange interaction is strong enough to align all spins in the same direction at a microscopic scale, this state cannot be preserved macroscopically unless an external magnetic field is applied. At a micromagnetic scale, not only the exchange interaction and thermal excitation contribute to the internal energy of the system: others energy

contributions related to additional factors such as the crystal structure, the shape, the external magnetic field, stress and magnetostriction have to be taken into account.

1.4 Micromagnetic energy

The equilibrium state of a ferromagnetic material is determined by the minimization of the total "magnetic" Gibbs free energy of the system [7], [8]. This expression is composed of the sum of several energy contributions:

$$\varepsilon_{tot} = \varepsilon_{ex} + \varepsilon_K + \varepsilon_d + \varepsilon_{Ze} + \varepsilon_{ms} \qquad \textit{Eq. 1.4.1}$$

where the first three terms are intrinsic to the ferromagnetic material: exchange (ε_{ex}), magnetocrystalline anisotropy (ε_K) and demagnetizing (ε_d) energies. The fourth energy, the Zeeman energy (ε_{Ze}), is associated with the response of the material to the application of an external magnetic field. The last energy term is related to applied stress and magnetostriction (ε_{ms}). A description of each energy term is given in the following.

1.4.1 Exchange energy

It is caused by the exchange coupling between the spins which tends to align them up in the same or opposite direction. A detailed description about this contribution is made in the section 1.2. Other models such superexchange [1], [2], [4] (in oxides) or Ruderman-Kittel-Kasuya-Yoshida (RKKY) interaction [1], [2] (in metals) are used to describe indirect exchange interactions.

Involved with this exchange energy, the *exchange stiffness constant* or simply *exchange constant*, A is a measure of the force which acts to maintain the electron spin alignment. It can be expressed as:

$$A = JS^2 \frac{Z_c}{a_0} \qquad \textit{Eq. 1.4.2}$$

where S is the value of the individual spins, a_0 is the lattice parameter, and Z_c is the number of atoms in the unit cell. The SI unit is [J/m].

1.4.2 Zeeman energy

The existence of an applied magnetic field influences the resulting magnetization. This energy is minimized or maximized when the magnetic moments are aligned parallel or antiparallel respectively to the applied magnetic field and is given by:

$$\varepsilon_{Ze} = -\int_V \boldsymbol{M} \cdot \boldsymbol{H} dV \qquad \textit{Eq. 1.4.3}$$

Eq. 1.4.3 describes the interaction of the magnetization $\boldsymbol{M}$ of a sample with an external magnetic field $\boldsymbol{H}$. This energy is minimal if $\boldsymbol{M}$ is parallel to the external field $\boldsymbol{H}$. In a homogeneous external field, only the average magnetization of the sample contributes to this energy.

1.4.3 Magnetocrystalline energy

This energy contribution reflects the influence of the crystal lattice on the magnetization. It is associated with the Coulomb interaction between the electrons of a magnetic ion and the surrounding ions in a crystal. The coordination and symmetry of the crystal environment affect the spatial distribution and population of the orbitals of the magnetic ions and, through the spin-orbit coupling, cause a preferred orientation of the magnetization with respect to the crystal. Thus, the *magnetization easy axis* depends on the crystal structure of the magnetic material. In the case of *uniaxial anisotropy*, the magnetocrystalline anisotropy energy will be:

$$\varepsilon_{KUni} = -\int_V (K_1 \sin^2\theta + K_2 \sin^4\theta) dV \qquad \textit{Eq. 1.4.4}$$

where θ is the angle between the easy axis and the magnetization, K_1, K_2 $[J/m^3]$ are the anisotropy constants and dV the volume element. In general for a system with a uniaxial anisotropy, the second term of the magnetocrystalline anisotropy energy can be neglected. In *cubic crystals* (with more than one preferential magnetization direction allowed by symmetry) the energy density is given by:

$$\frac{\varepsilon_{KCub}}{V} = K_0 + K_1(\alpha_1^2\alpha_2^2 + \alpha_2^2\alpha_3^2 + \alpha_1^2\alpha_3^2) \qquad \textit{Eq. 1.4.5}$$

where K_0 and K_1 are anisotropy constants, V the volume of the region and the α_s (s=1, 2 and 3) are direction cosines, i.e., the cosines of the angle between the magnetization and the crystal axis.

1.4.4 Demagnetizing energy (or magnetostatic energy):

The magnetostatic energy is an anisotropic term related to the geometry of the nanostructure. For example, it is equally easy to magnetize a sphere of a magnetic material without magnetocrystalline anisotropy along any direction, whilst non-spherical shapes are more easily magnetized along their long axis than their short axis. This phenomenon is known as *shape anisotropy*. The shape anisotropy arises from the magnetic dipolar interaction. The corresponding magnetic energy is given by:

$$\varepsilon_d = -\frac{1}{2}\int_V \mu_0 \boldsymbol{M} \cdot \boldsymbol{H}_\mathrm{d}\, dV \qquad \textit{Eq. 1.4.6}$$

where $\mu_0$is the magnetic permeability of the vacuum and $\boldsymbol{H}_\mathrm{d}$ is the *demagnetizing field,* which depends on the magnetic configuration of the system, which in turn depends on the shape of the magnetic material. If the magnetization of the specimen is oriented along one direction (for instance with a strong applied magnetic field), "magnetic free poles" appears producing a magnetic field opposite to the magnetization. Its intensity is proportional to the magnetic free pole density and the shape of the specimen.

$$H_{\mathrm{d}} = -NM \qquad \text{Eq. 1.4.7}$$

where M is the magnitude of the magnetization and N is the *demagnetizing factor*, which depends only on the shape of the specimen. In the Table 1.4.1 the demagnetizing factors for simples shapes is shown. The demagnetizing or stray field has important implications in ferromagnetic materials: it acts on the magnetic field produced by the permanent magnets and, at the same time, induces the formation of *"magnetic domains"*.

Table 1.4.1. Demagnetizing factors for simple shapes [1].

Shape	Magnetization direction	N
Long needle	Parallel to axis	0
	Perpendicular to axis	1/2
Sphere	Any direction	1/3
Thin film	Parallel to plane	0
	Perpendicular to plane	1
General ellipsoid of revolution	$N_c = 1 - 2N_a$ With N_c and N_a as demagnetizing factors for the *c* and *a* axes.	

1.4.5 Magnetostriction and stress energy

When a ferromagnetic material is exposed to a magnetic field, its dimensions change. This effect called *magnetostriction* (λ) [4] is defined as the fractional change $\Delta l/l$ in a material of length l. This fractional change in the length presents very small

values in the range of $10^{-5} - 10^{-6}$. The value is negative (positive) when the material shrinks (expands) for a Δl measured from the demagnetized state to the saturated state.

The associated energy when an external stress σ_{ij} is applied to a material is given by:

$$\varepsilon_{stress} = -\sum_{i,j} \sigma_{ij}\epsilon_{ij} \qquad \textit{Eq. 1.4.8}$$

where ϵ_{ij} is the magnetoelastic strain tensor, which depends on the magnetization and the external applied field.

1.4.6 Comparison of different energies

To summarize the different contributions to the final energy in a ferromagnetic material, the Table 1.4.2 gives the corresponding orders of magnitude.

Table 1.4.2. Energy contributions in a ferromagnet [1].

Energy	Order of magnitude (kJ/m^3)
Exchange	$10^3 - 10^5$
Crystalline anisotropy	$10^{-1} - 10^4$
Magnetostatic	$0 - 10^3$
Zeeman (for 1T)	$10^2 - 10^3$
Stress (under 1GPa)	$1 - 10^2$
Magnetostrictive	$0 - 1$

In the following, we will not consider the stress and magnetostrictive energies as they are not present in our systems.

1.5 Magnetic domains

The final stationary micromagnetic state of a magnetic body minimizes the total magnetic energy of the system, i.e., the sum of the different energy terms of the Eq. 1.4.1. If we consider an equilibrium state free of external magnetic fields ($\varepsilon_{Ze} = 0$), with a temperature sufficiently low that the thermal energy can be neglected (i.e. $T \ll T_C$), a saturation magnetization condition along the easy magnetization direction will minimize both exchange and magnetocrystalline energies. However, this configuration will induce the appearance of positive and negative magnetic charges at the surfaces, producing a large demagnetizing field. The best solution to decrease the demagnetizing energy is to create small regions where the magnitude of the magnetization is the same at each point, but with different directions. This effect favours the minimization of ε_d by the reduction of the stray field, but increases ε_{ex} and/or ε_K. Thus, the competition of the different terms of micromagnetic energy produces *magnetic domains* in a ferromagnetic material as presented in the Figure 1.5.1. The shape and size of each domain depend on the precise balance between these terms, which is determined by the magnetic parameters of the material (exchange constant A; anisotropy constant K, saturation magnetization M_S), the shape of the structure (demagnetizing factor N) and the magnetic history.

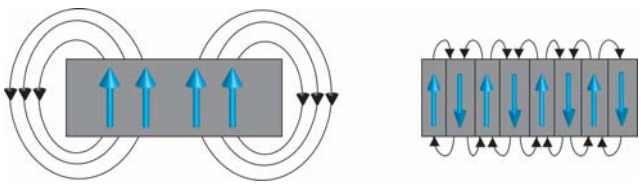

Figure 1.5.1. Formation of magnetic domains: a) alignment of the magnetization results in an intensive stray field (large magnetostatic energy); b) division into small magnetic domains permits the reduction of the magnetostatic energy [3].

The boundaries between the domains are known as *domain walls (DW)*. These are transition regions between adjacent domains where the magnetic moments realign over many atomic planes and not in one discontinuous jump across a single atomic plane. The total angular displacement of the magnetic moments across the wall is often 90° or 180°. Depending on the material thickness, two types of domain walls may occur, known as *Bloch* and *Néel* domain walls (Figure 1.5.2). The Bloch wall is usually preferable in bulk materials where the spins rotate in the plane parallel to the wall plane. The wall width of a 180° Bloch wall is most commonly defined by $\pi\sqrt{A/K}$. In thin films, however, a Bloch wall induces surface changes by its stray field. Then the Néel wall becomes more favourable when the film thickness becomes smaller than the wall width: the Bloch wall, which orientates locally the magnetization normal to the plane of the material, causes a large demagnetization energy, while the Néel wall, in which the moments rotate in the plane of the specimen but perpendicular to the wall plane, results in a lower energy [2], [4], [9].

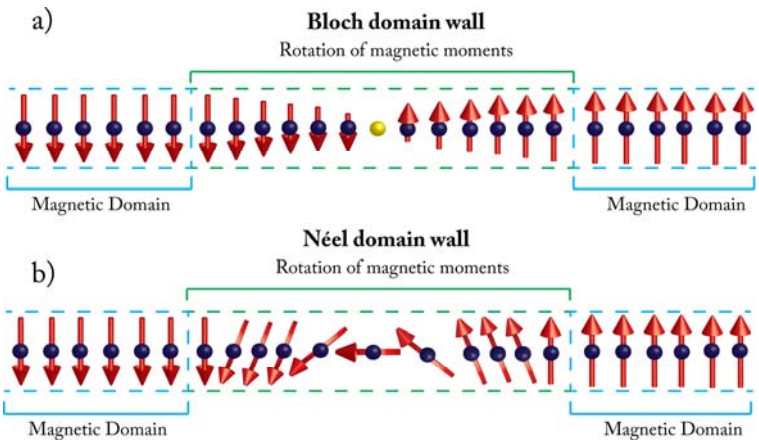

Figure 1.5.2. Schematic representation of: a) Bloch and b) Néel domain wall.

1.6 Magnetic states in magnetic nanowires

The equilibrium state of magnetic nanowires will be determined by the minimization of the several energy terms. The most observed state (but not the only) in magnetic nanowires of a single material is a monodomain state where the magnetization is aligned along the longest axis of the wire axis, due to the shape anisotropy.

When the magnetization is aligned along the wire, the demagnetization energy tries to keep this orientation by creating a demagnetizing field antiparallel to the magnetization. Figure 1.6.1 a) shows a scheme of a single nanowire with a limited length magnetized along the wire axis and the corresponding stray field at remnant state. This is the ideal case in which there is no other anisotropy source or external magnetic field than the one initially used to magnetize the sample. An "array" of nanowires composed by 3 NWs magnetized by an external magnetic field parallel to the wire axis is presented Figure 1.6.1 b) and c).In b) the magnetic moments of the wires are all aligned in the same direction, the magnetization is saturated and follows the initial applied magnetic field. For c) the magnetic moments of the outside wires are still in the same direction following the initial applied magnetic field but the middle wire has already switched. In this case, the distance between the nanowires is shorter than in b). The stray field interaction between neighbours causes the switching of the magnetization.

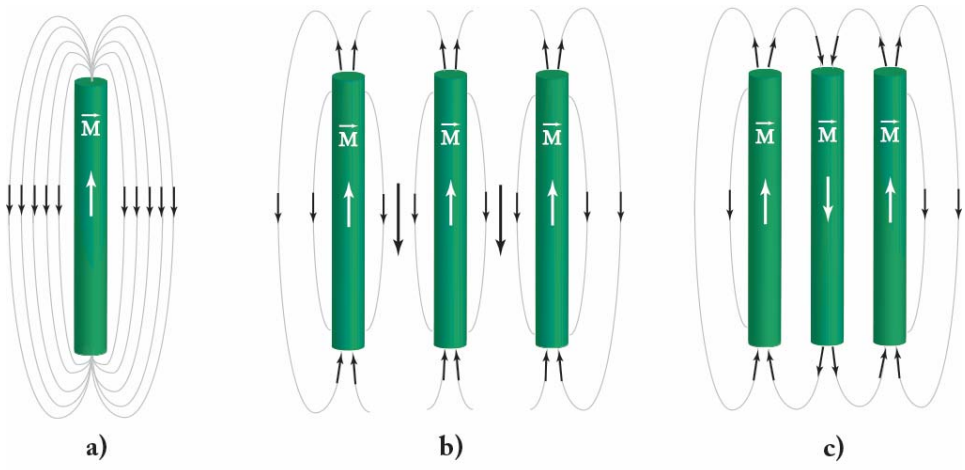

Figure 1.6.1. Magnetization configurations for: a) single wire saturated along the wire axis, b) three wires saturated in the same direction under an external magnetic field and c) three wires where the magnetization of middle wire has been switched antiparallel to the others due to the stray field interaction.

We can deduce from this basic analysis that the magnetic states of magnetic nanowires will depend on the material properties, its shape, and the interaction with other magnetic objects or external fields by dipolar coupling. Nanowires of high aspect ratio made of single elements or alloys present a magnetization lying along the wire axis in the case of zero magnetocrystalline anisotropy, due to the shape anisotropy or the demagnetizing field. If the nanowire has a magnetocrystalline anisotropy, the direction of the magnetization will be the result of the competition between the shape and the magnetocrystalline anisotropy. If the value of this magnetocrystalline anisotropy is small compared to the shape anisotropy of the NW, the magnetization direction will be still along the wire axis. However if the direction and magnitude of the crystal anisotropy compensate the shape anisotropy, the appearance of multi-domain magnetization configuration could be favoured. This kind of behaviour has been observed in Co nanowires with hcp structure and with the c-axis nearly perpendicular to the wire axis [10]. The magnetization is then waving along the wire due to the competition between the crystal anisotropy energy and the shape anisotropy. Other authors are also reporting single crystal structure Co NWs with c-axis perpendicular to wire axis and a magnetic

state consisting in magnetic vortices with alternating chirality along the wire at the remnant state [11]. For NWs arrays, magnetic properties depend on the nature of the wires and the interactions between them like dipole-dipole interaction. Vivas et al. [12] studied Co NWs arrays with an hcp structure and c-axis with different orientations: 0°, 45° and 90° with respect to the wire axis. Also, the control over the magnetic domains along the wire has been reached by the pinning and control of domain walls [13]. The global behaviour of the hysteresis loops was totally different and depends on the magneto-crystalline properties of the wire as well as on the interaction between them. On another hand Ivanov et al. [14] observed stable vortex states in arrays of Co NWs with diameters as small as 45 nm and lengths of 200 nm. They also show that multiple vortices with different chirality can exist along NWs with higher aspect ratios. A nearly negligible dipole-dipole interaction was found in the array of NWs.

In multilayered nanowires, in particular for non-magnetic/magnetic layer alternation, each magnetic layer can be considered as a small magnet whose behaviour will be determined by different parameters: shape anisotropy, crystal anisotropy and the possible interaction with the adjacent layers, this in the case of isolated NW. The interaction with the neighbouring NWs will also influence the magnetic behaviour in the case of a periodic arrangement of NWs (array). For an array of nanowires, we can use the effective field model [15] in which each nanowire is subject to a total field which is the sum of the applied field with the magnetostatic interaction field. This dipolar interaction field can be separated into the interwire and intrawire contributions. For multilayered nanowires (MNWs), the intrawire interaction can be further separated into the demagnetizing field of the single layers and the intrawire interaction between these layers. In addition to these interactions, the crystalline anisotropy will play an important role as in the case of single element NWs. Therefore, the resulting magnetic state in a

multilayered nanowire will be determined by the competition between energies linked to all previous parameters.

Multilayered nanowires can be considered as an ensemble of small cylinders. The fundamental analysis of these MNWs requires first the study of isolated magnetic cylinders. Depending on the aspect ratio (thickness/diameter), the magnetic configuration of nanocylinders with dimensions less than 100nm is based on one of three ground states: a single domain with in-plane magnetization (in-plane state), a single domain with out-of-plane magnetization (out-of-plane state), or a vortex state [16], [17] as presented Figure 1.6.2.

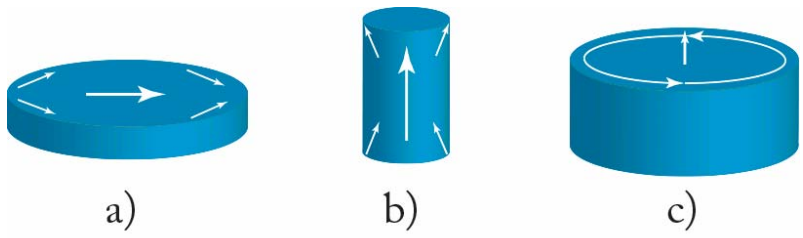

Figure 1.6.2. Schematic illustration of the three ground states for isolated magnetic nanocylinders: a) in-plane state, b) out-of-plane state and c) vortex state.

Chung et al. [17] calculated the phase diagram for NiFeMo nanocylinders. In the Figure 1.6.3 a) the three regions out-of-plane (O), in-plane (I) and vortex states (V) are delimited. However, the phase boundaries are not sharply defined. Near the boundaries and especially the triple point some metastable phases appear. These metastable regions are delimited in the Figure 1.6.3 b). In the metastable regions the capital letters correspond to the magnetic ground phase while the small letters represent metastable phases. They also used scanning electron microscopy with polarization analysis (SEMPA) to image the magnetic configurations in nanocylinders of $Ni_{80}Fe_{15}Mo_5$. They observe nanocylinders with a mixture of metastable ground states and also variations of the basic states, such as tilted vortex configuration.

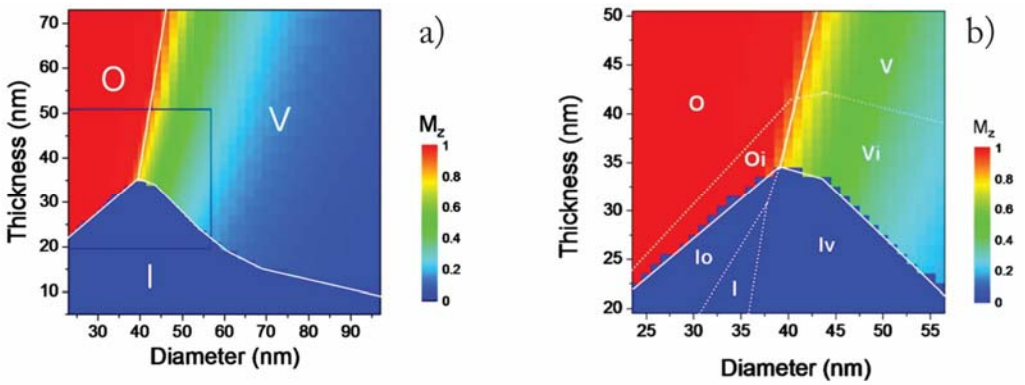

Figure 1.6.3. a) Phase diagram of the thickness in function of the diameter for NiFeMo nanocylinders obtained by micromagnetic simulations. Magnetization along the cylinder axis (M_z) in color scale, b) inset of a) showing the metastable phase boundaries. Extracted from [17].

Consequently, the magnetic states of multilayered nanowires will have in principle one or more of these ground states. However the crystalline anisotropy and the dipolar interaction between the layers can produce differences from these three magnetic states, with or without a magnetic coupling between them. This coupling between layers can be antiparallel, coupling vortices or monodomain-like with all the layers pointing in one direction for example. There are reports of antiparallel coupling between consecutive magnetic layers separated by a non-magnetic element [18], [19], and others having nanowires with vortices at remanence state while a magnetization reversal process is performed [20], [21]. Akhtari et al. [22] studied Cu/CoFeB isolated NWs in remnant state after applying a magnetic field. They found that the magnetization is lying along the long axis of the wire when a magnetic field parallel to the wire axis is applied. But with a perpendicular magnetic field, the orientation of the magnetization has an angle respect with the wire axis. This study also reported the vortex-shaped state in Cu/CoFeB/Cu tri-layers.

In summary, the final magnetic state will be the result of a competition between the different energies involved during the process. It can be "simple" or very complex

depending on the different energies and interactions involved. Reveal and analyse the magnetic states in Co-based NWs at remanent state is one of the aims of this work.

1.7 Micromagnetic simulations

Local measurements as electron holography give information about the magnetic state inside and outside the sample. This information is the result of the integration of the magnetic induction along the observation axis. Therefore, the phase images that reveals these magnetic states of the sample are the two-dimensionnal (2D) projection of a three-dimensional (3D) system. In order to complete the analysis of these magnetic states, micromagnetic simulations should be performed. These can reveal the 3D magnetic state inside and outside the sample by direct comparison between the simulated and experimental phase images.

Magnetic states in a ferromagnetic material can be simulated by the Landau-Lifshitz-Gilbert (LLG) equation [23], [24], which defines the time evolution of the magnetization under a local effective magnetic field $\boldsymbol{H}_{\text{eff}}$. Such magnetization equation of motion is usually expressed as:

$$\frac{d\boldsymbol{M}}{dt} = -|\bar{\gamma}|\boldsymbol{M} \times \boldsymbol{H}_{\text{eff}} - \frac{|\bar{\gamma}|\alpha}{M_s} M \times (\boldsymbol{M} \times \boldsymbol{H}_{\text{eff}}) \qquad \textit{Eq. 1.7.1}$$

where $\boldsymbol{M}$ is the magnetization, $\boldsymbol{H}_{\text{eff}}$ is the effective field, $\bar{\gamma}$ is the gyromagnetic ratio, and α is the damping constant. The effective field can be expressed as a functional derivate of the average energy density E_{tot}, as a function of the magnetization:

$$\boldsymbol{H}_{\text{eff}} = -\frac{1}{\mu_0}\frac{\partial E_{\text{tot}}}{\partial \boldsymbol{M}} \qquad \textit{Eq. 1.7.2}$$

where $\varepsilon_{tot} = \int_V E_{tot} dV$. This effective field is then associated with the different sources of energy that were discussed in section 1.4. It exerts a torque on the

magnetization vector of each "*magnetic unit cell*" that induces a precession movement, which is described by the first term of Eq. 1.7.1. The magnetization is reoriented toward the effective field following a damping process as a function of time, which is described by the second term of Eq. 1.7.1. There are very few situations where the LLG equation can be solved analytically; in general, we need to use numerical methods for its solution. In addition, Eq. 1.7.1 is only valid assuming that: (*i*) magnetization is a continuous function of the position $\boldsymbol{M} = \boldsymbol{M}(\boldsymbol{r})$; and (*ii*) magnetization modulus is constant in every point and equal to the saturation magnetization, $|\boldsymbol{M}| = M_S$.

There are several micromagnetic simulation packages available to solve the LLG equation such as MuMax3 [25], GPMagnet [26], Nmag [27], MicroMagnum [28] and OOMMF [29]. The OOMMF code has been chosen for this work to perform the micromagnetic simulations.

The aim of the simulations is to minimize the total energy of the magnetic system which is usually subdivided in a rectangular mesh of cubes (in the case of OOMMF) called the *magnetic unit cell*. These cells should have lateral sizes preferably less than the characteristic exchange length $l_{ex} = \sqrt{2A/\mu_0 M_S^2}$ of each magnetic material (in most ferromagnetic materials l_{ex} has a value of 2-6 nm) [1].

Depending on the specific problem OOMMF can use different "*evolvers*", which are responsible for updating the magnetization configuration from one step to the next. There are two types of evolvers: *time evolvers,* which track LLG dynamics, and *minimization evolvers*, the latter locate local minima in the energy surface through direct minimization techniques. For our case, the *minimization evolvers* were used. This allows stopping the simulation with a *torque criteria* for the spins that make part of the sample. This code allows also the entrance of an exchange constant, the magnetocrystalline

anisotropy as a vectorial value and the saturation magnetization for the whole sample. With these initial conditions, the simulation runs iteratively to minimize the energy until a given convergence criterion is satisfied, which can be a maximum number of iterations, or the minimization of the "torque" that experiences the spins, or the variation of the magnetization of the system with the time when this reaches a certain minimum value, etc. The final magnetic configuration is considered as being the equilibrium state for a given external magnetic field. The details about our particular simulations and the problem statement will be described in chapter 3.

References

[1] J. M. D. Coey, *Magnetism and magnetic materials*. Cambridge; New York: Cambridge University Press, 2009.

[2] S. Blundell, *Magnetism in condensed matter*. Oxford ; New York: Oxford University Press, 2001.

[3] C.-G. Stefanita, *Magnetism*. Berlin, Heidelberg: Springer Berlin Heidelberg, 2012.

[4] B. D. Cullity and C. D. Graham, *Introduction to magnetic materials*, 2nd ed. Hoboken, N.J: IEEE/Wiley, 2009.

[5] W. Heisenberg, "Zur theorie des ferromagnetismus," *Z. Für Phys.*, vol. 49, no. 9–10, pp. 619–636, 1928.

[6] P. Weiss, "L'hypothèse du champ moléculaire et la propriété ferromagnétique," *J. Phys.*, vol. 6, no. 661, p. 36, 1907.

[7] W. Brown, *Micromagnetics, by w.f. brown*. Interscience, 1963.

[8] T. Schrefl, D. Suess, W. Scholz, H. Forster, V. Tsiantos, and J. Fidler, "Finite element micromagnetics," in *Computational Electromagnetics*, Springer, 2003, pp. 165–181.

[9] D. Jiles, *Introduction to Magnetism and Magnetic Materials*. Boston, MA: Springer US, 1991.

[10] J. Cantu-Valle, I. Betancourt, J. E. Sanchez, F. Ruiz-Zepeda, M. M. Maqableh, F. Mendoza-Santoyo, B. J. H. Stadler, and A. Ponce, "Mapping the magnetic and crystal structure in cobalt nanowires," *J. Appl. Phys.*, vol. 118, no. 2, p. 24302, Jul. 2015.

[11] Y. P. Ivanov, L. G. Vivas, A. Asenjo, A. Chuvilin, O. Chubykalo-fesenko, and M. Vázquez, "Magnetic structure of a single-crystal hcp electrodeposited cobalt nanowire," *EPL Europhys. Lett.*, vol. 102, no. 1, p. 17009, Apr. 2013.

[12] L. G. Vivas, J. Escrig, D. G. Trabada, G. A. Badini-Confalonieri, and M. Vázquez, "Magnetic anisotropy in ordered textured Co nanowires," *Appl. Phys. Lett.*, vol. 100, no. 25, p. 252405, 2012.

[13] S. Da Col, S. Jamet, M. Staňo, B. Trapp, S. Le Denmat, L. Cagnon, J. C. Toussaint, and O. Fruchart, "Nucleation, imaging and motion of magnetic domain walls in cylindrical nanowires," *ArXiv Prepr. ArXiv160307240*, 2016.

[14] Y. P. Ivanov, A. Chuvilin, L. G. Vivas, J. Kosel, O. Chubykalo-Fesenko, and M. Vázquez, "Single crystalline cylindrical nanowires – toward dense 3D arrays of magnetic vortices," *Sci. Rep.*, vol. 6, p. 23844, Mar. 2016.

[15] L.-P. Carignan, C. Lacroix, A. Ouimet, M. Ciureanu, A. Yelon, and D. Ménard, "Magnetic anisotropy in arrays of Ni, CoFeB, and Ni/Cu nanowires," *J. Appl. Phys.*, vol. 102, no. 2, p. 23905, 2007.

[16] J. d'Albuquerque e Castro, D. Altbir, J. C. Retamal, and P. Vargas, "Scaling Approach to the Magnetic Phase Diagram of Nanosized Systems," *Phys. Rev. Lett.*, vol. 88, no. 23, May 2002.

[17] S.-H. Chung, R. D. McMichael, D. T. Pierce, and J. Unguris, "Phase diagram of magnetic nanodisks measured by scanning electron microscopy with polarization analysis," *Phys. Rev. B*, vol. 81, no. 2, Jan. 2010.

[18] C. Beeli, B. Doudin, J.-P. Ansermet, and P. Stadelmann, "Study of Co, Ni and Co/Cu nanowires: Magnetic flux imaging by off-axis electron holography," *J. Magn. Magn. Mater.*, vol. 164, pp. 77–90, 1996.

[19] L. Belliard, J. Miltat, A. Thiaville, S. Dubois, J. L. Duvail, and L. Piraux, "Observing magnetic nanowires means of magnetic force microscopy," *J. Magn. Magn. Mater.*, vol. 190, pp. 1–16, 1998.

[20] J. Zhang, H. Ma, S. Zhang, H. Zhang, X. Deng, Q. Lan, D. Xue, F. Bai, N. J. Mellors, and Y. Peng, "Nanoscale characterisation and magnetic properties of $Co_{81}Cu_{19}$/Cu multilayer nanowires," *J Mater Chem C*, vol. 3, no. 1, pp. 85–93, 2015.

[21] J. Wong, P. Greene, R. K. Dumas, and K. Liu, "Probing magnetic configurations in Co/Cu multilayered nanowires," *Appl. Phys. Lett.*, vol. 94, no. 3, p. 32504, 2009.

[22] A. Akhtari-Zavareh, L. P. Carignan, A. Yelon, D. Menard, T. Kasama, R. Herring, R. E. Dunin-Borkowski, M. R. McCartney, and K. L. Kavanagh, "Off-axis electron holography of ferromagnetic multilayer nanowires," *J. Appl. Phys.*, vol. 116, no. 2, p. 23902, 2014.

[23] L. D. Landau and E. Lifshitz, "On the theory of the dispersion of magnetic permeability in ferromagnetic bodies," *Phys Z Sowjetunion*, vol. 8, no. 153, pp. 101–114, 1935.

[24] T. L. Gilbert, "A Lagrangian formulation of the gyromagnetic equation of the magnetic field."

[25] A. Vansteenkiste, J. Leliaert, M. Dvornik, M. Helsen, F. Garcia-Sanchez, and B. Van Waeyenberge, "The design and verification of MuMax3," *AIP Adv.*, vol. 4, no. 10, p. 107133, Oct. 2014.

[26] L. Lopez-Diaz, D. Aurelio, L. Torres, E. Martinez, M. A. Hernandez-Lopez, J. Gomez, O. Alejos, M. Carpentieri, G. Finocchio, and G. Consolo, "Micromagnetic simulations using Graphics Processing Units," *J. Phys. Appl. Phys.*, vol. 45, no. 32, p. 323001, Aug. 2012.

[27] T. Fischbacher, M. Franchin, G. Bordignon, and H. Fangohr, "A systematic approach to multiphysics extensions of finite-element-based micromagnetic simulations: Nmag," *Magn. IEEE Trans. On*, vol. 43, no. 6, pp. 2896–2898, 2007.

[28] C. Abert, L. Exl, F. Bruckner, A. Drews, and D. Suess, "magnum.fe: A micromagnetic finite-element simulation code based on FEniCS," *J. Magn. Magn. Mater.*, vol. 345, pp. 29–35, Nov. 2013.

[29] M. J. Donahue and D. G. Porter, "OOMMF User's Guide, Version 1.0, Interagency Report NISTIR 6376." 1999.

Chapter 2
Experimental techniques

2.1 Introduction

Magnetic nanostructures with different shape, size and aspect ratios have been designed for technological applications and study of physical phenomena. The properties of these structures are usually studied macroscopically, but the reduction of device sizes requires spatially resolved measurement with a high sensitivity. The interest in the spintronic field and the nanomagnetism leads indeed to find local techniques that allow for a detailed description of the magnetic states in each part of the object under study.

A large part of this manuscript is focused on the study of magnetic nanowires which are particularly interesting for fundamentals studies of magnetic interactions at the nanoscale. They are also very good candidates to produce spin torque nano-oscillator connected in series to increase radio frequency (RF) output power [1]–[3]. This chapter gives an overview of the most important techniques to elaborate nanowires. A special emphasis in the electrodeposition process is presented followed by a review of the techniques used to image magnetic domains. Finally, transmission electron microscopy fundaments are explained and the electron holography technique is detailed.

2.2 Growth of nanowires

Synthesis of one-dimensional (1D) structures has been of great interest since the carbon nanotubes discovery by Iijima [4]. These structures offer models to study the

relationship between electrical, optical or magnetic properties with dimensionality and size confinement. In the last 15 years, a large variety of nanowires (semiconductors, metals, oxides) has been synthesised by several techniques, each of them presenting advantages and drawbacks. In the next sections, a review of several techniques of NWs growth will be presented.

2.2.1 Vapour-liquid-solid (VLS) technique

This technique described for the first time by Wagner and Ellis [5] uses Au particles as a catalyst to grow crystalline semiconductors whiskers. The process is the following: a droplet of Au is deposited on the surface of a Si substrate {111}, then the temperature is increased until 950°C forming a small droplet of Au-Si, and later a mixture of hydrogen and $SiCl_4$ is introduced. The liquid acts as a sink for the Si atoms. The Si atoms enter the liquid and freeze out with a very small concentration of Au in solid solution at the interface between solid Si and the liquid alloy. Then the droplet is separated from the substrate due to the growth of the whiskers. The growth direction of the nanowire normally is the same as the orientation of the <111> substrate (other orientations are possible depending on the lattice mismatch between the substrate and the NW material [6]). The whiskers grow in length by this mechanism until the Au is consumed or until the growth conditions are changed. A schema of the growing process is shown in Figure 2.2.1.

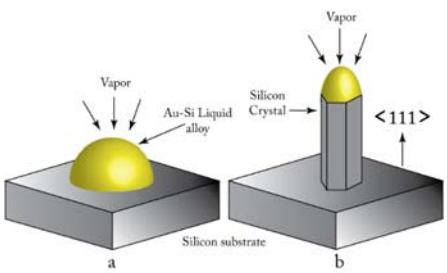

Figure 2.2.1. Schematic illustration: Growth of a silicon crystal by Vapour-liquid-solid technique. a) Initial conditions with Au-Si liquid droplet. b) Growing crystal with the liquid droplet at the tip.

The main characteristic of this technique is the possibility to grow mainly semiconductor nanowires with a high crystallinity. In Table 2.2.1 is consigned a list of some nanowires produced by this technique, their characteristics and applications.

Table 2.2.1. Nanowires grown by VLS technique.

Nanowire	Characteristic or application
Si	Single-crystal. Photoelectrodes for solar-to-fuel conversion devices [7] and FET transistors [8]
Ge	Single-crystal. Defect-Free Kinking [9]
GaN	Single crystal, Atomic resolution in-situ imaging growth [10]
NiO	Gas sensing device [11]
InAs/InP	Heterostructure keeping the crystallinity [12]

2.2.2 Laser-assisted growth

The laser-assisted growth technique consists in ablating the source materials with a laser source into a vapour phase and transferring it to the substrate where the nanowires nucleate and grow. A mixture of powders of the desired elements is enough to start the growth process. This method has the unique advantage over the other growth techniques to prepare nanowires containing complex chemical compositions. This is possible because a mixture of powders of the desired elements is enough to start the growth process. This is an advantage compared with other techniques in which a stoichiometric and crystalline phase of the elements should be present in the precursor material. There is also the possibility to add some metal particles to act as catalysts like in VLS [13]–[15]. The scheme of the laser-assisted growth consisting of a chamber with a laser source, the material to be ablated and the cold finger to capture the vapour

and act as a substrate for the nucleation of the nanowires is represented in the Figure 2.2.2.

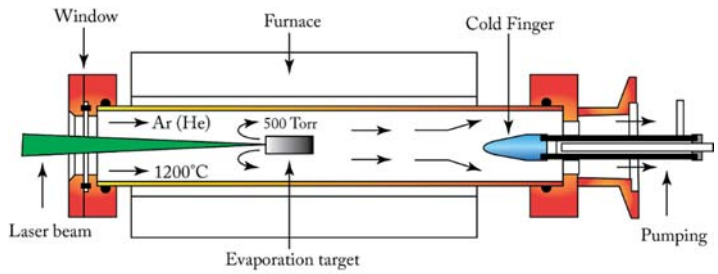

Figure 2.2.2. Experimental setup for the synthesis of nanowires by laser ablation.

The nanowires grown by this technique have diameters between 10-50 nm. The growth rate is around 500 μm/h for Si nanowires, which is higher than classical VLS growth (between 60-100μm/h for NWs with the same diameter) [16], [17].

2.2.3 Thermal evaporation

The set-up of this technique consists in a chamber with two temperatures, one in which the original materials as powder are evaporated and the second one with a substrate at a lower temperature to deposit the nanowires. A gas flux creates an inert atmosphere inside a quartz tube. In the Figure 2.2.3, a scheme of the set-up is presented.

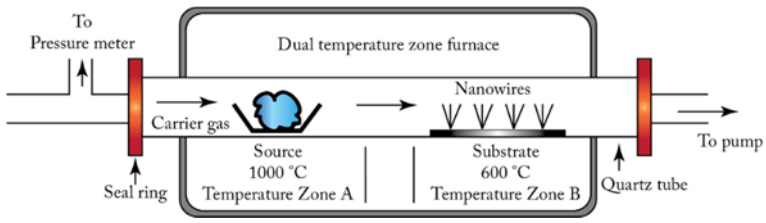

Figure 2.2.3. Experimental setup for the thermal evaporation technique to obtain nanowires.

The materials suitable for this fabrication are metal oxides like ZnO, SnO_2, In_2O_3, VO, etc. [18]. This method has been improved to grow pure semiconductors materials [19] by adding graphite, SiO_2 or other oxides. This feature permits an enhancement of the

nanowire growth process, decreasing the temperature at which the materials can be evaporated to form nanostructures [20]–[23].

2.2.4 Lithography from thin films and other modern methods

Nanowires can also be obtained from others nanostructures like thin films using techniques like soft nanoimprint lithography combined with lift-off process [24], [25] and e-beam lithography [26], [27]. These methods consist in designing a pattern on a thin film surface and removing part of the material from the surface until the desired shape is reached. One problem is that the wire is attached to the substrate of the thin film. But in some cases, this is also an advantage when electric contacts are required. These wires normally present a non-cylindrical shape. The combination of atomic force microscopy nanoscratching and lift-off process can be used as a way to design a nanowire too [28]. Focused ion beam technique is another method to make nanopatterned nanowires from thin films of complex oxides and metals [29], [30] forming square-sided nanowires. This technique can also be used to grow isolated nanowires by induced deposition [31]. The main drawback here being that it is time-consuming.

2.2.5 Solution methods

The solution based-technique in aqueous or non-hydrolytic media presents some advantages for the synthesis of nanomaterials: high yield, low cost and easy fabrication. Polyol soft chemistry process is one of these solution based-techniques and can be used to synthesize a wide range of metal nanowires with sizes ranging from 8 to 20nm in diameter and 50 to 400nm in length. It consists in a reduction of metal salts in a liquid. Besides this well-controlled morphology, these nanowires are single crystals [32]. For instance, pure Co nanowires with HCP structure have been grown by this method [33]. Other solution based methods have been developed for the synthesis of cobalt nanowires using organometallic chemistry [34]. Moutet et al. [35] have

synthetized ultrathin Au nanowires and studied the direct assembly of them by atomic force microscopy (AFM) nanoxerography.

2.2.6 Template-based synthesis

In this technique templates of anodic alumina and polymer ion track membranes [36]–[40] are used to host and give the shape to the nanostructure. The templates can be nanoscale canals filled by sol-gel, solutions or electrochemical methods. The most popular templates are the anodic aluminium oxide and polycarbonate membranes. Then the nanowires can be released by dissolving the membrane with a chemical solution [37]. Different materials have been synthesised like pure metals Co, Ni, Fe, Au [41]–[43]. There is the possibility to create some alloys like NiMn, CoNi [44], [45] and multilayered nanowires like Co/Cu, Ag/Cu, Ni-Fe/Cu/Co/Co [46]–[48]. Semiconductors as InSb [49], CdSe [50] and Bi_2Te_3 [51], and oxide-base materials as ZnO [52] and MnO_2 [53] have been also grown by this method. This wide variety of materials shows the versatility of this method. Compared with other technics, the template-based synthesis is less expensive and relatively easy. The only drawback is the difficulty to obtain materials with a single-crystal structure. However, some authors have obtained a single-crystal structure in InN, CdS, Ni and Co [54]–[56]. Figure 2.2.4 shows a scheme of a typical template used for the growing of the nanowires. It is composed of a holy polymeric or alumina membrane. The dimensions of the holes will define the diameter size of the nanowires. The membrane is covered by one side with a metal thin layer to act as an electrode and substrate.

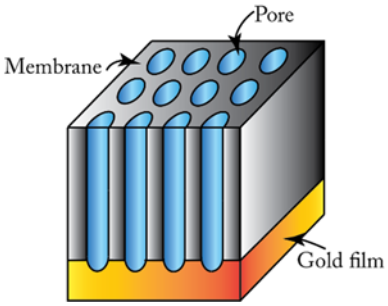

Figure 2.2.4. Scheme of a typical template used to grow nanowires.

One of the most used techniques to elaborate nanowires via template-based synthesis is the electrodeposition technique. This technique was employed to grow the nanowires studied in this thesis. In the next section, a description of the principles and the most relevant parameters of the electrodeposition in template membranes are discussed.

2.3 Electrodeposition

The electrodeposition of pure metals and alloys involve the reduction of cations by the gain of electrons. This process is carried out on the electrode surface called working electrode. The desired material is deposited over this electrode. We can simplify the deposition reaction by:

$$M^{n+} + ne^- \rightarrow M \qquad \text{Eq. 2.3.1}$$

where n indicates the number of electrons involved in the reaction with the metal (M). The electrochemical reaction can take place if there is a reaction of oxidation that gives the necessary electrons. For the basic electrodeposition system, three electrodes are required: anode, cathode and reference. The three electrodes are immersed into the solution so-called electrolyte (only aqueous solutions are analysed in this work). Normally the working electrode (anode) is made from a non-reactive material or a material which ions are already in the solution [57]. The reference electrode is used to

measure the characteristic response of current and voltage from the cathode. These electrodes are controlled by an external circuit called potentiostat or galvanostat (the difference between them will be explained later). The potentiostat controls the potential between the cathode and the reference electrode. It also allows maintaining the potential between the electrodes by providing the necessary electrical current. In the Figure 2.3.1, the scheme of the electrodeposition setup is represented.

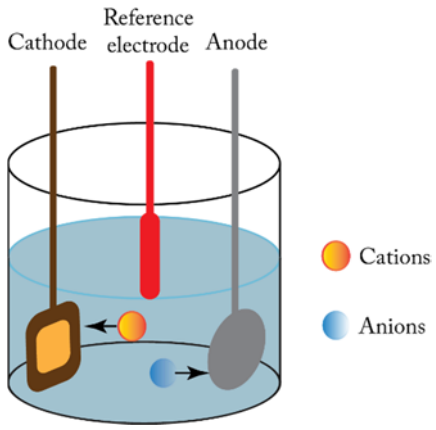

Figure 2.3.1. Electrodeposition scheme

During the electrodeposition process, two main processes are involved, and they are happening continuously and simultaneously: the transport of mass and the transfer of electrons. The slowest process is the limiting process.

In aqueous solutions, the electrodeposition mechanism is very complex. When a difference of potential is applied to the circuit, the ions close to the working electrode surface are regrouped. These create two layers: an electrical layer called Helmholtz double layer and a diffusion layer. All of these two layers is well known as Gouy-Chapman layer [58]. The scheme of this ions arrangement is shown in the Figure 2.3.2.

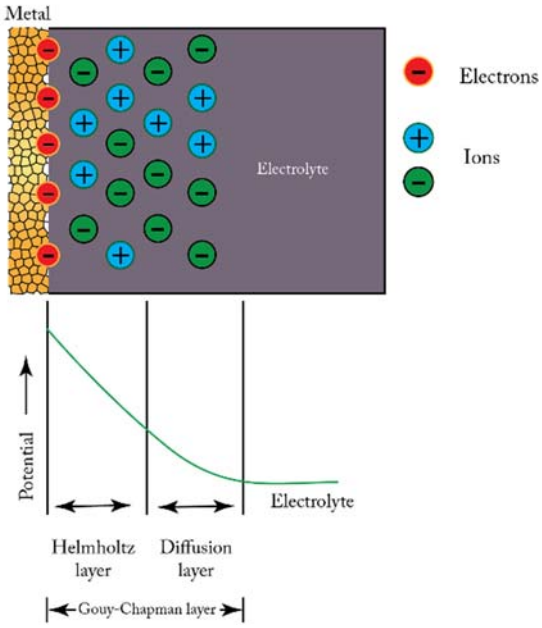

Figure 2.3.2. Scheme of the double layer.

The electrodeposition process follows these steps

- *Migration:* The hydrated metal ions in the solution migrate towards the cathode under the influence of current flow as well as by diffusion and convection (heat transfer due to the temperature increase by the current flow or heating the solution)
- *Electron transfer:* At the cathode surface, a hydrated metal ion enters the diffused double layer where the water molecules of the hydrated ion are aligned. Then the metal ion enters the Helmholtz double layer where it is deprived of its hydrate envelope
- The dehydrated ion is neutralised and adsorbed on the cathode surface.
- The adsorbed atom then migrates or diffuses to the growth point on the cathode surface.

2.3.1 Faraday laws

The relation between the charge flowing through the circuit during an electrochemical experience and the quantity of material released or deposited in each electrode is given by the Faraday laws:

- The chemical deposition due to flow current through an electrolyte is directly proportional to the quantity of charge passed through it.
- If the charge passing through several electrolytes is constant, the mass of the substance deposited is proportional to its chemical equivalent ($chemical\ equivalent = Atomic\ weight/Valence$) [59].

Combining the two laws, the charge that has flowed in the circuit must correspond to the charge provided by the reacting atoms in each electrode, and can be summarized in the equation:

$$q = \int_0^t I\,dt = neN_A\frac{m}{M} \qquad \textit{Eq. 2.3.2}$$

where q is the charge flowing through the circuit in a time t, N_A is the Avogadro's number, m the mass deposited or released, M the atomic weight of the reacting substance, n the valence number and e the electron charge. Eq. 2.3.2 is valid if only one substance is reacting on the working electrode. If there is more than one substance, each substance consumes one part of the charge and we should redefine this equation putting a fraction of charge for each substance.

2.3.2 Electron transfer

When a metal is immersed in a solution which contains ions of the same material, the surface atoms of the metal are hydrated and dissolved. On the same way, the solution ions are deposited over the metal. The potential in which the rates of both

processes are the same is called equilibrium potential. The equilibrium potential of any metal in a solution is determined by:

- The intrinsic electrolytic solution pressure of the metal
- The concentration of the ions of the metal in the adjacent solution

The mathematical expression that connects the concentration of each substance with the equilibrium potential of the reaction is called the Nernst equation:

$$E_{eq} = E^0 + \frac{RT}{nF} ln \frac{[C_o]}{[C_r]} \qquad \textit{Eq. 2.3.3}$$

where E^0 is the normal potential of reduction, R the gas constant, T the absolute temperature, n the valence of the metal (number of the transfer electrons), F the Faraday constant, C_o and C_r the concentrations of the elements that are oxidized and reduced respectively [60].

During the nanowire growth, a reference electrode with a well-defined and stable potential is used as only the difference of potentials can be measured. The current provides the energy necessary to defeat the spontaneous tendency to conserve its ionic state. Two main ways to perform the electrodeposition exist:

- *Galvanostatic deposition* in which the external source acts as a current source keeping the electrical current constant during the deposition process. The reference electrode is not necessary and we can obtain easily the value of the total charge passing through the circuit. The main problem is that during the deposition the concentration of the solution will change. This produces a different mass transfer during the whole experiment and the samples can have some inhomogeneity in composition.

- *Potentiostatic deposition* uses the source to keep a constant value of voltage. This source provides the necessary current to have the same potential difference between the working electrode and the reference electrode. This induces that the same composition is deposited during the time of the experiment. The only drawback is the requirement of the intensity curve as a function of the deposition time to obtain the total charge.

2.3.3 Parameters involved during the electrodeposition

During the electrodeposition process we must consider several parameters that affect the process and influence the properties of the resulting sample:

- *Temperature:* has a big influence on the ionic diffusion as well as the atoms already deposited. High temperatures provide solubility and electric conductivity improvement but on the other hand, this tends to accelerate solution evaporation and corrosion processes. There is also an influence on the rating process: a temperature increase of 1°C results in a 10% increase in the rate of electrochemical processes and in an enhancement in the rate of mass transfer of 2%.
- *Stirring of the solution:* enhances the ion transport to the substrate and decreases the thickness of the diffusion layer.
- *pH of the solution:* is a very important parameter that will influence the properties of the deposited metals. If the pH is too high, the presence of hydroxide ions surrounding the metal ions can affect the deposition. And if the pH is too low, the release in the cathode can be considerable [58].
- *Cathode potential:* allows choosing which metal is deposited when the electrodeposition bath contains two or more materials as in alloys or

multilayer structures. Its stability can affect the homogeneity of the composition along the process.

The electrodeposition process is a versatile technique that allows growing nanowires in a relatively easy way even if there are many parameters involved during the growth process. The average growth rates in some case are between 10 μm/h at a deposition temperature of 0 °C and 2682 μm/h for 60 °C [61]–[63]. We have used this technique to growth multilayered nanowires in polycarbonate membranes composed of pores of nanometric size. In the results chapter, the details about the specific process are presented.

2.4 Imaging magnetic domains

The study of the magnetic properties of nanoscale ferromagnets requires the combination of macroscopic characterization techniques which provide magnetic information averaged over large length scales with local techniques capable of probing magnetic properties with high spatial resolution and sensitivity. Among the latter, magnetic imaging techniques permit a direct study of the magnetic configurations, particularly magnetic domain structures at the submicron scale. The possibility of imaging ferromagnetic order together with the improvement of the computational time of micromagnetic simulations have significantly contributed to the understanding of the magnetic phenomena at the local scale that has enabled the latest technological applications in the field of nanomagnetism and spintronic [64]–[66]. Today, there are a substantial number of magnetic imaging techniques. Among them we can list the Kerr microscopy based on the magneto-optical Kerr effect (MOKE) [67]–[69]; the scanning electron microscopy with polarization analysis (SEMPA) [70]–[72]; the spin-polarized low-energy electron microscopy (SPLEEM) [70]; synchrotron radiation-based techniques such as x-ray magnetic circular dichroism, photoelectron emission

microscopy (XMCD-PEEM) [73], [74] and magnetic x-ray transmission microscopy (M-XTM) [70]; the scanning probe techniques such as magnetic force microscopy (MFM) [75], [76] and spin-polarized scanning tunnelling microscopy (SP-STM) [77]; and TEM-based techniques such as Lorentz microscopy (LM) and electron holography (EH) [78]–[80]. All these experimental methods offer a wide range of possibilities to study micromagnetic phenomena in different setups as can be seen in the comparative list of their main features presented in Table 2.4.1. Altogether they provide a spatial resolution ranging from microns to few angstroms, a high sensitivity to detect small changes of the local magnetization, probing the surface or the volume properties and sufficient versatility to enable the application of multiple external stimuli (temperature, electromagnetic fields, etc.). None of these techniques covers all the possibilities, and they are therefore complementary

From Table 2.4.1, we could classify the methods of magnetic imaging following different criteria that determine their range of application in terms of (spatial and time) resolution and sensitivity:

- The acquisition method: the image can be recorded using either a parallel acquisition of the signal at every point of the image simultaneously (e.g. XMCD-PEEM, LM) or a serial acquisition in which a fine probe is scanned across the sample (e.g. MFM, SP-STM).
- The probe-specimen interaction on which the magnetic contrast is based: the Lorentz force experienced by electrons in the magnetic field of the sample (e.g. LM and EH); the magnetic force on a magnetic tip caused by a stray field gradient (e.g. MFM); and magneto-optic coupling between photons and the magnetization of the material (e.g. Kerr microscopy).

- The depth sensitivity, directly related to the probe-specimen interaction determines whether the technique is sensitive only to the sample surface (e.g. MOKE, SPLEEM) or to the whole volume of the specimen such as in transmission techniques (e.g. M-XTM, LM and EH).

Table 2.4.1. Local techniques of magnetic mapping and theirs main characteristics.

Technique	Best spatial resolution (nm)	Information depth (nm)	Acquisition time (s)	Quantitative	Type of information depth	Type of imaging
XMCD–PEEM	20	2-20	0.03-10	Yes	Surface	Parallel
M-XTM	20	Sample thickness	3	Yes	Volume	Parallel-scanning
Kerr Microscopy	200	20	10^{-8} to 1	Yes	Surface	Parallel-scanning
MFM	30	200-500	300 to 1800	No	Surface	Scanning
SEMPA	10	2	60-6000	Yes	Surface	Scanning
SPLEEM	20	1	1	Yes	Surface	Parallel
DPC	2	Sample thickness	5-50	Yes	Volume	Parallel-scanning
Lorentz Microscopy	10	Sample thickness	0.04-30	Yes	Volume	Parallel
Electron Holography	2	Sample thickness	0.03-10	Yes	Volume	Parallel
SP-STM	0.02	0.2	30-1800	Yes	Surface	Scanning

For the study of the local magnetic states, one of the most important requests is the achievable spatial resolution. This makes the TEM-based techniques very powerful tools that provide quantitative magnetic information of the volume of the sample with flexibility to apply external stimuli (magnetic and electric fields, injection of the electrical current, changes in temperature, stress, light, etc.) with a spatial resolution going down to atomic scale. To achieve the goals of the current "nanotechnology revolution" - to understand and control matter at the nanoscale for the industrial and technological application that benefit the society – magnetic TEM imaging techniques have become an indispensable instrument for the development of magnetic-based nanodevices.

2.5 TEM imaging

Historically, the first attempts to study magnetic materials by TEM were to correlate the microstructure with the magnetic domain configuration measured by other techniques. Mayer [81] established the first method to observe the magnetism adapting an electron mirror microscope. He observed artificial magnetic domain patterns produced by an array of linear magnetic stray fields and the magnetic contrast of ferromagnetic barium and nickel ferrite films. In 1959, Hale et al. [82] developed the first methods to image domain patterns in ferromagnetic thin films through defocused TEM imaging and thanks to the use of an off-centred objective diaphragm to image magnetic domains [83]. They established the basis of LM in Fresnel and Foucault mode respectively. In the 1970s and 1980s, other TEM-based magnetic techniques such as phase contrast microscopy [84]–[87] and off-axis EH [88], [89] were developed. In EH, the magnetic information is obtained by retrieving the phase of the electron wave, although the electron beam phase shift measurements with sufficient sensitivity had to wait for the development of high coherence electron sources which were available in

commercial microscopes in the 90's. The basics principle of EH is based on an original idea proposed by Gabor [90], [91], in 1949 to overcome the resolution-limiting spherical aberration of the objective lens. In 1980 Tonomura [88] made use of the off-axis electron holography to observe the fine structure of magnetic domain walls. The principle of the off-axis electron holography is based in an interferometric experiment in TEM by overlapping the exit electron wave that interacts with the object with an unperturbed electron wave that passes entirely through the vacuum (reference wave), allowing extracting the full information of the exit electron wave (amplitude and phase). The reconstruction of the hologram was made by an optical method using a Mach Zender interferometer. Two years later he observed the Aharonov-Bohm effect in permalloy magnets by the same method [92]. And for a long time he focused his research on the applications of the electron holography in different systems [89], [93]. Thus, EH can be used to measure the phase shift of the electron wave that has interacted with a magnetic field and therefore to measure the magnetic induction. Several studies have been carried out using electron holography, Almeida et al. have studied the magnetic configurations of Fe_3O_4 nanoparticles of 150nm of length at different temperatures showing a vortex behaviour with the core parallel and perpendicular to the observation axis [94]. Midgley and Dunin-Borkowski have shown the versatility of the EH and the combination of this with electron tomography as a tool to reveal the 3D electrostatic and magnetic fields inside nanostructured materials [95]. McCartney and Smith highlighted the importance of EH at nanometric scale and presented the mapping of electrostatics potential in p-doped MOS device structure and the field emission of a carbon nanotube among others [96].

All these studies result in the quantitative and qualitative analysis of electrostatic potentials and magnetic states at the nanometric scale. Snoeck et al. studied the magnetic configurations of 30 nm iron nanocubes by EH. They found a vortex state and

determined the core size of this [97]. Biziere et al. used EH to image the fine structure of a domain wall in a Ni nanocylinder [98]. Later Gatel et al. reported the different spin configurations in the vicinity of the single-domain/vortex transition in isolated magnetic Fe nanocubes [99]. Marin, Rodriguez et al. also used the magnetic mapping result of the EH to observe the magnetic phase segregation in manganite thin films due to the strain [100]. In another study Wolf et al. combined electron holographic and tomography to reveal the 3D magnetic nanostructure of a 100 nm diameter cobalt nanowire grown by focused electron beam. They were capable of resolving magnetic features with a spatial resolution below 10nm and signal resolution of 0.1 T [101].

Electrostatic fields can be mapped using EH. McCartney et al. have performed a quantitative analysis of one-dimensional silicon p-n junction with a spatial resolution of 5 nm and sensitivity of 0.1 V [102], other p-n junctions in Si nanowires were studied too [103]. Linck, Lichte and Lehmann discussed the EH at atomic resolution for the material analysis, the interpretation of the atomic phase shift revealing that the interpretation of the measured phase shift in terms of atomic species is generally rather complex [104]. Hÿtch et al. have used the dark field EH for the strain mapping at the nanoscale obtaining quantitative results about the strain in MOSFET devices for instance [105].

2.5.1 Image formation in TEM

The overall process of the image formation in TEM can be summarized in six steps, which follow the electron wave trajectory:

1. Creation and acceleration of an electron beam from an electron source.
2. Illumination of the specimen with the (coherent) electron probe.
3. Scattering of the electron wave by the specimen,

4. Formation of a diffraction pattern in the *back focal plane* of the objective lens.
5. Formation of an image of the specimen in the *image plane* of the objective lens.
6. Projection of the image (or the diffraction pattern) on the detector plane.

In the first step, electrons are generated either by the thermionic emission of a filament (tungsten or LaB_6) heated at high temperatures, or by using cold Field Emission (C-FEG) where the electrons are extracted from an extremely sharp tungsten tip (W(310)) at room temperature or by the combination of both methods in the so-called Schottky Field Emission Gun (S-FEG). The C-FEG and S-FEG guns are highly coherent and produce bright electrons sources, essential for EH, while thermionic source provides more intense but poorly coherent beam. In the second step, electron waves are accelerated (typically up to 60 kV to 300 kV) and the illumination system (a set of two or three condenser lenses) allows defining the beam (probe size, convergence angle, electron dose) that irradiates the top surface of the specimen. The electron wave then interacts with the sample through various process of scattering, both elastic and inelastic. After that the formation of a diffraction pattern in the back focal plane occurs. Finally the formation of the image is possible in the image plane [106]. A schematic representation of the image formation in TEM following this simple idea is displayed in Figure 2.5.1.

The electron-specimen interaction makes that the incident electron wave changes its initial state by elastic and inelastic scattering phenomena. A summary of the signals generated by the electron-specimen interaction is also illustrated in Figure 2.5.1. In inelastic scattering processes, the electrons loose a small amount of energy that is

transferred to the specimen producing the emission of a wide range of secondary signals (x-rays, visible light, secondary electrons, phonons and plasmons excitations), also damaging the specimen [107]. These secondary signals are very useful to perform analytical TEM experiments such as X-ray energy-dispersive spectroscopy (XEDS), electron energy-loss spectroscopy (EELS) or cathodoluminescence. On the other hand, in elastic processes the electrons are scattered without losing energy. In crystalline materials, the elastic scattering gives rise to Bragg diffraction related to the constructive interference of the scattered electron waves in a periodic crystal. Thus, Bragg scattering results in a series of diffracted beams scattered at angles dependent on the lattice periodicities of the crystal structure. The elastically scattered electron beams are the ones used to form images in TEM techniques such as diffraction-contrast TEM [108] and phase-contrast High-Resolution TEM (HRTEM) [107].

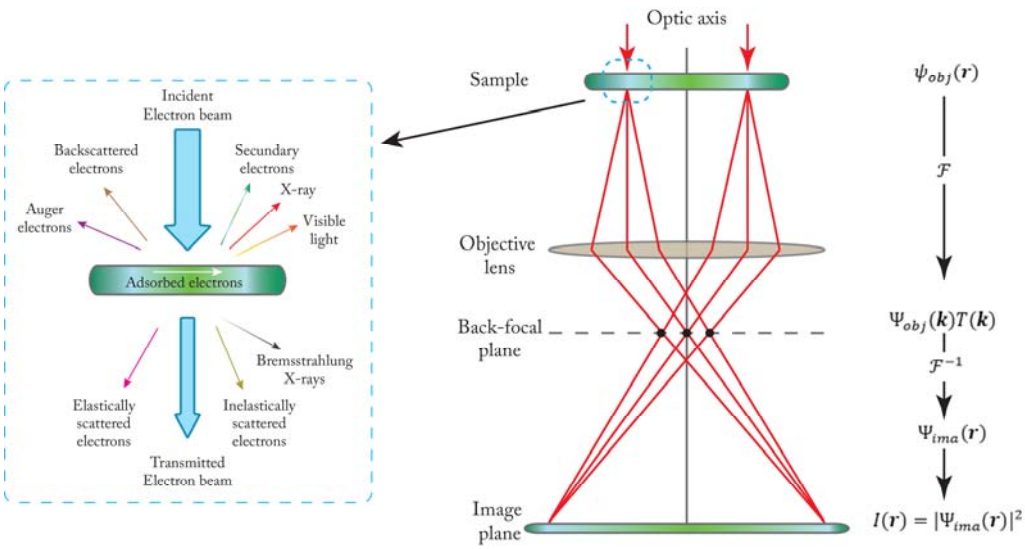

Figure 2.5.1. Left: signals generated by the electron beam-specimen interaction. Right: basic schematic representation of the image formation by the objective lens in a TEM. Red lines represent the optical path followed by the electrons during the image formation process.

The mathematical description of the image formation process in a TEM is described as follows. According to quantum mechanics, the scattering of a high energy

electron plane wave interacting with a crystalline specimen can be well explained by the relativistic time-independent Schrödinger equation, also known as Dirac equation [109]. Considering a *weak phase object approximation* (electrons are scattered elastically by a thin specimen and absorption effects are neglected), its solution at the exit surface of the specimen is a transmitted wave function in the direct space $\boldsymbol{r} = (x, y, z)$ called *object electron wave:*

$$\psi_{obj}(\boldsymbol{r}) = A(\boldsymbol{r})e^{i\phi(\boldsymbol{r})} \qquad \textit{Eq. 2.5.1}$$

where $A(\boldsymbol{r})$ is the amplitude of the exit wave function and $\phi(\boldsymbol{r})$ is a phase shift induced by the potential with which the electrons interact when passing through the sample. Next, the object electron wave is propagated by the objective lens to create a diffraction pattern in its back focal plane and an image of the specimen in its image plane. According to diffraction theory, electrons scattered by the same lattice planes converge in a common point in the back focal plane of the objective lens, creating a representation of the specimen in the reciprocal space (i.e. a diffraction pattern). From a mathematical point of view, such diffraction pattern is the *Fourier transform* ($\mathcal{F}$) of the object electron wave:

$$\Psi_{obj}(\boldsymbol{k}) = \mathcal{F}\left[\psi_{obj}(\boldsymbol{r})\right] \qquad \textit{Eq. 2.5.2}$$

where $\boldsymbol{k}$ is the reciprocal vector. The Fourier transform $\Psi_{obj}(\boldsymbol{k})$ is defined as:

$$\Psi_{obj}(\boldsymbol{k}) = \int \psi_{obj}(\boldsymbol{r})\, e^{(2\pi i \boldsymbol{k}\cdot\boldsymbol{r})} d\boldsymbol{r} \qquad \textit{Eq. 2.5.3}$$

In the image formation process, the object electron wave is modified by the aberrations of the objective lens (mainly defocus, astigmatism and spherical aberration). These optical artefacts can be introduced by means of a *transfer function,* $T(\boldsymbol{k})$,

multiplying the object electron wave in reciprocal space, $\Psi_{obj}(\boldsymbol{k})$. Thus, the diffraction wave function, $\Psi_{diff}(\boldsymbol{k})$, on the back focal plane becomes the following function [110], [111]:

$$\Psi_{diff}(\boldsymbol{k}) = \Psi_{obj}(\boldsymbol{k})T(\boldsymbol{k}) \qquad \textit{Eq. 2.5.4}$$

In general, the transfer function can be expressed as:

$$T(\boldsymbol{k}) = B(\boldsymbol{k})e^{i\chi(\boldsymbol{k})}e^{-ig(\boldsymbol{k})} \qquad \textit{Eq. 2.5.5}$$

where $B(\boldsymbol{k})$ is a pre-exponential function associated with the use of a cut-off aperture and magnification effects, $g(\boldsymbol{k})$ is a damping function which accounts for all the microscope instabilities (lens current, acceleration voltage, etc.) and the incoherence of the electron probe, and $\chi(\boldsymbol{k})$ is the *phase contrast function*, which contains the phase shift introduced by the lens aberrations (defocus, astigmatism, coma, spherical aberrations, etc.). Neglecting high order aberration factors, $\chi(\boldsymbol{k})$ can be expressed as:

$$\chi(\boldsymbol{k}) = \frac{2\pi}{\lambda}\left[\frac{C_S}{4}\lambda^4 k^4 + \frac{\Delta z}{2}\lambda^2 k^2 - \frac{C_A}{2}\left(k_y^2 - k_x^2\right)\lambda^2\right] \qquad \textit{Eq. 2.5.6}$$

where C_S is the spherical aberration coefficient, C_A is the axial astigmatism coefficient, λ is the electron wavelength and Δz is the defocus. Finally, the objective lens forms an image of the object in the image plane $\Psi_{img}(\boldsymbol{r})$ in real space, which corresponds to an *inverse Fourier transform* of $\Psi_{diff}(\boldsymbol{k})$.

$$\Psi_{img}(\boldsymbol{r}) = \mathcal{F}^{-1}\left[\Psi_{diff}(\boldsymbol{k})\right] = \mathcal{F}^{-1}\left[\Psi_{obj}(\boldsymbol{k})T(\boldsymbol{k})\right] \qquad \textit{Eq. 2.5.7}$$

Afterwards, a series of projector lenses transfers the image of the object to a conjugated plane where the detector (e.g. fluorescent screen, charge-coupled-device

CCD camera, CMOS camera, direct electron detector,…) records the image as an intensity map of the image electron wave. The image intensity is expressed as the squared modulus of $\Psi_{img}(\boldsymbol{r})$:

$$I(\boldsymbol{r}) = \left|\Psi_{img}(\boldsymbol{r})\right|^2 = \Psi_{img}(\boldsymbol{r}) \cdot \left(\Psi_{img}(\boldsymbol{r})\right)^* \qquad \textit{Eq. 2.5.8}$$

In an ideal microscope free of optical defects where images are recorded at zero defocus (Gaussian focus), without aberrations, aperture cut-off or incoherence, $T(\boldsymbol{k}) = 1$, and the intensity is:

$$I(\boldsymbol{r}) = \left|\Psi_{img}(\boldsymbol{r})\right|^2 = |A(\boldsymbol{r})|^2 \qquad \textit{Eq. 2.5.9}$$

In such ideal case, $I(\boldsymbol{r})$ only records the amplitude of the object electron wave, losing the information contained in the phase shift, $\phi(\boldsymbol{k})$. Furthermore, in weak phase objects the amplitude is homogeneous, resulting an image without any contrast at all. As we will see in the next section, the study of magnetic materials by TEM experiments requires being able to record the phase shift of the object electron wave.

2.5.2 Electron beam phase shift measurements: recording the magnetism

The phase of an electron wave is modified when interacting with an object and with any electromagnetic field around it. From quantum mechanics, we know that the electron function that describes the behaviour of relativistic electrons in an electromagnetic field can be deduced from the Dirac equation, where the electron spin would be neglected:

$$\frac{1}{2m_e}(-i\hbar\nabla + e\boldsymbol{A})^2\Psi(x,y,z) = e[U^* + \gamma V]\Psi(x,y,z) \qquad \textit{Eq. 2.5.10}$$

where $\boldsymbol{A}$ and V are the magnetic and electric potential respectively, e is the electron charge, m_e is the rest mass of the electron, γ is the relativistic Lorentz factor [$\gamma = 1 + eU/m_e c^2$] and U^* is the relativistic corrected accelerating potential [$U^* = (U/2)(1+\gamma)$, where U is the non-relativistic accelerating potential]. The solution of this equation corresponds to the object electron wave $\psi_{obj}(\boldsymbol{r}) = A(\boldsymbol{r})e^{i\phi(\boldsymbol{r})}$ (Eq. 2.5.1), where its phase shift is modified due to the Aharonov-Bohm effect [112]:

$$\phi(x) = \frac{\pi\gamma}{\lambda U^*}\int \mathrm{V}(x,z)dz - \frac{e}{\hbar}\int A_z(x,y)dz \qquad \textit{Eq. 2.5.11}$$

where $\lambda = \hbar/(2em_e U^*)^{1/2}$ is the electron relativistic wavelength, and $A_{\boldsymbol{z}}$ is the component of the magnetic vector potential $\boldsymbol{A}$ along the beam direction. This 1D equation for the phase shift can be generalise to a 2D vector in the case of a two-dimensional phase shift $\phi(x,y)$ in the plane (x,y). Eq. 2.5.11 can be written in terms of the corresponding magnetic induction as [113]:

$$\phi(x) = C_E\int V(x,z)dz - \frac{e}{\hbar}\int_{-\infty}^{+\infty}\int_{-\infty}^{x} B_y(x',z)dx'dz \qquad \textit{Eq. 2.5.12}$$

where V corresponds to the mean inner potential and B_y is the magnetic component of the induction along the y direction and $C_E = (\pi\gamma/\lambda U^*)$ is an interaction constant that only depends on the energy of the incident electron beam. C_E takes values of 7.29×10^6, 6.53×10^6 and $5.39 \times 10^6\ rad.V^{-1}.m^{-1}$ at accelerating voltages of 200kV, 300kV and 1MV, respectively [114]. Eq. 2.5.11 underlines that when the electrons propagate through a ferromagnetic specimen, the phase shift will contain information about the electrostatic potential (mean inner potential related to the composition and density) and the magnetic vector potential (magnetic induction). Therefore, the imaging

of magnetic properties by TEM methods requires measuring the magnetic contribution of the phase shift resulting from the interaction of the object electron wave with the magnetic induction.

A common strategy to extract information from the phase shift of the electron wave is to tune the transfer function of the microscope in order to modulate the electron wave and obtain an image whose intensity is related to the phase shift. This strategy is used in HRTEM to resolve atomic columns, and it is known as *phase-contrast imaging*. In advanced TEM with C_S-aberration corrector, the transfer function can be modulated through the phase contrast function by slight variation of the focal distance Δz. The main problem of such reconstruction is the fact that HRTEM imaging requires the use of the conventional objective lens of the microscope, which cannot be used for magnetic imaging.

2.5.3 The objective lens

The objective lens (OL) is the most important of the different lenses that constitute a TEM. It forms the first highly magnified image of the object and therefore determines the quality and the spatial resolution of the final image. The OL, as all the lenses of the electron microscope, is an electromagnetic lens that creates a magnetic field with a focusing effect on the electron beam. It is composed of a copper coil winded inside a cylindrical magnetic yoke excited with a high electric current to generate an axial magnetic field. The pole pieces of the yoke are designed to concentrate the flux lines in a small region where the electrons pass through the pole piece gap.

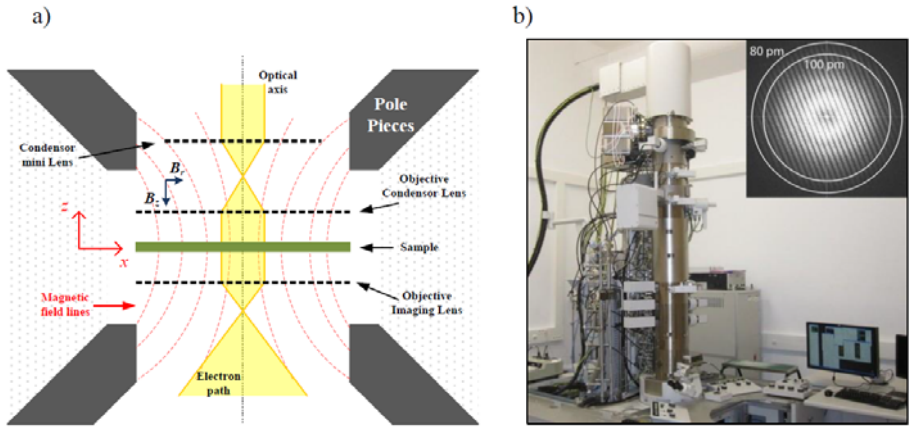

Figure 2.5.2. a) Schematic representation of the magnetic field lines (dash red lines) inside a twin type OL. (b) The column of I2TEM microscope (CEMES-CNRS). In the inset, Young fringes experiment revealing the limit of the spatial resolution of the I2TEM in HRTEM mode (80 pm) [115].

In Figure 2.5.2 a), we schematize a twin-type OL used in advanced microscopes. In this optical system, the specimen is placed just in the centre of the gap between the pole pieces of two symmetric magnetic lenses, immersing the sample in a very intense and uniform magnetic field. The disposition of these two pole pieces, together with a mini-condenser lens placed in the upper part of the OL, gives the possibility to easily change the operation mode of the microscope between microprobe and nanoprobe modes.

For the OL of an electron microscope, the magnetic field in the centre of the pole pieces gap B_0 can be experimentally measured using a special holder equipped with a dedicated Hall probe fitted in the sample position. Rodríguez et al. have reported an approximate value of $B_0 = 2.4\,T$ in the HRTEM mode for a FEI Titan^3 microscope [116]. This magnetic field has also been measured at about 1T for the Hitachi HF3300 (I2TEM) we used for this work. Therefore, the magnetic field of the OL is sufficiently high to saturate most ferromagnetic materials, aligning the magnetization almost parallel to the optical axis. This does not only alter the magnetic state of the specimen but also minimizes the magnetic contrast because the TEM magnetic imaging

techniques are only sensitive to magnetic induction components perpendicular to the optical axis. Thus classical HRTEM conditions is not adequate to study the magnetic configurations of ferromagnets.

The OL has then to be switched off for TEM magnetic studies and other optical alignments of the microscope have to be set in which the sample remains in a field-free environment. In dedicated TEM a special lens called *Lorentz lens*, located just below the OL is used in this case to magnify and form the image of the object. The Lorentz lens has a weak focusing power in order to produce a very weak magnetic field on the specimen. The combined effect of the Lorentz lens and the remnant field of the OL leads to a residual magnetic field of the order of few mT, which can be eventually compensated with the mini-condenser lens. This imaging mode called *Lorentz mode* can be used in EH as well as in LM. Both allow studying magnetic materials in a remnant state without altering their magnetic states. Due to its long focal length (few tens of millimetres), the Lorentz lens has a large spherical aberration, degrading the spatial resolution to few nanometers and limiting the total magnification up to approximately × 70.000. Fortunately, recent developments in aberration correction set-ups have made possible to correct the spherical aberration of the Lorentz lens, improving the spatial resolution [117]. Furthermore, recent prototypes of dedicated Lorentz microscopes like Hitachi I2TEM (*Interferometry In-situ TEM*), designed between CEMES-CNRS and Hitachi High Technology can reach a spatial resolution of 0.5 nm in Lorentz mode using another stage above the OL to guarantee field-free conditions. Once we provide a field free environment for the sample, a phase contrast method is then able to recover the magnetic contribution to the phase shift of the electron wave using a Lorentz mode to form the image of the object. Under these conditions, the two magnetic imaging techniques currently available in TEM can come into play: Lorentz microscopy and Electron Holography.

2.6 Electron holography

When an electron beam passes through a material, the amplitude and phase of the electron wave will change. In conventional TEM imaging, the amplitude and phase information are mixed and only the spatial distribution of the intensity (the square of the amplitude) of the electron wave is recorded as we saw in the previous section. While a single recorded image considered as a bright-field TEM image has information about the structure of the material, any information about the phase of the electron wave function is lost. Electron holography (EH) is an interferometric technique that allows recording directly the phase shift of the high-energy electron wave that passed through a specimen. The phase shift can, in turn, be used to provide information about local variations in the magnetic induction and electrostatic potential within and around the specimen.

The concept of electron holography was initially proposed and developed in 1948 by Denis Gabor [91], [118], who was interested in overcoming electron microscope instrument limitations due to the unwanted aberration in electromagnetic lenses [90]. The type of holography initially proposed by Gabor is called in-line holography, but this one has for the most part been superseded by off-axis holography, which does not suffer from the twin image problem. An explanation of the technique is detailed in the next section. There are, in fact, many other proposed schemes for holography, both in-line and off-axis using TEM and STEM as discussed in the review of Cowley [107].

2.6.1 Off-axis electron holography

In *off-axis electron holography*, the phase shift can be extracted by performing an interferometry experiment where the object electron wave interferes with a reference

electron wave. The resulting interference pattern, the *hologram*, is a set of fringes with local periodicity variations and shifts due to the relative difference of the phase of the object wave and the reference wave. The hologram intensity and contrast are related to the amplitude of the object wave [93] and its stability over the exposure time. To implement this technique, the electron microscope requires the use of a high brightness and highly coherent electron source associated with an *electron biprism* to create the overlap of the two beams [120]. Particularly a high spatial coherence and a high brightness permit recording holograms with a very good fringe contrast and intensity within a short acquisition time, of few seconds, to avoid specimen and/or beam drift effects. This has been possible with the generalization of a new generation of instruments with high-brightness coherent and stable electron sources such as Schottky and Cold Field Emission Guns (S-FEG and C-FEG). The electron biprism is usually a very thin Au-coated glass fibre or a Pt wire with a diameter of ~1μm, it is used to deflect both object and reference electron wave to produce an overlap region that enables the interference phenomenon [121], [122]. Such deflection is achieved by the application of a positive voltage to the biprism. Although there is an optimum geometric arrangement of the biprism in the column of the microscope to obtain the highest hologram quality [123], most electron microscopes have to assemble it among the selected area apertures for technical reasons. As the interference is produced between one electron wave that passes by the vacuum and another through the sample, a vacuum area close to the sample is required. Then, both electron waves are deflected by the electric potential induced by the biprism, they overlap and interfere to form a hologram in the image plane. A scheme of the off-axis electron holography arrangement is shown in Figure 2.6.1.

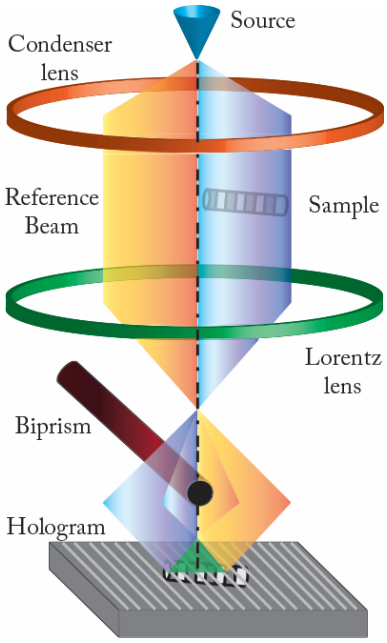

Figure 2.6.1. Off-axis electron holography scheme

Mathematically, the hologram formation is described as follow. We consider that the reference electron wave is a plane wave $\psi_{ref}(\boldsymbol{r}) = e^{i2\pi\boldsymbol{k}\cdot\boldsymbol{r}}$, and the object electron wave is the wave function of Eq. 2.5.1. The action of the biprism makes that both reference and object electron waves are tilted with a certain angle ($\alpha_h/2$ and $-\alpha_h/2$, respectively). Thus the wave function resulting from the interferences along the x-axis is given by:

$$f_{int}(\boldsymbol{r}) = A(\boldsymbol{r})exp\left[-\pi i\frac{\alpha_h}{\lambda}x + i\phi(\boldsymbol{r})\right] + exp\left[\pi i\frac{\alpha_h}{\lambda}x\right] \qquad \textit{Eq. 2.6.1}$$

and the intensity is:

$$I_{hol}(\boldsymbol{r}) = |f_{int}(\boldsymbol{r})|^2 = 1 + A^2(\boldsymbol{r}) + 2A(\boldsymbol{r})\cos\left[2\pi\frac{\alpha_h}{\lambda}x - \phi(\boldsymbol{r})\right] \qquad \textit{Eq. 2.6.2}$$

From Eq. 2.6.2, we see that the hologram is formed by the conventional bright field image $I_{BF} = 1 + A^2(\boldsymbol{r})$, superimposed over the sinusoidal term that represents mathematically the fringe pattern of the hologram, and depends on both amplitude and

phase shift of the object wave. Thus the hologram contains all the information of the object electron wave. The period of the interference fringes, λ/α_h, depends on the deflection angle induced by the biprism voltage. Performing a Fourier transform on the hologram, we obtain:

$$F|I_{hol}(\boldsymbol{r})| = \delta(\boldsymbol{u}) + F[A^2(\boldsymbol{r})] + F\left[A(\boldsymbol{r})e^{i\phi(r)}\right] \otimes \delta\left(\boldsymbol{u} + \frac{\alpha_h}{\lambda}\widehat{\boldsymbol{X}}\right) + F\left[A(\boldsymbol{r})e^{-i\phi(r)}\right] \otimes \delta\left(\boldsymbol{u} - \frac{\alpha_h}{\lambda}\widehat{\boldsymbol{X}}\right) \qquad \textit{Eq. 2.6.3}$$

where $\otimes$ indicates the convolution operation, $\boldsymbol{u}$ and $\widehat{\boldsymbol{X}}$ are the variables in the Fourier space for $\boldsymbol{r}$ and $\boldsymbol{x}$ respectively. In the Fourier space, the hologram is represented by a central spot (central band) and two collinear spots (sidebands) equally spaced with respect to the centre. The central band contains the conventional bright-field image, while each sideband stores the information of the amplitude and phase. Choosing one of the sidebands and performing the inverse Fourier transform allows to extract the object electron wave.

$$F^{-1}\left\{F\left[A(\boldsymbol{r})e^{i\phi(r)}\right] \otimes \delta(\boldsymbol{u})\right\} = A(\boldsymbol{r})e^{i\phi(r)} = \psi_{obj}(\boldsymbol{r}) \qquad \textit{Eq. 2.6.4}$$

From Eq. 2.6.4, we can reconstruct the complete object electron wave.

2.6.2 Phase reconstruction

The reconstruction process starts calculating the fast Fourier transform of a digitally recorded hologram through, for instance, a CCD camera in order to obtain the spectrum image. Using a numerical mask, one of the sidebands is isolated and centred before calculating its inverse Fourier transform. Finally, the calculation of the amplitude and phase shift of the resulting complex image can be done through the following expression:

$$\phi(\boldsymbol{r}) = arctan\left[\frac{Im\left(\Psi_{obj}(\boldsymbol{r})\right)}{Re\left(\Psi_{obj}(\boldsymbol{r})\right)}\right] \qquad \textit{Eq. 2.6.5}$$

$$A(\boldsymbol{r}) = \sqrt{\left[Im\left(\Psi_{obj}(\boldsymbol{r})\right)\right]^2 + \left[Re\left(\Psi_{obj}(\boldsymbol{r})\right)\right]^2} \qquad \textit{Eq. 2.6.6}$$

where $Im\left(\Psi_{obj}(\boldsymbol{r})\right)$ and $Re\left(\Psi_{obj}(\boldsymbol{r})\right)$ are the imaginary and real parts of the wave function respectively. [124]. The choice of the type and the size of the numerical mask is essential as it defines partly the final resolution but also the noise of the phase images. The fringe space (S_f) is another important factor for the spatial resolution of the reconstructed image [125]. A summary of the phase reconstruction process is represented in the Figure 2.6.2, using as example a Co/Cu multilayered magnetic nanowire.

In addition, it is important to record a reference hologram in some place of the vacuum, free of electric and magnetic stray fields produced by the specimen. The phase shift of this reference hologram is extracted following the same procedure than the initial hologram and is used to remove unavoidable Fresnel fringes due to the biprism itself as well as to compensate for phase artefacts caused by distortions of the imaging and recording system [126].

Although many EH users develop their own computational routines, there are commercial scripts that run under Digital Micrograph (Gatan©) software to perform the complete phase reconstruction. In our case, we have used the *GPA* software developed by M. Hÿtch and extended for EH applications by C. Gatel to extract the amplitude and the phase [124].

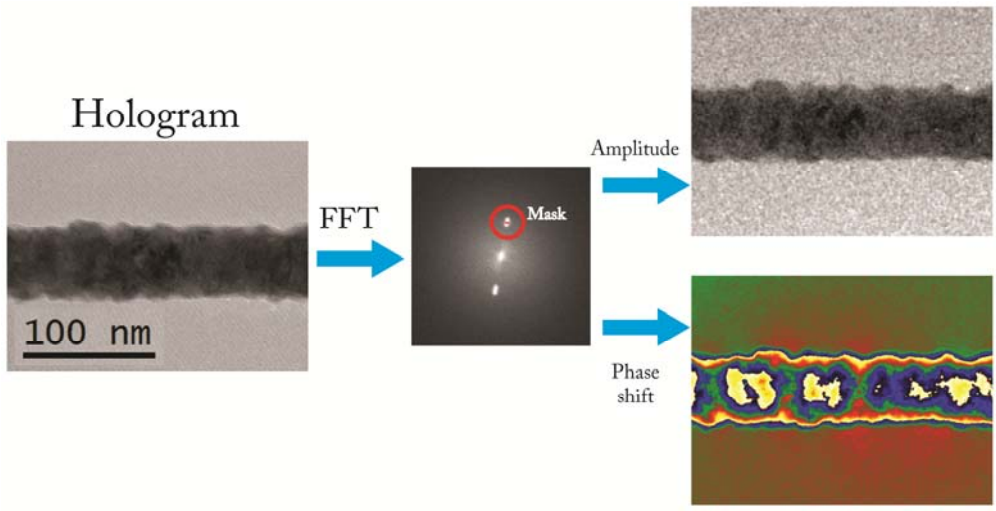

Figure 2.6.2. Scheme of the reconstruction process of a multilayered Co/Cu nanowire: the hologram, Fourier transform with the sideband choice, phase shift image and amplitude image.

2.6.3 Separation of the phase shift contributions

The electrostatic potential and the in-plane component of the magnetic induction in the specimen can be determined from the phase image. According to Eq. 2.5.12, the corresponding phase shift can be expressed as a lineal combination of each potential contribution given by:

$$\phi(x) = \phi_{EL}(x) + \phi_{MAG}(x) \qquad \text{Eq. 2.6.7}$$

where $\phi_{EL}(x)$ and $\phi_{MAG}(x)$ are the electrostatic and magnetic phase shift contributions (first and the second term of Eq. 2.5.12) respectively. Several procedures have been proposed to separate the two contributions; some of them are more or less suitable depending on the magnetic behaviour of the sample and their implementation:

- *Saturating the sample magnetization in two opposite directions:* this procedure can be reached by recording two holograms after saturating the magnetization of the sample in two opposite direction [127]. This method uses either the conventional objective lens or a dedicated magnetizing

holder to switch and saturate the magnetization in opposite directions. Perfectly antiparallel saturation states induce a change of the sign in the magnetic phase shift contribution keeping constant the electrostatic contribution. This method is very useful in nanostructures with high in-plane shape anisotropy (e.g. nanowires, nanostripes, TEM lamellas for polycrystalline magnets or in-plane magnetic anisotropy thin films) where the magnetostatic energy confines the magnetization in specific and stable orientations. But non saturated magnetic state (different magnetic domains separated by walls…) cannot be studied.

- *Change the electron acceleration voltage:* in this procedure, two holograms are taken at two different electron acceleration voltages. In this way, the potential of the electron's relativistic acceleration U^* is modified while the magnetic phase shift contribution remains constant (independent of the electron velocity) and therefore can be obtained by dividing both phase shifts. According to Eq. 2.5.12 and Eq. 2.6.7, such division can be expressed as:

$$\frac{U_2^*}{U_1^*} = \frac{\phi_1(x) - \phi_{MAG1}(x)}{\phi_2(x) - \phi_{MAG2}(x)} \qquad \textit{Eq. 2.6.8}$$

where the subscripts 1 and 2 are associated with each acceleration voltage. As the magnetic phase shift does not depend on the electron acceleration, $\phi_{MAG1} = \phi_{MAG2} = \phi_{MAG}$, and therefore:

$$\phi_{MAG}(x,y) = \frac{U_1^*\phi_1(x) - U_2^*\phi_2(x)}{U_1^* - U_2^*} \qquad \textit{Eq. 2.6.9}$$

Unfortunately, the change of the acceleration voltage modifies dramatically the optical alignment of the microscope such as the image magnifications, aberrations, resolution and the Lorentz deflection angles. This makes the image reconstruction difficult and also compromises the optical stability of the microscope. This method is rarely used.

- *Take two holograms at two different temperatures:* the two holograms are recorded above and below the Curie temperature (T_C) of the material [128], [129]. In this way, at $T > T_C$ corresponding to the paramagnetic state, the phase shift only contains information of the electrostatic contribution. Subtracting this phase shift with those obtained at $T < T_C$ allows extracting the magnetic phase shift contribution. The implementation of this procedure requires the use of cooling/heating holders in order to induce the magnetic transition. The main drawbacks are the sample drift due to the high temperature, also it is not suitable for many systems as materials with high T_C (e.g. Fe, Co and Ni oxides [130], [131]), nanoparticles (deterioration, coalescence or reaction with ligands [132], [133]).

- *Switching upside down the sample:* The main advantage of this method is that it can be applied in all the cases. It consists in recording two holograms where one of them is taken after manually flipping the sample upside down. It was proposed by Tonomura considering the "time-reversal operation of the electron beam" [134], where the sign of the magnetic phase shift contribution is changed by flipping the sample while the electrostatic phase shift (a scalar) remains constant. By this way the magnetic state of the specimen is not altered. The main drawback is the realignment of the phase

images for correcting their relative shift and rotation before computing the half sum and the half difference. We have chosen this method for our study

An example of the phase shift separations using switching upside down method for a Co/Cu NW is shown in the Figure 2.6.3. The phase shift image resulting from the first experiment is called *Up*, then the second phase shift image (*Down*) is obtained. The two phase shift images are aligned, then the half sum and the half subtraction of them resulting in the contribution corresponding to the main inner potential (MIP) and the magnetic (MAG) contribution.

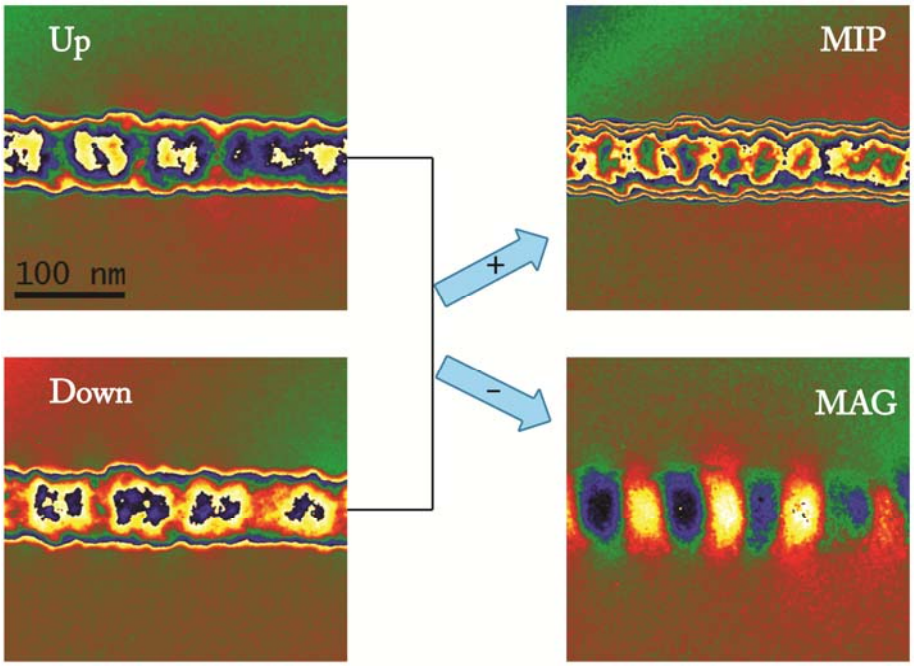

Figure 2.6.3. Phase separation in a multilayered nanowire. Left: up and down holograms from switching upside down the sample. Right: MIP phase shift map and magnetic phase shift map resulting of add or subtract the two phases of the left.

The final phase images have values between $-\pi$ and $+\pi$ and phase discontinuities appears at positions where the phase exceeds this amount (wrapped image). The phase image can be *"unwrapped"* using some suitable algorithms (developed at CEMES by M. Hÿtch and C. Gatel) to remove the phase jumps and to obtain a continuous variation of

the phase shift. In the Figure 2.6.4 MIP and magnetic phase shift maps unwrapped are shown.

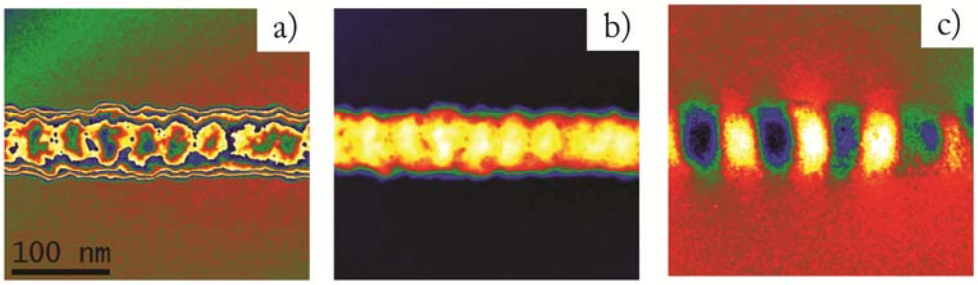

Figure 2.6.4. a) MIP phase shift map, b) unwrapped MIP and c) magnetic phase shift map unwrapped.

A Hitachi HF 3300C (I2TEM) microscope was used for electron holography experiments. This microscope has been specially designed to perform in-situ and interferometry experiments. Associated to a cold field emission source with an accelerating voltage up to 300kV, two goniometers are available on the column: one of them is called Lorentz stage and is located above of the objective lens, where the sample can be in real free magnetic field position and the other one is the normal stage in which the sample is located in the middle of the OL. This microscope has a spherical aberration corrector (B-Corr) dedicated to large field of view modes allowing to reach a spatial resolution < 0.5 nm in Lorentz mode. Four rotatable electrostatic biprisms have been installed. We have used two of them in a double biprism configuration [125] to avoid artefacts linked to Fresnel fringes [135] and to set separately the interference area size W and the fringe spacing S_f. The fringe space partly determines the spatial resolution of a reconstructed image, and W is related to the observable size of the specimen [125].

The I2TEM microscope has also another biprism placed in the condenser system of the microscope. This allows to split the beam of electrons for off-axis electron holography experiments. That feature permits to increase the distance between the

object and the reference wave at the object plane [136]. This allows to tilt the reference wave, which is useful in the dark-field electron holography [137]. In Figure 2.6.5 a photo of the I2TEM microscope is shown.

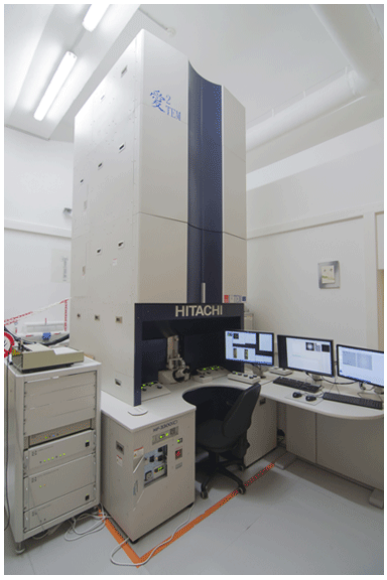

Figure 2.6.5. Photo of Hitachi HF 3300C located in CEMES-CNRS, Toulouse.

References

[1] W. Rippard, M. Pufall, S. Kaka, T. Silva, S. Russek, and J. Katine, "Injection Locking and Phase Control of Spin Transfer Nano-oscillators," Phys. Rev. Lett., vol. 95, no. 6, Aug. 2005.

[2] J.-V. Kim, "Spin-Torque Oscillators," in Solid State Physics, vol. 63, Elsevier, 2012, pp. 217–294.

[3] M. D. Stiles and J. Miltat, "Spin-transfer torque and dynamics," in Spin dynamics in confined magnetic structures III, Springer, 2006, pp. 225–308.

[4] S. Iijima, "Helical microtubules of graphitic carbon," Nature, vol. 354, no. 6348, pp. 56–58, Nov. 1991.

[5] R. S. Wagner and W. C. Ellis, "VAPOR-LIQUID-SOLID MECHANISM OF SINGLE CRYSTAL GROWTH," Appl. Phys. Lett., vol. 4, no. 5, p. 89, 1964.

[6] B. Krishnan, R. V. K. G. Thirumalai, Y. Koshka, S. Sundaresan, I. Levin, A. V. Davydov, and J. N. Merrett, "Substrate-Dependent Orientation and Polytype Control in SiC Nanowires Grown on 4H-SiC Substrates," Cryst. Growth Des., vol. 11, no. 2, pp. 538–541, Feb. 2011.

[7] Y. Su, C. Liu, S. Brittman, J. Tang, A. Fu, N. Kornienko, Q. Kong, and P. Yang, "Single-nanowire photoelectrochemistry," Nat. Nanotechnol., Mar. 2016.

[8] K. Winkler, E. Bertagnolli, and A. Lugstein, "Origin of Anomalous Piezoresistive Effects in VLS Grown Si Nanowires," Nano Lett., vol. 15, no. 3, pp. 1780–1785, Mar. 2015.

[9] Y. Li, Y. Wang, S. Ryu, A. F. Marshall, W. Cai, and P. C. McIntyre, "Spontaneous, Defect-Free Kinking via Capillary Instability during Vapor–Liquid–Solid Nanowire Growth," Nano Lett., vol. 16, no. 3, pp. 1713–1718, Mar. 2016.

[10] A. D. Gamalski, J. Tersoff, and E. A. Stach, "Atomic Resolution in Situ Imaging of a Double-Bilayer Multistep Growth Mode in Gallium Nitride Nanowires," Nano Lett., vol. 16, no. 4, pp. 2283–2288, Apr. 2016.

[11] N. Kaur, E. Comini, D. Zappa, N. Poli, and G. Sberveglieri, "Nickel oxide nanowires: vapor liquid solid synthesis and integration into a gas sensing device," Nanotechnology, vol. 27, no. 20, p. 205701, May 2016.

[12] M. T. Björk, B. J. Ohlsson, T. Sass, A. I. Persson, C. Thelander, M. H. Magnusson, K. Deppert, L. R. Wallenberg, and L. Samuelson, "One-dimensional Steeplechase for Electrons Realized," Nano Lett., vol. 2, no. 2, pp. 87–89, Feb. 2002.

[13] Y. Zhang, R. E. Russo, and S. S. Mao, "Femtosecond laser assisted growth of ZnO nanowires," Appl. Phys. Lett., vol. 87, no. 13, p. 133115, 2005.

[14] X. Duan and C. M. Lieber, "Laser-Assisted Catalytic Growth of Single Crystal GaN Nanowires," J. Am. Chem. Soc., vol. 122, no. 1, pp. 188–189, Jan. 2000.

[15] Y. F. Zhang, Y. H. Tang, H. Y. Peng, N. Wang, C. S. Lee, I. Bello, and S. T. Lee, "Diameter modification of silicon nanowires by ambient gas," Appl. Phys. Lett., vol. 75, no. 13, p. 1842, 1999.

[16] T. E. Clark, P. Nimmatoori, K.-K. Lew, L. Pan, J. M. Redwing, and E. C. Dickey, "Diameter Dependent Growth Rate and Interfacial Abruptness in Vapor–Liquid–Solid Si/Si1-xGex Heterostructure Nanowires," Nano Lett., vol. 8, no. 4, pp. 1246–1252, Apr. 2008.

[17] D. Shakthivel, W. Taube, S. Raghavan, and R. Dahiya, "VLS growth mechanism of Si-nanowires for flexible electronics," in Ph. D. Research in Microelectronics and Electronics (PRIME), 2015 11th Conference on, 2015, pp. 349–352.

[18] Z. R. Dai, Z. W. Pan, and Z. L. Wang, "Novel nanostructures of functional oxides synthesized by thermal evaporation," Adv. Funct. Mater., vol. 13, no. 1, pp. 9–24, 2003.

[19] Z. W. Pan, Z. R. Dai, and Z. L. Wang, "Nanobelts of semiconducting oxides," Science, vol. 291, no. 5510, pp. 1947–1949, 2001.

[20] B. D. Yao, Y. F. Chan, and N. Wang, "Formation of ZnO nanostructures by a simple way of thermal evaporation," Appl. Phys. Lett., vol. 81, no. 4, p. 757, 2002.

[21] N. Wang, Y. H. Tang, Y. F. Zhang, C. S. Lee, and S. T. Lee, "Nucleation and growth of Si nanowires from silicon oxide," Phys. Rev. B, vol. 58, no. 24, p. R16024, 1998.

[22] J. Niu, J. Sha, and D. Yang, "Silicon nanowires fabricated by thermal evaporation of silicon monoxide," Phys. E Low-Dimens. Syst. Nanostructures, vol. 23, no. 1–2, pp. 131–134, Jun. 2004.

[23] Y. J. Xing, Z. H. Xi, X. D. Zhang, J. H. Song, R. M. Wang, J. Xu, Z. Q. Xue, and D. P. Yu, "Thermal evaporation synthesis of zinc oxide nanowires," Appl. Phys. A, vol. 80, no. 7, pp. 1527–1530, Apr. 2005.

[24] A. Pierret, M. Hocevar, S. L. Diedenhofen, R. E. Algra, E. Vlieg, E. C. Timmering, M. A. Verschuuren, G. W. G. Immink, M. A. Verheijen, and E. P. A. M. Bakkers, "Generic nano-imprint process for fabrication of nanowire arrays," Nanotechnology, vol. 21, no. 6, p. 65305, Feb. 2010.

[25] R.-H. Horng, H.-I. Lin, and D.-S. Wuu, "ZnO nanowires lift-off from silicon substrate embedded in flexible films," in Nanoelectronics Conference (INEC), 2013 IEEE 5th International, 2013, pp. 1–3.

[26] P. Mohan, J. Motohisa, and T. Fukui, "Controlled growth of highly uniform, axial/radial direction-defined, individually addressable InP nanowire arrays," Nanotechnology, vol. 16, no. 12, pp. 2903–2907, Dec. 2005.

[27] S. F. A. Rahman, U. Hashim, M. N. M. Nor, A. M. M. Nuri, M. E. A. Shohini, S. Salleh, M. Rusop, and T. Soga, "Nanowire Formation Using Electron Beam Lithography," 2009, pp. 504–508.

[28] Y.-J. Chen, J.-H. Hsu, and H.-N. Lin, "Fabrication of metal nanowires by atomic force microscopy nanoscratching and lift-off process," Nanotechnology, vol. 16, no. 8, pp. 1112–1115, Aug. 2005.

[29] L. Marín, L. Morellón, P. A. Algarabel, L. A. Rodríguez, C. Magén, J. M. De Teresa, and M. R. Ibarra, "Enhanced Magnetotransport in Nanopatterned Manganite Nanowires," Nano Lett., vol. 14, no. 2, pp. 423–428, Feb. 2014.

[30] D. McGrouther and J. N. Chapman, "Nanopatterning of a thin ferromagnetic CoFe film by focused-ion-beam irradiation," Appl. Phys. Lett., vol. 87, no. 2, p. 22507, 2005.

[31] A. Fernández-Pacheco, L. Serrano-Ramón, J. M. Michalik, M. R. Ibarra, J. M. De Teresa, L. O'Brien, D. Petit, J. Lee, and R. P. Cowburn, "Three dimensional magnetic nanowires grown by focused electron-beam induced deposition," Sci. Rep., vol. 3, Mar. 2013.

[32] F. Ott, I. Panagiotopoulos, E. Anagnostopoulou, M. Pousthomis, L.-M. Lacroix, G. Viau, and J.-Y. Piquemal, "Soft chemistry nanowires for permanent magnet fabrication," in Magnetic Nano- and Microwires, Elsevier, 2015, pp. 629–651.

[33] M. Pousthomis, E. Anagnostopoulou, I. Panagiotopoulos, R. Boubekri, W. Fang, F. Ott, K. A. Atmane, J.-Y. Piquemal, L.-M. Lacroix, and G. Viau, "Localized magnetization reversal processes in cobalt nanorods with different aspect ratios," Nano Res., vol. 8, no. 7, pp. 2231–2241, Jul. 2015.

[34] K. Soulantica, F. Wetz, J. Maynadié, A. Falqui, R. P. Tan, T. Blon, B. Chaudret, and M. Respaud, "Magnetism of single-crystalline Co nanorods," Appl. Phys. Lett., vol. 95, no. 15, p. 152504, 2009.

[35] P. Moutet, L.-M. Lacroix, A. Robert, M. Impéror-Clerc, G. Viau, and L. Ressier, "Directed Assembly of Single Colloidal Gold Nanowires by AFM Nanoxerography," Langmuir, vol. 31, no. 14, pp. 4106–4112, Apr. 2015.

[36] B. B. L. Guangli Che and C. R. M. Ellen R. Fisher, "Carbon nanotubule membranes for electrochemical energy storage and production," science, vol. 393, pp. 346–349, 1998.

[37] T. L. Wade and J.-E. Wegrowe, "Template synthesis of nanomaterials," Eur. Phys. J. Appl. Phys., vol. 29, no. 1, pp. 3–22, Jan. 2005.

[38] Y. Henry, K. Ounadjela, L. Piraux, S. Dubois, J.-M. George, and J.-L. Duvail, "Magnetic anisotropy and domain patterns in electrodeposited cobalt nanowires," Eur. Phys. J. B-Condens. Matter Complex Syst., vol. 20, no. 1, pp. 35–54, 2001.

[39] J. Y. Miao, Y. Cai, Y. F. Chan, P. Sheng, and N. Wang, "A Novel Carbon Nanotube Structure Formed in Ultra-Long Nanochannels of Anodic Aluminum Oxide Templates," J. Phys. Chem. B, vol. 110, no. 5, pp. 2080–2083, Feb. 2006.

[40] M. Vázquez, M. Hernández-Vélez, K. Pirota, A. Asenjo, D. Navas, J. Velázquez, P. Vargas, and C. Ramos, "Arrays of Ni nanowires in alumina membranes: magnetic properties and spatial ordering," Eur. Phys. J. B, vol. 40, no. 4, pp. 489–497, Aug. 2004.

[41] T. Mehmood, B. Shahzad Khan, A. Mukhtar, X. Chen, P. Yi, and M. Tan, "Mechanism for formation of fcc-cobalt nanowires in electrodeposition at ambient temperature," Mater. Lett., vol. 130, pp. 256–258, Sep. 2014.

[42] D. L. Zagorskiy, V. V. Korotkov, K. V. Frolov, S. N. Sulyanov, V. N. Kudryavtsev, S. S. Kruglikov, and S. A. Bedin, "Track Pore Matrixes for the Preparation of Co, Ni and Fe Nanowires: Electrodeposition and their Properties," Phys. Procedia, vol. 80, pp. 144–147, 2015.

[43] L. Soleimany, A. Dolati, and M. Ghorbani, "A study on the kinetics of gold nanowire electrodeposition in polycarbonate templates," J. Electroanal. Chem., vol. 645, no. 1, pp. 28–34, Jun. 2010.

[44] R. Fathi, S. Sanjabi, and N. Bayat, "Synthesis and characterization of NiMn alloy nanowires via electrodeposition in AAO template," Mater. Lett., vol. 66, no. 1, pp. 346–348, Jan. 2012.

[45] Y. Rheem, B.-Y. Yoo, W. P. Beyermann, and N. V. Myung, "Electro- and magneto-transport properties of a single CoNi nanowire," Nanotechnology, vol. 18, no. 12, p. 125204, Mar. 2007.

[46] A. Fert and L. Piraux, "Magnetic nanowires," J. Magn. Magn. Mater., vol. 200, no. 1, pp. 338–358, 1999.

[47] X. R. Zhu, C. M. Wang, Q. B. Fu, Z. Jiao, W. D. Wang, G. Y. Qin, and J. M. Xue, "Preparation of Ag/Cu Janus nanowires: Electrodeposition in track-etched polymer templates," Nucl. Instrum. Methods Phys. Res. Sect. B Beam Interact. Mater. At., vol. 356–357, pp. 57–61, 2015.

[48] H. Wang, B. Huang, H. Deng, H. Li, W. Zhang, and S. Yao, "Effect of sub-layer thickness on magnetic and giant magnetoresistance properties of Ni–Fe/Cu/Co/Cu multilayered nanowire arrays," Chin. J. Chem. Eng., vol. 23, no. 7, pp. 1231–1235, Jul. 2015.

[49] A. Mohammad, S. R. Das, Y. P. Chen, T. D. Sands, and D. B. Janes, "Electrodeposition of Indium Antimonide Nanowires in Porous Anodic Alumina Membranes," in 2010 18th Biennial University/Government/Industry Micro/Nano Symposium, 2010, pp. 1–4.

[50] K. Yu-Zhang, D. Z. Guo, J. Mallet, M. Molinari, A. Loualiche, and M. Troyon, "Electrodeposition and Characterization of CdSe Semiconducting Nanowires," J. Nanosci. Nanotechnol., vol. 8, no. 4, pp. 2022–2028, Apr. 2008.

[51] İ. Şişman, "Template-assisted electrochemical synthesis of semiconductor nanowires," in Nanowires–Implementations and Applications, InTech, 2011, pp. 41–58.

[52] F. L. Boughey, T. Davies, A. Datta, R. A. Whiter, S.-L. Sahonta, and S. Kar-Narayan, "Vertically aligned zinc oxide nanowires electrodeposited within porous polycarbonate templates for vibrational energy harvesting," Nanotechnology, vol. 27, no. 28, p. 28LT02, Jul. 2016.

[53] W. C. West, N. V. Myung, J. F. Whitacre, and B. V. Ratnakumar, "Electrodeposited amorphous manganese oxide nanowire arrays for high energy and power density electrodes," J. Power Sources, vol. 126, no. 1–2, pp. 203–206, Feb. 2004.

[54] Z. Chen, Y. Li, J. Jiang, C. Cao, T. Xu, Q. Chen, X. Xu, and H. Zhu, "Template-assisted synthesis of ordered single crystal InN nanowires," RSC Adv., vol. 2, no. 17, p. 6806, 2012.

[55] H. Q. Cao, Y. Xu, J. M. Hong, H. B. Liu, G. Yin, B. L. Li, C. Y. Tie, and Z. Xu, "Sol–Gel Template Synthesis of an Array of Single Crystal CdS Nanowires on a Porous Alumina Template," Adv. Mater., vol. 13, no. 18, pp. 1393–1394, 2001.

[56] H. Pan, B. Liu, J. Yi, C. Poh, S. Lim, J. Ding, Y. Feng, C. H. A. Huan, and J. Lin, "Growth of Single-Crystalline Ni and Co Nanowires via Electrochemical Deposition and Their Magnetic Properties," J. Phys. Chem. B, vol. 109, no. 8, pp. 3094–3098, Mar. 2005.

[57] S.-I. Pyun, H.-C. Shin, J.-W. Lee, and J.-Y. Go, "Electrochemical Methods," in Electrochemistry of Insertion Materials for Hydrogen and Lithium, Berlin, Heidelberg: Springer Berlin Heidelberg, 2012, pp. 11–32.

[58] Y. D. Gamburg and G. Zangari, Theory and Practice of Metal Electrodeposition. New York, NY: Springer New York, 2011.

[59] "Faraday's laws in one equation," J. Chem. Educ., vol. 38, no. 2, p. 98, 1961.

[60] W. Blum, "Teaching principles of electrodeposition," J. Chem. Educ., vol. 2, no. 7, p. 556, 1925.

[61] S. Shin, B. H. Kong, B. S. Kim, K. M. Kim, H. K. Cho, and H. H. Cho, "Over 95% of large-scale length uniformity in template-assisted electrodeposited nanowires by subzero-temperature electrodeposition," Nanoscale Res. Lett., vol. 6, no. 1, p. 1, 2011.

[62] Giray Kartopu and Orhan Yalçın, Fabrication and Applications of Metal Nanowire Arrays Electrodeposited in Ordered Porous Templates. INTECH Open Access Publisher, 2010.

[63] X. Dou, G. Li, H. Lei, X. Huang, L. Li, and I. W. Boyd, "Template Epitaxial Growth of Thermoelectric Bi/BiSb Superlattice Nanowires by Charge-Controlled Pulse Electrodeposition," J. Electrochem. Soc., vol. 156, no. 9, p. K149, 2009.

[64] F. Nasirpouri and A. Nogaret, Eds., Nanomagnetism and spintronics: fabrication, materials, characterization and applications. Singapore: World Scientific, 2011.

[65] J. Kim, Advances in Nanotechnology and the Environment. CRC Press, 2011.

[66] T. Shinjō, Ed., Nanomagnetism and spintronics. Amsterdam ; New York: Elsevier, 2009.

[67] J. McCord, "Progress in magnetic domain observation by advanced magneto-optical microscopy," J. Phys. Appl. Phys., vol. 48, no. 33, p. 333001, Aug. 2015.

[68] B. Mozooni and J. McCord, "Direct observation of closure domain wall mediated spin waves," Appl. Phys. Lett., vol. 107, no. 4, p. 42402, Jul. 2015.

[69] E. Nikulina, O. Idigoras, P. Vavassori, A. Chuvilin, and A. Berger, "Magneto-optical magnetometry of individual 30 nm cobalt nanowires grown by electron beam induced deposition," Appl. Phys. Lett., vol. 100, no. 14, p. 142401, 2012.

[70] W. Kuch, "Magnetic imaging," in Magnetism: A Synchrotron Radiation Approach, Springer, 2006, pp. 275–320.

[71] S. A. Gusev, V. N. Petrov, and E. V. Skorokhodov, "Problems of implementing SEMPA in experiments," J. Surf. Investig. X-Ray Synchrotron Neutron Tech., vol. 4, no. 4, pp. 582–587, Aug. 2010.

[72] T. Kohashi and K. Koike, "A spin-polarized scanning electron microscope with 5-nm resolution," Jpn. J. Appl. Phys., vol. 40, no. 11B, p. L1264, 2001.

[73] O. Boulle, J. Vogel, H. Yang, S. Pizzini, D. de Souza Chaves, A. Locatelli, T. O. Menteş, A. Sala, L. D. Buda-Prejbeanu, O. Klein, M. Belmeguenai, Y. Roussigné, A. Stashkevich, S. M. Chérif, L. Aballe, M. Foerster, M. Chshiev, S. Auffret, I. M. Miron, and G. Gaudin, "Room-temperature chiral magnetic skyrmions in ultrathin magnetic nanostructures," Nat. Nanotechnol., Jan. 2016.

[74] J. Vogel, W. Kuch, M. Bonfim, J. Camarero, Y. Pennec, F. Offi, K. Fukumoto, J. Kirschner, A. Fontaine, and S. Pizzini, "Time-resolved magnetic domain imaging by x-ray photoemission electron microscopy," Appl. Phys. Lett., vol. 82, no. 14, p. 2299, 2003.

[75] L. Abelmann, S. Porthun, M. Haast, C. Lodder, A. Moser, M. E. Best, P. J. van Schendel, B. Stiefel, H. J. Hug, G. P. Heydon, and others, "Comparing the resolution of magnetic force microscopes using the CAMST reference samples," J. Magn. Magn. Mater., vol. 190, no. 1, pp. 135–147, 1998.

[76] M. R. Koblischka and U. Hartmann, "Recent advances in magnetic force microscopy," Ultramicroscopy, vol. 97, no. 1–4, pp. 103–112, Oct. 2003.

[77] R. Wiesendanger, "Spin mapping at the nanoscale and atomic scale," Rev. Mod. Phys., vol. 81, no. 4, pp. 1495–1550, Nov. 2009.

[78] H. Hopster and H. P. Oepen, Eds., Magnetic microscopy of nanostructures, 1st ed. Berlin ; New York: Springer, 2004.

[79] Y. Zhu, Ed., Modern techniques for characterizing magnetic materials. Boston: Kluwer Academic Publishers, 2005.

[80] R. J. Celotta, J. Unguris, M. H. Kelley, and D. T. Pierce, "Techniques to measure magnetic domain structures," Charact. Mater., 1999.

[81] L. Mayer, "Electron Mirror Microscopy of Magnetic Domains," J. Appl. Phys., vol. 28, no. 9, p. 975, 1957.

[82] M. E. Hale, H. W. Fuller, and H. Rubinstein, "Magnetic Domain Observations by Electron Microscopy," J. Appl. Phys., vol. 30, no. 5, p. 789, 1959.

[83] H. W. Fuller and M. E. Hale, "Domains in Thin Magnetic Films Observed by Electron Microscopy," J. Appl. Phys., vol. 31, no. 10, p. 1699, 1960.

[84] J. N. Chapman, P. E. Batson, E. M. Waddell, and R. P. Ferrier, "The direct determination of magnetic domain wall profiles by differential phase contrast electron microscopy," Ultramicroscopy, vol. 3, pp. 203–214, 1978.

[85] E. M. Waddell and J. N. Chapman, "Linear imaging of strong phase objects using asymmetrical detectors in STEM," Opt. Stuttg, vol. 54, pp. 83–96, 1979.

[86] J. N. Chapman, "The investigation of magnetic domain structures in thin foils by electron microscopy," J. Phys. Appl. Phys., vol. 17, no. 4, p. 623, 1984.

[87] J. N. Chapman, I. R. McFadyen, and S. McVitie, "Modified differential phase contrast Lorentz microscopy for improved imaging of magnetic structures," Magn. IEEE Trans. On, vol. 26, no. 5, pp. 1506–1511, 1990.

[88] A. Tonomura, T. Matsuda, J. Endo, T. Arii, and K. Mihama, "Direct Observation of Fine Structure of Magnetic Domain Walls by Electron Holography," Phys Rev Lett, vol. 44, no. 21, pp. 1430–1433, May 1980.

[89] A. Tonomura, "Applications of electron holography," Rev. Mod. Phys., vol. 59, no. 3, p. 639, 1987.

[90] D. Gabor, "A New Microscopic Principle," \nat, vol. 161, pp. 777–778, May 1948.

[91] D. Gabor, "Microscopy by Reconstructed Wave-Fronts," Proc. R. Soc. Math. Phys. Eng. Sci., vol. 197, no. 1051, pp. 454–487, Jul. 1949.

[92] A. Tonomura, T. Matsuda, R. Suzuki, A. Fukuhara, N. Osakabe, H. Umezaki, J. Endo, K. Shinagawa, Y. Sugita, and H. Fujiwara, "Observation of Aharonov-Bohm Effect by Electron Holography," Phys Rev Lett, vol. 48, no. 21, pp. 1443–1446, May 1982.

[93] A. Tonomura, "Electron-holographic interference microscopy," Adv. Phys., vol. 41, no. 1, pp. 59–103, Feb. 1992.

[94] T. P. Almeida, A. R. Muxworthy, A. Kovacs, W. Williams, P. D. Brown, and R. E. Dunin-Borkowski, "Direct visualization of the thermomagnetic behavior of pseudo-single-domain magnetite particles," Sci. Adv., vol. 2, no. 4, pp. e1501801–e1501801, Apr. 2016.

[95] P. A. Midgley and R. E. Dunin-Borkowski, "Electron tomography and holography in materials science," Nat. Mater., vol. 8, no. 4, pp. 271–280, 2009.

[96] J. Cumings, A. Zettl, M. R. McCartney, and J. C. H. Spence, "Electron Holography of Field-Emitting Carbon Nanotubes," Phys. Rev. Lett., vol. 88, no. 5, Jan. 2002.

[97] E. Snoeck, C. Gatel, L. M. Lacroix, T. Blon, S. Lachaize, J. Carrey, M. Respaud, and B. Chaudret, "Magnetic Configurations of 30 nm Iron Nanocubes Studied by Electron Holography," Nano Lett., vol. 8, no. 12, pp. 4293–4298, Dec. 2008.

[98] N. Biziere, C. Gatel, R. Lassalle-Balier, M. C. Clochard, J. E. Wegrowe, and E. Snoeck, "Imaging the fine structure of a magnetic domain wall in a Ni nanocylinder," Nano Lett., vol. 13, no. 5, pp. 2053–2057, 2013.

[99] C. Gatel, F. J. Bonilla, A. Meffre, E. Snoeck, B. Warot-Fonrose, B. Chaudret, L.-M. Lacroix, and T. Blon, "Size-Specific Spin Configurations in Single Iron Nanomagnet: From Flower to Exotic Vortices," Nano Lett., vol. 15, no. 10, pp. 6952–6957, Oct. 2015.

[100] L. Marín, L. A. Rodríguez, C. Magén, E. Snoeck, R. Arras, I. Lucas, L. Morellón, P. A. Algarabel, J. M. De Teresa, and M. R. Ibarra, "Observation of the Strain Induced Magnetic Phase Segregation in Manganite Thin Films," Nano Lett., vol. 15, no. 1, pp. 492–497, Jan. 2015.

[101] D. Wolf, L. A. Rodriguez, A. Béché, E. Javon, L. Serrano, C. Magen, C. Gatel, A. Lubk, H. Lichte, S. Bals, G. Van Tendeloo, A. Fernández-Pacheco, J. M. De Teresa, and E. Snoeck, "3D Magnetic Induction Maps of Nanoscale Materials Revealed by Electron Holographic Tomography," Chem. Mater., vol. 27, no. 19, pp. 6771–6778, Oct. 2015.

[102] M. R. McCartney, M. A. Gribelyuk, J. Li, P. Ronsheim, J. S. McMurray, and D. J. Smith, "Quantitative analysis of one-dimensional dopant profile by electron holography," Appl. Phys. Lett., vol. 80, no. 17, p. 3213, 2002.

[103] Z. Gan, D. E. Perea, J. Yoo, S. Tom Picraux, D. J. Smith, and M. R. McCartney, "Mapping electrostatic profiles across axial p-n junctions in Si nanowires using off-axis electron holography," Appl. Phys. Lett., vol. 103, no. 15, p. 153108, 2013.

[104] M. Linck, H. Lichte, and M. Lehmann, "Off-axis electron holography: Materials analysis at atomic resolution: Dedicated to Professor Dr. Knut Urban on the occasion of his 65th birthday," Z. Für Met., vol. 97, no. 7, pp. 890–898, 2006.

[105] M. Hÿtch, C. Gatel, F. Houdellier, E. Snoeck, and K. Ishizuka, "Darkfield electron holography for strain mapping at the nanoscale," Microsc. Anal., vol. 121, pp. 6–10, 2012.

[106] H. Köhler, "On Abbe's Theory of Image Formation in the Microscope," Opt. Acta Int. J. Opt., vol. 28, no. 12, pp. 1691–1701, Dec. 1981.

[107] D. B. Williams and C. B. Carter, Transmission electron microscopy: a textbook for materials science, 2nd ed. New York: Springer, 2008.

[108] B. Fultz and J. M. Howe, Transmission Electron Microscopy and Diffractometry of Materials. Berlin, Heidelberg: Springer Berlin Heidelberg, 2002.

[109] R. Jagannathan, "Quantum theory of electron lenses based on the Dirac equation," Phys. Rev. A, vol. 42, no. 11, p. 6674, 1990.

[110] E. J. Kirkland, Advanced Computing in Electron Microscopy. Boston, MA: Springer US, 2010.

[111] J. C. H. Spence, High-resolution electron microscopy, Fourth edition. Oxford: Oxford University Press, 2013.

[112] Y. Aharonov and D. Bohm, "Significance of electromagnetic potentials in the quantum theory," Phys. Rev., vol. 115, no. 3, p. 485, 1959.

[113] H. Lichte and M. Lehmann, "Electron holography—basics and applications," Rep. Prog. Phys., vol. 71, no. 1, p. 16102, Jan. 2008.

[114] A. Kirkland and S. Haigh, Eds., "Front Matter," in RSC Nanoscience & Nanotechnology, 2nd ed., Cambridge: Royal Society of Chemistry, 2015, pp. P001–P006.

[115] L. A. Rodríguez González, "In situ Lorentz microscopy and electron holography in magnetic nanostructures," Université Paul Sabatier/Universidad de Zaragoza, France/Spain, 2014.

[116] L. A. Rodríguez, C. Magén, E. Snoeck, C. Gatel, L. Marín, L. Serrano-Ramón, J. L. Prieto, M. Muñoz, P. A. Algarabel, L. Morellon, J. M. De Teresa, and M. R. Ibarra, "Quantitative in situ magnetization reversal studies in Lorentz microscopy and electron holography," Ultramicroscopy, vol. 134, pp. 144–154, Nov. 2013.

[117] N. Nuhfer, A. Budruk, and M. De Graef, "Aberration-Corrected Lorentz Microscopy," Microsc. Microanal., vol. 16, no. S2, pp. 142–143, Jul. 2010.

[118] D. Gabor, "Microscopy by reconstructed wave fronts: II," Proc. Phys. Soc. Sect. B, vol. 64, no. 6, p. 449, 1951.

[119] J. M. Cowley, "Twenty forms of electron holography," Ultramicroscopy, vol. 41, no. 4, pp. 335–348, 1992.

[120] H. Lichte, "Parameters for high-resolution electron holography," Ultramicroscopy, vol. 51, no. 1, pp. 15–20, 1993.

[121] H. Lichte, "Gottfried Möllenstedt and his electron biprism: four decades of challenging and exciting electron physics," J. Electron Microsc. (Tokyo), vol. 47, no. 5, pp. 387–394, 1998.

[122] R. E. Dunin-Borkowski, T. Kasama, M. Beleggia, and G. Pozzi, "Lorentz Microscopy and Electron Holography of Magnetic Materials," in Handbook of Nanoscopy, vol. 1&2, Wiley-VCH, 2012, pp. 221–251.

[123] H. Lichte, "Electron holography: optimum position of the biprism in the electron microscope," Ultramicroscopy, vol. 64, no. 1, pp. 79–86, 1996.

[124] M. J. Hÿtch, E. Snoeck, and R. Kilaas, "Quantitative measurement of displacement and strain fields from HREM micrographs," Ultramicroscopy, vol. 74, no. 3, pp. 131–146, 1998.

[125] K. Harada, T. Akashi, Y. Togawa, T. Matsuda, and A. Tonomura, "Optical system for double-biprism electron holography," J. Electron Microsc. (Tokyo), vol. 54, no. 1, pp. 19–27, 2005.

[126] W. J. de Ruijter and J. K. Weiss, "Detection limits in quantitative off-axis electron holography," Ultramicroscopy, vol. 50, no. 3, pp. 269–283, 1993.

[127] R. E. Dunin-Borkowski, M. R. McCartney, B. Kardynal, and D. J. Smith, "Magnetic interactions within patterned cobalt nanostructures using off-axis electron holography," J. Appl. Phys., vol. 84, no. 1, p. 374, 1998.

[128] J. C. Loudon, N. D. Mathur, and P. A. Midgley, "Charge-ordered ferromagnetic phase in La0.5Ca0.5MnO3," Nature, vol. 420, no. 6917, pp. 797–800, Dec. 2002.

[129] J. H. Yoo, Y. Murakami, D. Shindo, T. Atou, and M. Kikuchi, "Behavior of magnetic domains in La 0.46 Sr 0.54 MnO 3 during the ferromagnetic phase transformation studied by electron holography," Phys. Rev. B, vol. 66, no. 21, Dec. 2002.

[130] D. Levy, R. Giustetto, and A. Hoser, "Structure of magnetite (Fe3O4) above the Curie temperature: a cation ordering study," Phys. Chem. Miner., vol. 39, no. 2, pp. 169–176, Feb. 2012.

[131] B. Chatterjee, "Oxidation of iron, cobalt and nickel at the Curie temperature," Solid State Commun., vol. 27, no. 12, pp. 1455–1458, 1978.

[132] D. R. Glenn, H. Zhang, N. Kasthuri, R. Schalek, P. K. Lo, A. S. Trifonov, H. Park, J. W. Lichtman, and R. L. Walsworth, "Correlative light and electron microscopy using cathodoluminescence from nanoparticles with distinguishable colours," Sci. Rep., vol. 2, Nov. 2012.

[133] W. D. Pyrz and D. J. Buttrey, "Particle size determination using TEM: a discussion of image acquisition and analysis for the novice microscopist," Langmuir, vol. 24, no. 20, pp. 11350–11360, 2008.

[134] A. Tonomura, T. Matsuda, J. Endo, T. Arii, and K. Mihama, "Holographic interference electron microscopy for determining specimen magnetic structure and thickness distribution," Phys. Rev. B, vol. 34, no. 5, p. 3397, 1986.

[135] J. Endo, J. Chen, D. Kobayashi, Y. Wada, and H. Fujita, "Transmission laser microscope using the phase-shifting technique and its application to measurement of optical waveguides," Appl. Opt., vol. 41, no. 7, pp. 1308–1314, 2002.

[136] T. Tanigaki, S. Aizawa, H. S. Park, T. Matsuda, K. Harada, and D. Shindo, "Advanced split-illumination electron holography without Fresnel fringes," Ultramicroscopy, vol. 137, pp. 7–11, Feb. 2014.

[137] F. Röder, F. Houdellier, T. Denneulin, E. Snoeck, and M. Hÿtch, "Realization of a tilted reference wave for electron holography by means of a condenser biprism," Ultramicroscopy, vol. 161, pp. 23–40, Feb. 2016.

Chapter 3
Methodology

3.1 Introduction

This chapter is dedicated to the detailed description of the methodology used during this work. The first part of this chapter gives the detailed process of elaboration of multilayered Co/Cu NWs in LSI-Palaiseau. This knowledge was used to install a similar set-up where Ni NWs were grown in the CEMES lab. The second part shows the process to perform electron holography (EH) and the hologram treatment to obtain the magnetic phase shift maps. Finally, the micromagnetic simulations process are detailed.

3.2 Growth of nanowires

Three different magnetic NWs have been studied in this thesis: Co/Cu multilayered NWs, Ni NWs and FeCoCu NWs with modulated diameter. In this section, the two first cases are treated and the last one will be detailed in chapter 5.

3.2.1 Growth of Co/Cu nanowires in the template

For this study, Co/Cu multilayered nanowires were grown by template synthesis, using pulsed electrodeposition technique. These multilayered Co/Cu NWs were grown with the help of Travis Wade at the "Laboratoire des Solides Irradiés" (LSI) which is located inside the "Ecole Polytechnique". Through this collaboration possible thanks to Nicolas Biziere, we have learnt the growth process, produced the

electrodeposited Co/Cu NWs and obtained the expertise to dissolve and clean the NWs.

A global scheme of the electrodeposition set-up is shown in Figure 3.2.1. The electrodeposition process refers to a film growth process which consists in the formation of a metallic coating onto a base material occurring through the electrochemical reduction of metal ions from an electrolyte. This process can be made into templates and form materials with different shapes as nanowires. The electrolyte is an ionic conductor, where chemical species containing the metal of interest are dissolved into a suitable solvent or brought to the liquid state to form a molten salt.

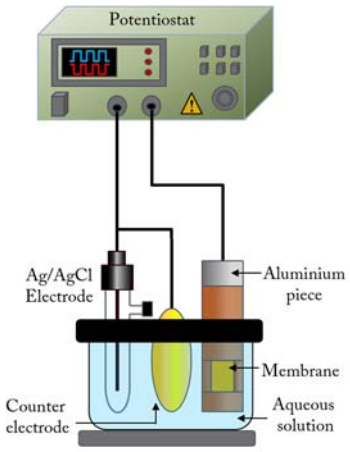

Figure 3.2.1. Scheme of the electrodeposition set-up

The principle of electrodeposition consists essentially of the immersion of the object where the deposition will be held (membrane) in a vessel containing the electrolyte (aqueous solution) and a counter electrode, followed by the connection of the two electrodes to an external power supply to make current flow possible (potentiostat). The object to be filled is connected to a negative terminal of the power supply, in such a way that the metal ions are reduced to metal atoms, which eventually perform the deposition on the templates. A reference electrode is added to measure the real voltage between the counter electrode and the membrane (Ag/AgCl electrode).

In the first place, an aqueous solution composed of the elements in an ionic form is prepared. Table 3.2.1 shows the different compounds in the solution.

Table 3.2.1. The molar concentration of the compounds involves in the solution for the electrodeposition process.

Molar concentration (mol/L)	Chemical compound
0.43	$CoSO_4 \cdot H_2O$
0.01	$CuSO_4$
0.58	H_3BO_4

Cu is the nobler element, hence easier to deposit and the voltage range used to deposit Cu is overlapping with the voltage at which the Co is deposited. This produces a codeposition of the two metals during the deposition of the Co. In order to minimize this problem, the Cu concentration in the solution has to be very low with respect to the Co concentration (less than 3% of the Co concentration in this case).

Commercial polycarbonate membranes (Main manufacturing, LLC) with a pore size of 30nm were used to the deposition process. To create a substrate with electrical contact for the deposition of the nanowires, a thin film of gold of 100nm thick was deposited by sputtering over one side of the membrane as shown Figure 3.2.2.

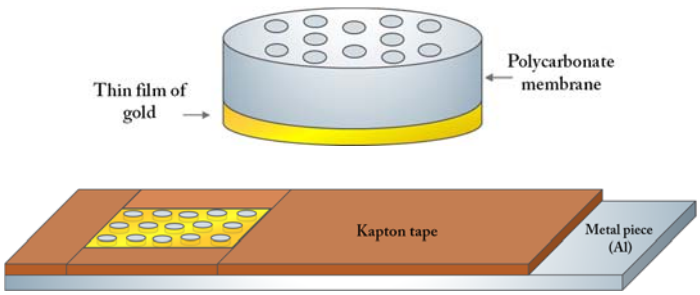

Figure 3.2.2. Scheme of the polycarbonate membrane with the thin film of gold and how this is attached to the aluminium piece.

The membrane is attached to an aluminium piece by scanning electron microscope (SEM) commercial double-faced tapes, which allows the electrical conduction between the aluminium piece and the gold film. These SEM tapes are a helpful solution when the dissolution of the membrane is carried out as we will see in next sections. The set of membrane and SEM tape are surrounded by Kapton tape to electrically isolate the aluminium piece as shown Figure 3.2.2. The electrodeposition was carried out using a potentiostat in pulsed mode with a reference electrode of Ag/AgCl and a gold sheet acting as a counter electrode. The potential used for the Co and Cu deposition were -1.0V and -0.3V respectively. In the Figure 3.2.3, pulses applied to grown the multilayered nanowires are detailed.

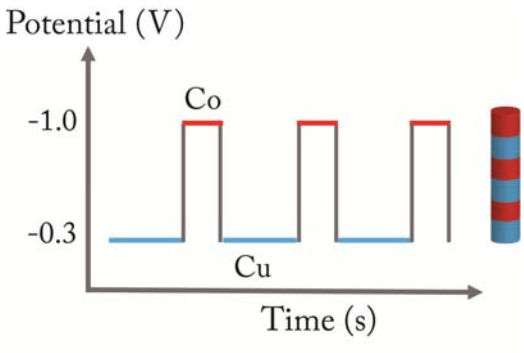

Figure 3.2.3. Scheme for the electrodeposition set-up and the pulses to grown the multilayered nanowire.

Different thickness of Co and Cu layers were grown varying the time of the pulses. Each pulse at -1.0V or -0.3V corresponds to one layer of Co or Cu respectively. In the Figure 3.2.4 a relation of the samples, time of each pulse and the nominal thickness are given. A single element (Co) nanowire was grown to study the inclusion of the Cu during the deposition of Co due to the single bath technique. The single Co NWs allowed us to extract experimentally the saturation magnetization of Co for this particular case.

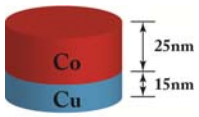

Sample M1	Co	Cu
Time (s)	1.00	10.00
Thickness (nm)	25	15

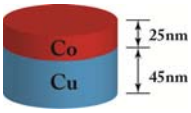

Sample M2	Co	Cu
Time (s)	1.00	30.00
Thickness (nm)	25	45

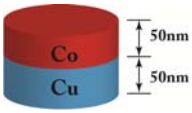

Sample M3	Co	Cu
Time (s)	2.00	35.00
Thickness (nm)	50	50

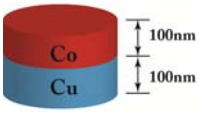

Sample M4	Co	Cu
Time (s)	4.00	70.00
Thickness (nm)	100	100

Sample M5	Co	Cu
Time (s)	300.00	0.00
Thickness (nm)	7500	

Figure 3.2.4. Relation of samples grown, time of pulses and nominal thickness for Co and Cu layers.

3.2.2 Growth of Ni nanowires in the template

With the help of Nicolas Biziere, I installed a similar set-up to electrodeposit NWs at CEMES laboratory. For this purpose, a potentiostat-galvanostat 2549 from the AMEL Company was used. The setup and a photo of the potentiostat are shown in the Figure 3.2.5. The main difference of this potentiostat with the one used in the LSI is that the last one is specially designed to perform pulsed electrodepositions. A current source and other instruments should be added to this setup in order to perform pulsed electrodeposition with as in the case of Co/Cu multilayer NW. However, this system is good enough to perform electrodeposition of pure materials and alloys.

In this particular case, I report the first attempts of electrodeposition of nickel NWs at CEMES. Polycarbonate membranes with *30 nm* of pore sizes were used. The membrane was prepared in the same way as for the electrodeposition of Co/Cu NWs (section 3.2.1). The membrane is immersed into an aqueous electrolytic solution. For this, 65.5 g of nickel sulfate ($NiSO_4 \cdot 6H_2O$) and 15 g of boric acid H_3BO_3 are dissolved in 500 mL deionized water. The electric potential between the golden surface of the membrane (working electrode) and an Ag/AgCl reference electrode is set to -1 volts.

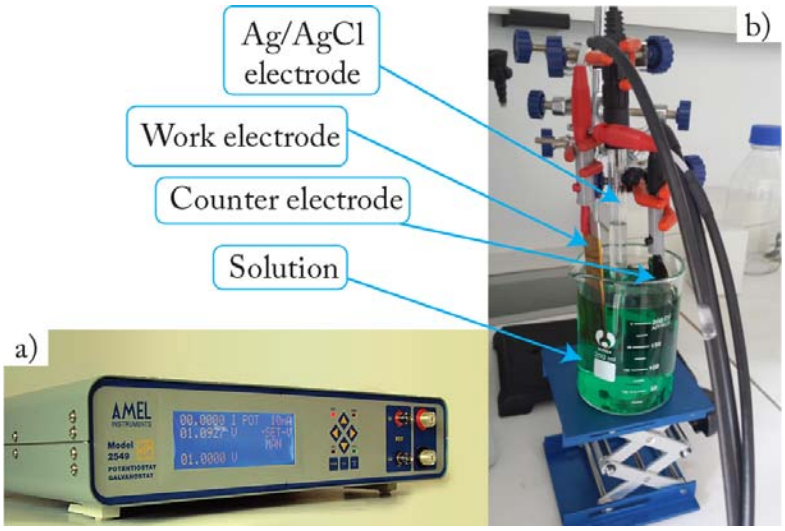

Figure 3.2.5. a) Potentiostat-galvanostat used at CEMES and b) setup indicating the different electrodes for the electrodeposition of NWs.

Before performing the electrodeposition of the desired sample, a calibration of the system should be done. Calibration curves of current vs time were performed in order to determine when the pores are filled. When the pores are filled, a layer of the same material as the NWs is deposited on top and the NWs will be stacked on one side in the film of gold and on the other one by the deposited material Figure 3.2.6 shows the calibration curve for a polycarbonate membrane of *30 nm* of pore size and their different stages during the filling pores. In the stage (1) the pores are filling, in the second stage (2) the current is increasing and the pores are full filled, then a huge change

in the current followed by a stabilization of this indicates that a film is depositing on the top of the membrane surface.

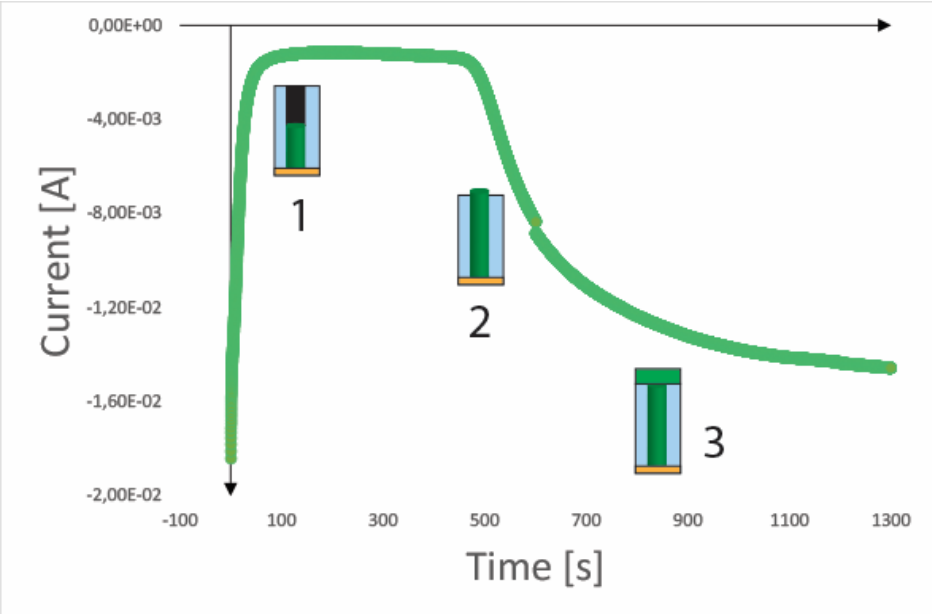

Figure 3.2.6. Calibration curve for a polycarbonate membrane of 30 nm of pore size into a solution to growing Ni NWs.

The deposition time was sufficient to obtain long NWs (≈ *300 s*) without creating the film on the top of the membrane. A photo of the membranes for the calibration and the sample of *300 s* of deposition time is shown Figure 3.2.7.

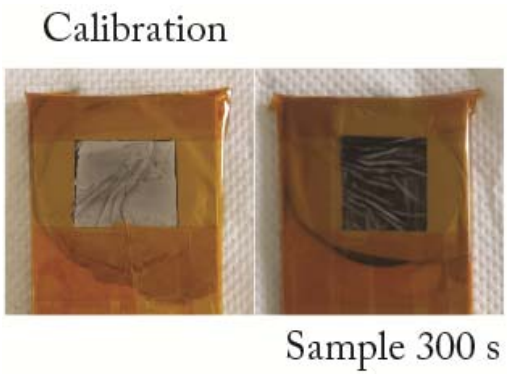

Figure 3.2.7. Photo of a) calibrate and b) sample for 300 s electrodeposited membranes of 30 nm of pore size.

The color difference between the calibration and the sample with *300 s* of deposition time on Figure 3.2.7, is due to the Ni film created on top of the surface for the calibration sample, whilst in the sample deposited during *300 s* all the pores are not filled totally. White lines observed on this last sample corresponds to places where the membrane is not totally flat. Unfortunately, we could not have enough time to perform more experiments, particularly using EH, but the electrodeposition set-up is ready to be used. Few results obtained by conventional TEM observations are given in the next section.

3.2.3 Dissolution of the membrane

After the electrodeposition process, the NWs are in an array stuck on the membranes: the first step to obtaining isolated nanowires is to dissolve the membrane. The membrane that contains the NWs is immersed into dichloromethane. The wires will be released from the membrane but they will contain still some trace of the membrane. In order to minimize the amount of remaining membrane a repetitive cleaning process is made as follows:

- The membrane with the NWs is immersed into the dichloromethane during 1 minute.
- The nanowires will be released into the dichloromethane, this mixture is placed in the ultrasound box during 1 minute.
- The solution is centrifuged during 3 minutes at 10.000 rpm.
- The dichloromethane is discarded while the NWs are retaining by putting a magnet close to the baker that contains the solution.
- New dichloromethane is added to the NWs and the process is repeated at least 3 times.

This cleaning process is essential to perform EH experiments of high quality by minimizing the artefacts due to the membrane (noise and edges effects during the alignment of phase shift maps to extract the magnetic contribution). We should say that the SEM tapes allow avoiding the impurities coming from the gold layer during the dissolution process. These impurities of gold have been found for the process where the SEM tapes are not used and they are significant. This cleaning process allows obtaining NWs free of membrane traces or with just a small amount of this. The NWs are put now into ethanol to avoid the agglomeration. The agglomeration in other systems prepared by solution methods is treated by the presence of ligands [1]–[3]. But these ligands can only separate the NWs a couple of nm which unfortunately is not enough for our purpose of having totally isolated NWs. In order to observe theses NWs in the TEM, some drops of the solution that contains the NWs are deposited on a TEM holey-carbon grid. After depositing the NWs into the TEM grid, bright field images at low magnification were acquired.

3.2.4 Observations of Co/Cu and Ni isolated nanowires

Groups of hundreds of Co/Cu NWs but also isolated NWs can be found as we can observe Figure 3.2.8. An exhaustive selection up to 85 isolated wires for each Co/Cu thickness configuration was made to select NWs with the axis orientated along the bars of the grids. This is mandatory to make sure that the saturation magnetic field is applied along a direction parallel or perpendicular to the wire axis. We should remark that only 10 to 15% of all selected NWs will allow obtaining a clear identification of the magnetic mapping (problem of adjacent NWs, carbon foil, loss of interfringes due to diffraction contrast, poor alignment of images,…).

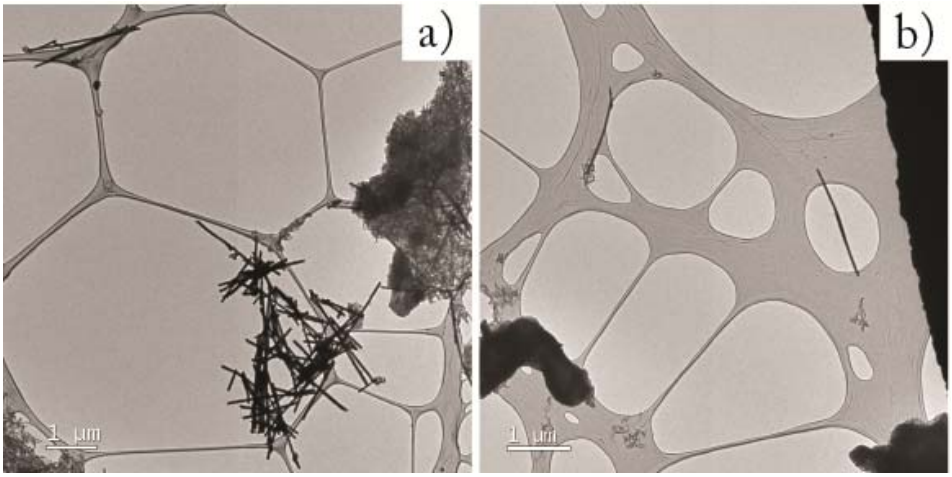

Figure 3.2.8. Bright field images at low magnification, a) group of nanowires. b) Isolated nanowires

3.2.4.1 Ni nanowires

For Ni NWs grown at CEMES, the same process of dissolution than for the Co/Cu NWs was carried out. Groups of Ni NWs were obtained: some of NWs are long enough that a portion is so far from the rest and it can be considered for potential EH experiments as "isolated" NWs. Figure 3.2.9 shows the two different configurations found for the Ni NWs.

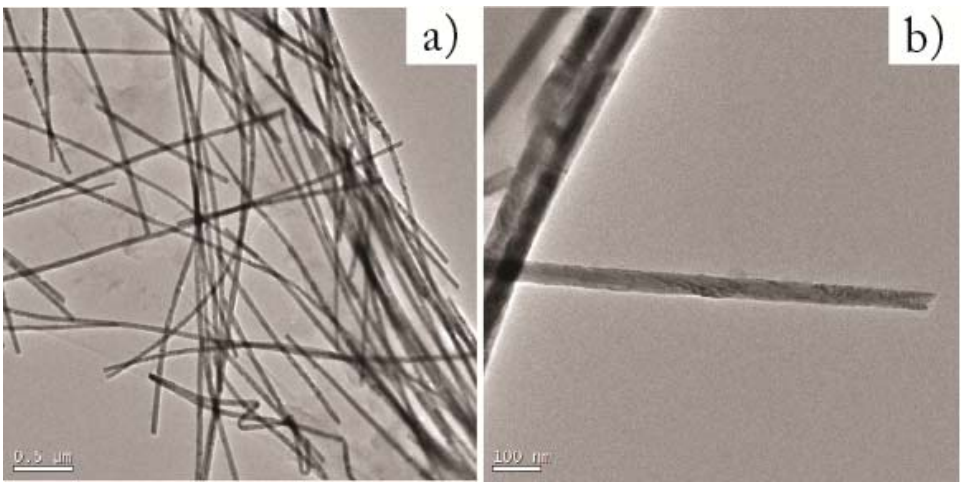

Figure 3.2.9. a) A group of Ni NWs and b) Potential Ni NW for EH experiments.

Ni NWs have an average diameter of 44 ± 2 nm. The distribution of these diameters is shown on Figure 3.2.10. Their diameters have a small dispersion as in the case of the Co/Cu NWs. In chapter 4, a discussion about the diameter changes along the NWs deposited into polycarbonate membranes is made. An important fact is that the cleaning process has been successful and most of the Ni NWs are free of residual pieces coming from the membrane.

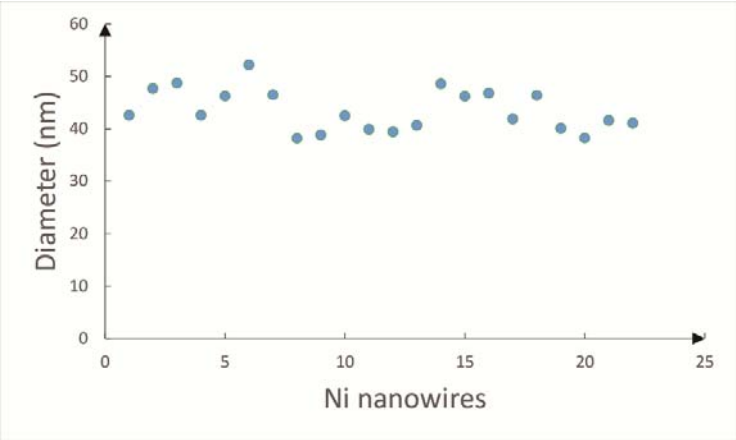

Figure 3.2.10. Distribution of diameters for Ni NWs

3.3 Magnetic configurations in Co/Cu nanowires

An exact localization and study of the orientation of the wires axis are mandatory to determine the direction of the magnetic field applied. This is possible by scanning the whole TEM carbon grid to find NWs with the axis perpendicular (PP) or parallel (PL) to an arbitrary reference axis located in the same grid (sides of the grid), then the external magnetic field is applied PP or PL respect to this reference axis. One of the major interests of this work consists in quantitatively mapping the remnant magnetic configurations at the nanoscale. Prior to the first EH observation, the nanowires have been saturated using a magnetic field of 1 T produced by an external electromagnet in the direction parallel to the wire axis. Then a second observation is

performed for an ex-situ saturation field applied in the sample plane but now perpendicular to the wire axis. In the Figure 3.3.1, a photograph of the electromagnet used and the scheme of the two different configurations are shown.

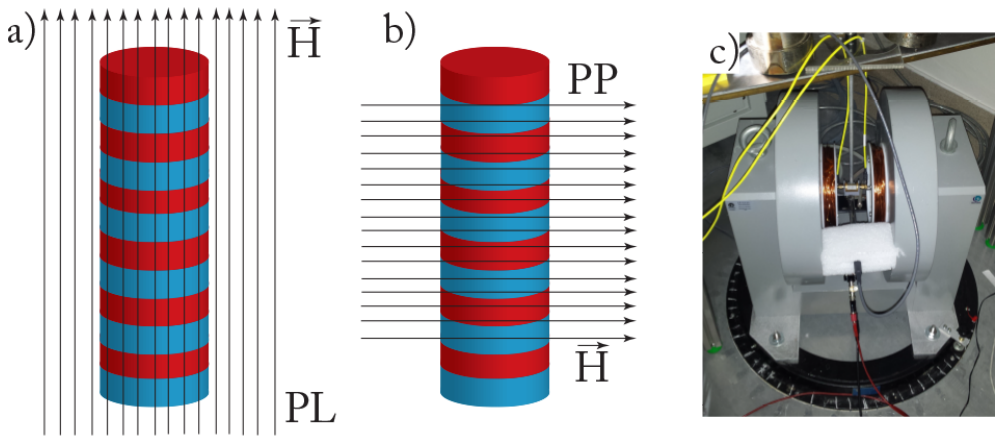

Figure 3.3.1. Scheme for the magnetic field applied: a) parallel (PL) and b) perpendicular (PP) respect to the wire axis. c) Electromagnet used to apply the external magnetic field.

3.3.1 Electron holography

Off-axis electron holography experiments were performed using a dedicated HF3300C Hitachi TEM fitted with a cold emission gun to achieve a high phase shift sensitivity, and a special corrected Lorentz mode allowing for an unprecedented spatial resolution of 0.5nm. This microscope has two stages: the normal stage where the sample is placed between the polar pieces of the objective lens, and the Lorentz stage which offers a perfect magnetic field-free sample environment keeping the objective lens on as shown Figure 3.3.2. The electron holography observations were performed just after applying a magnetic field PP and PL to the wire axis as we saw in the previous section. Several wires of micrometric length were studied (around 25 to 30 % of NWs located previously) for each Co/Cu thickness configurations. For instance, it corresponds to 20 NWs studied by EH from 85 selected NWs using conventional TEM observations.

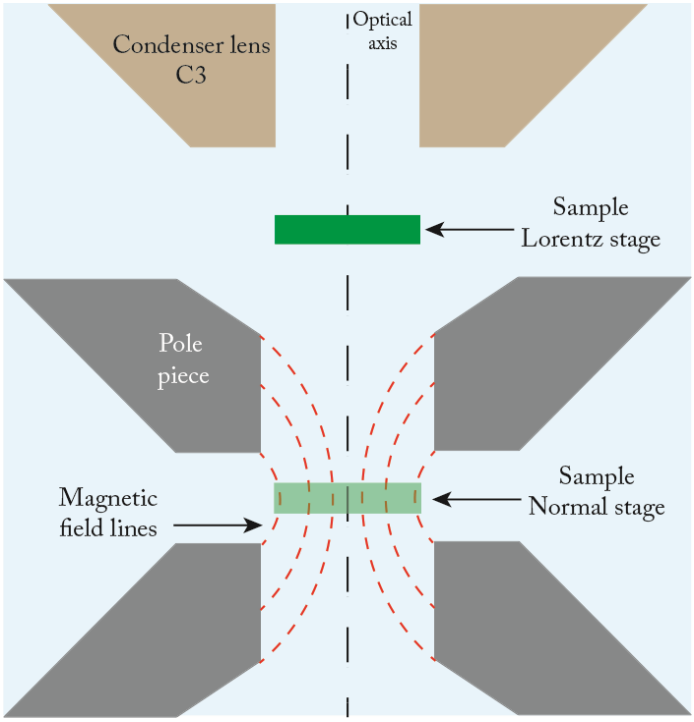

Figure 3.3.2. Scheme of the double stage in the I2TEM microscope, the sample can be placed into the normal stage under the influence of the objective lens or in a free magnetic field environment in the Lorentz stage.

An initial standard TEM alignment is performed before the biprism alignment. Two biprisms were used in order to avoid Fresnel fringes and to have a completely independent control of the field of view and the fringe spacing. In a low magnification, the first biprism (BP1) is placed parallel to the wire axis (the interference fringes will be oriented in the same direction). Then the second biprism (BP2) is aligned in the same orientation as the first to create the interference region. The process is repeated until reaching the desired high magnification. An elliptical illumination is required to perform EH: its long axis has to be perpendicular to the fringe orientations to maximize the contrast into the fringes. BP1 governs the fringe spacing by changing the applied voltage while BP2 controls the field of view. If we increase the voltage on BP1 and BP2 the fringe spacing decreases and the field of view increases. In practice, the fringe spacing is defined in order to obtain a good contrast between the interference fringes

and the desired spatial resolution on the phase shift maps. Then the field of view is fixed depending on the region of interest. Finally, the fringe spacing of the interference area should be adjusted for the new field of view. The voltages of the two biprisms are adjusted such that the fringe spacing is lower than 1 nm in the interest area. This fringe spacing partly determines the spatial resolution of a reconstructed image (see Figure 3.3.3). The typical values of voltage for a field of view 0.4 μm of width are $BP1 = 80\ V$ and $BP1 = 140\ V$ (these values are just a reference and can vary of some tens of volts). Another important parameter to take into account is the interference fringe contrast. This can be adjusted by putting the elongation direction of the illumination aligned exactly perpendicular to the biprism wire. A slight misalignment can lead to a dramatic decrease in the interference fringe contrast. This contrast was adjusted to be the highest and corresponds at about 20-25% for most of the holograms. An important parameter linked to the contrast is the noise along the fringes, this parameter is even more important than the contrast. It is better to minimize the noise with a low contrast than to have a huge contrast with a lot of noise. Thus, there is a compromise between the contrast and the noise along the fringes. The arrangement of the BP1 and BP2 inside the microscope can be founded in the work of Harada et al. [4]

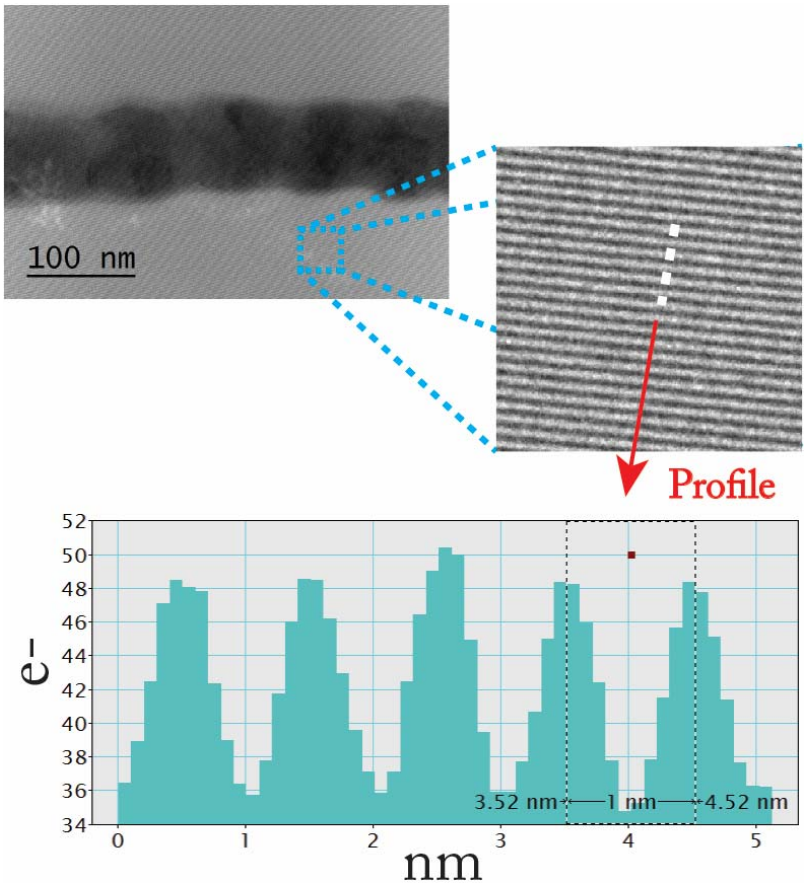

Figure 3.3.3. Hologram of a Co/Cu NW. The interference fringes are shown and their corresponding profile showing a fringe space of ≈ 1nm.

Besides the orientation, these nanowires should be isolated nanowires and be near to a vacuum area to perform off-axis electron holography. This constraint reduces considerably the number of nanowires suitable on the grid for this study (60 to 70% of NWs do not fulfil this condition). Once the system is aligned, holograms for the first configuration (up-PL) are acquired using a CCD 4k camera and displayed by Digital micrograph (Gatan Inc.) software. The interest of "up" and "down" experiments will be detailed below. Finally, a home-made software (phase live GPA) was used to perform live processing of the phase extraction. This software was very important because it allows us to select the regions with magnetic signal and avoid others than presents phase jumps due to several reasons as diffraction reflections.

The exposure time for each hologram was of 4s. The holograms were taken along the wire with a minimum of 3 holograms and a maximum of 8 holograms for each NW allowing to map a large field of view, in the up or down configuration. After acquiring all the holograms for the up-PL configuration, the sample was flipped thanks to a special sample holder allowing for a direct 180° rotation of the sample. The same NW portions acquired for the up-PL configuration were obtained for the down-PL configuration using the same settings.

It is important to note that 6 holograms were acquired to obtain a magnetic map for every single portion of each NW: an "up" hologram with two reference holograms (recorded in the vacuum) and a "down" hologram with other two reference hologram. This process was also repeated for the PP configuration. In the next section, an example of the hologram reconstruction and the separation of the electrostatic and magnetic contributions to the phase is shown.

3.3.2 Hologram reconstruction

A special treatment of the holograms has to be performed to obtain nice phase shift maps. In this section, the specific data treatment using GPA software developed by M. Hÿtch and extended for EH applications by C. Gatel is shown [5]. This software is running under Digital Micrograph (Gatan Inc) software.

We used a new procedure using two reference holograms instead one. This allow to solve the problems occurring during the reconstruction process due to the undetermined phase slopes in the corresponding phase shift maps. We also used the method of switching upside down the sample to separate the magnetic contribution from the MIP (chapter 2). The following steps have to be performed for the reconstruction of the magnetic phase maps. As an example, the phase reconstruction of a Ni NW electrodeposited at CEMES will be used.

- *Phase shift map from the reference hologram:*

  The microscope and the camera are responsible for distortions that could modify the signal from the wire itself. A first reference hologram $R1_{up}$ recorded in the vacuum is then used to get these distortions for up observation. A second reference $R2_{up}$ is used to set properly the centre of the sideband used to reconstruct the phase shift map from the FFT. If the centre of the sideband is not accurately selected, then an artificial gradient can be introduced into the reconstructed phase shift map.

  $R1_{up}$ FFT is calculated and a numerical mask is used to choose one of the sidebands. Figure 3.3.4 shows the phase shift map extracted from this reference hologram. After the sideband selection, the inverse of the FFT is calculated using just the information enclosed by the mask (phase calculation). The software allows choosing the type (cosine, or circular) and size of the mask applied to the sideband. The mask size is directly linked to the spatial resolution achieved on the phase shift map. With a large mask, the spatial resolution increases, but more noise is kept and the signal over noise ratio decreases. To improve this ratio, a smaller mask can be applied leading to a reduced spatial resolution. Thus the choice of mask size is very important and should be chosen carefully as a balance between the optimized signal over noise ratio and a nice spatial resolution. The phase shift map in the Figure 3.3.4 is the result of the first stage of this process.

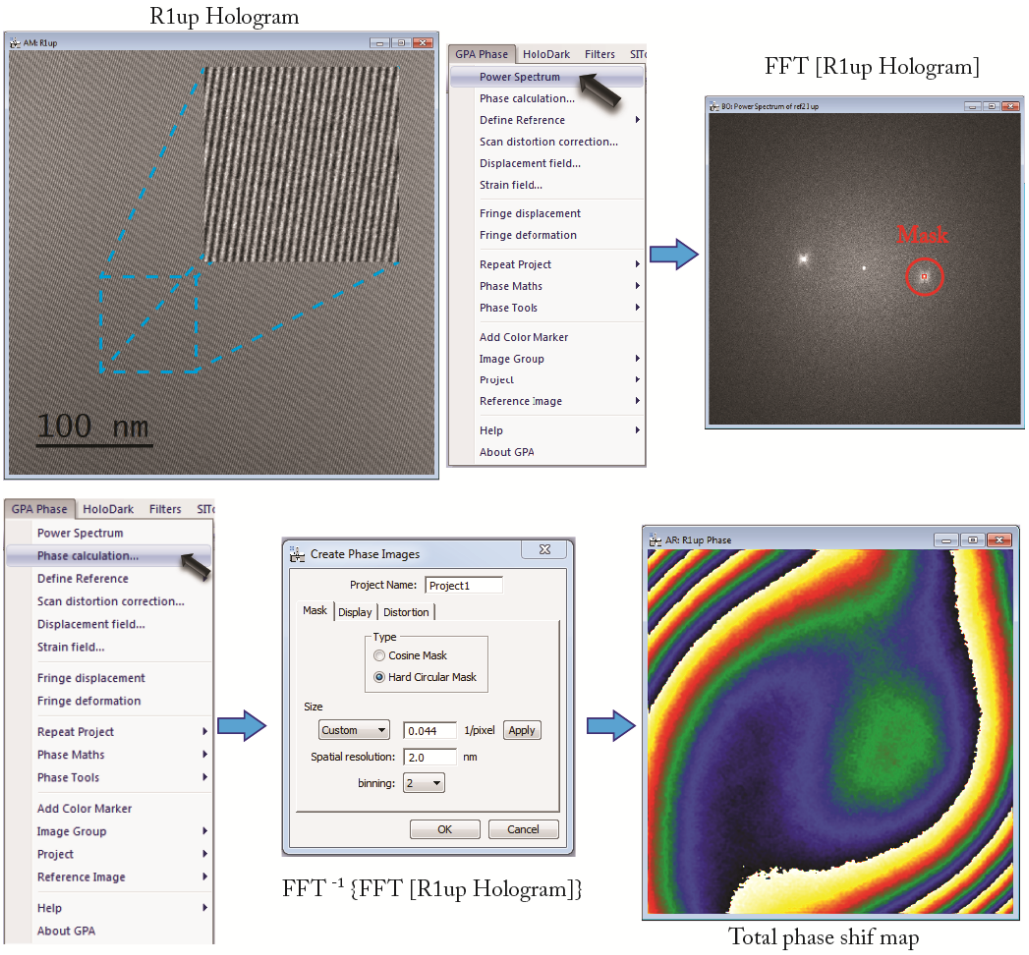

Figure 3.3.4. Phase obtaining from a reference hologram by GPA software.

To remove the slope linked to the approximation in the sideband position, the exact localization of the carrier frequency g_x and g_y should be identified and applied to the hologram of interest (recorded on a portion of a NW). The procedure shown in the Figure 3.3.4 is repeated for the $R2_{up}$ choosing the same carrier frequency g_x and g_y (By locating the mask in the same position than for $R1_{up}$). These two phase shift maps are subtracted and the carrier frequency $g(g_x, g_y)$ is extracted from the image information after correcting the linear slope using a polynomial fit applied on the whole image (Define Reference

Area). For instance, the values obtained in this case were $g_x = 0.194518$ and $g_x = -0.0289014$.

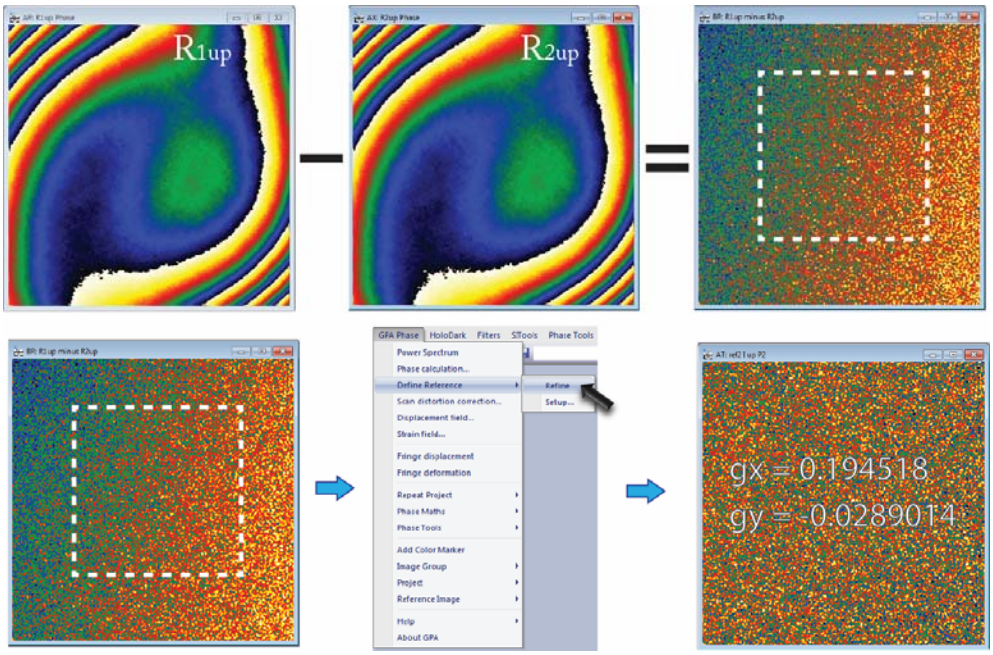

Figure 3.3.5. Obtaining of the phase carrier frequency from the reference holograms.

- *Phase shift map for the sample, removing distortions and the phase slope:* for this step the phase shift map of the region of interest on the sample (H_{up}) is obtained by the same procedure as shown Figure 3.3.4. The only difference with that process is that the amplitude image is recorded too. The phase shift map for the sample up (P_{up}) is shown Figure 3.3.6. Once we have obtained P_{up}, a simple subtraction with the phase shift map of the references up ($R1_{up}$ phase) is performed. This procedure removes the phase shift contributions coming from the camera and microscope set-up distortions. The resulting phase shift image P_{up} *corrected* has some phase jumps and a linear slope around the NW. To remove this slope, the g_x and g_y values calculated previously are applied to P_{up} *corrected*. The mentioned procedure to define a reference manually is shown Figure 3.3.6. This new procedure is essential when a stray field is visible around

the NW. The magnetic induction inside and outside the NW can thus be mapped with a high accuracy without losing or modifying any information.

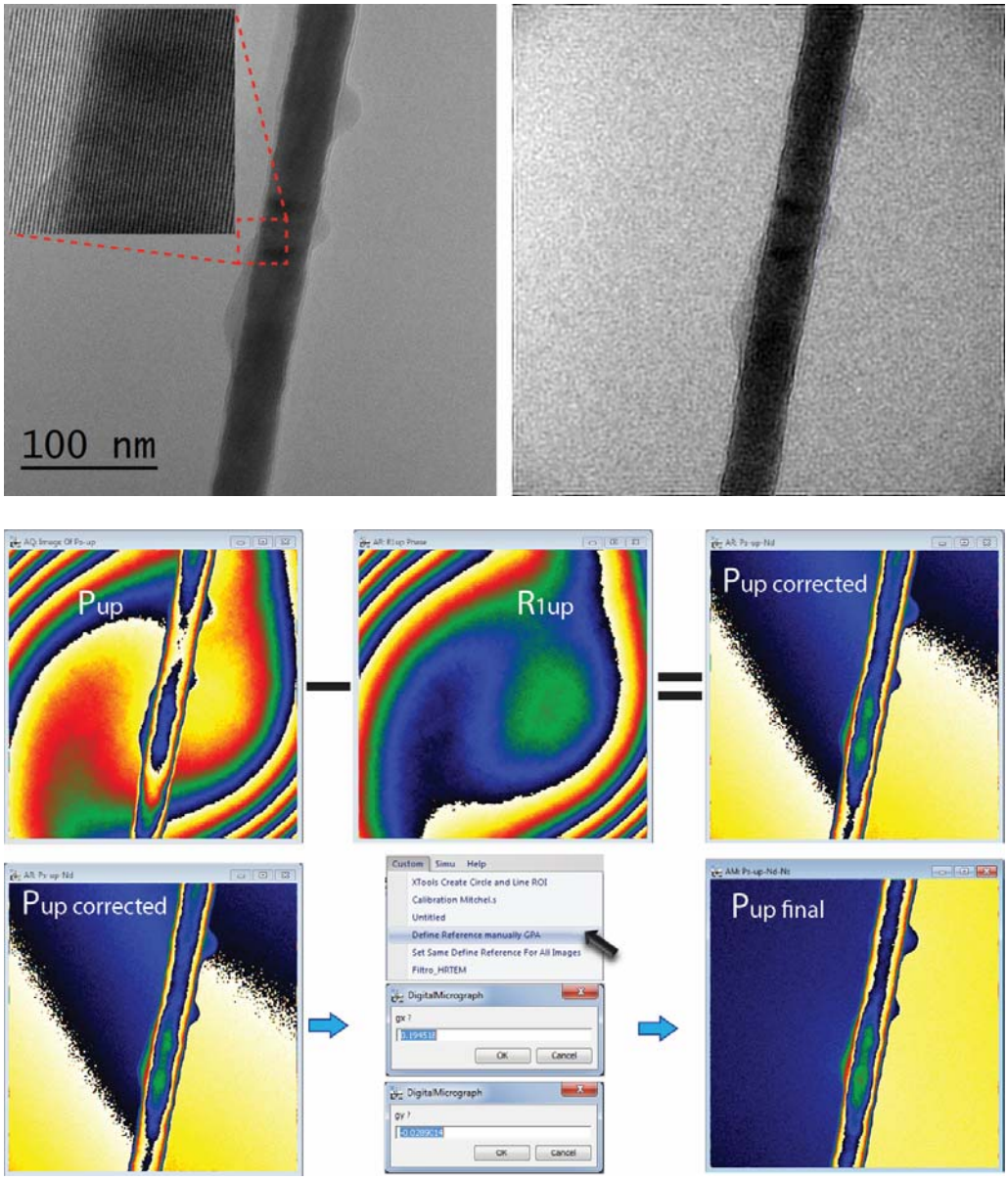

Figure 3.3.6. Hologram and amplitude image, below the removing the camera distortions and the phase shift slope process are shown.

The whole process described in this subsection is performed for each studied area of NWs in the down configuration.

- *Phase separation:* the phase obtained for each portion of the sample in up and down configurations is composed by the electrostatic contribution and the magnetic one as we discussed in chapter 2. In order to separate these contributions, we should add and subtract the two total phases for the up and down configurations. An alignment of the amplitude images is performed. Two lines of interest (ROI) are placed into the amplitude images as is shown in the Figure 3.3.7. These two lines are placed specifically delimiting the same region of the NW in both images.

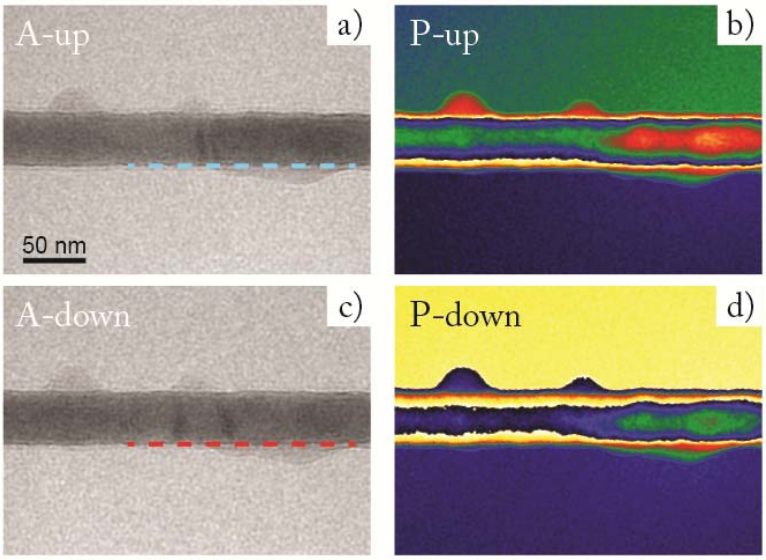

Figure 3.3.7. Up configuration: a) Amplitude image, b) Phase shift image. For down configuration: c) Amplitude image, b) phase shift image.

A special script to perform the alignment is used to add and subtract the two phase shift maps. Then the electrostatic contribution (MIP) is separated from the magnetic phase contribution (MAG) as detailed Figure 3.3.8 a) and b). The final phase shift maps have values between -π and +π (wrapped images). The phase shift maps can be unwrapped using suitable algorithms: this unwrapping process removes the phase jumps and allows obtaining a continuous variation of

the phase shift. Figure 3.3.8 shows the unwrapped phase shift maps for the MIP and the MAG. The last step is the division by 2 of the unwrapped phase shift images. As we sum or subtract the final phase shift maps resulting from the up and down configurations the final phase shift maps has the double of contribution to the phase shift map.

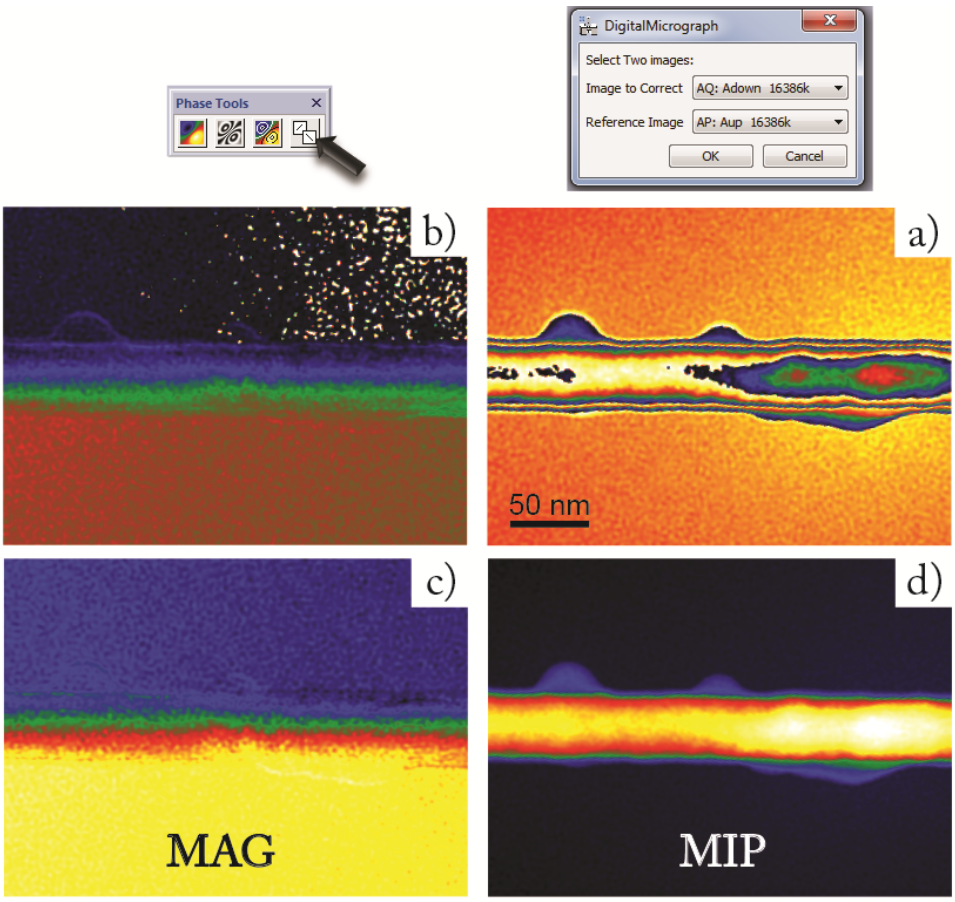

Figure 3.3.8. Phase tools used to align the two phase shift maps. a) Magnetic contribution to the phase (MAG). b) Electrostatic contribution to the phase (MIP). c) The unwrapped phase shift image from the MAG. D) Unwrapped phase shift image from the MIP

3.3.3 Important facts to consider in phase shift maps

Some important facts need to be discussed about the phase shift maps and also some concepts must be clarified.

Regarding the phase shift maps in multilayered Co/Co NWs, it is important to determine the exact position of the Co layers along the NW. These Co layers were identified by EFTEM images as we will see in chapter 4. A superimposition of the elemental maps and the corresponding magnetic phase shift images was performed. It is important to note that for this work a complete identification of each NW is crucial. Each EFTEM experiment has been realized on the same portion of the NWs allowing the identification of structural and chemical properties. With the superimposition of the EFTEM elemental maps and the phase shift maps we can identify each Co and Cu layer into the phase shift maps. An important fact to consider is the tilt character of the layers. The measure of these tilted layers has been discussed by Pullini [6]. He noticed this tilt behaviour in Co/Cu NWs and discussed the importance to measure these layers in the normal direction of the layer plane. In our case, the Co and Cu thicknesses can be measured accurately from the EFTEM elemental maps. The identification of the diameter of the NWs is obtained using the EFTEM elemental maps, the amplitude images and bright-field images of the same portion of NWs. Some imperfections can arise due to a thin oxide layer around the wire.

If the diameters and layers are identified, the next step is to perform the analysis of the direction of the magnetization on the phase shift maps. The phase shift maps have a color scale (radians) which corresponds to the value of the phase shift in each point. Figure 3.3.9 shows an example of the phase variation through a Ni wire.

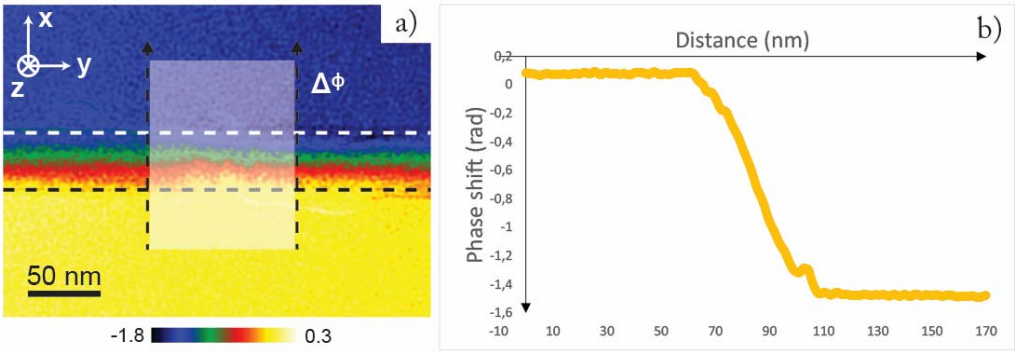

Figure 3.3.9. a) Magnetic phase shift image. b) Profile of the phase shift obtained on the dotted rectangle drawn along X direction in a)

Figure 3.3.9 b) shows the profile of the phase shift map obtained for the rectangle drawn in Figure 3.3.9 a). Now, taking into account the Aharanov-Bohm equation for a 1D dimension:

$$\phi_{MAG}(x) = -\frac{e}{\hbar}\int_{-\infty}^{+\infty}\int_{-\infty}^{x} B_y(x',z)dx'dz \qquad \textit{Eq. 3.3.1}$$

Taking the differential function along the X direction:

$$\frac{d\phi_{MAG}}{dx}(x) = -\frac{e}{\hbar}\int B_y(x,z)dz \qquad \textit{Eq. 3.3.2}$$

This equation suggests that a change of the phase shift along the X direction is the result of a magnetic induction along the Y axis. In the particular case of Figure 3.3.9, this magnetic induction is pointing along the wire axis and can be deduced from the phase shift change along the direction perpendicular to the NW. The regions where the phase shift keep the same value are called *isophases*. In Figure 3.3.10, show the corresponding induction lines (in black).

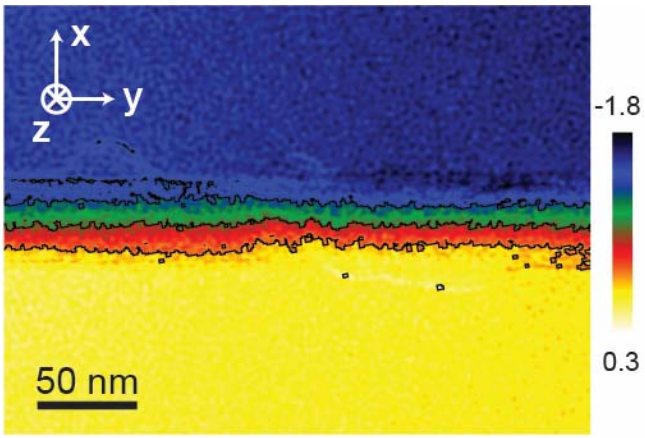

Figure 3.3.10. Isophase lines delimiting the isophase regions.

One of the main problems of EH is that the phase shift linked to the electromagnetic signal is integrated along the electron path. This can result in misinterpretations of the magnetic configurations. Accurate knowledge of the specimen thickness is a basic prerequisite for making quantitative measurements of electrostatic and magnetic fields via EH [7]. If the magnetic induction remains constant in terms of amplitude and direction along the incident beam (observation direction), the Eq. 3.3.1 and Eq. 3.3.2 can be written as:

$$\phi_{MAG}(x) = -\frac{e}{\hbar}\int_{-\infty}^{x} B_y(x')t(x')dx' \qquad \textit{Eq. 3.3.3}$$

$$\frac{d\phi_{MAG}}{dx}(x) = -\frac{e}{\hbar}B_y(x)t(x) \qquad \textit{Eq. 3.3.4}$$

where $t(x)$ is the sample thickness. In our case, we have a cylindrical volume where the integration of the magnetic induction is performed perpendicular to the NW axis. Thus the calculation of the magnetic induction should be performed taking into account the cross-section of the NW as we will see in the next section.

By EH the internal magnetic configuration of the sample and the fields that acts outside the structures are observed. This is the case for the stray field which is the demagnetizing field outside the magnetic structure.

3.3.4 Measurement of the Co magnetization

Co NWs were also grown with the set of Co/Cu samples (sample M5 as presented in 3.2.1). These NWs were deposited using the same electrochemical bath than for the Co/Cu NWs. Co NWs has some Cu impurities as detected for the Co layers in the multilayered Co/Cu NWs. The Co NWs were dissolved from the membrane by the method explained previously before to be placed in ethanol solution. Then a drop of the solution was deposited in a holey carbon grid. EH experiments were carried out in Co isolated NWs in order to study the remnant magnetic state. The magnetic induction of the NWs can be affected by the Cu impurities [8]. Figure 3.3.11 shows a magnetic phase shift map after the extraction process and the phase separation (magnetic and electrostatic contribution). The isophase lines parallel to the Y direction reflect an integrated magnetization pointing toward the wire axis.

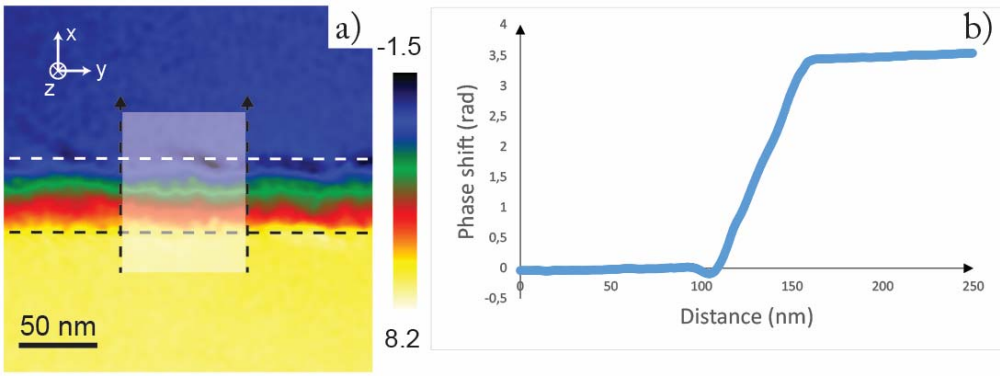

Figure 3.3.11. a) Experimental magnetic phase shift map. b) Profile of the phase shift obtained from the dotted rectangle drawn in a).

Figure 3.3.11 b) shows a profile of the phase shift obtained from the dotted rectangle drawn in the Figure 3.3.11 a). Now the magnetic phase shift $\phi_{MAG}(x)$ along the X axis corresponding to a magnetic induction along the Y axis B_y:

$$\phi_{MAG}(x) = -\frac{e}{\hbar}\int_{-\infty}^{+\infty}\int_{-\infty}^{x} B_y(x',z)dx'dz \qquad \textit{Eq. 3.3.5}$$

Assuming that our NW is a perfect cylinder, an integration over the area should be performed. Eq. 3.3.5 show the relation between the change of the phase and the magnetic induction for a uniformly-magnetized infinite cylinder of radius *a* [9].

$$|\Delta\phi_{MAG}| = \frac{e}{\hbar}|B_y|\pi a^2 \qquad \textit{Eq. 3.3.6}$$

Using Eq. 3.3.6, the magnetic induction in the Co NWs can be found. The phase shift change can be extracted from the profile of Figure 3.3.11 b) $|\Delta\phi_{MAG}| = 3.5\ rad$. The Co NW under study has a diameter of *44.3* ± *2* nm, determined by bright field TEM images, thus, replacing these values into Eq. 3.3.6 the magnetic induction along the Z direction is $B_y = 1.5$ T. This value is slightly lower than for the bulk for Co (*1.78* T) [10]. The reduction on the magnetic induction can be explained by the inclusion of Cu into the Co due to the single bath technique used. This behaviour has been discussed by Akhtari et al. [8], where the magnetization of CoFeB was reduced by the inclusion of up to 50% of Cu. The calculation of this magnetic induction is very useful because it will be used as a parameter into the micromagnetic simulations.

3.3.5 Micromagnetic simulations

To deeper analyse the experimental results, the 3D remnant magnetic states and stray fields of 20 bilayers of Co/Cu have been simulated using the 3D OOMMF freeware [11] in a universe of $1000 \times 500 \times 500$ nm^3 with a cell size of 2nm corresponding to the spatial resolution of the experimental magnetic phase shift maps. The saturation field is applied at 10° from the *Y* or *X* axis to reproduce the uncertainty

of the experimental conditions. However, a verification that all simulations performed with angles less than 10° lead to similar results was done. Geometrical parameters obtained from structural and chemical studies are implemented in the 3D calculations (averaged tilted angle of the layers, thickness and diameter). The magnetization of the Co layers was set to 1200×10^3 A/m ($\mu_0 M_s$ 1.5T), which is the averaged value determined from the electron holography experiments on single Co nanowires grown from the same electrochemical bath (see section 3.3.4). Finally, the adjustable magnetic parameters in the simulations are the direction and amplitude of the magnetocrystalline anisotropy constant as well as the exchange value A. To take into account the polycrystalline nature of the Co layers, we choose to define a simple model with a uniaxial magnetocrystalline anisotropy, which is randomly distributed from one layer to the other, instead of a cubic anisotropy as for fcc materials. This is valid whatever the crystal structure of the Co, i.e fcc or hcp. In Figure 3.3.12, a scheme for the uniaxial model used to perform the micromagnetic simulations is shown. In this scheme, θ corresponds to tilt angle of the layers with respect to the wire axis, and θ_{Hk} is the angle between the uniaxial anisotropy and θ angle. The anisotropy orientations are lying in a cone delimited by $-\Delta\theta_{Hk}$ and $+\Delta\theta_{Hk}$ and are randomly distributed as was mentioned before. A home-made program to obtain the component of 3D vectors, change the different adjustable parameters and implement these to the code for OOMMF was designed by Nicolas Biziere.

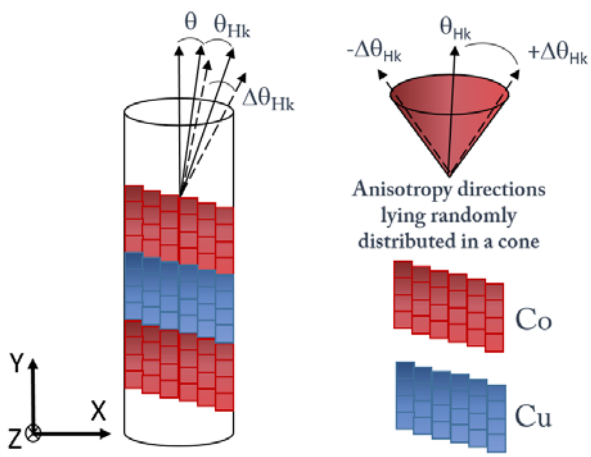

Figure 3.3.12. Schema of the uniaxial anisotropy model used to perform micromagnetic simulations.

As we have used a cell size of *2 nm* and a universe of $1000 \times 500 \times 500$ nm^3, the simulations must be performed in a supercomputer located in the centre of calculations of midi-pyrénées (Calmip). The supercomputer used was EOS which has 128 cores in 16 processors. Previous to the calculations in the supercomputer, small calculations were performed with a cell size of 5 nm in order to test some configurations of the magnetocrystalline anisotropy, tilt of the layers and anisotropy orientation.

For each simulation, the magnetization and the demagnetization field were calculated. On the basis of these simulations, we calculated the corresponding in-plane components of the induction field *B* before integrating them along the electron path (direction *Y*) to obtain the electron phase shift map using the Aharanov-Bohm equation as detailed in chapter 3. The integration of the magnetic induction was carried out by another home-made software designed by Nicolas Biziere. The data result of the integration is treated in Digital Micrograph software using a script developed by Christophe Gatel, which converts these data into maps of the magnetic induction and subsequently into magnetic phase shift images. This simulated magnetic phase shift map was then quantitatively compared to the experimental one to discretize between the different observed magnetic states. The exchange and anisotropy values were

adjusted to reproduce the magnetic behaviour as a function of the saturation field but also to get a quantitative agreement between the experimental and the calculated magnetic phase shift. The 3D representation of the data was possible by two software: MuView and MayaVi (both of them are freeware). The 3D representation of the magnetization is usually displayed by the color scale of one component of this. Figure 3.3.13 gives an example of a Co cylinder of 80 nm in diameter and 60 nm in thickness. The magnetic state displayed by this layer is a vortex with the core parallel to the Y direction. Figure 3.3.13 a) shows in the color scale the X-component of the magnetization, this indicates that the magnetization is rotating in the XZ plane. From the Figure 3.3.13 b) the direction of the core is seen easily due to the color scale which represents the Y-component of the magnetization. Therefore different color scales corresponding to the different directions of the magnetization will be used in order to give a clear representation of each magnetic state.

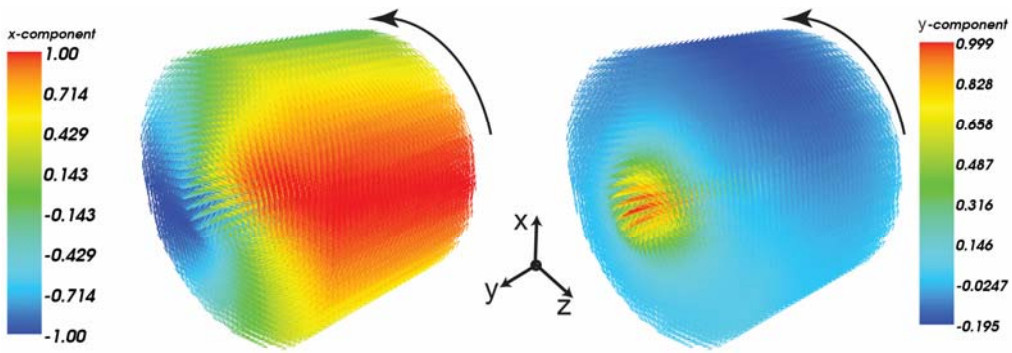

Figure 3.3.13. 3D representation of the magnetization for a Co layer of 80 nm in diameter and 60 nm in thickness. The color scales correspond to a) x-component of the magnetization and b) y-component of the magnetization. Black arrows shows the chirality of the vortex

References

[1] A. Loubat *et al.*, "Ultrathin Gold Nanowires: Soft-Templating versus Liquid Phase Synthesis, a Quantitative Study," *J. Phys. Chem. C*, vol. 119, no. 8, pp. 4422–4430, Feb. 2015.

[2] L.-M. Lacroix, R. Arenal, and G. Viau, "Dynamic HAADF-STEM Observation of a Single-Atom Chain as the Transient State of Gold Ultrathin Nanowire Breakdown," *J. Am. Chem. Soc.*, vol. 136, no. 38, pp. 13075–13077, Sep. 2014.

[3] N. Liakakos *et al.*, "Co–Fe Nanodumbbells: Synthesis, Structure, and Magnetic Properties," *Nano Lett.*, vol. 14, no. 5, pp. 2747–2754, May 2014.

[4] K. Harada, A. Tonomura, Y. Togawa, T. Akashi, and T. Matsuda, "Double-biprism electron interferometry," *Appl. Phys. Lett.*, vol. 84, no. 17, p. 3229, 2004.

[5] M. J. Hÿtch, E. Snoeck, and R. Kilaas, "Quantitative measurement of displacement and strain fields from HREM micrographs," *Ultramicroscopy*, vol. 74, no. 3, pp. 131–146, 1998.

[6] D. Pullini, G. Innocenti, D. Busquets, and A. Ruotolo, "Investigation of multilayer local tilt within long portion of single Co/Cu nanowires," *Appl. Phys. Lett.*, vol. 90, no. 13, p. 133106, 2007.

[7] M. R. McCartney and D. J. Smith, "Electron holography: phase imaging with nanometer resolution," *Annu Rev Mater Res*, vol. 37, pp. 729–767, 2007.

[8] A. Akhtari-Zavareh *et al.*, "Off-axis electron holography of ferromagnetic multilayer nanowires," *J. Appl. Phys.*, vol. 116, no. 2, p. 23902, 2014.

[9] T. Kasama, M. Beleggia, and R. E. Dunin-Borkowski, *Electron holography of magnetic materials*. INTECH Open Access Publisher, 2011.

[10] B. D. Cullity and C. D. Graham, *Introduction to magnetic materials*, 2nd ed. Hoboken, N.J: IEEE/Wiley, 2009.

[11] M. J. Donahue and D. G. Porter, "OOMMF User's Guide, Version 1.0, Interagency Report NISTIR 6376." 1999.

Chapter 4
Co/Cu multilayered nanowires

4.1 Introduction

Magnetic and structural properties of single element nanowires are of great interest due to their application in the data storage field [1]–[4]. Some years ago, Henry et al. [5] grew electrodeposited Co nanowires into polycarbonate membranes. The resulting NWs had lengths of *10* or *20* μm and diameters ranging from *30* to *450* nm with a hcp structure. They used magnetic torque measurements, as well as magnetic force microscopy to characterize such nanowires. These experimental results revealed that crystal anisotropy either competes with shape anisotropy in maintaining the Co magnetization aligned along the wire or favours an orientation of the magnetization perpendicular to the wire. This competition is linked to the diameter of the wires, smaller or larger than a critical diameter of *50* nm. An important relation between the first order magnetocrystalline anisotropy constant K_1 and the diameter of the Co NWs was found as shown in the Figure 4.1.1.

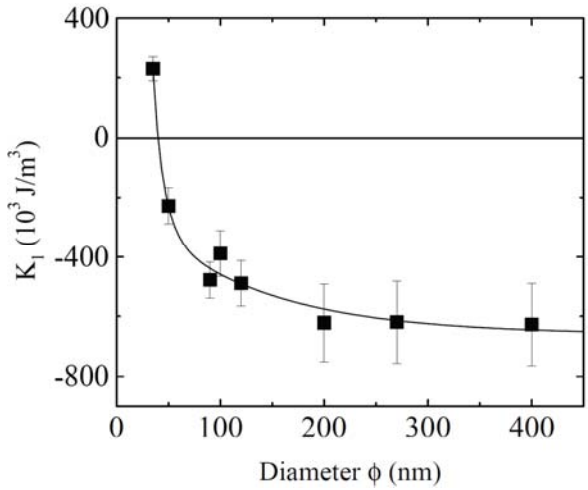

Figure 4.1.1. Variation of the first order magnetocrystalline anisotropy constant K_1 with the average diameter of the Co nanowires. Extracted from [5].

The sign of K_1 changes when the diameter exceeds a critical diameter $\approx 50\ nm$. Below this critical diameter, for example, $35\ nm$, K_1 is positive. It means that magnetocrystalline anisotropy collaborates with the shape anisotropy in maintaining the magnetization aligned along the wire axis. Above the critical diameter, K_1 is negative. Thus, magnetocrystalline anisotropy tends to align the Co magnetization perpendicular to the wires and competes with the shape anisotropy. Considering the remnant magnetic states in these Co NWs after application of a magnetic field of 1.3T perpendicular (PP) and parallel (PL) to the wire axis, they found that:

- *NWs with diameter values below 50 nm:* for the PL configuration a homogeneous longitudinal magnetization was found. For the PP configuration, the magnetization is divided into domains and domain walls appear along the wire.
- *NWs with diameter values above 50 nm:* a mixture of states is displayed for both directions of the magnetic field applied (PP and PL). Stripe-shape domains are formed with transversal and longitudinal domain walls.

Following the work of Henry et al. [5], several authors studied the tuning of the magnetic properties by changing the deposition parameters. Vivas et al. [6] have been working on Co NWs produced by electrodeposition in membranes prepared by anodized aluminium membranes (AAO). They changed the pH of the solution in order to obtain a Co with a hcp structure presenting different orientations of the c-axis. For a pH value of 3.5, 5.0 and 6.7, the corresponding direction of c-axis was nearly perpendicular, inclined at 45° and parallel to the wire axis respectively. They also studied the magnetization reversal process of these NWs and, using comparaison with simulation, concluded that this process is dominated by the appearance of a transverse wall. Similar Co NWs with the c-axis at 75°±5° respect to the wire axis were studied by Ivanov et al. [7]. The magnetic structure in the remnant state consists of magnetic vortices with alternating chirality along the wire axis.

Two recent studies on Co nanowires have investigated their magnetic states. The first one published by Cantu-Valle and co-workers [8] correlates the structure of the Co NWs grown by electrodeposition in AAO templates and the magnetization distribution along the wires. The wires are $95\ nm \pm 5nm$ of diameter and have lengths of $240\ nm - 5.75\ \mu m$ which corresponds to aspect ratios varying from 2.5 to 60. Precession electron diffraction (PED) experiments demonstrate that NWs are composed of several large Co grains (200-300 nm) presenting a hcp structure with different orientations. The c-axis is lying nearly perpendicular to the NW axis. The tip contains smaller grains ($<80\ nm$) with a random orientation. The remnant magnetic state of the NWs was analysed by off-axis electron holography. In Figure 4.1.2 the crystal orientation and the magnetic phase contour of the Co nanowire are shown. The magnetization is aligned in a direction parallel to the wire axis but with a wavy character. This feature is explained by the competition between the shape anisotropy and the

magnetocrystalline anisotropy of the hcp cobalt. This kind of frustration was also observed by Bergmann et al. [9]. Finally, a vortex structure is present at the tip of the nanowire where the magnetic flux lines follow a clockwise direction. The observed vortex axis lies perpendicular to the main axis of the nanowire, as a consequence of the local competing easy axis promoted by the random orientation of the polycrystalline structure at the tip.

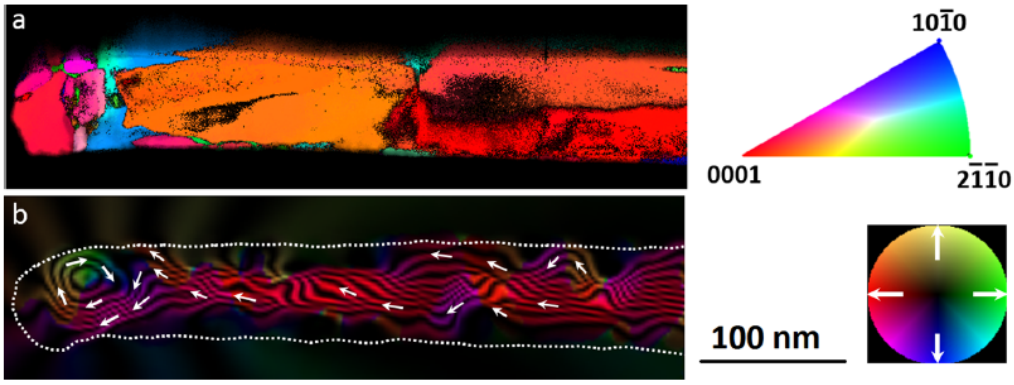

Figure 4.1.2. a) Crystal orientation and b) magnetic phase contour maps of the Co nanowire. The crystal orientation map is displayed with respect to the direction of observation z (color key code displayed on the right) and is over-layered with the reliability map to reveal zones where crystallites overlap. The magnetic phase contour map is obtained by amplifying 3 times the cosine of the unwrapped magnetic phase (magnetic flux direction color-wheel displayed on the right). The outline of the nanowire is marked by the thin white line. Arrows represent the magnetic flux direction. Extracted from [8]

Ivanov et al. [7] studied the magnetic configurations of monocrystalline Co NWs deposited in AAO membranes. These NWs have the c-axis perpendicular to the wire axis, which creates a competition between the shape and magnetocrystalline anisotropy. The vortex states were observed by Lorentz microscopy on arrays of NWs with diameters as small as *45nm* and lengths of *200 nm*. This is an important difference with permalloy dots and nanopillars, which show no vortex state at similar dimensions. Micromagnetic simulations performed on this system confirm a stable vortex state for NWs with dimensions that exceed a critical aspect ratio. They also show that multiple vortices with different chirality can exist along NWs with higher aspect ratios.

Beyond the static magnetic configuration, some studies have also been dedicated to the domain wall motion.

Numerical studies have been performed by Usov and co-workers [10] in soft nanowires with diameters (D) between *100-300 nm* and lengths (L) which satisfy the high aspect ratio condition $L/D \gg 1$. The magnetocrystalline anisotropy was oriented parallel to the NW axis with values of 1×10^3, 5×10^3 and $10 \times 10^3\ \mathrm{J/m^3}$. The remnant states found were: symmetrical Néel type domain wall, deformed Néel type wall and a toroidal domain wall. Other authors such as He et al. [11] have studied notched permalloy nanowires to pin transverse domain walls (TDWs). Their nanowires were fabricated using electron-beam lithography, with a length of *5 μm*, *400 nm* in with and *20 nm* of thickness. They have observed the nucleation, injection, pinning and depinning of this kind of domain walls: an *in situ* experiment was carried out in a TEM using the objective lens to apply a magnetic field of *440 Oe* and thus to control the movement of the DW during the observation. Lorentz microscopy was firstly used to qualitatively identify the DW positions before applying electron holography for the quantification of DW configurations. Micromagnetic simulations completed the study. The relative chirality of the notch and the nucleation pad had a major influence in determining the TDW propagation: the walls were preferentially pinned for a notch of opposite chirality, but simply passed through when the notch had the same chirality.

Focusing our attention on cylindrical NWs (NWs with a circular section), 2 main types of domain walls have been predicted to exist: the transverse wall (TW) and the Bloch-point wall (BPW) [12], [13]. Biziere et al. [14] presented the first experimental imaging of the internal DW structure in Ni nanocylinders of *55* and *85nm* of diameter. They used a combination of EH and micromagnetic simulations to demonstrate the transition between a hybrid magnetic state with both vortex and transverse DW in *85 nm* diameter Ni nanocylinders to a pure transverse wall in thinner

nanowires. Another interesting study by Yan et al. [15] on permalloy NWs with a cylindrical shape shows transverse domain wall for NWs with diameters below *50* nm which differ significantly from those know from flat nanostripes. These domain walls are zero-mass micromagnetic objects: as a consequence, they are not subject to the breakdown velocity known as the Walker limit [16], [17]. In recent studies Da Col et al. [18] discussed the importance that represents the Bloch point (BP). As zero-dimensional objects, they were predicted to be required in the transient state allowing magnetization reversal along one-dimensional objects, such magnetic vortices. Da Col and co-workers combined surface and transmission x-ray magnetic circular dichroism photoemission electron microscopy to confirm the existence of the Bloch-point domain wall in permalloy cylindrical magnetic nanowires. Micromagnetic simulations were performed to confirm the experimental results and compute simulated contrast that can be compared directly with the measured ones. This demonstration of the existence of BPWs opens the way for the investigation of its peculiar motion behaviour. They mentioned that its expected steady motion and high velocity [13].

Several studies have been carried out on multi-layered NWs. Using off-axis electron holography, Beeli and co-workers [19], [20] studied the magnetic states in Co/Cu NWs grown in polycarbonate membranes. Single Co/Cu NWs were studied in the remnant state after applying a magnetic field of $2T$ in a direction parallel to the grid plane. The Co segments were $1.2\ \mu m$ long separated by Cu segments of $0.3\ \mu m$ long in a NW of $40 \pm 2.5\ nm$ of diameter. The Co segments were large enough to keep the magnetic anisotropy along the nanowire axis. The observation and analysis of the phase shift maps confirmed a magnetization along the wire axis. This parallel configuration (along the wire axis) of the Co segments remnant is theoretically favoured as it minimizes the magnetic energy of the NW. They also found an antiparallel

configuration (→ ← → ←): each segment acts as an individual magnet and six different possibilities are found as metastable states.

A couple of years after the work of Beeli [20], several works were published on Co/Cu NWs obtained by electrodeposition methods in template membranes. Two main works can be highlighted, Blondel et al. [21] and Piraux et al. [22]. They produced multilayered Co/Co NWs and performed the first measurement of giant magnetoresistance (GMR) in the current perpendicular to the layer plane (CPP) geometry for these Co/Cu NWs. They obtained values of 14% and 15% respectively at room temperature. Years later Fert and Piraux [23] proposed a review about the recent developments in the field of research on magnetic nanowires electrodeposited into pores membranes. They present a description of the preparation methods, typical examples of structural characterization and the magnetic properties on isolated and arrays of NWs. They do a special emphasis about the magnetoresistance properties of multilayered nanowires by focusing on the great interest of the CPP-GMR configuration and the determination of the spin diffusion lengths. They discuss about the complex magnetic states found in Co and Co/Cu nanowires observed by MFM and how a mixture of magnetic configurations can appear along the wire. These configurations were observed by Henry [5] as was previously discussed in Co NWs but also in Co/Cu multilayered NWs by Belliard et al. [24]. The last team observed the antiparallel coupling between the Co layers, but they also pay a special attention to the limit of MFM measurements to distinguish between the in-plane and perpendicular to the plane magnetization distributions for some configurations. This limitation comes from the fact that this probing technique measures only the stray field of the NW surface. In Figure 4.1.3 the scheme showing the incapacity of the MFM to distinguish between the two antiparallel states in Co/Cu NWs is shown.

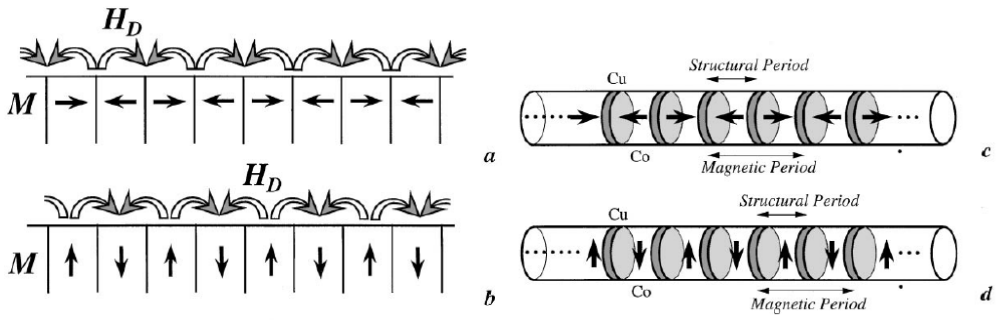

Figure 4.1.3. a), b) On the incapacity of MFM to distinguish between periodic in-plane and perpendicular to the plane magnetization distributions. c), d) Magnetic period doubling for antiparallel type magnetization sequences. Extracted from [24]

Wong et al. [25] have studied the magnetic configurations of Co/Cu NWs by magnetometry-based first order reversal curves (FORC) technique to investigate the magnetization reversal process. NWs of *200 nm* in diameter, Cu layers of *250-350 nm* (to minimize the dipolar interaction between the Co layers) and Co layer thickness of *10-50 nm* were investigated. When the thickness of the Co layer is *10-32 nm*, the magnetization reversal process presents a single domain behaviour. However, for the range of *37-55 nm* of thickness in the Co layer, vortex state reversal dominates. In this last configuration, a superposition of giant magnetoresistance and anisotropy magnetoresistance was found and measured.

After the articles of Blondel et al. [21], Piraux et al. [22] and Fert and Piraux [23], different works on Co/Cu multilayered nanowires appeared about the tuning of the structural and magnetic properties. Cho et al. [26] fabricated Co/Cu Nws arrays using DC electrodeposition in AAO templates. These NWs were *200 nm* of diameter with segments of *145 nm* of Co and *80 nm* of Cu. They reported the decrease of the thickness of the Co layer after several periods of deposition. This problem can be explained by the kind of electrodeposition used (DC electrodeposition). For this system, the aspect ratio of the Co layers < 1: the shape anisotropy of each layer is thus expected

perpendicular to the wire axis. This idea was confirmed by hysteresis loops which show a magnetic easy axis perpendicular to the wire axis.

The electrodeposition technique is known to be "straightforward" and it is often assumed that layers are parallel to each other along the entire length of the nanowires; for this reason, the thickness of the layers are usually calculated from the efficiency or directly measured only over small portions of single nanowires. Pullini et al. [27], [28] found a dispersion of the nanowire diameter (around *20%* between the NW ends and their central part), this results in smaller and smaller bilayers period from the end to the centre of the wires. This effect can be produced because the thickness of the template is not perfectly constant or the electric field is not uniform over the deposition area (top electrode not perfectly shaped), the nanowires start emerging at different times. Pullini also reported the increase of the layer tilt layer when the diameter of the NW increases. An angle of *24°* to *31°* is measured when the diameter change from *50* to *100 nm*.

Two important facts can influence the magnetic properties and/or the observation of the magnetic states inside the multilayer NWs: impurities of the non-magnetic material inside the magnetic layers and process of preparation to obtain isolated NWs. For Co/Cu NWs Tan et al. [29] found by EDX that Cu impurities in Co layers were about *7%* and Co impurities in Cu were less than *1%*. Bran et al. [30] described the Co layers as an alloy of Co-rich with *10-15%* of Cu. Similar results have been obtained by other authors for similar systems [31], [32].

About the preparation to obtain isolated NWs, the first step is to dissolve the membrane in order to recover the NWs into a solution. Pullini and co-workers [28] used an alternative method to the centrifugal separation. They propose to place a part of the membrane on a proper sample holder (Al stab for SEM or Cu grid for TEM) and they flushed several times with the solvent; this method promises to save time and

avoid the nanowire aggregation. Another problem arises when the diameter of the NWs is so high that the electrons in a TEM cannot go through them. In this case a special preparation to decrease the thickness of this is performed by methods like focus ion beam (FIB). The direct consequence of the use of this technique is the implantation of gallium ions but also a modification of the magnetic properties as the diameter/length ratio will be modified. Thus the importance of having an appropriate reduction of the impurities into the magnetic layers and the preparation process is of vital importance in this kind of multilayered systems.

Concerning the observation method, transmission electron microscopy (TEM) is one the most appropriate tools: its broad sensitivity ranges from atomic structure to electromagnetic fields and includes atomic-scale analysis of valence states and chemistry. Its ability to probe individual nano-objects instead of assemblies of nano-objects provides a remarkable potential. Among the different TEM methods, off-axis electron holography (EH) [33] is a powerful interferometric method, which gives access to the in-plane induction inside and outside of the nano-object [34], [35]. Few studies using EH have been performed on magnetic nanowires. One of the recent studies using EH was performed by Akhtari et al. [36]. They investigated the local magnetic behaviour of isolated multilayered NWs composed by Cu/CoFeB and electrodeposited in nanoporous alumina membranes. They observed the remnant states after applying a magnetic field parallel and perpendicular to the wire axis. When the CoFeB layer was thicker than the diameter (*50 nm*), magnetization was axial for all external field orientations, while thinner layers could be randomized via a perpendicular field. In some cases, magnetization inside the wire was detected at an angle with respect to the axis of the wires. They also studied combinations of tri-layers of Cu/CoFeB/Cu (<*10 nm* each) where magnetic field vortices were detected. EDS profiles were traced showing the abrupt character of the interfaces magnetic/non-magnetic material. However, Cu is

found inside the magnetic layers with a content that varied from 5% to 50%. This inclusion of the Cu into the magnetic layer produces a significant reduction of the magnetic induction measured (*0.2-1 T*) compared with the CoFeB in bulk (*1.7 T*). Micromagnetic simulations complete this study.

Two more works about multilayered NWs were performed by Cantu-Valle et al. [37] and Ivanov et al. [38] in $Co_{54}Ni_{46}/Co_{85}Ni_{15}$ and Co/Ni NWs respectively. For the reference [37], the remnant magnetic state displayed by EH for the multisegmented wires correspond to a magnetization lying along the wire axis, except for a zigzag pattern orientation observed at the interfaces between the segments. In the case of Ivanov et al., they used the interfaces between the Co and Ni as pinning sites for DW. This is produced by the change of the value and direction of anisotropy. The Co uniaxial anisotropy is lying nearly perpendicular to the wire axis while the Ni has a cubic anisotropy. By combining electron holography with micromagnetic simulations, the pinning effect can be explained by the interaction of the stray fields generated at the interface and the domain wall. They also used differential phase contrast imaging to visualize the pinned domain wall with a high resolution, revealing its three-dimensional vortex structure with the previously predicted Bloch point at its centre. The application suggested for this kind of NWs is the development of high-density, three-dimensional data storage devices.

In my thesis, Co/Cu multilayers in nanocylinders are grown by template synthesis. This method is one of the most used techniques due to the ability to obtain nanowires with different sizes, shapes and composition in a relative easy and inexpensive way. The magnetic configurations of these nanocylinders are quantitatively mapped by EH, the structural and chemical properties have been obtained by high resolution TEM (HRTEM) associated with electron energy-loss spectroscopy and imaging. By 3D

micromagnetic simulations including the geometrical parameters extracted from electron microscopy experiments, we recovered the different remnant configurations by electron phase shift reconstruction. A comparison of the remnant magnetic states obtained by EH and the states of isolated nanocylinders are compared using phase diagrams.

4.2 Nanowires growth

The list of the grown nanowires is given Figure 4.2.1. The different thicknesses of the Co and Cu layers were chosen to study the aspect ratio between the Co layer and the diameter of each NW and also the magnetic coupling between the adjacent Co layers along the wire. As we discussed in chapter 3, a NW of pure Co was grown to extract the magnetization of saturation of the Co with the Cu impurities due to the single bath technique.

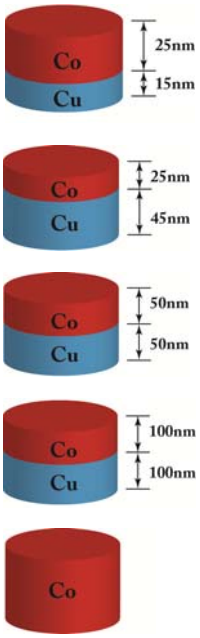

Sample M1	Co	Cu
Time (s)	1.00	10.00
Thickness (nm)	25	15

Sample M2	Co	Cu
Time (s)	1.00	30.00
Thickness (nm)	25	45

Sample M3	Co	Cu
Time (s)	2.00	35.00
Thickness (nm)	50	50

Sample M4	Co	Cu
Time (s)	4.00	70.00
Thickness (nm)	100	100

Sample M5	Co	Cu
Time (s)	300.00	0.00
Thickness (nm)	7500	

Figure 4.2.1. List of grown samples, time of pulses and nominal thickness for Co and Cu layers

The 25nm/15nm sample was grown to study the magnetic coupling produced by a small separation of copper compared with the 25nm/45nm where the dipolar effects should be smaller. The 50nm/50nm sample was grown to study the weak dipolar effect between the adjacent Co layers and increase the shape anisotropy in the direction parallel to the wire axis respect to the 25nm/15 and 25nm/45nm samples. Finally, a 100nm/100nm sample was grown with the expectation of avoiding the dipolar coupling and study the limit case for a shape anisotropy totally oriented parallel to the wire axis (high aspect ratio between the Co thickness and the diameter of the NW). We can say in summary that the interest of this set of samples is the study of magnetic states considering different influences, like dipolar coupling and the aspect ratio.

4.3 Structural and morphological properties

4.3.1 TEM analyses of the Co/Cu nanowires

A bright field (BF) TEM image of a typical Co/Cu multilayered NW with 25nm/15nm of nominal thickness is shown in the Figure 4.3.1. The NW in Figure 4.3.1 a) presents an average diameter of 64 ± 4nm. The polycrystalline character of the Co and Cu layers is shown by selected area diffraction pattern (SADP) as presented in Figure 4.3.1 c). The analysis of the ring diameters and spacing indicates polycristalline cubic (fcc) phases for Co and Cu as expected when some Cu is inserted in the Co layer [39]. High resolution (HR) TEM images confirm the polycrystalline structure of Co and Cu layers with grains randomly oriented and sizes of 7nm ± 2 (Figure 4.3.1 b).

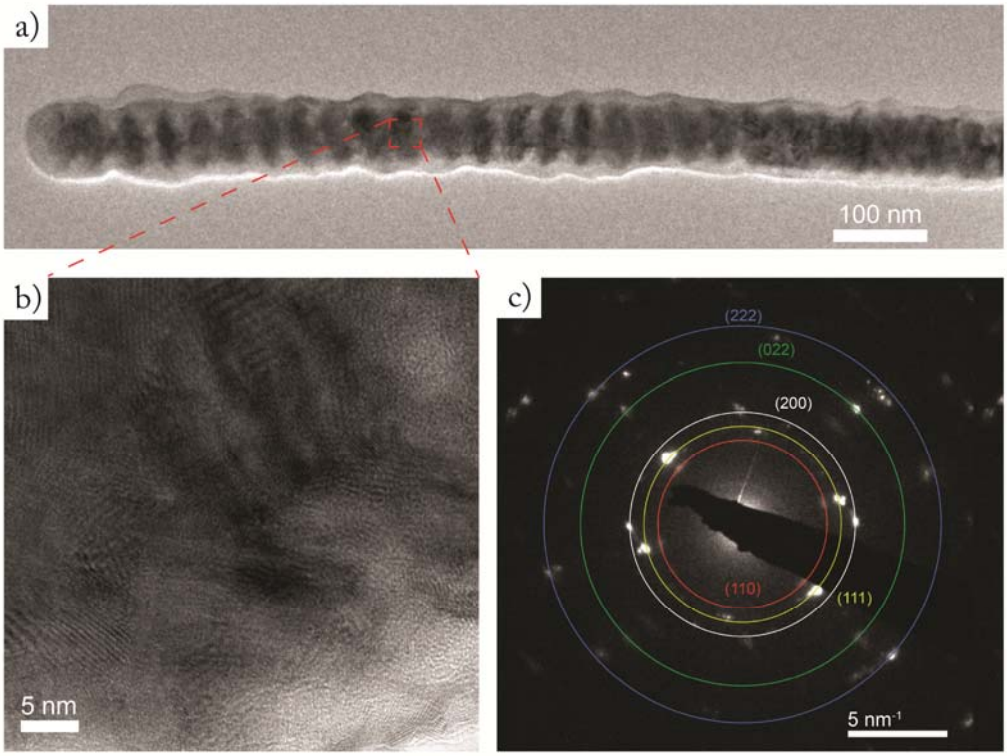

Figure 4.3.1. a) Bright field TEM image of a typical Co/Cu multilayer nanowire for 25nm/15nm configuration, b) High resolution TEM image, c) diffraction pattern of a Co area.

Regarding the configuration of a 50nm/50nm Co/Cu wire, Figure 4.3.2 a) shows a wire of *85 ± 2nm* of diameter and the multilayered character of the NWs is easily seen from the bright field image. The change in diameter along the different periods and the decrease of the layer thickness on the tip is also evidenced. Figure 4.3.2 b) shows a high resolution TEM (HRTEM) in which different grains are clearly oriented in different directions. This polycrystalline character can be seen in the fast Fourier transform (FFT) applied to the HRTEM image (Figure 4.3.2 d)) in which different orientations for the Co can be indexed.

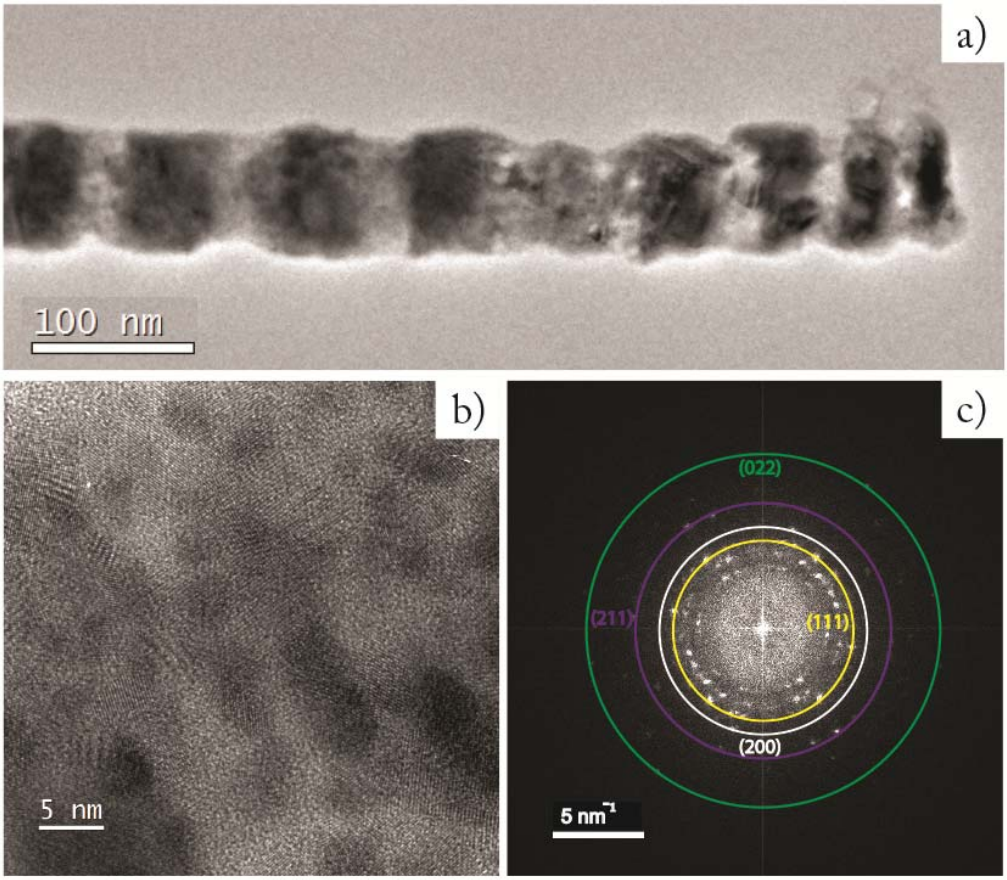

Figure 4.3.2. a) Bright field TEM image of a typical Co/Cu multilayer nanowire for 50nm/50nm configuration, b) High resolution TEM image, c) FFT pattern of a Co area.

Similar characteristics as the ones presented in the Figure 4.3.1 and Figure 4.3.2 are found for all multilayered Co/Cu NWs whatever the Co and Cu thicknesses. The diameter of the wires varies between 50-90nm regardless the thickness of the layers. These values represent an increment of 2 and even 3 times the nominal pore size labelled by the manufacturer (*30 nm*).

Generally, this kind of nanowires with a polycrystalline texture, Co presents many structural defects as stacking faults. It can become difficult to make the difference between hcp and fcc structures: it is then possible to get polycrystalline Co with

structural properties mainly similar to fcc but with some magnetic characteristics corresponding to an hcp structure.

Attempts to map the crystal structure of the entire wire were made by electron precession diffraction (using the ASTAR setup). This is an automatic crystallographic indexing and orientation/phase mapping tool. The electron beam is scanned in combination with beam precession through the sample area of interest. A number of electron diffraction (ED) patterns from several sample locations are acquired at high speed using a dedicated fast CCD camera placed in front of the TEM screen; local crystalline orientations are obtained by comparing all individually obtained ED spots patterns via cross-correlation matching techniques with pre-calculated ED templates. The precession resolution on a TEM is determined by the electron probe size [40]–[42]. This technique has been used on NWs [43] to observe the misorientation of Co and Ge NWs. Also, Cantu-Valle et al. [8] mapped the crystal structure of the Co as we discussed in the introduction of this chapter. In our case, several measurements were performed in order to map the crystalline orientations of the Co/Cu NWs and to distinguish between the possible hcp and fcc phases of Co. Indeed Maurice et al. [39] found that the inclusion of the fcc Cu into Co layers in multilayered Co/Cu NWs induces a preferential fcc structure but they also found that few hexagonal regions can be found.

Unfortunately, the experiments in precession electron diffraction were not successful due to the grain size of our samples and the resolution achieved in the microscope. In the case of most reports the grain size are bigger than in our case: we measured a mean size of 7 ± 2 *nm* using HRTEM images while in the case of Cantu-Valle et al. [8] the grains present a size of about *200-300 nm* in the intermedia part of the wire and just a few grains on the top $<$*80 nm*.

4.3.2 Pore size and nanowires diameters

The pore size distribution is a key characteristic in NWs growth. In the case of track-etched membranes of polycarbonate, scanning electron microscopy (SEM) is the standard method used by manufacturers for pore size determination, but becomes hardly applicable for sizes below *100* nm due to charging effects (limiting the resolution). Gold coatings can reduce these charge problems, but they can be *20* nm of thickness: the holes may be partly covered, leading to an underestimate of the actual pore diameter. Another disadvantage is the missing information about the internal shape of the membrane. Also, these membranes have been assumed to be cylindrical with an inner diameter that corresponds to the one tabulated by the manufacturer (nominal diameter). This hypothesis was challenged first by Chlebny et al. [44]. They used a replica method, whereby the pores were filled by a metal electrodeposition. Co and Ni metals were used; after the dissolution of the membrane, the remaining metallic replicas were observed by transmission electron microscope (TEM), which resolves nanometric dimensions. Three different templates labelled A, B and C with different pore sizes were studied. Table 4.3.1 presents the results found by Chlebny et al. for the different commercial polycarbonate membranes with several pore sizes. They found that diameters of nanowires analysed by TEM could be larger by up to a factor of 3 compared to the nominal diameter of the nanopores.

Schönenberger et al. [45] observed the cross section variation along the wire: the wire diameter, which is argued to directly reflect the pore diameter, is observed to be substantially larger in the middle than at both ends (Also discussed by Pullini et al. [28]). Therefore, the pores are not cylindrical with constant cross-section, but appear to be “cigar-like”. They also found that inside the membrane, the pores are wider by up to

a factor 3. The values obtained by Chlebny and Schönenberger teams are compared in Table 4.3.2.

Table 4.3.1. Comparison between nominal pore diameters and mean values deduced from metallic replicas. Manufacturers are indicated in parentheses. Values extracted from [44].

Nominal diameter (nm)	Diameter measured by Chlebny et al. (nm)
10 (A)	36 ± 3
10 (C)	36 ± 2
15 (C)	43 ± 2
30 (A)	57 ± 3
50 (A)	61 ± 2
50 (B)	81 ± 3
80 (A)	164 ± 9
100 (A)	184 ± 6
200 (A)	260 ± 4

Table 4.3.2. Comparison of values: nominal pore size, results from Schönenberger and Chlebny teams.

Nominal diameter (nm)	Diameter by Schönenberger (SEM) (nm)	Diameter by Chlebny (TEM) (nm)
10	50 ± 18	36 ± 3
30	80 ± 20	57 ± 3
80	180 ± 40	164 ± 10

The question about why the pores are wider inside the membrane than close to the surface was treated by Schönenberger et al. [45]. They discussed that this effect is a consequence of the ion impact during "exposure". Each pore is formed by a single highly

energetic ion traversing the membrane. The direct impact interaction produces a damage zone along the ion track (damage track). The membrane is then etched in a solution with a high selectivity for damage tracks; i.e., the etching rate for damaged zone is much larger than for the undamaged material. During this process, a physical hole is opened in the membrane. Since etching proceeds from the top and bottom surface, the pore is expected to assume a shape with a thinner middle cross section. This is just the opposite of what is observed in our work and Schönenberger studies. However, the primary damage zone is localized within a very narrow region. A typical damage diameter is *10 nm*. Once the pores are open, they widen with progressive etching time, ideally homogeneously, in which case cylindrical holes will develop. Besides the primary damage, caused by the ion impact, a large number of secondary electrons are generated at any point along the track (electronic collision cascade) [46], [47]. These electrons themselves have sufficient energy to interact destructively with the polymer membrane. The resulting smaller polymeric fragments are etched more easily than the original polymer, and since the range of secondary electrons is large (up to $\approx 1\ \mu m$), the etch rate can also be enhanced at positions away from the track centre. This effect is well-known in electron beam lithography (e-beam lithography). Here, a focused medium energy electron is used to expose a resist. In the developing step (etching), the exposed material is dissolved. A fundamental problem in e-beam lithography is that also secondary electrons expose the resist, often they even dominate the exposure. Since secondary electrons can penetrate the polymer over rather long distances, the resist is effectively exposed laterally away from the position of the primary beam. This effect has been termed "*proximity effect*" in e-beam lithography (Figure 4.3.3). Schönenberger and co-workers proposed that the pore widening is a consequence of the proximity exposure. This suggestion allows one to understand why etched pores are generally wider inside than at the top and bottom end of the membrane. Let us assume that the secondary

electrons are generated isotropically at each point along the ion track, but sufficiently inside the membrane, receives exposure from secondary electrons generated above and below this point. This is different from a point close to the membrane surface. On the top surface, for example, impinging secondary electrons can only originate from below this point, since the impacting ion moves through vacuum above. For this reason, proximity exposure is reduced by approximately a factor of 2 close to the membrane surface. Thus, the pore will develop a smaller diameter at the top and bottom of the membrane compared to regions inside.

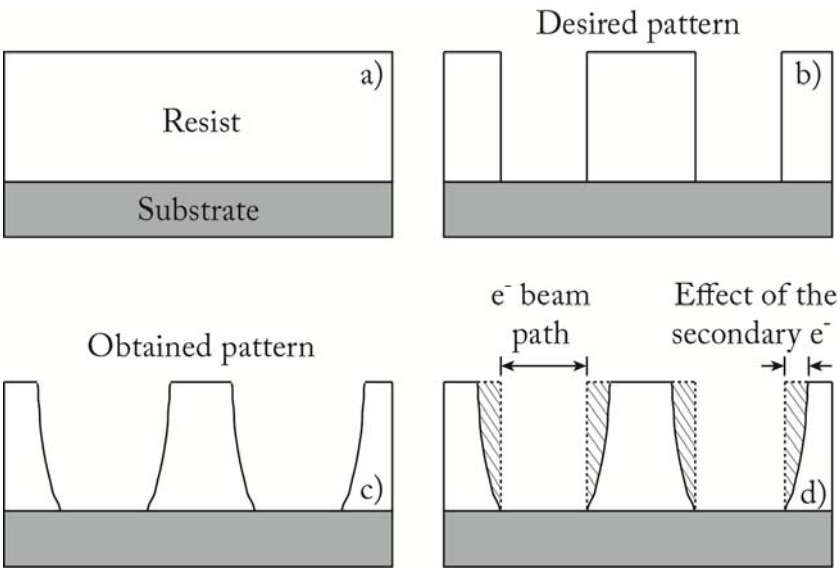

Figure 4.3.3. Variation of the width due to the proximity effect in an electron beam lithography a) Initial resist and substrate. b) Desired pattern. c) Obtained pattern after performing the lithography. d) Comparison of the remaining resist profile with the desired one.

In a more recent work [48] Apel et al. showed that the paradoxical profile of track-etched is governed at least by two factors: the heterogeneity of the polycarbonate cast films and the hindered diffusion of surfactants into the etched out nanochannels. However during their work they removed the "dense" surface layers from the polycarbonate film and showed that even in this case the cigar-like pores can be produced by the surfactant-controlled etching. The combination of several factors

makes the process quite intricate and difficult to explain quantitatively. Fink et al. [49] suggested that the polymer becomes denser due to a complex interaction with the etching solution. They mentioned that the etchant penetration into polycarbonate membranes proceeds by different stages. Apparently, ion irradiation enables a slightly enhanced surface-near etchant uptake.

4.4 Local chemical analysis

Figure 4.4.1 a) shows a TEM image of a representative wire with a mean diameter of 64 ± 2 nm (configuration 25nm/15nm). Local chemical analysis has been performed by electron energy loss spectroscopy (EELS) and energy-filtered TEM (EFTEM) to distinguish the layers. Figure 4.4.1 b) and Figure 4.4.1 c) present the corresponding elemental maps of Co and Cu, respectively. Figure 4.4.1 d) is the combination of the previous maps where the alternation of Co and Cu layers is clearly seen in red and blue, respectively. We observe that some of the layers are rotated a few degrees with respect to the wire axis. While Co impurities are barely visible in the Cu layers, a non-negligible amount of Cu seems to be present into the Co layers.

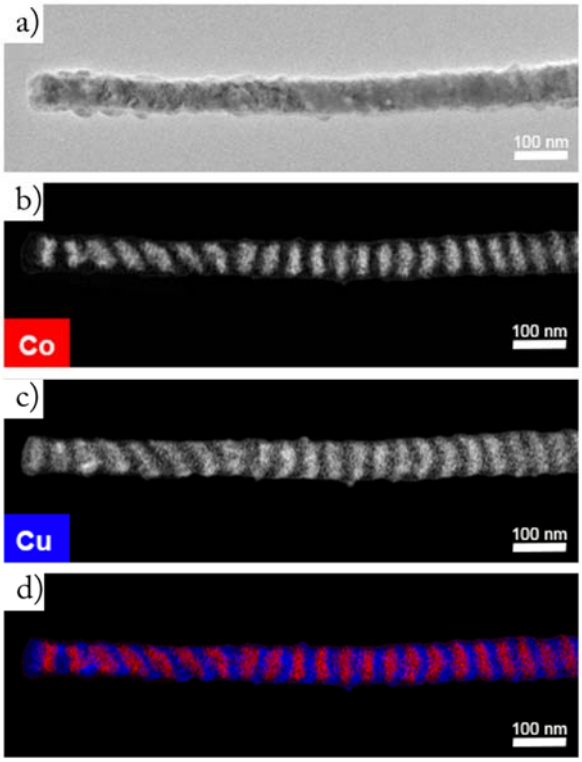

Figure 4.4.1. a) BF-TEM image of a Co/Cu nanowire. b) EFTEM image of the wire recorded at the cobalt edge. c) EFTEM image of the wire recorded at the copper edge. c) Cobalt (red) and copper (blue) map as the result of the superimposition of b and c maps.

To quantify the proportion of the Cu impurities, EELS spectra have been recorded on Co/Cu multilayered nanocylinders. Figure 4.4.2 shows a scheme to perform STEM-EELS. The probe of the TEM scans the sample and the high-energy convergent electron beam in STEM mode provides local information of the sample. With the use of EELS, elemental identification is possible. The low-angle inelastically scattered electrons used in EELS are complementary to the high-angle scattered electrons in the annular dark field detector (ADF). The energy losses of the inelastically scattered electrons are collected and separated using a magnetic prism as shown Figure 4.4.2.

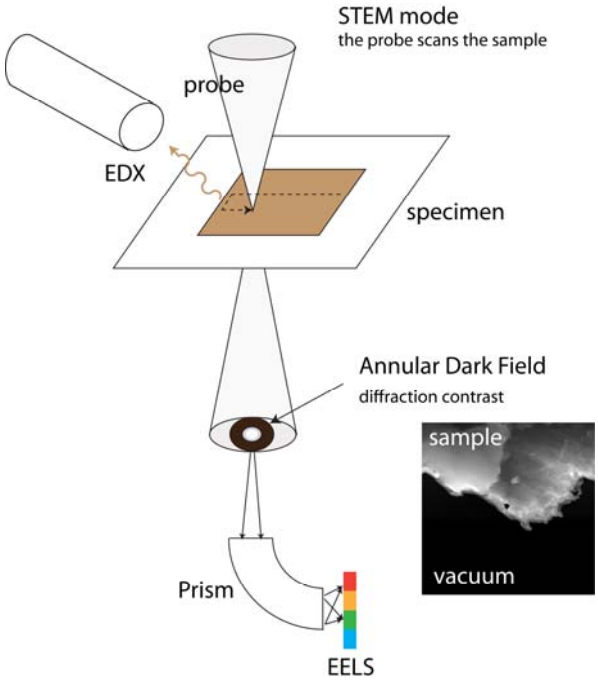

Figure 4.4.2. Scheme for STEM-EELS measurement.

To avoid projection problems, the EELS profiles have been performed on thick layers (100nm), as the layers are not strictly parallel to the electron beam. If thin layers are used, the tilt of the layers will make the electron beam pass through adjacent cobalt and copper layers and the determination of the composition of a single layer will be difficult. By working on 100nm thick layers for cobalt and copper, we can get rid of the projection problem and as the deposition conditions are the same for all the wires, the relative composition measured on these wires can be transferred to the thinner ones.

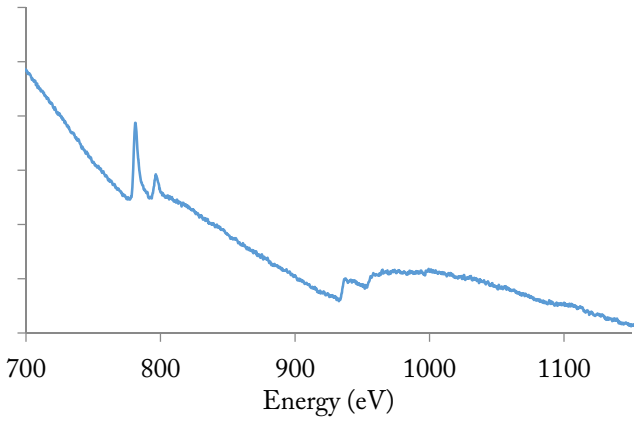

Figure 4.4.3. EELS spectrum extracted from a line scan, the Co L edge is at 778eV, the Cu L edge at 930eV.

Scanning TEM has been used to get the dark field image presented on Figure 4.4.4 a) and to acquire EELS spectra along a line drawn on the wire. For each position of the probe, a spectrum is recorded between 700eV and 1100eV to have access to both Co-L edge (778ev) and Cu-L edge (931eV) (Figure 4.4.3). Using a quantification routine, the relative composition between the cobalt and copper is extracted for each position on the spectrum line. Figure 4.4.4 b) shows the composition profiles. Around 15% of copper is measured in the cobalt layers, whereas nearly pure copper is observed in the copper layer. This result has already been obtained in other works [31], [32], [50] and its explanation is well known: as the deposition potential is lower for Co (-1.0V) than for the Cu (-0.3V), a small amount of Cu is codeposited during the Co deposition if a single bath method is used in the electrodeposition process. This inclusion of fcc Cu into the Co layers favours the fcc structure of the cobalt [39], [51].

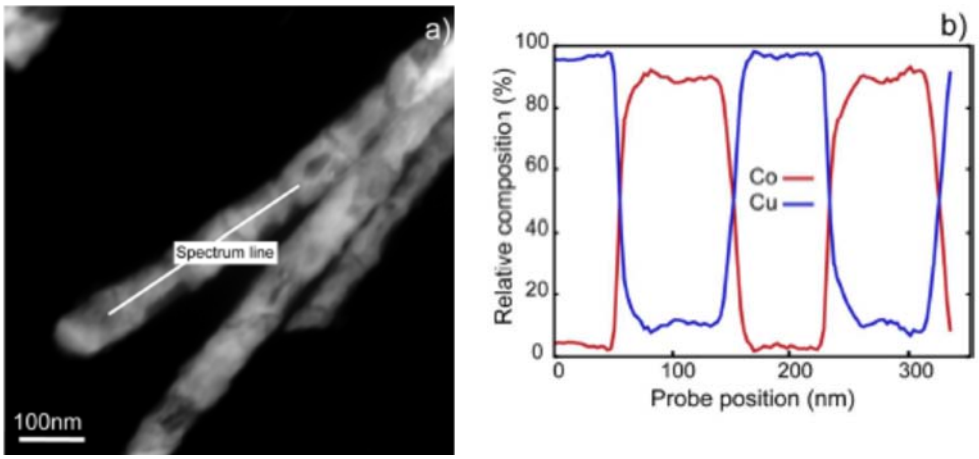

Figure 4.4.4. STEM dark field image of Co/Cu multilayered nanowire (layers of 100nm each) and b) line profile used for the EELS quantification.

A statistical analysis was performed from the EFTEM images on tens of layers observed in the different wires and configurations (layer thickness) that give a distribution of thickness for each configuration. In Figure 4.4.5, the histograms for the distribution of the thickness for each configuration of samples and element (Co and Cu) are shown. The nominal and real average thicknesses (for Co and Cu layers) t_N and t_R respectively are shown also in Figure 4.4.5.

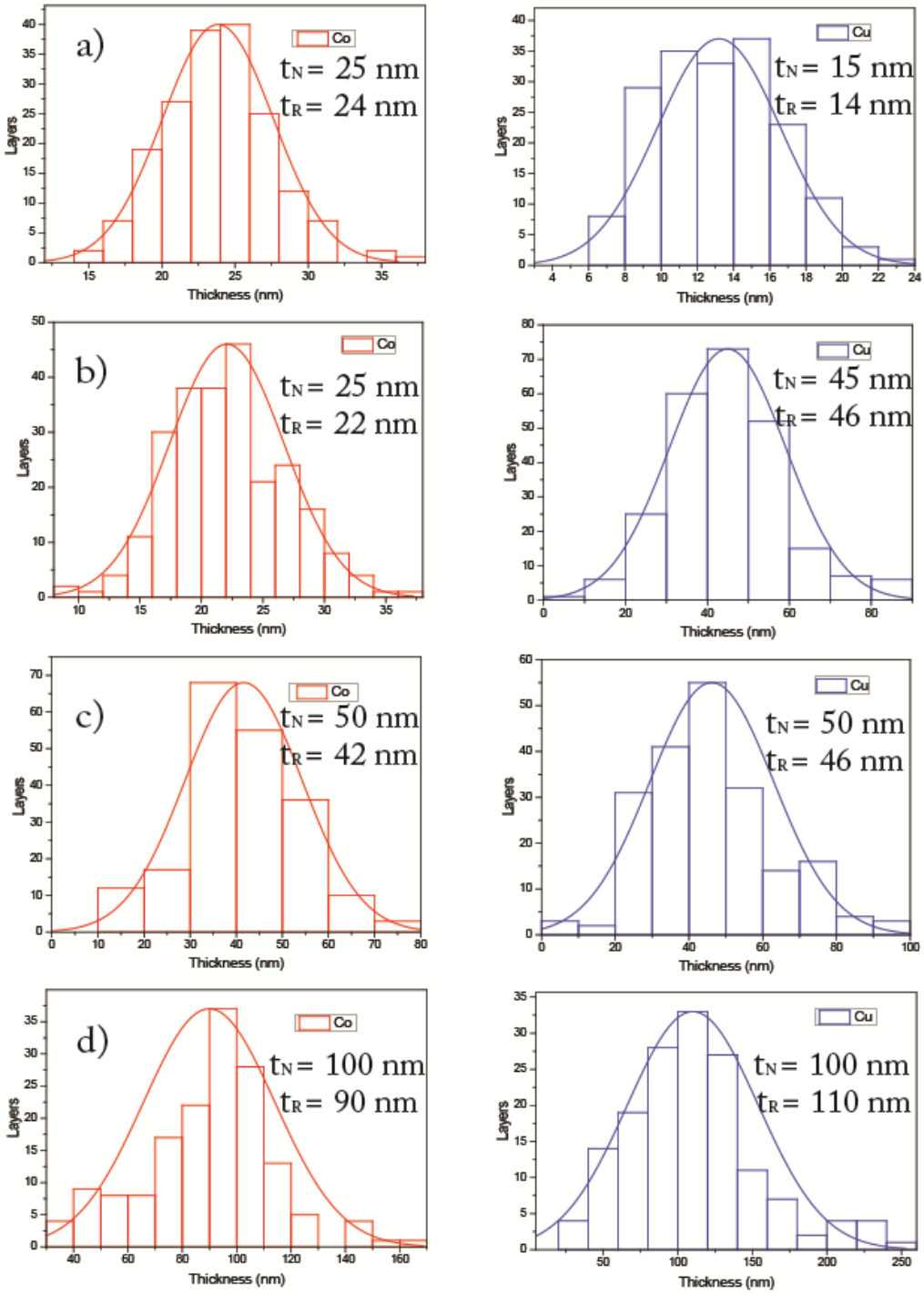

Figure 4.4.5. Distribution of thickness layer for Co/Co nanowires, nominal and real values: a) 25nm/15nm, b) 25nm/45nm, c) 50nm/50nm, d) 100nm/100nm configuration.

In Table 4.4.1 the relation of the nominal, measured thickness of the layers and its corresponding standard deviation are shown. The distribution shows that the standard deviation increases with the increase of the nanowires thickness. However, the mean thickness of the electrodeposited layers remains with a good agreement between the nominal thicknesses. The layers close to extremities/tips increase the standard deviation due to the non-constant diameter of the membrane pores as was discussed in previous sections. As an example, Figure 4.4.6 shows four different configurations for Co/Cu NWs in which the ends display a decreasing of the thickness layer compare to its central part. Pullini, Chlebny and Schönenberger have found this behaviour and also proposed some possible reasons to this features [28], [44], [45] as we discussed in previous sections.

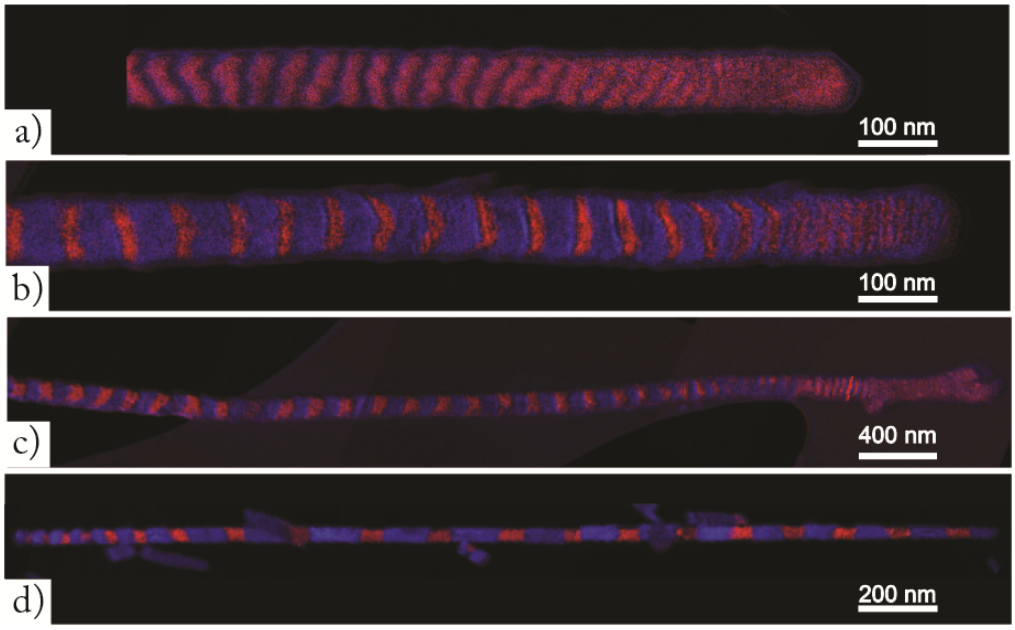

Figure 4.4.6. EFTEM elemental maps, in red Co and Cu in blue for Co/Cu NWs with configurations of: a) 25/15, b) 25/45, c) 50/50 and d) 100/100. The NWs ends show a decreasing of the thickness layer compare to its central part.

Table 4.4.1. Nominal and measured thickness for the different configurations of Co/Cu nanowires with the corresponding standard deviation extracted from the statistical analysis.

Nominal Co/Cu (nm/nm)	Real Configuration Co/Cu (nm/nm)	Standard deviation (nm/nm)
25/15	24/14	4/4
25/45	22/46	5/14
50/50	42/46	13/17
100/100	90/110	24/44

4.5 Magnetic configurations in Co/Cu nanowires

4.5.1 Co/Cu = 25nm/15nm

As we discussed in chapter 3, around 20 NWs from the 85 located previously were studied. Figure 4.5.1 shows the hologram, EFTEM map and the phase shift maps for the two configurations PL and PP of a whole NW corresponding to the 25nm/15nm configuration. We can identify the different phase variations along the NW and the changes produced by the PL and PP configurations.

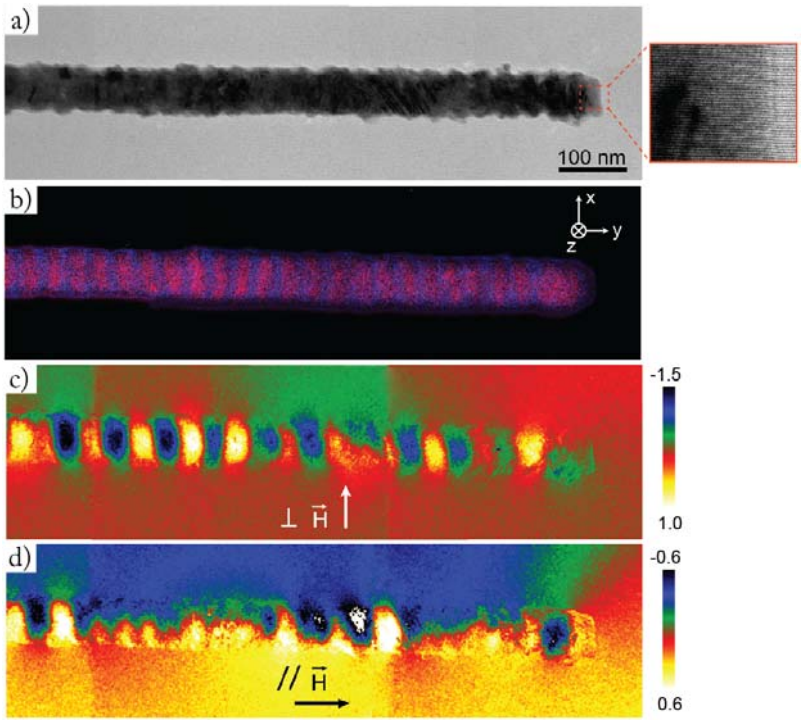

Figure 4.5.1. Reconstruction of a whole Co/Cu NW (25nm/15nm): a) hologram, b) EFTEM map, c) phase shift map for PL configuration and d) phase shift map for PP configuration.

In order to study the local magnetic states in the Co/Cu NWs, a representative portion of the whole NW is taken. Figure 4.5.2 presents two different remnant magnetic states on the same portion of the NW shown in Figure 4.5.1, which has a diameter of 64 ± 2nm. Figure 4.5.2 a) and Figure 4.5.2 b) show the hologram and the chemical map obtained by EFTEM. The magnetic phase maps extracted from the holograms are given in Figure 4.5.2 c) and Figure 4.5.2 d). They correspond respectively to the remnant magnetic states of the same layers for an applied field perpendicular (defined as the X direction) and parallel (Y direction) with respect to the wire axis. The positions of the Co and Cu layers deduced from the EFTEM chemical maps have been added for clarity on each figure. We can clearly observe that the two experimental remnant states are different as a function of the direction of the applied field. In Figure 4.5.2 c) shows an alternation of contrast corresponding to magnetization in opposite X-directions from

one Co layer to the other. Differently, Figure 4.5.2 d), the isophase lines parallel to the Y direction reflect an integrated magnetization pointing toward the wire axis.

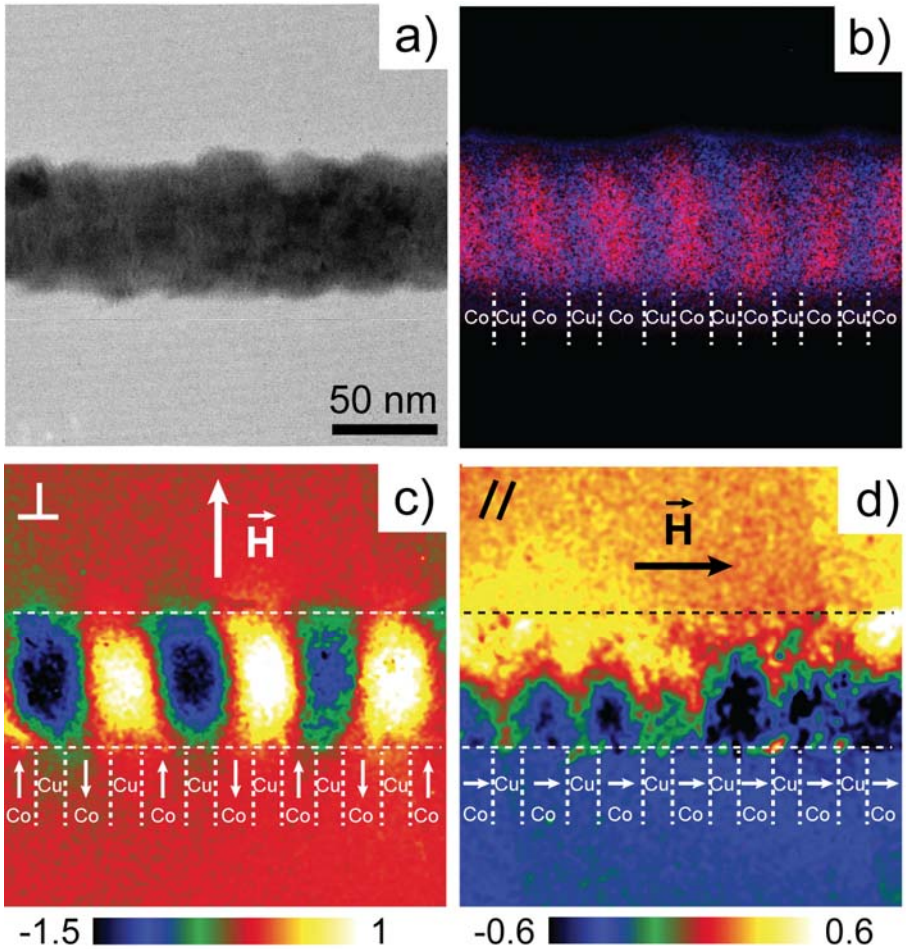

Figure 4.5.2. Nominal configuration Co/Cu NW 25nm/15nm: a) Hologram of the observed wire. b) EFTEM image of the same area to distinguish the copper (blue) and cobalt (red) layers. c) Magnetic phase shift map obtained after the application of the perpendicular saturation field with respect to the wire axis. d) Magnetic phase shift map obtained after the application of the saturation field parallel to the wire axis.

In the Figure 4.5.3 and Figure 4.5.4, the result of the micromagnetic simulations applied to the portion under study for the PL and PP configuration is presented. Here we quantitatively compared the phase shift amplitude and not the magnetic induction due to the integration problem. The remnant state in Figure 4.5.3 is found as an antiparallel coupling of the magnetizations in the Co layers. The variation

of the phase shift is located within the Co layers and remains the same in the Cu layers where no magnetic signal is present. Interestingly the amplitude varies from one layer to another. The magnetization direction in each individual Co layer is slightly different because of the randomly distributed anisotropy direction in each layer. Here this parameter was adjusted successfully for a few layers to fit the experiment. Finally, Figure 4.5.3 d) shows the 3D configuration for the magnetization resulting from micromagnetic simulations. The color scale represents the component of the magnetization along the X axis.

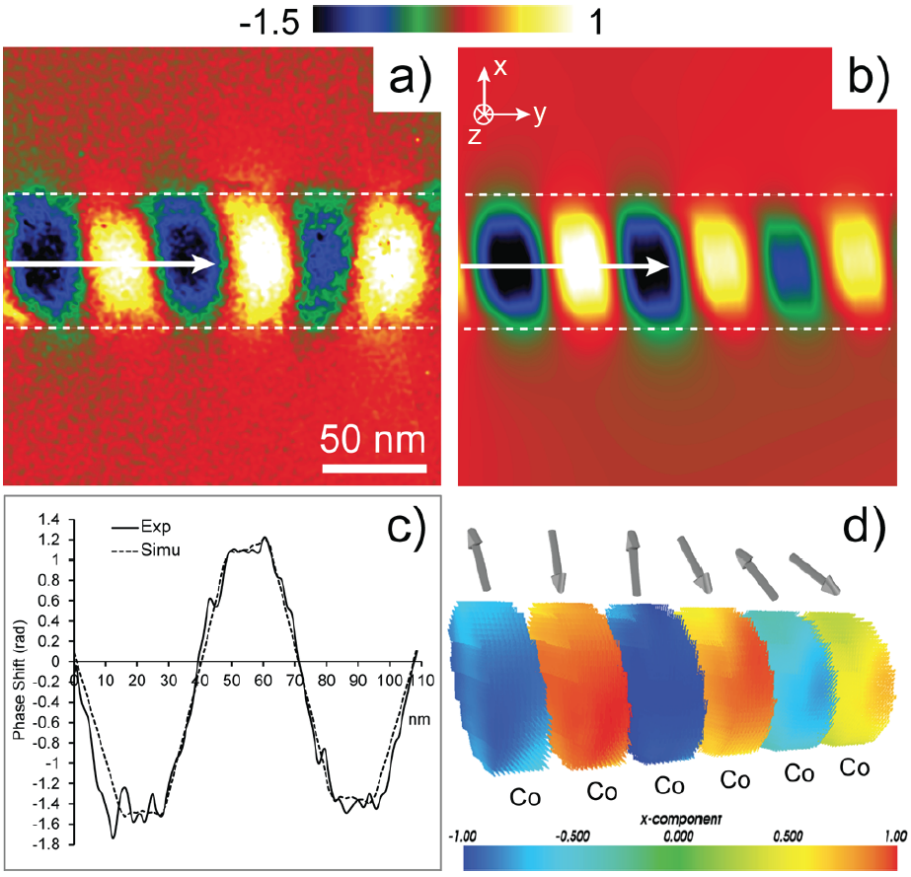

Figure 4.5.3. Configuration Co/Cu (25nm/15nm): a) Experimental magnetic phase shift map extracted from the holograms. b) Simulated phase shift map. c) Comparison of the experimental and simulated profiles of the magnetic phase shift obtained along the white arrow in a). d) 3D magnetic configuration of the cobalt layers corresponding the simulated phase image in b).

The remnant state in Figure 4.5.4 corresponds to magnetic vortices in each Co layers, with the cores of the vortices pointing along the wire axis (Figure 4.5.4 d)). The integration of the magnetization over the observation axis permits only to observe the core of these vortices because the components of the body of these are compensated (cancelled). From the micromagnetic simulations in Figure 4.5.4 d), it is worth mentioning that vortices often show an alternatively clockwise and anticlockwise orientation due to the initial interlayer coupling when the field is decreased from saturation. It should be noticed that the polarity of the vortices in the up direction (if we define as up when it is pointing to the +Y direction and down to the –Y direction). However, in the experimental phase shift maps, it is not possible to discern between these clockwise or anticlockwise orientations using EH, only the direction of the vortex core can be determined.

These conclusions obtained about the magnetic states resulted are based on the direct quantitative comparison of the simulated (Figure 4.5.3 b) and Figure 4.5.4 b)) and experimental (Figure 4.5.3 a) and Figure 4.5.4 a)) phase images. The magnetic simulations reproduce the experimental magnetic behaviour as a function of the direction of the applied field and propose a perfect quantitative agreement as shown by the extracted phase profiles (located by the arrows in Figure 4.5.4 a) and Figure 4.5.4 b)) averaged over one or two Co/Cu periods. This agreement was also found for the profile traced in the rectangles of Figure 4.5.4 a) and Figure 4.5.4 b).

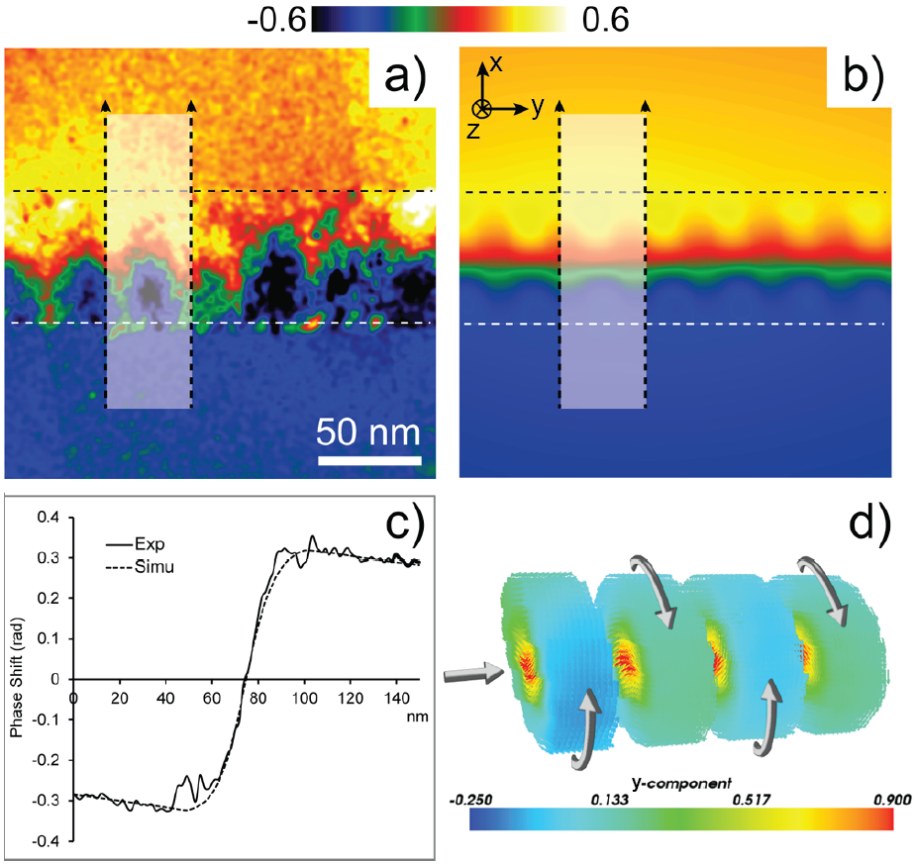

Figure 4.5.4. Configuration Co/Cu (25nm/15nm): a) Experimental magnetic phase shift map extracted from the holograms. b) Simulated phase shift map. c) Comparison of the experimental and simulated profiles of the phase shift obtained on the dotted rectangles drawn in a) and b). d) 3D magnetic configuration of the cobalt layers corresponding to the simulated phase image in b).

To get such quantitative agreement in both configurations (antiparallel and vortex state), the exchange constant A has been set to 22×10^{-12} J/m. This exchange value is especially important because it defines (also with the anisotropy constant but to a much less extent) the size of the vortex core. As the component of the magnetization pointing in the Y direction sets the amplitude of the phase shift, a direct correlation between the phase shift amplitude and the exchange constant in the vortex state can be established.

As already mentioned in chapter 3, our model for micromagnetic simulations is simplified to take into account the polycrystallinity of the layers (uniaxial anisotropy instead of cubic for fcc materials). While the magnetization decrease can be accounted by Cu impurities in the Co, the lower values of the exchange and anisotropy constants have been observed in others studies [5], [52]–[54]. For example, Henry et al. [5] found that the anisotropy axis of the electrodeposited hcp Co nanocylinders rotates from perpendicular to almost parallel to the wire axis at a critical diameter value around 60 nm, leading to a decrease of the measured anisotropy constant down to $200 \times 10^3\ \mathrm{J/m^3}$ at the transition due to the random distribution of the grains. In our study, we believe we encounter a similar situation. It is worth reminding that the exchange and anisotropy parameters we deduce here for this configuration rely on the averaged magnetization value of $1200 \times 10^3\ \mathrm{A/m}$ set for the simulations. For another set of parameters, one could obtain slightly different values. To reproduce the transition between the antiparallel state to the coupled vortices, with the quantitative agreement of the phase shift amplitude in the vortex state, the anisotropy constant has been set to $100 \times 10^3\ \mathrm{J/m^3}$, and the direction of the anisotropy has been randomly distributed from one layer to the other in a cone with a 20° aperture angle from the normal of the layers as was explained before.

The antiparallel coupling is the most difficult configuration to fit (Figure 4.5.3). Indeed, if the random distribution of the anisotropy axis has a small effect on the vortices amplitude, its impact upon the magnetization orientation in the antiparallel state, and so on the related phase shift, is important. Indeed, the phase shift amplitude will be maximum (respectively minimum) if the magnetization points in the X (respectively Z) direction. This can be explained by the fact that EH has only sensibility to the in-plane components of the magnetization. While the global behaviour of the numerous layers is faithfully reproduced, it is very challenging to recover the anisotropy directions of all

the layers by fitting quantitatively the experimental signal. However, we show that our method is powerful enough to recover the magnetic parameters of the different layers.

By reproducing our methodology for 20 different wires from the same batch, we demonstrate that another remnant magnetic state can appear in others nanowires for this Co/Cu configuration of 25nm/15nm. Additionally to the antiparallel and vortices configurations presented earlier, we also observed a monodomain-like state for which all the magnetizations of the Co layers point uniformly along the wire axis direction (Figure 4.5.5). The phase image shows similar features as coupled vortices, but the amplitude of the phase shift extracted on one Co/Cu period is here about three-times higher. Then it is interesting to note that discretization between the vortex and monodomain states can be done only by quantitatively comparing the calculated and measured phase shift profiles.

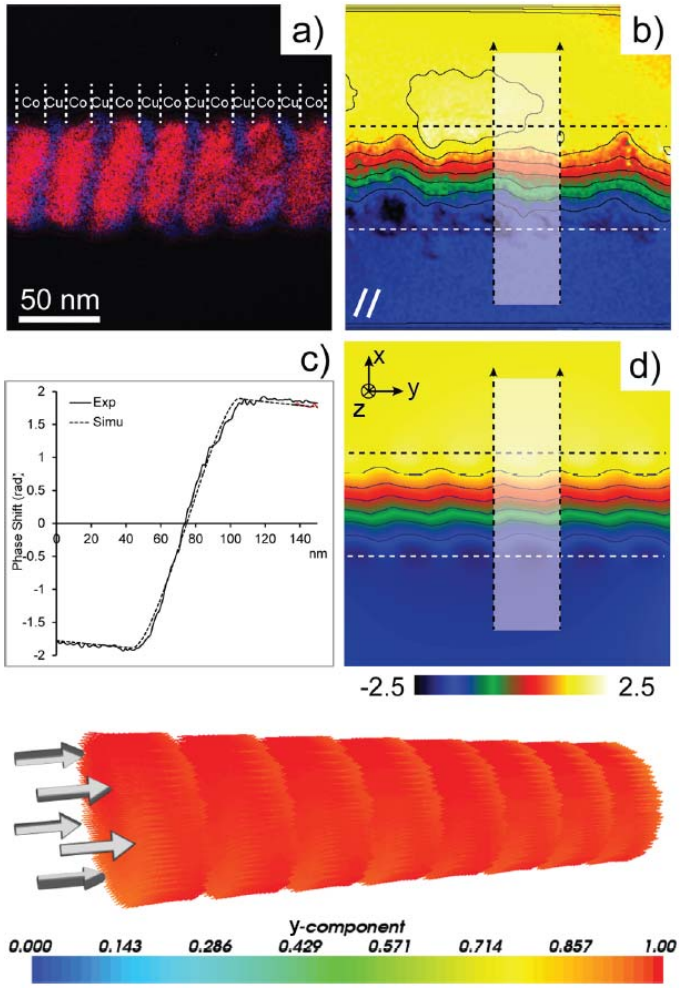

Figure 4.5.5. Cu/Co NW with 25nm/15nm of thickness layers: a) EFTEM image of the studied wire. b) Experimental magnetic phase shift map with the corresponding induction lines (in black). c) Comparison of the experimental and simulated profiles of the phase shift obtained for the rectangles drawn in b) and d). d) Simulated magnetic phase shift map with the corresponding induction lines (in black). e) 3D magnetic configuration of the cobalt layers corresponding to the simulated phase image in d).

Finally, we can also do some statistics on the different magnetic states in this Co/Cu configuration (25nm/15nm) as a function of the saturation field direction. First, if the averaged anisotropy direction in the Co layers is mostly in-plane, the magnetizations will remain in-plane whatever the direction of the applied field with a preferred antiparallel coupling due to the dipolar interaction between Co layers. This configuration is the most common in our wires (≈70%). If the anisotropy direction is

mostly oriented around the normal of the layers, several configurations can arise. If the combined effect of the magnetocrystalline anisotropy and dipolar coupling between layers is sufficient to counterbalance the shape anisotropy, the magnetizations will exhibit a mono domain-like behaviour. This configuration has been obtained on a few wires (≈10%) and has been reproduced in the simulations (as for example in Figure 4.5.5 e)) for an anisotropy constant above $200 \times 10^3\ \mathrm{J/m^3}$ randomly orientated around the normal of the Co layers in a cone with an aperture angle up to 20°. It is interesting to note that such values of anisotropy amplitude and direction are similar to the one observed in [5], [52]–[54] for electrodeposited hcp Co. As we said before, generally, in such nanowires with a polycrystalline texture, Co presents many structural defects as stacking faults. It can become difficult to make the difference between hcp and fcc structures: it is then possible to get polycrystalline Co with structural properties mainly similar to fcc but with some magnetic characteristics corresponding to an hcp structure. For 25nm/15nm configuration, the lower values of the anisotropy constant, the magnetocrystalline anisotropy will still tend to keep the magnetization out-of-plane of the layers, but the shape anisotropy will push the spin perpendicularly to the wire axis. This leads to transition between vortices when the field is parallel to the wire axis to an antiparallel coupling for the perpendicular field. This configuration appears for about 20% of the wires. Typically, such magnetic transitions appear if the anisotropy constant is below $180 \times 10^3\ \mathrm{J/m^3}$ and if the anisotropy is distributed with a 40° cone aperture.

4.5.2 Co/Cu = 25nm/45nm

Regarding the nominal configuration of Co/Cu NWs of 25nm/45nm, Figure 4.5.6 shows the reconstruction of a whole representative NW for the PL and PP configuration. The two configurations do not present strong changes between them. It is clear that similar features as for the antiparallel coupling between the Co layers in the

25nm/15nm thicknesses PP configuration appears also for these thickness. A total of 180 NWs were selected to perform EH for this configuration, but, just 25 of them could be observed by EH.

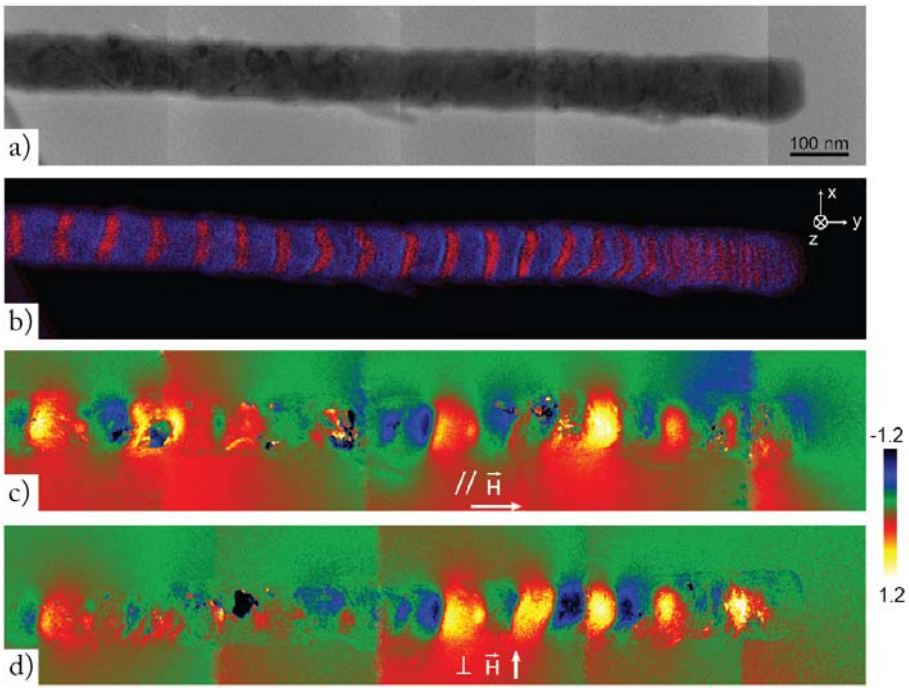

Figure 4.5.6. Reconstruction of a Co/Cu NW (25nm/45nm): a) hologram, b) EFTEM map, c) phase shift map for PL configuration and d) phase shift map for PP configuration.

Figure 4.5.7 presents the two remnant states for the nominal Co/Cu nominal configuration of 25nm/45nm and a diameter of 80 ± 2nm for a portion of the NW reconstructed in Figure 4.5.6. We have found that both magnetic configurations are similar and the effect of the magnetic field has not a big influence in most of the resulting magnetic states into the Co layers. Figure 4.5.7 c) and Figure 4.5.7 d) show a magnetization almost opposite in each Co layer as in the Figure 4.5.2.

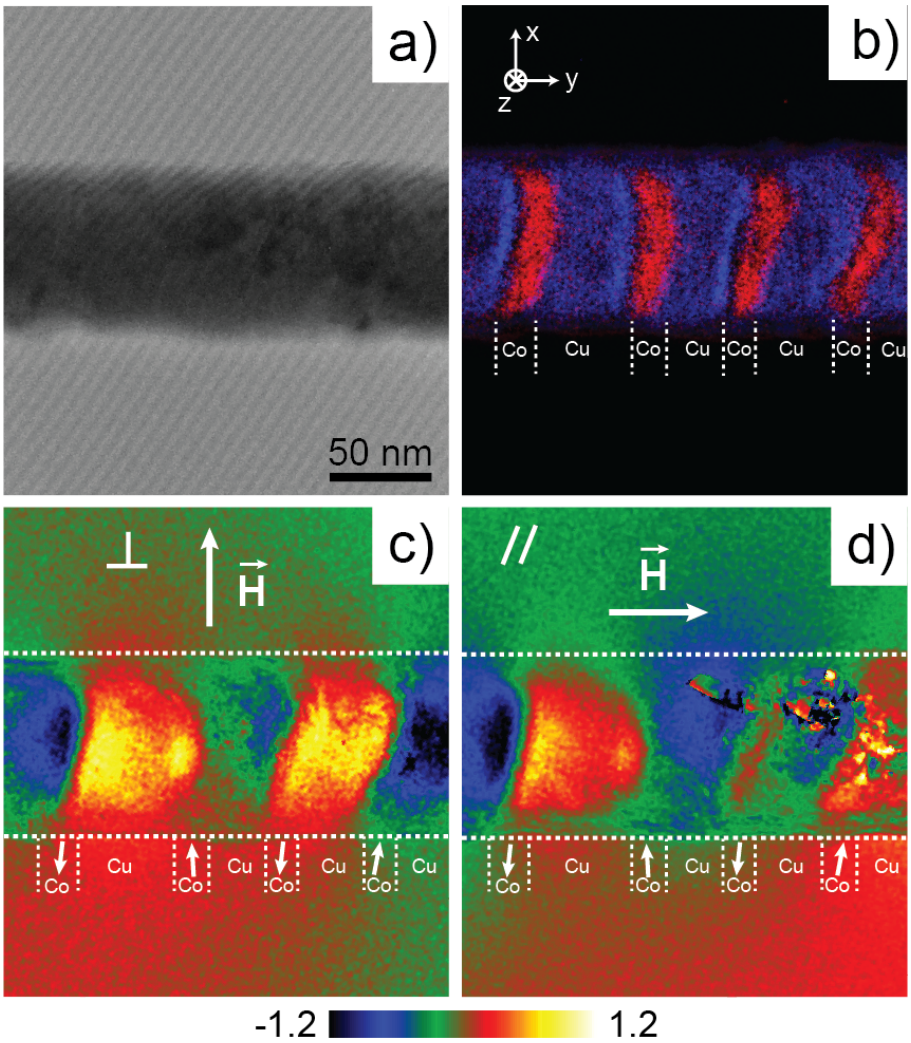

Figure 4.5.7. Nominal configuration Co/Cu 25nm/45nm: a) TEM image of the observed wire. b) EFTEM image of the same area to distinguish the copper (blue) and cobalt (red) layers. c) Magnetic phase shift map obtained after the application of the perpendicular saturation field with respect to the wire axis. d) Magnetic phase shift map obtained after the application of the saturation field parallel to the wire axis.

On Figure 4.5.8 the experimental and the simulated phase shift maps are shown. For this configuration, the magnetic states remain almost unchanged when the magnetic field is applied parallel or perpendicular to the wire axis. There are some exceptions and special cases where slight changes are present in the phase shift amplitude. By micromagnetic simulations we can deduce that the remnant state showed in Figure 4.5.8 a) and Figure 4.5.8 b) corresponds to layers oriented perpendicular to

the wire axis and a vortex state between them. This vortex state has a core shifted with respect to the centre of the layer. By micromagnetic simulations it can be deduced that the core is tilted ≈15° with respect to the wire axis in the *XY* plane. The tilt of the core orientation with respect to the wire axis is produced by different facts: the direction of the uniaxial anisotropy, the dipolar coupling with adjacent layers and the fact that the layers are tilted (10° in this case) with respect to the wire axis. The combination of these facts produces an alteration of the vortex core. It is important to note that the direction of the uniaxial magnetocrystalline anisotropy for the layer corresponding to the vortex state is oriented 27° respect to the wire axis.

In this Co/Cu (25nm/45nm) configuration, the remnant magnetic states are a combination of layers with the magnetization oriented in the place of the layer (perpendicular to the wire axis) and vortices states. This mixture is due to the close values of the energy between these two magnetic states. It should be noticed that just a qualitative analysis of the phase shift images on this configuration can produce a false interpretation as it could be seen as a pure antiparallel coupling between the Co layers. Thanks to micromagnetic simulations we can have different points of view and finally observe the qualitative information comparing phase shift profiles.

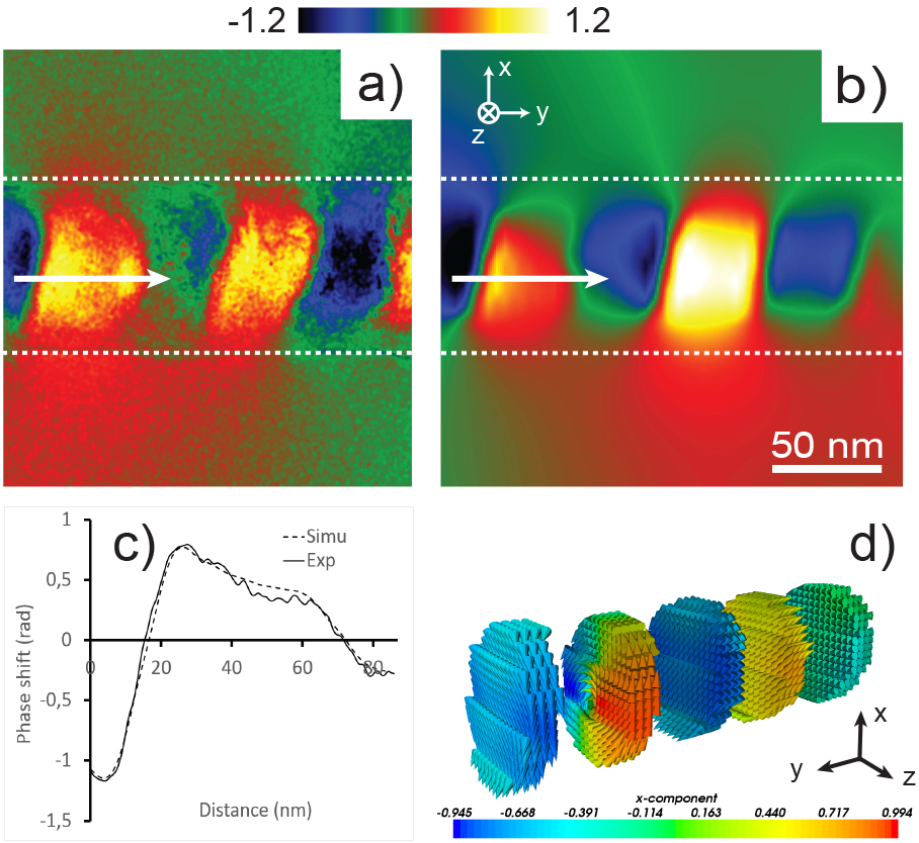

Figure 4.5.8. Configuration Co/Cu (25nm/45nm): a) Experimental magnetic phase shift map extracted from the holograms. b) Result of the simulated phase shift map. c) Comparison of the experimental and simulated profiles of the magnetic phase shift obtained along the arrows in a) and b). d) 3D magnetic configuration of the cobalt layers corresponding the simulated phase image in b).

The mixture of magnetic states was corroborated studying several configurations with randomly distributed magnetocrystalline anisotropy. In the case of the Figure 4.5.8, the vortex core is coupled with the nearest layers. For the simulated magnetic state, the magnetic anisotropy was randomly distributed in a cone of 30° of aperture respect to the wire axis (20° respect to the normal of the layer). The value of this uniaxial magnetocrystalline anisotropy was set to $100 \times 10^3\ \mathrm{J/m^3}$ in the particular case of the Figure 4.5.8 but the mixture of states is well represented in a range of $100 - 280 \times 10^3\ \mathrm{J/m^3}$. The exchange constant and magnetization of saturation were kept as in the 25nm/15nm configuration $22 \times 10^{-12}\ \mathrm{J/m}$ and $1200 \times$

10^3 A/m ($\mu_0 M_s$ 1.5T) respectively. Micromagnetic simulations show that for a uniaxial magnetocrystalline anisotropy lower than 100×10^3 J/m^3 only pure vortices with the core lying along the wire axis are obtained, as using a cubic anisotropy. If the value of the magnetic anisotropy arises above 280×10^3 J/m^3 but with small angles of the magnetocrystalline direction, the Y component of the magnetization is favoured and the layer magnetization tends to orient parallel to the wire axis. For higher angles (>30°) one favouring of the antiparallel state is achieved.

Another magnetic state for this system (Co 25nm/Cu 45 nm) can be seen Figure 4.5.9. It shows a phase shift map in which the integrated induction creates a kind of circular-like shape of the magnetization. The diameter of the shown NW is 82 ± 2 nm. This "circular" shape was obtained by micromagnetic simulations and corresponds to vortices with the core tilted respect to the wire axis (Figure 4.5.9 c) and Figure 4.5.9 d)). In this case, these vortices have the core tilted more than 30° respect to the wire axis which is almost two times the angle of the vortices found in the magnetic state of the Figure 4.5.8. The configuration of the Figure 4.5.9 is obtained for a magnetocrystalline anisotropy oriented in a cone of 30° with a value of 130×10^3 J/m^3. In this case, we can observe a big influence of the magnetic anisotropy which makes the vortex core tilt respect to the wire axis. We can conclude that for this Co/Cu configuration a mixture of states between antiparallel and vortices states are obtained for both directions of the magnetic field applied. A transition from AP to vortex state is not clearly seen as in the previous configuration (Co 25nm/ Cu 15nm). The behaviour where the magnetic states present no big changes, when the magnetic field is applied PP or PL to the wire axis, can be attributed to the loss of coupling due to the increase of the Cu layer with respect to the 25nm/15nm configuration.

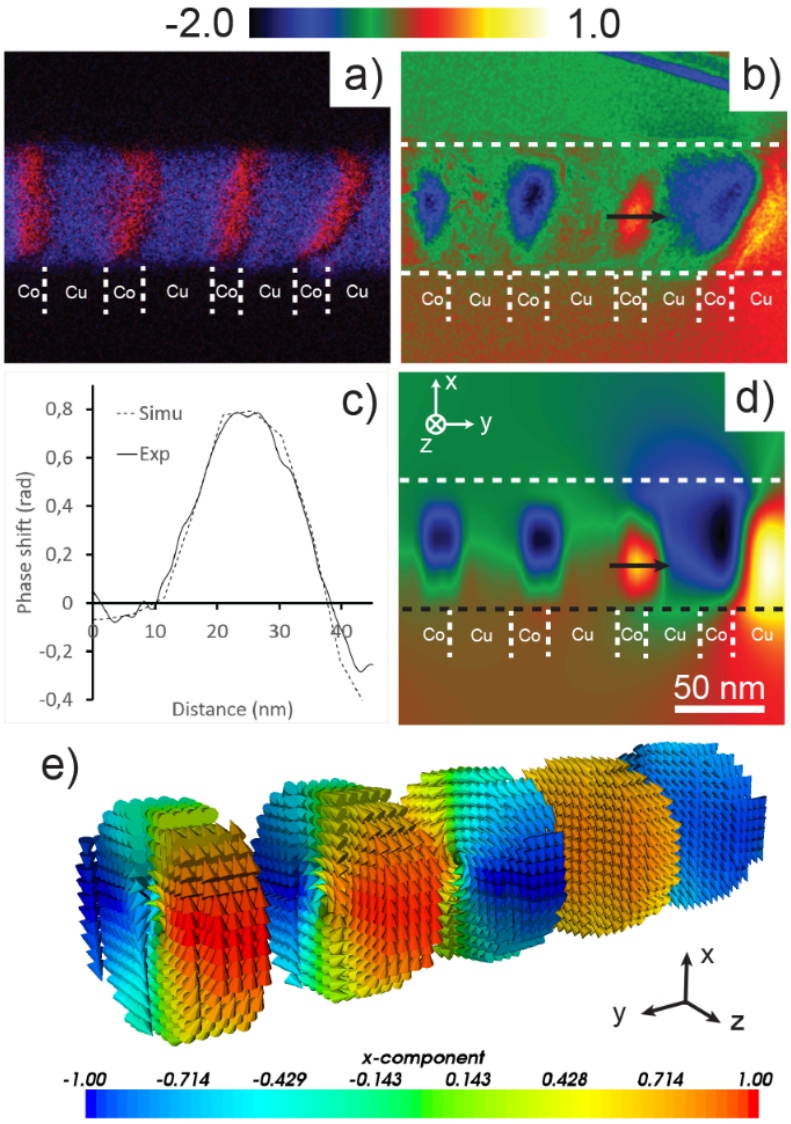

Figure 4.5.9. Cu/Co nanowire with 25nm/45nm of thickness layers: a) EFTEM image of the studied wire. b) Experimental magnetic phase shift map. c) Comparison of the experimental and simulated profiles of the phase shift obtained for the arrow drawn in d). d) Simulated magnetic phase shift map with the corresponding. e) 3D magnetic configuration of the cobalt layers corresponding to the simulated phase image in d).

4.5.3 Co/Cu = 50nm/50nm

Figure 4.5.10 shows a large field of view of a typical NW for the 50nm/50nm configuration. The phase images present circular features characteristic of the vortices previously observed. There are no significant changes between the two PL and PP

configurations for all observed wires. A total of 70 NWs were selected, of which 15 NW could be observed.

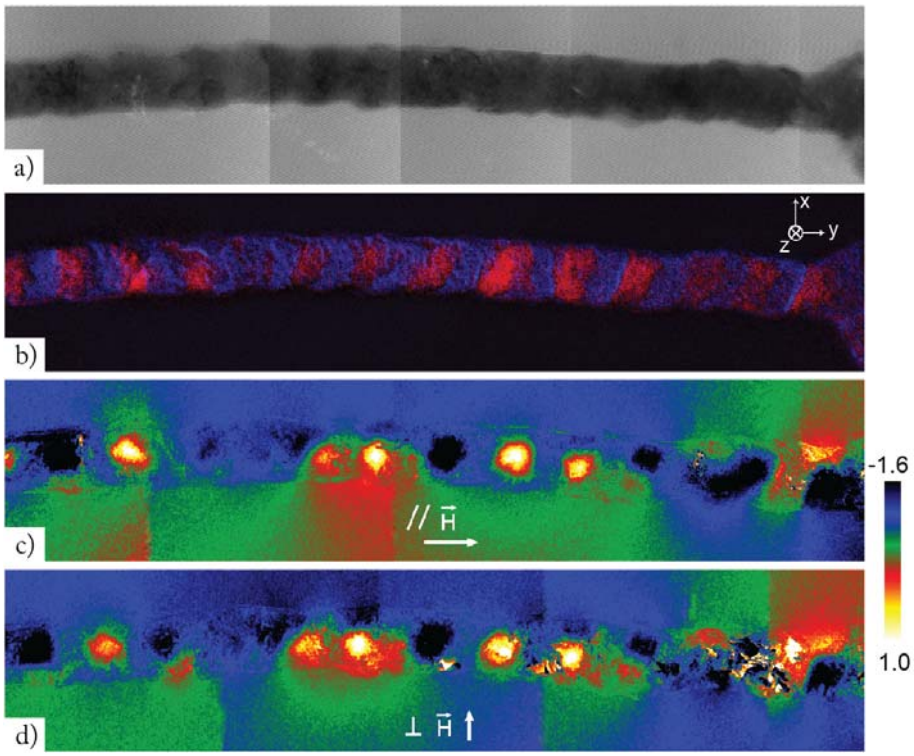

Figure 4.5.10. Reconstruction of a Co/Cu (50nm/50nm): a) hologram, b) EFTEM map, c) phase shift map for PL configuration and d) phase shift map for PP configuration.

Figure 4.5.11 shows the two remnant magnetic states of a representative portion of the NW shown in Figure 4.5.10. The diameter of this part of the NW is 90 ± 2 nm. For this thickness, the magnetic states are the same no matters the direction of the magnetic field. The magnetization can be interpreted as rotating in the XY plane (image plane). The two circular features showed in Figure 4.5.11 represent the integrated magnetization rotating with opposite directions.

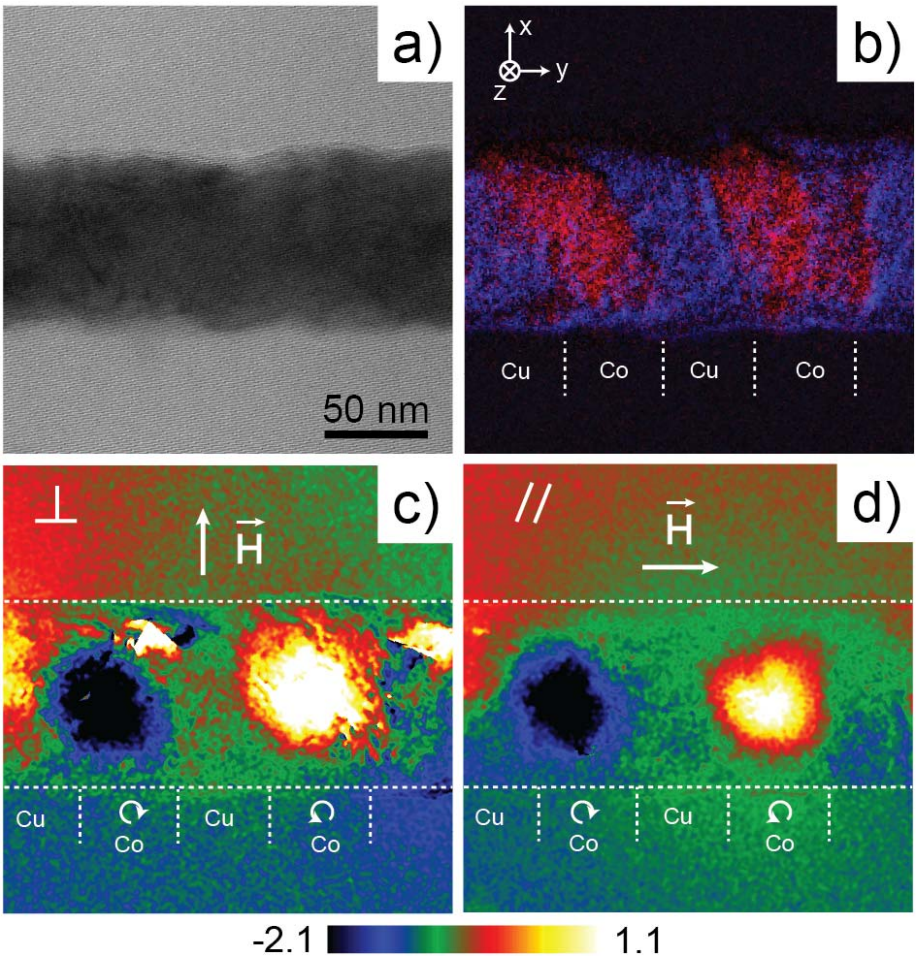

Figure 4.5.11. Nominal configuration Co/Cu 50nm/50nm: a) TEM image of the observed wire. b) EFTEM image of the same area to distinguish the copper (blue) and cobalt (red) layers. c) Magnetic phase shift map obtained after the application of the perpendicular saturation field with respect to the wire axis. d) Magnetic phase shift map obtained after the application of the saturation field parallel to the wire axis.

In Figure 4.5.12, we present the fine analysis of the phase image given in Figure 4.5.11d). The simulated phase shift image is shown in the Figure 4.5.12 b), corresponding to the 3D configuration result of the micromagnetic simulation in Figure 4.5.12 d). Micromagnetic calculations demonstrate that the circular features found in the Figure 4.5.12 a) correspond to vortices with the core pointing almost perpendicular to the wire axis. Thus, this circular behaviour of the magnetization is the body of the vortex. A quantitative analysis is performed by the profiles traced over one of the circular

features in the experimental and simulated phase shift maps. In the Figure 4.5.12 c) the agreement between both profiles can be seen. It is not possible to determine the precise direction ($+Z$ or $-Z$) of the vortex cores from experimental phase images as these cores are parallel to the electron beam. If the cores are aligned, it should be noticed that the two vortices have a different chirality. Otherwise the chirality is the same but the magnetization is reversed. Micromagnetic simulations indicate that the two vortices have an up polarization leading to a change of chirality between both vortices. However we cannot discard the possibility that both can have different polarization: the analysis of other layers shows similar behaviour.

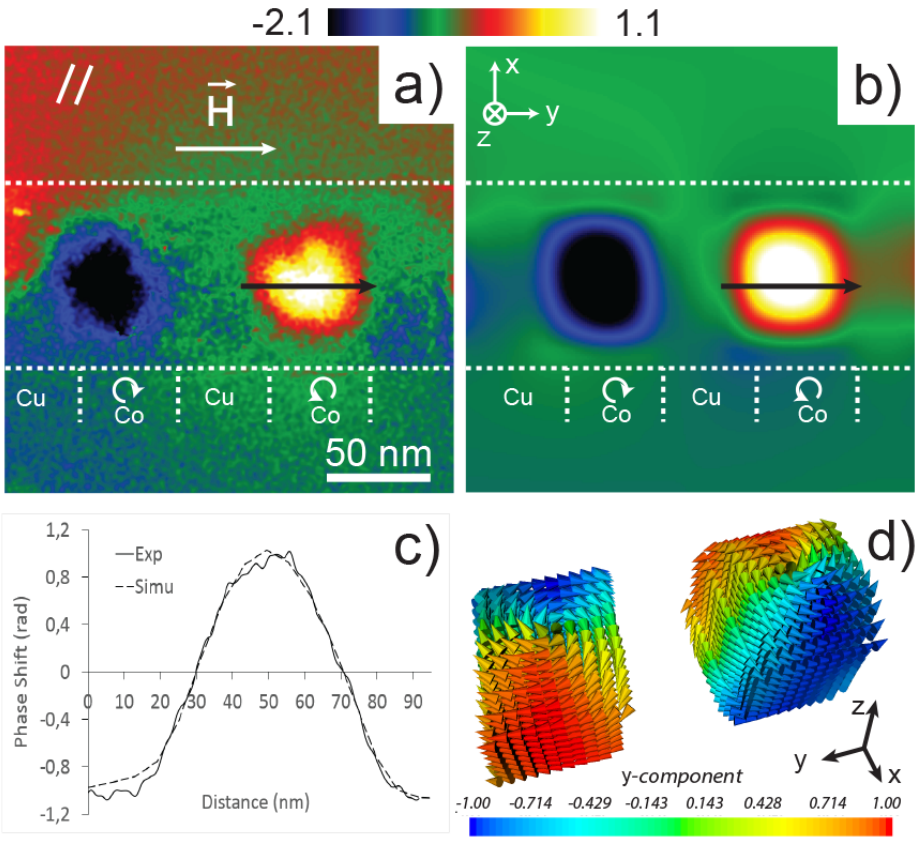

Figure 4.5.12. Configuration Co/Cu (50nm/50nm): a) Experimental magnetic phase shift map extracted from the holograms. b) Result of the simulated phase shift map. c) Comparison of the experimental and simulated profiles of the magnetic phase shift obtained along the arrows in a) and b). d) 3D magnetic configuration of the cobalt layers corresponding the simulated phase image in b).

Other typical features of the Co 50nm/Cu 50 nm system has been observed. Figure 4.5.13 presents the experimental and simulated phase shift maps for two coupled vortices with the core almost parallel to the wire axis. This NW has a lower diameter of 62nm ± 2 nm and confirms that for this diameter the coupled vortices with the core almost parallel to the wire axis are the most stable state. One of the vortices in the Figure 4.5.13 e) shows a tilt of the core respect to the wire axis: due to the direction of the anisotropy which is lying in a cone of 20° respect to the wire axis. The qualitative agreement between the profiles traced between the experimental and simulated phase maps is presented in Figure 4.5.13 d). A statistical analysis over 15 NWs (each of them composed in average by 6 parts) of the magnetic states present in this configuration shows that about 45% of the NWs present the coupled vortices with the core almost parallel to the wire axis while 55% of them have canted vortices.

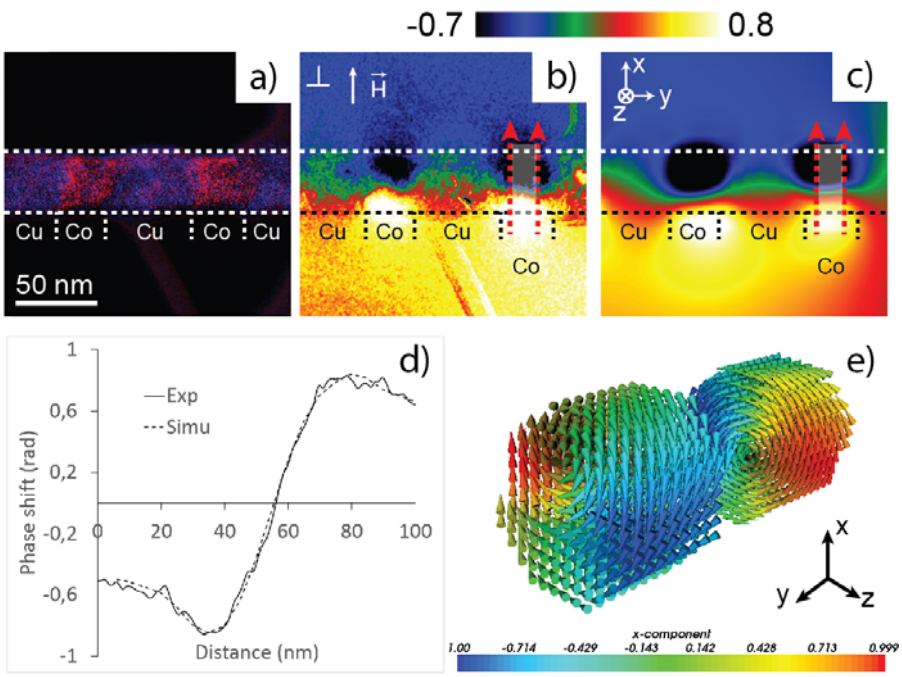

Figure 4.5.13. Configuration Co/Cu (50nm/50nm): a) EFTEM map for Co and Cu. b) Experimental magnetic phase shift map extracted from the holograms. c) Result of the simulated phase shift map. d) Comparison of the experimental and simulated profiles of the magnetic phase shift obtained along the rectangles in b) and c). e) 3D magnetic configuration of the cobalt layers corresponding the simulated phase image in c).

By calculating different micromagnetic configurations, it is possible to conclude that when a cone of an aperture larger than 45° is used for the magnetic anisotropy, the canted vortices with the core pointing perpendicular to the axis of the wires becomes more probable. The same happens with the increase of the diameter and the Co layer thickness.

The orientation of the vortex core is very sensitive to the Co thickness layer t_{Co}, for: $t_{Co} \geq 50\,nm$ more canted vortex states appears while $40\,nm \leq t_{Co} < 50\,nm$ vortices with the core aligned along the wire axis are more probable.

For vortices aligned along the wire axis, the magnetic coupling favours a parallel alignment of the cores. On the contrary, canted vortices are less sensitive to the coupling when their cores are oriented an angle >45° with respect to the wire axis. These vortex states present the core pointing in different orientations: along the wire for diameters between 50-60 nm and others lying in angles between 45° and 90° respect to the wire axis (70-90 nm). In particular, the values of magnetocrystalline anisotropy are in the range of $100 - 300 \times 10^3$ J/m^3. With an aperture of 30° respect to the axis for the magnetocrystalline anisotropy, most of the configurations can be achieved. The exchange constant and the magnetization of saturation were kept at 22×10^{-12} J/m and 1200×10^3 A/m ($\mu_0 M_s$ 1.5T) respectively as the previous cases for all the simulations performed in this 50nm/50nm configuration. Table 4.5.1 summarize the relation between the diameters, magnetic states and the magnetic anisotropy for the sample of Co 50nm/ Cu 50nm.

Table 4.5.1. Relation of diameters, magnetic states corresponding to the different magnetocrystalline anisotropy and the cone of aperture.

Co/Cu (nm/nm)	Diameter (nm)	Magnetic state	Magnetocrystalline anisotropy ($\times 10^3$ J/m^3)	Cone of random anisotropy (Degrees)
50/50	50-60	Coupled vortices (vortex core almost // to the wire axis)	100-130	20-30
	70-90	Canted vortices (vortex core almost ⊥ to the wire axis)	200-300	≥30

4.5.4 Co/Cu = 100nm/100nm

Figure 4.5.14 presents the reconstruction of two Co/Cu periods for a NW corresponding to the 100nm/100nm configuration. The PL and PP configuration do not seem to present changes between them and the integrated magnetization is oriented along the wire axis. The number of NWs selected for this thickness of Co/Cu (100nm/100nm) were around 120 NWs. From all these NWs just 18 NWs could result in a magnetic signal which can be used to study the magnetic states. For this system, 80% of the observed NWs present the same magnetic configuration as is shown in Figure 4.5.14 c) and Figure 4.5.14 d).

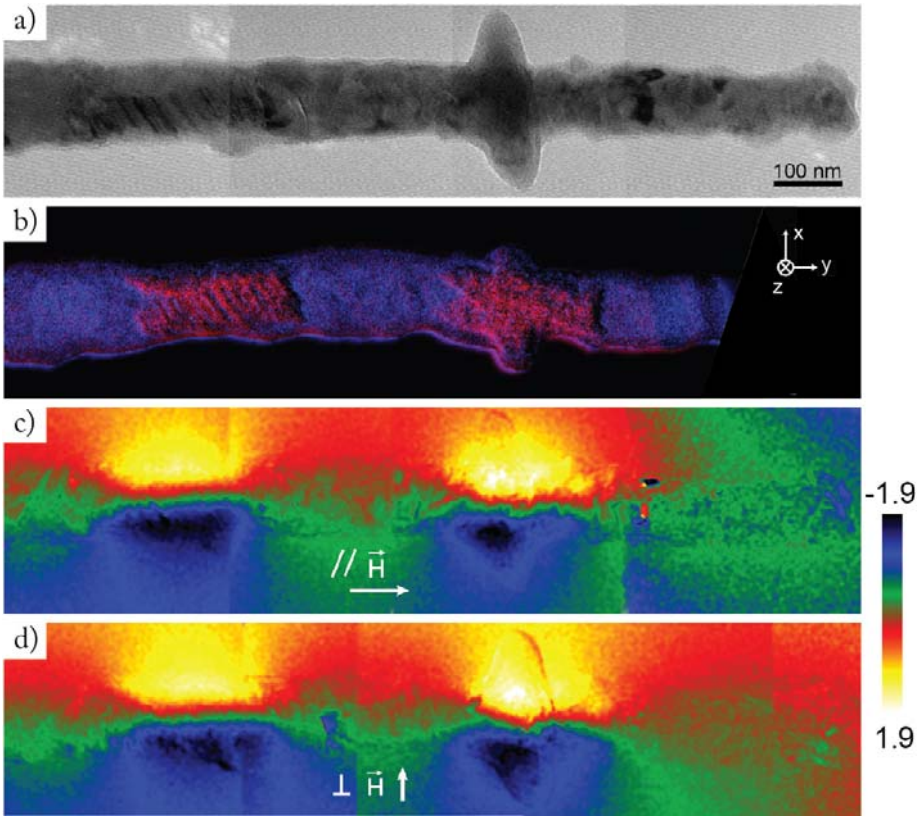

Figure 4.5.14. Reconstruction of a Co/Cu (100nm/100nm): a) hologram, b) EFTEM map, c) phase shift map for PL configuration and d) phase shift map for PP configuration.

A portion of the NW shown in the Figure 4.5.14 with a diameter of 65 ± 2nm is consigned in Figure 4.5.15. The two remnant configurations are showed: as said previously, no changes are present for the application of the magnetic field perpendicular and parallel to the wire axis. The two states present an integrated induction pointing along the wire axis. Such features in Figure 4.5.15 c) and Figure 4.5.15 d) could be characteristic of a monodomain state (uniform magnetization) or a vortex state along the wire axis.

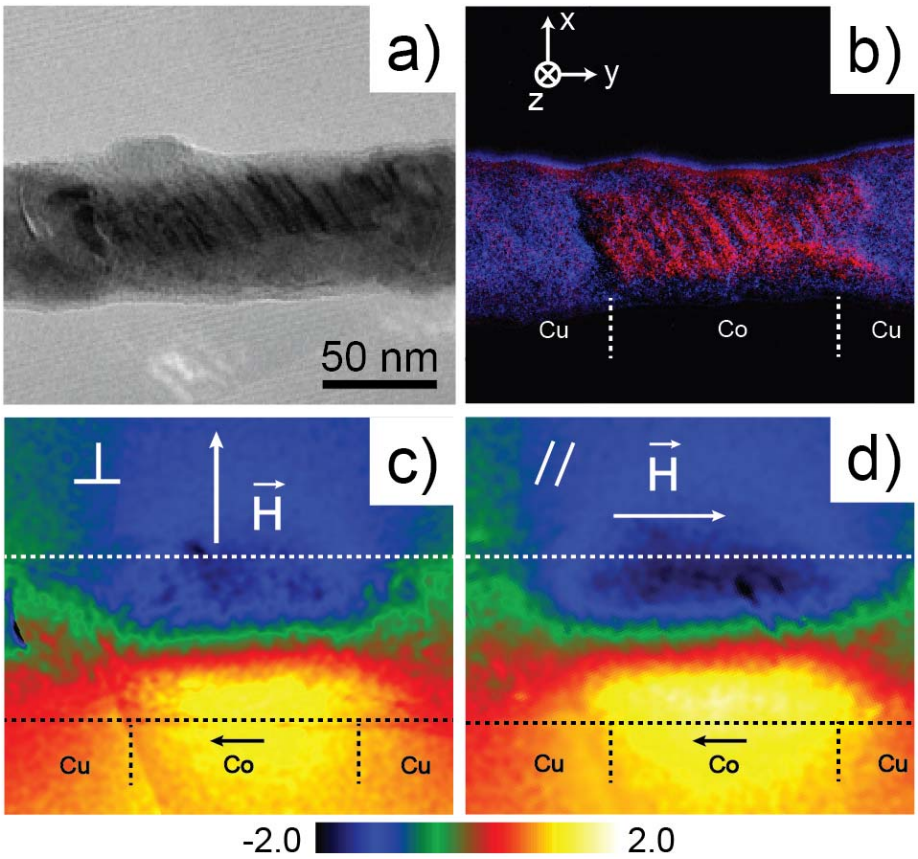

Figure 4.5.15. Nominal configuration Co/Cu 100nm/100nm: a) TEM image of the observed wire. b) EFTEM image of the same area to distinguish the copper (blue) and cobalt (red) layers. c) Magnetic phase shift map obtained after the application of the perpendicular saturation field with respect to the wire axis. d) Magnetic phase shift map obtained after the application of the saturation field parallel to the wire axis.

Using micromagnetic simulations, these phase shift maps can also be produced by three states: the monodomain-like state (all the magnetization oriented along the Y axis), vortices with the core pointing along the wire axis or with an angle between 0-30° and an intermedia state between these two. These three states are very close between then in terms of energy and the simulated phase shift maps looks very similar. These magnetic states can be only distinguished by a quantitative analysis of the phase shift as in the case of Co/Cu (25nm/15nm). Figure 4.5.16 shows the experimental and simulated phase shift maps. The quantitative and qualitative agreement on the experimental and simulated profiles traced along the rectangles in Figure 4.5.16 a) and

Figure 4.5.16 b) confirm that the vortex state is presented for this configuration. Figure 4.5.16 d) shows the 3D representation of the magnetization for this vortex state. The simulated vortex state corresponds to a magnetocrystalline anisotropy of 130×10^3 J/m^3 orientated at 20° with respect to the wire axis. It should be noticed that several periods of Co/Cu have been used for the micromagnetic simulations: some of the layers find their ground state in the vortex configuration, but others presents a monodomain-like state. The two states are possible by the random anisotropy, which favours the monodomain states for a cone of aperture of <15° respect to the wire axis and the vortex state for >15°.

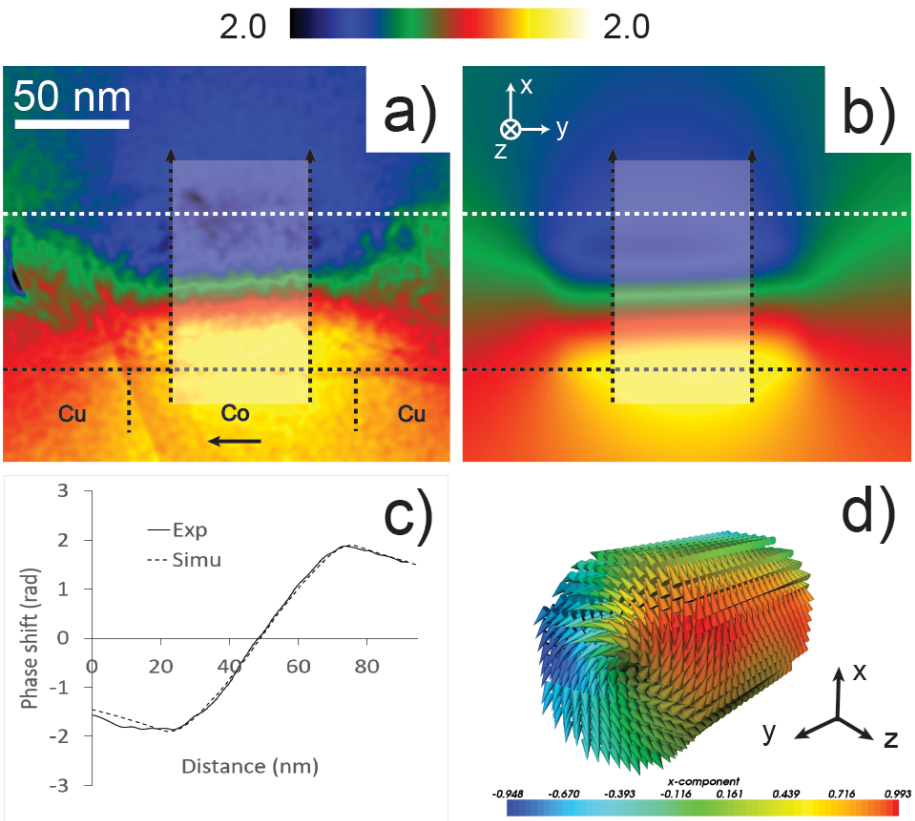

Figure 4.5.16. Configuration Co/Cu (100nm/100nm): a) Experimental magnetic phase shift map extracted from the holograms. b) Simulated phase shift map. c) Comparison of the experimental and simulated profiles of the magnetic phase shift obtained along the rectangles in a) and b). d) 3D magnetic configuration of the cobalt layers corresponding to the simulated phase image in b).

Another feature found in this thickness configuration (100nm/100nm) is a kind of "arc-shape" shown in the Figure 4.5.17 b). This phase shift map corresponds to a vortex state with the core tilted at certain angle between 10°-30° with respect to the wire axis. This produces a shift of the head and tail vortex core. In Figure 4.5.17 c), the simulated phase shift map is shown presenting a qualitative agreement with the experimental result. A phase shift profile is traced along the rectangles in Figure 4.5.17 b) and Figure 4.5.17 c) for the experimental and simulated phase shift map finding an excellent quantitative agreement between the simulated and experimental results. Figure 4.5.17 presents the 3D configuration for this vortex state with the core tilted 15° respect to the wire axis. Finally in Figure 4.5.17 f) a cross section view of the vortex is displayed, this view reveal the shape of the vortex core, an arc-shape is formed between the head and the tail of the core. These head and tail are shifted from the centre of the XZ plane. The difference between this state and the state shown in the Figure 4.5.16 is the shape of the vortex core. For the Figure 4.5.16 the vortex core form almost a line between the tail and the head of the core while the Figure 4.5.17 create an arc between them.

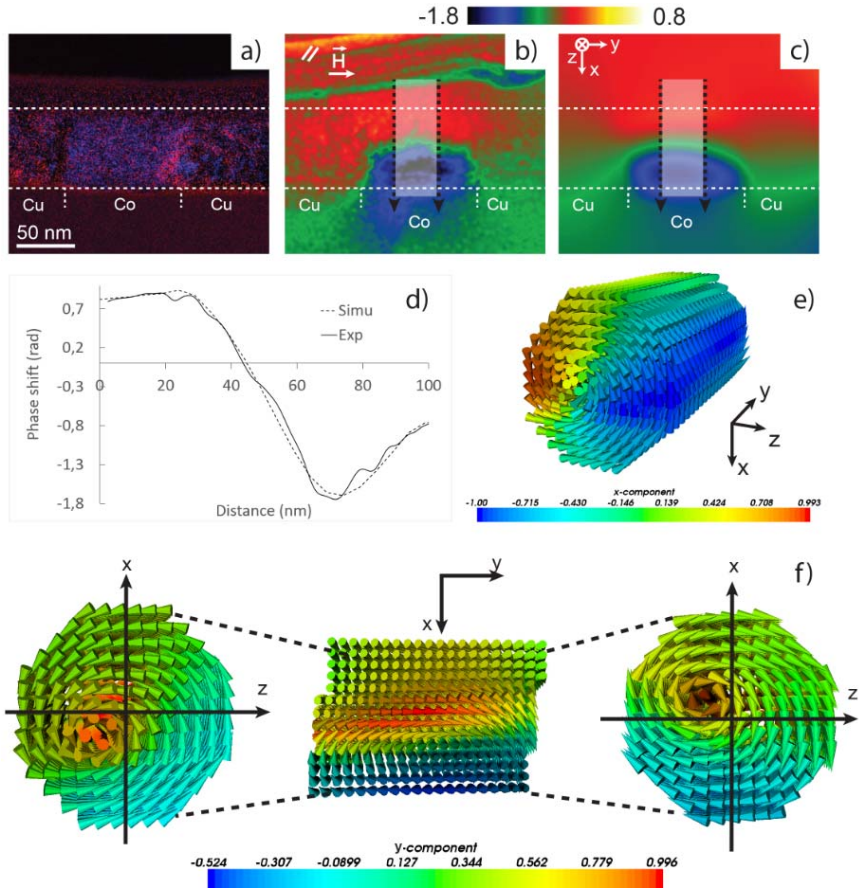

Figure 4.5.17. Configuration Co/Cu (100nm/100nm): a) EFTEM map for Co and Cu. b) Experimental magnetic phase shift map extracted from the holograms. c) Simulated phase shift map. d) Comparison of the experimental and simulated profiles of the magnetic phase shift obtained along the rectangles in b) and c). e) 3D magnetic configuration of the cobalt layers corresponding the simulated phase image in c). f) Cross section of the layer showing the vortex core and its arc-shape, also the views from the head and the tail of the vortex core are shown, revealing the tilted core.

With the increase of the diameter (>80nm) combining with a thickness < 100 nm in some Co layers (75-80 nm) the core of these vortex states is tilted higher angles (>45°) with respect to the wire axis until it produces a canted vortex as is shown in Figure 4.5.18 b) for a NW of 90 ± 2 nm in diameter. These circular features can be produced for the same magnetocrystalline anisotropy (130×10^3 J/m^3) and a cone of aperture of 20°. Thus, the effect of the rotation of the core vortex occurs with an increase of diameter and a change of direction of the shape anisotropy of the Co layer. The

qualitative and quantitative analysis of such a circular feature by micromagnetic simulations reveal that it corresponds to canted vortex with the core pointing to an intermedia direction between the X and Z axis. This core is tilted 45° respect to the wire axis. In the 3D representation of the micromagnetic simulation can be seen the canted vortex (Figure 4.5.18 e)). Also, some cross sections along the Z direction are shown to illustrate the tilted core of the vortex. About 20% of the NWs for this configuration present these canted vortices.

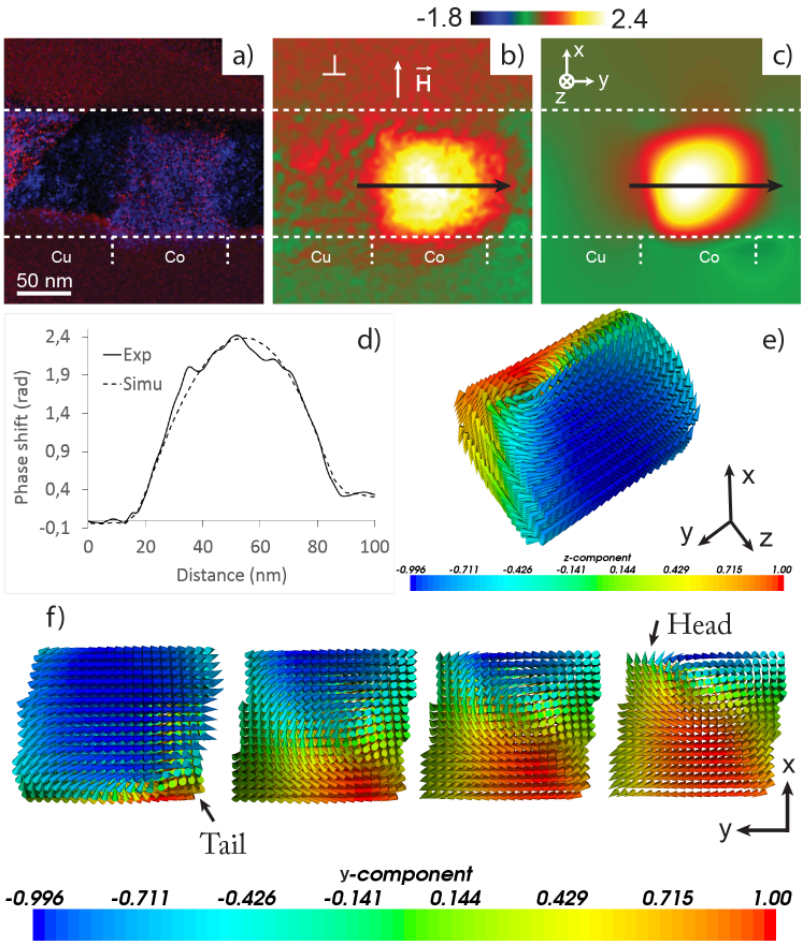

Figure 4.5.18. Configuration Co/Cu (100nm/100nm): a) EFTEM map for Co and Cu. b) Experimental magnetic phase shift map extracted from the holograms. c) Simulated phase shift map. d) Comparison of the experimental and simulated profiles of the magnetic phase shift obtained along the arrows in b) and c). e) 3D magnetic configuration of the cobalt layers corresponding the simulated phase image in c). f) Cross sections along Z direction, showing the tilt of the core, the head and the tail of the core are shown.

4.5.5 Summary of magnetic states

While some NWs show a transition from antiparallel to vortices when changing from PL to PP, a majority of layers always exhibit the same remnant state, which can be either antiparallel coupling, a mixture of antiparallel and vortex or monodomain. These different behaviours can be explained by the competition between the different magnetic interactions. Typically in a single magnetic disk [55], with different diameter and thickness, one could expect vortex, out-of-plane or in-plane magnetization. In the case of multilayers, the dipolar coupling plays a crucial role. To explain fully every magnetic configuration, one should conduct a full micromagnetic analysis to get the phase diagram of the magnetic states versus the amplitude and direction of the anisotropy. Even if this is far beyond the scope of this work, we are able to give some limiting cases depending on the magnetic behaviour observed. For this purpose in the next section, micromagnetic simulations are performed to construct phase diagrams corresponding to these limit cases.

Table 4.5.2 shows a summary of the magnetization orientations for each configuration (PP or PL) of the applied magnetic field and for each nominal thickness of the Co/Cu NWs. These magnetic states were determined from the EH experiments after the analysis of about 20 NW for each nominal thickness. Some of these configurations were taken into account but not presented in figures. We can observe that most of the configurations remain almost unchanged at least for a qualitative point of view. Thus we insist on the importance to perform micromagnetic simulations to obtain the 3D configuration corresponding to the phase shift maps resulting from the integration of the induction along the observation axis.

Table 4.5.2. Summary of the different magnetic states observed boy EH for the different Co/Cu configurations.

Co/Cu Configuration (nm/nm)	Magnetic field applied perpendicular (⊥) or parallel (//)	Magnetization orientation	
25/15	⊥	Antiparallel to the wire axis	⇧⇩⇧⇩
	//	Along the wire axis	➡ ➡
	//, ⊥	Along the wire axis	➡ ➡
25/45	//, ⊥	Antiparallel to the wire axis	⇧⇩⇧⇩
	//, ⊥	Along the wire axis	➡ ➡
	//, ⊥	Rotating in the XZ plane	↻
50/50	//, ⊥	Along the wire axis	➡ ➡
	//, ⊥	Rotating in the XZ plane	↻
	//, ⊥	Mixture of the two previous states	➡ ↻
100/100	//, ⊥	Along the wire axis	➡ ➡
	//, ⊥	Rotating in the XZ plane	↻

From the micromagnetic simulations, the magnetic states corresponding to the orientations of the magnetization were revealed. The magnetization of saturation was kept constant and the exchange constant was changed in some cases to control the size of the vortex core and the amplitude of the phase shift. The main parameter to be changed is the magnitude and orientation of the magnetocrystalline anisotropy to obtain the different magnetic states. Table 4.5.3 present the magnetic states for each

configuration, the magnetocrystalline anisotropy and its orientation obtained from the simulations which have the best match with the experimental results.

Table 4.5.3. Magnetic states and parameters for Co/Cu multilayered NWS

Co/Cu (nm/nm)	Magnetic field	Magnetic state	Magnetocrystalline anisotropy ($\times 10^3$ J/m^3)	Cone of random anisotropy (Degrees)
25/15	⊥	Antiparallel	180	40
	//	Vortex (core along the wire axis)	100	20
	//, ⊥	Monodomain-like	200	20
25/45	//, ⊥	Antiparallel-vortex	100	≥30
	//, ⊥	Vortex (core along the wire axis)	<100	20
	//, ⊥	Vortex core tilted	130	30
50/50	//, ⊥	Vortex (core along the wire axis)	100-130	30
	//, ⊥	Vortex core tilted 90°	200-300	≥30
100/100	//, ⊥	Monodomain-like	130	20
	//, ⊥	Vortex (core along the wire axis)	130	20
	//, ⊥	Vortex core tilted 90°	130	20

4.6 Magnetic properties of Co nanocylinders

As we discuss in chapter 1, cylindrical multilayered nanowires are composed of several periods of magnetic/non-magnetic layers. The magnetic layers can be assumed as small cylinders separated by a distance determined by the non-magnetic layer. For this cylinder, there are three main configurations: out-of-plane, in-plane and vortices

states (Figure 4.6.1). These three configurations will be determined by the shape anisotropy and the exchange energy, the crystalline anisotropy and the external magnetic field applied. In order to place the different configurations with the different thicknesses and diameters than we can find in our Co/Cu system, we have constructed a phase diagram as a result of simulated isolated Co nanocylinders for different thicknesses and diameters.

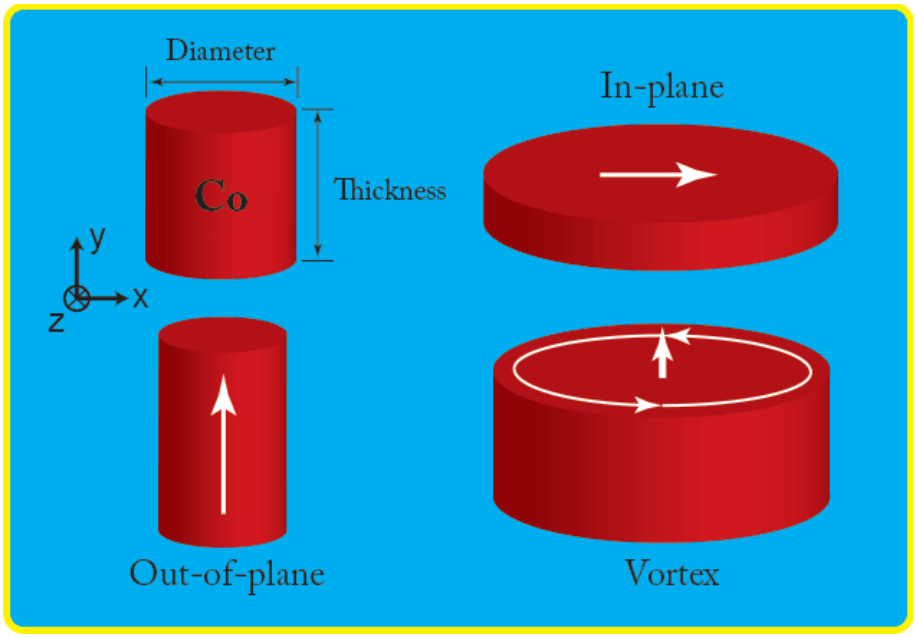

Figure 4.6.1. Co nanocylinder: reference axis and the three main magnetic configurations: in-plane, out-of-plane and vortex.

The magnetic ground states of isolated Co nanocylinders were calculated using OOMMF [56]. The material parameters used were: the saturation magnetization $M_S = 1200 \times 10^3$ A/m (the same used for the calculation of Co/Cu multilayered NWs), the exchange stiffness constant $A = 22 \times 10^{-12}$ J/m and the crystalline anisotropy. The last one was set to 0 in a first trial in order to have a reference phase diagram and then was changed to 100×10^3 J/m^3 which is the value in which most of the remnant magnetic states can be reproduced. Two limit cases were conducted for the direction of

the magnetocrystalline anisotropy: "parallel" (with 20° respect to the wire axis) and "perpendicular" (80° respect to the wire axis). We have chosen these values because 20° is the most common case where the magnetic anisotropy is lying almost parallel to the wire axis, and it can have angles between 0°-20° and 80° give us the possibility to have angles near to 90° where the antiparallel coupling is presented for some of the configurations. The unit cell size for the three-dimensional simulation was $1\text{nm} \times 1\text{nm} \times 1\text{nm}$ which is much smaller than the exchange length $l_{ex} = \sqrt{2A/\mu_0 M_S^2} = 4.9\text{nm}$ for the cobalt in the case of this work.

Micromagnetic calculations were carried out using different initial states. For each nanocylinder geometry, separate energy minimizations were carried out starting from out-of-plane-like, in-plane-like, vortex-like and random magnetization initial states. In each case, the initial states were constructed slightly asymmetric to avoid metastable states. The ground state phase diagram was determined by selecting the state with the smallest energy.

Figure 4.6.2 shows the magnetic ground state phase diagram of Co nanocylinders as a function of the cylinder diameter and thickness derived from the micromagnetic simulation results. In this case the magnetocrystalline anisotropy H_k and the applied magnetic field $|\vec{H}|$ are zero. The phase diagram presents three phases: the in-plane (I), out-of-plane (O), and the vortex state (V). The approximate phase boundaries are delimited by a solid line. The color zones correspond to the normalized Y component of the magnetization (M_y) equivalent to the out-of-plane component (parallel to the wire axis of the cylinder). We can observe that the in-plane phase has $M_y \approx 0$, and the out-of-plane has $M_y \approx 1$. The vortex phase shows decreasing M_y with increasing diameter. The triple point where the three phases coexist corresponds to a diameter of $\approx 37\text{nm}$ and a thickness of $\approx 37\text{nm}$. Regarding M_y, the transition between

the regions is not totally abrupt allowing some intermedia magnetic states between two regions.

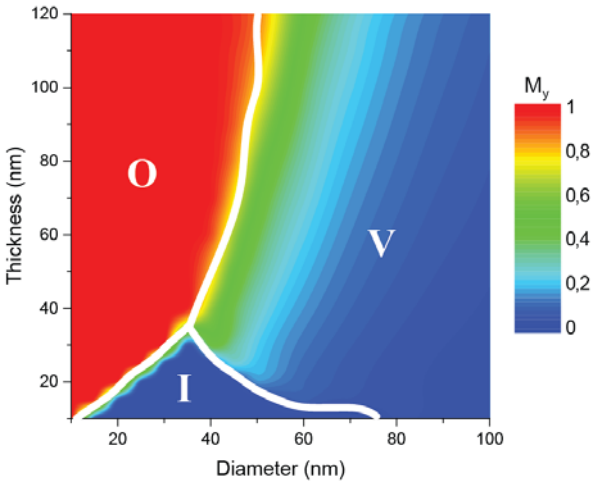

Figure 4.6.2. Nanocylinder magnetic state phase diagram derived from micromagnetic simulations as a function of the thickness and diameter for a magnetic field and magnetocrystalline anisotropy equal to zero. In colour scale the magnetization along the Y component. In dotted line, the main boundaries for the out-of-plane (O), in-plane (I) and vortex (V) states are delimited.

Proceeding with the first limit case where the magnetization lies in a cone of aperture near an angle of 20°, the magnetocrystalline anisotropy was set to $100 \times 10^3\ \mathrm{J/m^3}$. In the first instance, the applied magnetic field was set to zero.

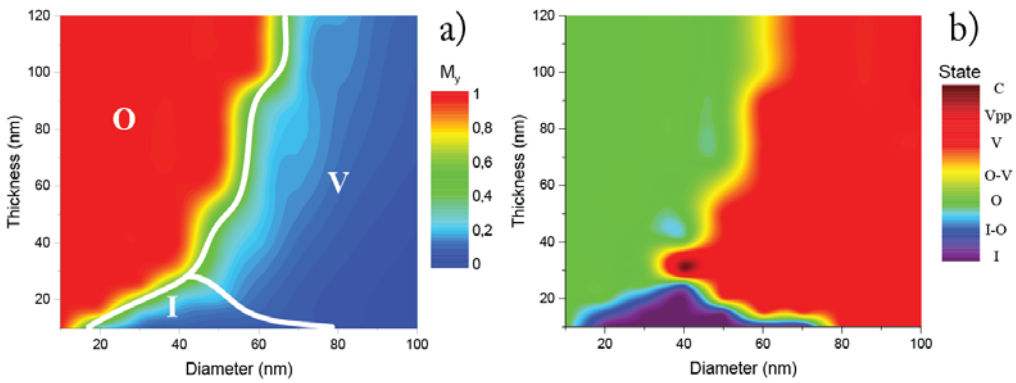

Figure 4.6.3. Phase diagram for Co nanocylinders with a magnetocrystalline anisotropy of $100 \times 10^3\ \mathrm{J/m^3}$ *oriented 20° respect to the wire axis and absence of a magnetic field: a) Colour representation with the Y component of the magnetization, b) Colour representation of the main magnetic states and intermedia states.*

From the phase diagrams of the Figure 4.6.3 we can deduce two important things:

- The reduction of the in-plane (I) and the increase of the out-of-plane areas with respect to the phase diagram without magnetocrystalline anisotropy. This is expected due to the orientation of the magnetocrystalline anisotropy (almost parallel to the axis of the wire).
- The apparition of intermedia states as we can notice from the phase diagram in Figure 4.6.3 b) where the different magnetic states are displayed. These intermedia states are:
    - *"I-O"*: This state is a transition between the in-plane state and the out-of-plane state, the magnetization is typically aligned in 45° respect to the wire axis.
    - *"O-V"*: Is a mixture of the out-of-plane and vortices states. The magnetization is rotating along the wire axis in a kind of spiral.
    - *"Vpp"*: Configuration obtained when the vortices have the core pointing perpendicular to the axis of the wire.
    - *"C"*: A less common state in which the part of the magnetization is forming a "C" shape and the other is in an intermedia state between the in-plane and out-of-plane, this states was commonly found near to the triple point.

In Figure 4.6.4, the phase diagrams at the remnant state as a function of the thickness and diameter for Co nanocylinders with a magnetic anisotropy of 100×10^3 J/m^3 lying an angle of 20° with respect to the wire axis and <u>with an applied magnetic field</u> are shown. Figure 4.6.4 a) and Figure 4.6.4 b) correspond to the PL configuration where a magnetic field has been applied parallel to the wire axis. Figure

4.6.4 c) and Figure 4.6.4 d) correspond to the PP configuration with a magnetic field applied perpendicular to the wire axis.

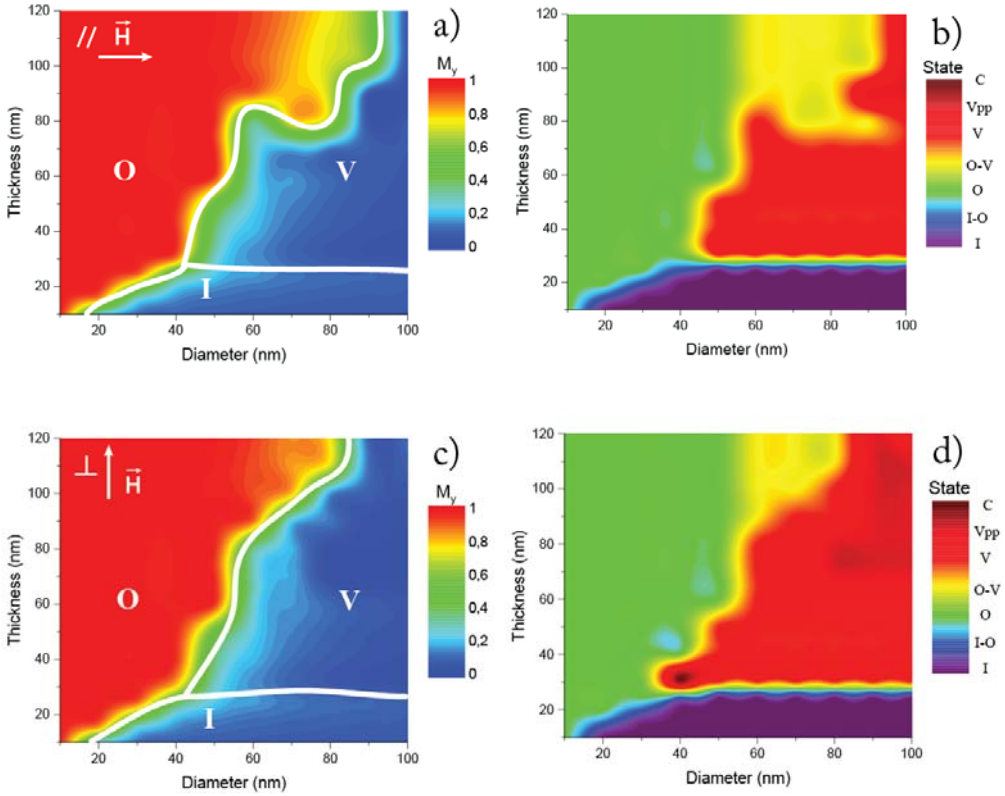

Figure 4.6.4. Phase diagrams for Co nanocylinders with an anisotropy of $100 \times 10^3\ J/m^3$ *lying 20° respect to the wire axis: a) Phase diagram as a function of the thickness and diameter of the cylinders for the PL configuration (colour scale M_y component of the magnetization), b) Phase diagram displaying the different main and intermedia states for the PL configuration, c) Phase diagram as a function of the thickness and diameter of the cylinders for the PP configuration (colour scale M_y component of the magnetization), d) Phase diagram displaying the different main and intermedia states for the PP configuration.*

In Figure 4.6.4 a) and Figure 4.6.4 b) (PL configuration), the out-of-plane area (O) area is increasing for thickness above *80 nm* and diameters larger than *50 nm* with respect to the phase diagram where no magnetic field is applied. A similar situation occurs with the in-plane (I) zone for diameters >*50 nm*. From Figure 4.6.4 c) and Figure 4.6.4 d), the in-plane zone also increases as in the Figure 4.6.4 a) but the increment of the out-of-plane area is less drastic than in the Figure 4.6.4 a) for the PL configuration.

It is important to note that the in-plane zone for both configurations of the magnetic field is almost the same. Another important fact in the Figure 4.6.4 d) is the apparition of a zone corresponding to the vortex state with the core pointing perpendicular to the wire axis (red-dark zone) for diameters >*80 nm* and thickness >*70 nm*.

On the other side the magnetic states when the magnetocrystalline anisotropy is oriented almost perpendicular to the wire axis ($H_k = 100 \times 10^3\ \mathrm{J/m^3}$ oriented 80°) are calculated. In Figure 4.6.5, the phase diagrams show the main ground-states and the intermedia states for Co nanocylinders for the anisotropy direction above mentioned and <u>without any magnetic field applied</u>.

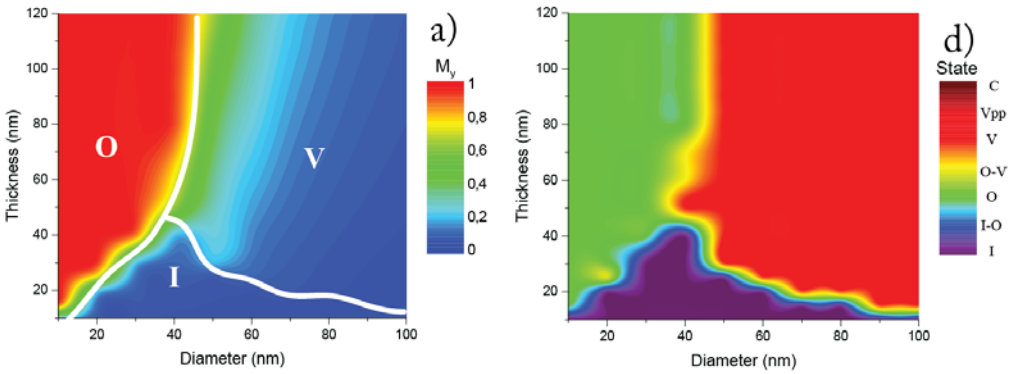

Figure 4.6.5. Phase diagram for Co nanocylinders with a magnetocrystalline anisotropy of $100 \times 10^3\ J/m^3$ *oriented 80° respect to the wire axis and absence of a magnetic field: a) Colour representation with the Y component of the magnetization, b) Colour representation of the main magnetic states and intermedia states.*

From Figure 4.6.5, we note an increment of the in-plane area for diameters in the range of *30-50 nm*. The vortex zone is also increased with respect to the previous phase diagrams while the out-of-plane zone is reducing respect to the crystalline anisotropy oriented 20° respect to the wire axis.

The resulting phase diagrams <u>when a magnetic field is applied parallel and perpendicular to the wire axis</u> in nanocylinders with the magnetocrystalline anisotropy $H_k = 100 \times 10^3\ \mathrm{J/m^3}$ oriented 80° respect to the wire axis are presented in the Figure

4.6.5. A strong increase of the in-plane areas for both directions of the magnetic field can be observed. This kind of behaviour is expected due to the orientation of the magnetocrystalline anisotropy (80° respect to the wire axis). For the PL configuration, the transition between out-of-plane state and the vortex state (O-V) is wider than the PP configuration. Something important to notice is the red-dark area in the Figure 4.6.6 d), this corresponds to the *"Vpp"* state. These canted vortices appear for diameters and thickness smaller than when the magnetocrystalline anisotropy is lying 20° respect to the wire axis.

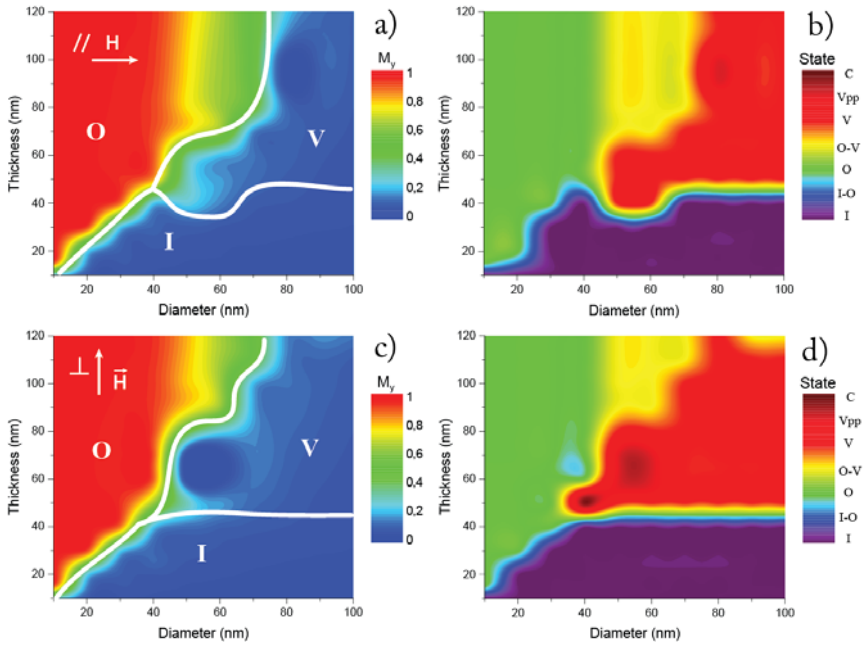

Figure 4.6.6. Phase diagrams for Co nanocylinders with an anisotropy of $100 \times 10^3\ J/m^3$ *lying 80° respect to the wire axis: a) Phase diagram as a function of the thickness and diameter of the cylinders for the PL configuration (colour scale* M_y *component of the magnetization), b) Phase diagram displaying the different main and intermedia states for the PL configuration, c) Phase diagram as a function of the thickness and diameter of the cylinders for the PP configuration (colour scale* M_y *component of the magnetization), d) Phase diagram displaying the different main and intermedia states for the PP configuration.*

4.7 Relation between magnetic states in Co/Cu NWs and Co nanocylinders phase diagrams

A simple but carefully analysis of the experimental results with the micromagnetic simulations of multilayered Co/Cu nanowires and Co nanocylinders can be done. We have to take into account the two limit cases where the magnetocrystalline anisotropy lies at 20° and 80° with respect to the wire axis but also consider the effect of the dipolar coupling of the layers which can affect the remnant magnetic state in some of the configurations.

4.7.1 Co/Cu = 25nm/15nm

For this configuration, we obtained three states: antiparallel coupling, coupled vortices with the core oriented along the wire axis and monodomain-like state. Regarding the phase diagram where the magnetocrystalline anisotropy is oriented at 20° with respect to the wire axis (Figure 4.6.4) for diameters between 40-100 nm and thickness of 25 nm, the in-plane and vortex states are very close: the antiparallel coupling and the vortex state can be obtained for a small change in the thickness. An important check on the proximity on the energy values between the antiparallel (AP) and vortex state was made obtaining close values between this two states. For example for Co nanocylinders of *60 nm* in diameter and thickness of *25 nm* the energy for the remnant magnetic in-plane state is 2.06×10^{-17}J while for the same diameter and a thickness of *30 nm* the energy corresponding to a vortex state is 1.92×10^{-17}J. As we described previously the transition between the AP state and the V state can be achieved for a magnetocrystalline anisotropy of $H_k = 180 \times 10^3$ J/m^3 in a cone of aperture of 40°.

The in-plane state which corresponds to the antiparallel state increases its area in the phase diagram when the magnetocrystalline anisotropy changes from 20-80°

respect to the wire axis. This confirms that these two states should be in a cone >20° of aperture to obtain a transition between them.

The monodomain-like state is obtained for a higher anisotropy ($H_k = 200 \times 10^3\ \mathrm{J/m^3}$) which is not shown in the phase diagrams. Regarding the two limit cases, this state can be obtained because a higher value of the anisotropy in a 20° of aperture is enough to increase the out-of-plane behaviour until the values of diameters found here (≈64nm).

4.7.2 Co/Cu = 25nm/45nm

The change in the remnant magnetic states with respect to the orientation of the magnetic field applied to this configuration is not significant.

Regarding the position of this configuration in the phase diagram (the same as for 25nm/15nm), we can confirm that the mixtures of in-plane and vortex states are reasonable due to the proximity to the transition region between these two states. The difference between these configurations is discriminated by the thickness of the Cu layer. In this configuration, this Cu thickness layer is the triple than for the 25nm/15nm configuration that the Co layers can thus be less affected by the dipolar coupling resulting in a diversity of remnant magnetic states where just a couple of layers are coupled.

4.7.3 Co/Cu = 50nm/50nm

For this configuration, a variety of vortex states with the core pointing in several orientations is obtained. The comparison between the phase diagram and this configuration is logic because the vortex state is the dominant magnetic state for this thickness. An important difference between the PL and PP configuration is not found as easily confirmed by the phase diagram. The main difference between the magnetic

states along the layers of the NWs are the orientation of vortex core. This vortex core orientation is defined by the magnetocrystalline anisotropy orientation, the dipolar coupling and the tilted layers. A vortex with the core along almost the wire axis has an energy very close to one with the core pointing perpendicular to the wire axis. It should be noted that the dipolar coupling acts in wires with diameters between *50-60 nm* and thickness layer of Cu <*50nm* producing coupled vortices with the core aligned parallel to the wire axis (Figure 4.5.13). For Cu thickness >*50nm* the dipolar coupling is weak and the core of the vortices has a bigger probability of forming canted vortex uncoupled (Figure 4.5.12).

4.7.4 Co/Cu = 100nm/100nm

The remnant magnetic states for this configuration are: mainly vortices with the core almost parallel to the wire axis, and some canted vortices with the core perpendicular to the wire axis (*Vpp* state). The phase diagram in the Figure 4.6.4 b) and Figure 4.6.4 c) show that both states are possible. The canted vortices are found when the diameters are >*80nm*. This *Vpp* state is also deducted from the phase diagram: for NWs with a diameter >*80 nm* and thickness between *70-120 nm* (Figure 4.6.4 d)). The coupling between the layers is not present due to the large thickness of the Cu layers. Therefore each layer acts a small cylinder as in the phase diagram.

As our systems have a wide variety of diameters, thickness in Cu and Co layers, we will discuss the case when one of these parameters is constant and try to observe how the magnetic states change with the others. The following observations were made as a combination of the experimental results and the micromagnetic simulations.

4.8 Aspect ratio and influence of the diameter and thickness on the magnetic states

When the diameter remains constant and we observe the magnetic states along the different configurations, we found some similarities and differences. It is important to have in mind the importance of the aspect ratio between the Co layer thickness and the diameter (t_{Co}/d). For the configurations 25nm/15nm and 25nm/45nm, taken as a reference, the range of diameters is found between 50nm and 90nm. These systems present aspect ratios ≤ 0.5 and it is expected that the shape anisotropy of each Co layer is oriented perpendicular to the wire axis. Thus the inclusion of the uniaxial anisotropy lying at an angle <90° respect to the wire axis is a source of competition of energy. These two systems present antiparallel coupling and vortices states with the core almost parallel to the wire axis. The antiparallel coupling can be explained by the shape anisotropy which is reflected in the phase diagrams for Co nanocylinders. The vortex state with the core lying along the wire axis or almost parallel to this, for the diameters found, is a reflection of the small changes in the Co layer. With small changes in the Co layer for constant diameters, the magnetic state can pass easily from in-plane state to a vortex state. For Co thickness larger than 30 nm the vortex state is more probable, but, for thickness below 25 nm, the in-plane state is the predominate one (for a uniaxial anisotropy nearly lying along the wire axis).

It should be noted that the nominal Co thickness of 25 nm is very close to the transition area between the in-plane and the out-of-plane state when the magnetocrystalline anisotropy is oriented along the wire axis or with an angle ≈ 30°. The transition of magnetic states in these systems can be done by the influence of a magnetic field as we observed from the antiparallel (magnetic field applied perpendicular to the wire axis) to the vortex state (magnetic field applied parallel to the wire axis). The

magnetic field is another source of energy which competes with the magnetic anisotropy and the shape anisotropy as we discussed in the chapter 1. This is not the case for a magnetic anisotropy oriented perpendicular or nearly perpendicular to the wire axis, in which, the in-plane magnetic state is the most stable energetically as we can see in the phase diagrams of the Figure 4.6.6.

If the Co layer increases until 50 nm for the range of diameter studied, the aspect ratio of these layers will be between 1 and 0.5. This fact suggests that the shape anisotropy will have different preferential orientations, either parallel to the wire axis or perpendicular to this. For diameters of 50 nm, the magnetic states of these layers will be dominated mainly by the magnetocrystalline anisotropy and the magnetic field applied parallel or perpendicular to the wire axis resulting in a vortex state. For diameters >50 nm, the shape anisotropy of the layer is oriented perpendicular to the wire axis and enter to compete with the uniaxial anisotropy and the magnetic field. Only vortex states are obtained for thickness of 50 nm and different diameters. Changes of ± 10 nm on the Co thickness do not produce a change of magnetic state, but it can create changes in the orientation of the vortex core.

Concerning to the 100nm/100nm configuration, the aspect ratio is between 1 and 2, which stabilizes a shape anisotropy along the wire axis. If we consider changes in the Co thickness at 50 nm of diameter, the out-of-plane magnetic state is produced no matter what the magnetic field applied and/or the direction of the magnetic anisotropy, as we can see in the Figure 4.6.4 and Figure 4.6.6. Also, the EH experiments confirm these conclusions. If we increase the diameter to 70 nm for example, the Co thickness is of great importance: for this diameter, we are close to the transition area between the vortex state and the out-of-plane state. This is mostly relevant if the magnetic field is applied perpendicular to the wire. So a small change of ± 5 nm is enough to change from

out-of-plane to vortex state, or a mixture between the two. For bigger diameters ≥ 80 nm, the vortex state is the most probable state. From an energetic point of view, the competition between the shape anisotropy, the magnetic field and magnetocrystalline anisotropy favour this magnetic vortex structure. We could confirm that the core of the vortex is tilted 45°-90° respect to the wire axis for diameters ≥80 nm. The vortex state for this aspect ratios has been reported by several authors using phase diagrams at remnant state [55], [57]–[59].

Our system allows the possibility of tuning different parameters as the Co thickness and the diameter of our NW, which change the aspect ratio and produces different magnetic states as we saw previously. This aspect ratio determines the orientation of the shape anisotropy of the Co layers. The study of electrodeposited cylinder arrays (composed of Ni, Co, CoP or CoNi) was performed by Ross et al. [60] who found the three main states and, with different aspect ratios, could build the phase diagram for this system. Metlov et al. [58] performed an analytical study of the metastable regions for magnetic nanocylinders. They found the different combinations of states that coexist near to the transition areas between magnetic states. An important fact is the inclusion of a "*c*" state which was found also in our study in the section 0. Chung et al. [55] reported the phase diagram of permalloy nanocylinders. They found vortices states where the vortex core was shifted respect to the cylinder axis as in our work. They discuss that the transitions between two magnetic states are not sharped and that exist metastable regions where two magnetic states can exist. An important fact should be mentioned with respect to nanocylinders of diameter >200 nm Prejbeanu [61], Cimpoesu [62] and their teams found the apparition of a double vortex for particles of cylindrical shape for in the range of 200-500 nm. For another hand Novais et al. [59] present two important states detailed in this thesis: the vortex-out-of-plane state which

is a mixture of this two states near to their transition area, and the vortex with the core canted 90° respect to the wire axis.

Magnetic properties of Co nanocylinders can be applied to Co based multilayers in which the Co layers are separate by a non-magnetic material. The competition of the different energy sources produces different magnetic states. These can be deduced from the properties of these Co nanocylinders. Also, the dipolar coupling plays an important role in the final magnetic state. Thus each one of this energy sources should be studied and analysed in detail.

References

[1] S. H. Charap, P.-L. Lu, and Y. He, "Thermal stability of recorded information at high densities," *Magn. IEEE Trans. On*, vol. 33, no. 1, pp. 978–983, 1997.

[2] R. F. L. Evans, R. W. Chantrell, U. Nowak, A. Lyberatos, and H.-J. Richter, "Thermally induced error: Density limit for magnetic data storage," *Appl. Phys. Lett.*, vol. 100, no. 10, p. 102402, 2012.

[3] "Sony creates an 185TB tape cartridge!," *StorageServers*, 01-May-2014. .

[4] "FujiFilm achieves 154TB data storage record on Tape," *StorageServers*, 20-May-2014. .

[5] Y. Henry, K. Ounadjela, L. Piraux, S. Dubois, J.-M. George, and J.-L. Duvail, "Magnetic anisotropy and domain patterns in electrodeposited cobalt nanowires," *Eur. Phys. J. B-Condens. Matter Complex Syst.*, vol. 20, no. 1, pp. 35–54, 2001.

[6] L. G. Vivas, J. Escrig, D. G. Trabada, G. A. Badini-Confalonieri, and M. Vázquez, "Magnetic anisotropy in ordered textured Co nanowires," *Appl. Phys. Lett.*, vol. 100, no. 25, p. 252405, 2012.

[7] Y. P. Ivanov, L. G. Vivas, A. Asenjo, A. Chuvilin, O. Chubykalo-fesenko, and M. Vázquez, "Magnetic structure of a single-crystal hcp electrodeposited cobalt nanowire," *EPL Europhys. Lett.*, vol. 102, no. 1, p. 17009, Apr. 2013.

[8] J. Cantu-Valle *et al.*, "Mapping the magnetic and crystal structure in cobalt nanowires," *J. Appl. Phys.*, vol. 118, no. 2, p. 24302, Jul. 2015.

[9] G. Bergmann, J. G. Lu, Y. Tao, and R. S. Thompson, "Frustrated magnetization in Co nanowires: Competition between crystal anisotropy and demagnetization energy," *Phys. Rev. B*, vol. 77, no. 5, Feb. 2008.

[10] N. A. Usov, A. Zhukov, and J. Gonzalez, "Remanent Magnetization States in Soft Magnetic Nanowires," *IEEE Trans. Magn.*, vol. 42, no. 10, pp. 3063–3065, Oct. 2006.

[11] K. He, D. J. Smith, and M. R. McCartney, "Observation of asymmetrical pinning of domain walls in notched Permalloy nanowires using electron holography," *Appl. Phys. Lett.*, vol. 95, no. 18, p. 182507, 2009.

[12] H. Forster *et al.*, "Domain wall motion in nanowires using moving grids (invited)," *J. Appl. Phys.*, vol. 91, no. 10, p. 6914, 2002.

[13] B. Hillebrands and A. Thiaville, Eds., *Spin dynamics in confined magnetic structures III*. Berlin ; New York: Springer, 2006.

[14] N. Biziere, C. Gatel, R. Lassalle-Balier, M. C. Clochard, J. E. Wegrowe, and E. Snoeck, "Imaging the fine structure of a magnetic domain wall in a Ni nanocylinder," *Nano Lett.*, vol. 13, no. 5, pp. 2053–2057, 2013.

[15] M. Yan, A. Kákay, S. Gliga, and R. Hertel, "Beating the Walker Limit with Massless Domain Walls in Cylindrical Nanowires," *Phys. Rev. Lett.*, vol. 104, no. 5, Feb. 2010.

[16] N. L. Schryer, "The motion of 180° domain walls in uniform dc magnetic fields," *J. Appl. Phys.*, vol. 45, no. 12, p. 5406, 1974.

[17] M. Hayashi, L. Thomas, C. Rettner, R. Moriya, and S. S. P. Parkin, "Direct observation of the coherent precession of magnetic domain walls propagating along permalloy nanowires," *Nat. Phys.*, vol. 3, no. 1, pp. 21–25, Jan. 2007.

[18] S. Da Col *et al.*, "Observation of Bloch-point domain walls in cylindrical magnetic nanowires," *Phys. Rev. B*, vol. 89, no. 18, May 2014.

[19] C. Beeli, B. Doudin, J.-P. Ansermet, and P. Stadelmann, "Study of Co, Ni and Co/Cu nanowires: Magnetic flux imaging by off-axis electron holography," *J. Magn. Magn. Mater.*, vol. 164, pp. 77–90, 1996.

[20] C. Beeli, B. Doudin, J.-P. Ansermet, and P. A. Stadelmann, "Measurement of the remanent magnetization of single Co/Cu and Ni nanowires by off-axis TEM electron holography," *Ultramicroscopy*, vol. 67, no. 1–4, pp. 143–151, 1997.

[21] A. Blondel, J. P. Meier, B. Doudin, and J.-P. Ansermet, "Giant magnetoresistance of nanowires of multilayers," *Appl. Phys. Lett.*, vol. 65, no. 23, p. 3019, 1994.

[22] L. Piraux *et al.*, "Giant magnetoresistance in magnetic multilayered nanowires," *Appl. Phys. Lett.*, vol. 65, no. 19, p. 2484, 1994.

[23] A. Fert and L. Piraux, "Magnetic nanowires," *J. Magn. Magn. Mater.*, vol. 200, no. 1, pp. 338–358, 1999.

[24] L. Belliard, J. Miltat, A. Thiaville, S. Dubois, J. L. Duvail, and L. Piraux, "Observing magnetic nanowires means of magnetic force microscopy," *J. Magn. Magn. Mater.*, vol. 190, pp. 1–16, 1998.

[25] J. Wong, P. Greene, R. K. Dumas, and K. Liu, "Probing magnetic configurations in Co/Cu multilayered nanowires," *Appl. Phys. Lett.*, vol. 94, no. 3, p. 32504, 2009.

[26] J. U. Cho, Q. X. Liu, J. H. Min, S. P. Ko, and Y. K. Kim, "Synthesis and magnetic anisotropy of multilayered Co/Cu nanowire array," *J. Magn. Magn. Mater.*, vol. 304, no. 1, pp. e213–e215, Sep. 2006.

[27] D. Pullini, D. Busquets, A. Ruotolo, G. Innocenti, and V. Amigó, "Insights into pulsed electrodeposition of GMR multilayered nanowires," *J. Magn. Magn. Mater.*, vol. 316, no. 2, pp. e242–e245, Sep. 2007.

[28] D. Pullini, G. Innocenti, D. Busquets, and A. Ruotolo, "Investigation of multilayer local tilt within long portion of single Co/Cu nanowires," *Appl. Phys. Lett.*, vol. 90, no. 13, p. 133106, 2007.

[29] L. Tan and B. J. H. Stadler, "Fabrication and magnetic behavior of Co/Cu multilayered nanowires," *J. Mater. Res.*, vol. 21, no. 11, pp. 2870–2875, Nov. 2006.

[30] J. Bran, M. Jean, R. Larde, X. Sauvage, J.-M. Le Breton, and A. Pautrat, "Elaboration and characterization of Cu/Co multilayered nanowires," *J. Korean Phys. Soc.*, vol. 62, no. 12, pp. 1744–1747, Jul. 2013.

[31] M. Darques *et al.*, "Controlled growth of CoCu nanowires and application to multilayered CoCu/Cu nanowires with selected anisotropy," *J. Phys. Appl. Phys.*, vol. 39, no. 23, pp. 5025–5032, Dec. 2006.

[32] M. Almasi Kashi, A. Ramazani, F. A. Najafabadi, and Z. Heydari, "Controlled Cu content of electrodeposited CoCu nanowires through pulse features and investigations of microstructures and magnetic properties," *Appl. Surf. Sci.*, vol. 257, no. 22, pp. 9347–9350, Sep. 2011.

[33] M. R. McCartney and D. J. Smith, "Electron holography: phase imaging with nanometer resolution," *Annu Rev Mater Res*, vol. 37, pp. 729–767, 2007.

[34] E. Snoeck *et al.*, "Magnetic Configurations of 30 nm Iron Nanocubes Studied by Electron Holography," *Nano Lett.*, vol. 8, no. 12, pp. 4293–4298, Dec. 2008.

[35] C. Gatel *et al.*, "Size-Specific Spin Configurations in Single Iron Nanomagnet: From Flower to Exotic Vortices," *Nano Lett.*, vol. 15, no. 10, pp. 6952–6957, Oct. 2015.

[36] A. Akhtari-Zavareh *et al.*, "Off-axis electron holography of ferromagnetic multilayer nanowires," *J. Appl. Phys.*, vol. 116, no. 2, p. 23902, 2014.

[37] J. Cantu-Valle *et al.*, "Quantitative magnetometry analysis and structural characterization of multisegmented cobalt–nickel nanowires," *J. Magn. Magn. Mater.*, vol. 379, pp. 294–299, Apr. 2015.

[38] Y. P. Ivanov, A. Chuvilin, S. Lopatin, and J. Kosel, "Modulated Magnetic Nanowires for Controlling Domain Wall Motion: Toward 3D Magnetic Memories," *ACS Nano*, vol. 10, no. 5, pp. 5326–5332, May 2016.

[39] J.-L. Maurice *et al.*, "Microstructure of magnetic metallic superlattices grown by electrodeposition in membrane nanopores," *J. Magn. Magn. Mater.*, vol. 184, no. 1, pp. 1–18, 1998.

[40] E. F. Rauch, M. Véron, J. Portillo, D. Bultreys, Y. Maniette, and S. Nicolopoulos, "Automatic crystal orientation and phase mapping in TEM by precession diffraction," *Microsc. Anal.-UK*, no. 128, p. S5, 2008.

[41] E. F. Rauch and A. Duft, "Orientation maps derived from TEM diffraction patterns collected with an external CCD camera," in *Materials Science Forum*, 2005, vol. 495, pp. 197–202.

[42] D. Viladot *et al.*, "Orientation and phase mapping in the transmission electron microscope using precession-assisted diffraction spot recognition: state-of-the-art results: REVIEW OF PACOM (ASTAR) APPLICATION," *J. Microsc.*, vol. 252, no. 1, pp. 23–34, Oct. 2013.

[43] S. Estradé *et al.*, "Assessment of misorientation in metallic and semiconducting nanowires using precession electron diffraction," *Micron*, vol. 43, no. 8, pp. 910–915, Aug. 2012.

[44] I. Chlebny, B. Doudin, and J.-P. Ansermet, "Pore size distributions of nanoporous track-etched membranes," *Nanostructured Mater.*, vol. 2, no. 6, pp. 637–642, 1993.

[45] C. Schönenberger *et al.*, "Template synthesis of nanowires in porous polycarbonate membranes: electrochemistry and morphology," *J. Phys. Chem. B*, vol. 101, no. 28, pp. 5497–5505, 1997.

[46] C. Race, "A Radiation Damage Cascade," in *The Modelling of Radiation Damage in Metals Using Ehrenfest Dynamics*, Berlin, Heidelberg: Springer Berlin Heidelberg, 2011, pp. 9–13.

[47] B. E. Fischer and R. Spohr, "Production and use of nuclear tracks: imprinting structure on solids," *Rev. Mod. Phys.*, vol. 55, no. 4, p. 907, 1983.

[48] P. Apel, I. Blonskaya, S. Dmitriev, O. Orelovitch, and B. Sartowska, "Structure of polycarbonate track-etch membranes: Origin of the 'paradoxical' pore shape," *J. Membr. Sci.*, vol. 282, no. 1–2, pp. 393–400, Oct. 2006.

[49] D. Fink *et al.*, "On the penetration of etchant into tracks in polycarbonate," *Radiat. Meas.*, vol. 32, no. 4, pp. 307–313, 2000.

[50] M. T. Bryan, S. Bance, J. Dean, T. Schrefl, and D. A. Allwood, "Transverse and vortex domain wall structure in magnetic nanowires with uniaxial in-plane anisotropy," *J. Phys. Condens. Matter*, vol. 24, no. 2, p. 24205, Jan. 2012.

[51] V. Scarani, B. Doudin, and J.-P. Ansermet, "The microstructure of electrodeposited cobalt-based nanowires and its effect on their magnetic and transport properties," *J. Magn. Magn. Mater.*, vol. 205, no. 2, pp. 241–248, 1999.

[52] M. Rivera, C. H. Rios-Reyes, and L. H. Mendoza-Huizar, "Magnetic transition phase diagram of cobalt clusters electrodeposited on HOPG: Experimental and micromagnetic modelling study," *J. Magn. Magn. Mater.*, vol. 323, no. 7, pp. 997–1000, Apr. 2011.

[53] F. Dumas-Bouchiat *et al.*, "Cobalt cluster-assembled thin films deposited by low energy cluster beam deposition: Structural and magnetic investigations of deposited layers," *J. Appl. Phys.*, vol. 100, no. 6, p. 64304, 2006.

[54] D. Grujicic and B. Pesic, "Micromagnetic studies of cobalt microbars fabricated by nanoimprint lithography and electrodeposition," *J. Magn. Magn. Mater.*, vol. 285, no. 3, pp. 303–313, Jan. 2005.

[55] S.-H. Chung, R. D. McMichael, D. T. Pierce, and J. Unguris, "Phase diagram of magnetic nanodisks measured by scanning electron microscopy with polarization analysis," *Phys. Rev. B*, vol. 81, no. 2, Jan. 2010.

[56] M. J. Donahue and D. G. Porter, "OOMMF User's Guide, Version 1.0, Interagency Report NISTIR 6376." 1999.

[57] K. Y. Guslienko, "Magnetic Vortex State Stability, Reversal and Dynamics in Restricted Geometries," *J. Nanosci. Nanotechnol.*, vol. 8, no. 6, pp. 2745–2760, publication date 2008.

[58] K. L. Metlov and Y. Lee, "Map of metastable states for thin circular magnetic nanocylinders," *Appl. Phys. Lett.*, vol. 92, no. 11, p. 112506, 2008.

[59] E. R. P. Novais and A. P. Guimaraes, "Phase diagram of magnetic configurations for soft magnetic nanodots of circular and elliptical shape obtained by micromagnetic simulation," *ArXiv Prepr. ArXiv09095686*, 2009.

[60] C. A. Ross *et al.*, "Micromagnetic behavior of electrodeposited cylinder arrays," *Phys. Rev. B*, vol. 65, no. 14, Mar. 2002.

[61] I. L. Prejbeanu *et al.*, "In-plane reversal mechanisms in circular Co dots," *J. Appl. Phys.*, vol. 91, no. 10, p. 7343, 2002.

[62] D. Cimpoesu, L. Stoleriu, and A. Stancu, "Generalized Stoner-Wohlfarth model accurately describing the switching processes in pseudo-single ferromagnetic particles," *J. Appl. Phys.*, vol. 114, no. 22, p. 223901, 2013.

Chapter 5
FeCoCu diameter-modulated nanowires

5.1 Introduction

Nowadays there is an increasing interest for searching novel magnetic nano-objects allowing the control of individual magnetic domain walls (DWs) motion. One-dimensional nanostructures such as ferromagnetic self-standing nanowires (NWs) or patterned planar nanostripes are used to achieve a precise DW manipulation either by the application of magnetic fields or by the injection of electric current. Magnetic one-dimensional nanostructures are therefore of large interest for possible application in the new generation of spintronic devices for information storage technologies, permanent magnets, logic systems, sensors and biomedical applications [1]–[8]. One of the most promising route to manipulate DWs in planar nanostripes is patterning lateral defects like notches or anti-notches that will act as nucleation, pinning and depinning centres of DWs [9]–[16]. Inspired by the same idea, modulation in the diameter of cylindrical NWs is expected to be efficient to control the DW propagation. Micromagnetic and Monte Carlo simulations [17]–[20] have shown that such modulation of the NW diameter can indeed pin DWs. Allende et al. [17] have studied the nucleation and propagation of a domain wall along Ni modulated nanowires by Monte Carlo simulations as shown in Figure 5.1.1. They focused on nanowires with diameters ranging from 30 to 120 nm and lengths of 1.1 and 1.3 μm. These NWs have an aspect

ratio greater than 10. They have measured hysteresis curves to study the magnetization reversal process. In all the cases, the nucleation of the DW starts at the thicker section and propagates toward the thinner section, regardless of the reversal mode. The reversal mode was determined by the geometry of each section. They found that for diameters below a limit of approximately 55 nm, the magnetization reversal is driven by the nucleation and propagation of a transverse wall, while for diameters beyond the limit of 55 nm, the inversion starts with the nucleation of a vortex domain wall. The switching process between the vortex and the transverse reversal mode when the radius decreases can be understood by looking at the competition between dipolar and exchange energies.

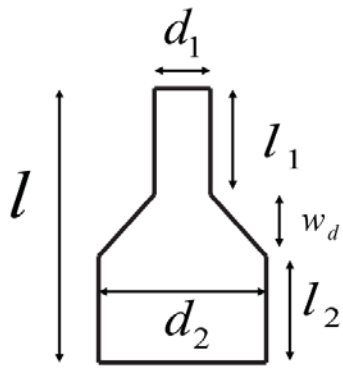

Figure 5.1.1. Diameter-modulated NW studied by Allende et al. Extracted from [17].

Salem et al. [18] investigated the magnetic properties of $Ni_{80}Fe_{20}$ diameter-modulated nanowires with diameters of 150 and 250 nm and lengths of 6.5 and 2.5 μm. They were produced by electrodeposition inside anodic alumina membranes. Micromagnetic simulations showed that the reversal process occurs via the nucleation and propagation of a vortex domain wall. These DWs are generating in the ends and in the regions between the two segments. They observed that the nucleation began at the thicker section (as Allende et al. [17]) and propagated toward the thinner section, regardless of the length of the segments. Tejo et al. [19] performed also investigations in cylindrical diameter-modulated $Ni_{80}Fe_{20}$. As Allende and Salem [17], [18], they

found that the system always starts reversing its magnetization through the thickest segment. They studied the angular dependence of the reversal process with the magnetic field applied. A transition from vortex DWs to a coherent-mode rotation for the thinnest segment as a function of the angle in which the external magnetic field is applied was found. Also, a non-monotonic behaviour for the coercivity and saturation field as a function of the angle at which the external magnetic field is applied was obtained.

Experimental studies performed by magnetic force microscopy (MFM), X-ray magnetic circular dichroism (XMCD-PEEM) and magneto-optic Kerr effect (MOKE) [21]–[23] have confirmed this DW pinning behaviour. Pitzschel et al. [21] studied Ni diameter-modulated NWs where the diameter modulations of the wires were 90 and 170 nm ± 10 nm. They used magneto-optical Kerr effect magnetometry and MFM on single NW to characterize the magnetic properties. They showed that pinning at the modulation was not systematic in their NWs. It can be explained by the energy difference of a domain wall between thick and thin wire segments is too small with respect to the influence of magnetocrystalline anisotropy and thermal fluctuations. Such factors will introduce a stochastic component into the pinning phenomena. Bran et al. [22] have determined the superficial and the internal magnetic structure of a FeCoCu and Co bamboo-like cylindrical nanowires with tailored diameter modulations. For this purpose, they have used photoemission electron microscopy combined with X-ray magnetic circular dichroism, as well as complementary magnetic force microscopy and micromagnetic simulations. These NWs with 130 and 140 nm and a modulation periodicity of 400 nm were electrochemically grown into the pores of alumina templates. For FeCoCu the remnant spin configuration consists of a main longitudinal domain with vortex structures at the ends as well as around the diameter modulations. The reversal process is expected to take place by the propagation of a vortex domain wall.

This DW can be pinned at the modulation places. For another hand, the Co diameter-modulated NWs with nearly perpendicular magnetocrystalline anisotropy showed a radically different configuration characterized by a series of vortices with alternating chirality not connected with the position of the modulations.

In parallel, recent improvements in the electrochemical route allow for the simultaneous fabrication of a great number of cylindrical NWs with a length of tens of microns and the possibility to tune the diameter-modulation (DM) geometry of the wires [24]–[27]. The wires show of a high DW propagation velocity favoured by the absence of a Walker breakdown phenomenon [28]. A precise DW manipulation can be done by an efficient diameter-modulated geometry. These two previous arguments make cylindrical NWs more powerful systems compared to their planar counterpart.

However, the achievement of a controlled and reproducible DW handling requires a preliminary exhaustive study focused on understanding how the remnant local spin configuration is altered by changes in the lateral geometry in individual and isolate NWs, free of magnetic interaction among neighbouring nanowires. Pitzschel et al. [21] studied the magnetic behaviour of nickel NWs with modulated diameters. They were able to observe hints of domain boundary pinning in some cases. By MFM a strong contrast was observed in the region with varying diameter. This contrast directly evidences the enhanced stray field present in the vicinity of the diameter modulation. In a later work, Iglesias-Freire et al. [29] used high-sensitive MFM measurements combined with micromagnetic simulations allowing an approach of the spin configuration of much thinner individual DM FeCoCu NWs. At remanence, bright and dark contrast appeared along the wire associated with the increase of the stray field in the transition zone where the diameter changes (see Figure 5.1.2). Micromagnetic simulations supporting the MFM images suggest that the single-domain state is

favourable at remanence, with a curling of the magnetization at the transition regions between the segments of different diameter.

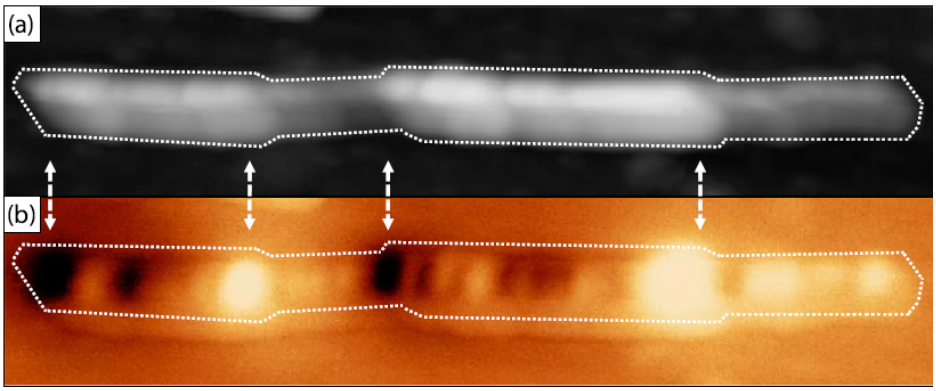

Figure 5.1.2. a) Topography and b) MFM images of a single FeCoCu NW in remanence. Extracted from [29].

This non-trivial interpretation can be substantially improved by performing more resolved magnetic imaging techniques such as electron holography (EH). In addition, the internal magnetic structure can be analysed. If a three-dimensional (3D) tomographic reconstruction is not carried out [30]–[32], EH only has access to the image-plane [two-dimensional (2D)] projected magnetic induction, resulting from the integration of the magnetic induction along the optical axis (perpendicular to the image plane), as we discussed before (chapter 2 and 3). Thus, the EH experiments should be supported by micromagnetic simulations in order to reveal the magnetic configuration inside and outside the sample. Several works have demonstrated that a quantitative combination of EH and micromagnetic simulations will be able to elucidate the 3D magnetic states in ferromagnetic NWs [33], [34]. In this chapter, we have exploited the potential of EH and micromagnetic simulations to perform a high-resolution quantitative magnetic characterization of cylindrical FeCoCu NWs with a diameter-modulated (DM) geometry. The possibility to reconstruct the magnetic induction field distribution both inside (magnetization) and outside (stray fields) of the NW allows a

deeper insight on the optimal geometry characteristics to achieve a controlled DW propagation.

5.2 Growth of nanowires

Cylindrical DM FeCoCu NWs were prepared by filling self-assembled pores of anodic aluminium oxide (AAO) templates by electroplating. The templates were obtained by pulsed hard anodization in oxalic aqueous solution (0.3M) containing 5 vol.% ethanol at a constant temperature of 0°C. During the anodization, a constant voltage of 80 V was first applied for 600 s to produce a protective aluminium oxide layer at the surface of the disc which avoids breaking or burning effects during subsequent pulsed hard anodization (Figure 5.2.1).

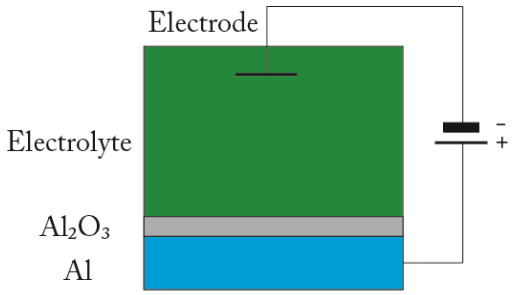

Figure 5.2.1. Scheme of the hard anodization template. A protective aluminium oxide layer is produced.

After the growth of the aluminium oxide layer, the voltage was slowly increased (0.05 V/s) up to 100V and kept constant for 400s, which ensures the alignment of the nanochannels. Nanopores with tailored periodical diameter modulations were produced by applying pulses of 130 V and 100 V for 5 and 150 s, respectively. The pulse was repeated 30 times to obtain a total length of the modulated pores of about 50 μm. The resulting cylindrical pores are formed by segments with diameters of about 100 and 140 nm, respectively, while the centre to centre inter-pore distance is kept constant at 320 nm. Finally, the residual Al and alumina barrier layer at the bottom of the foils were

chemically etched, and an Au layer was sputtered to serve later as an electrode for final electroplating of nanowires. A scheme of the whole process is shown in Figure 5.2.2.

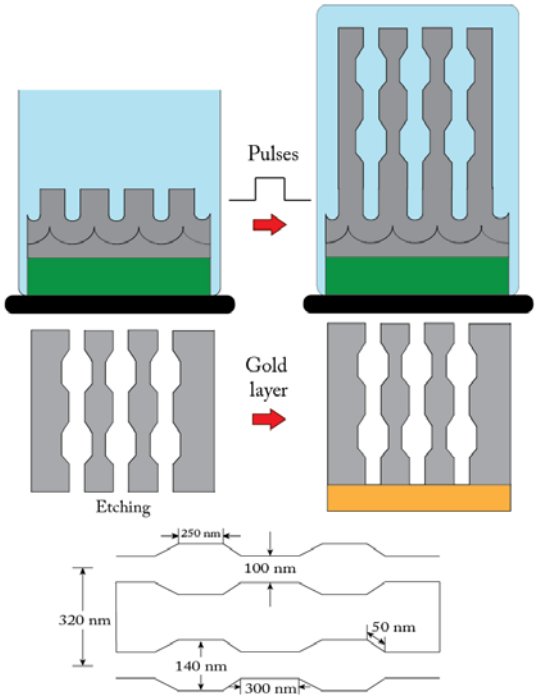

Figure 5.2.2. Scheme of the pores formation and the preparation to deposit the NWs. The last part of the figure details the geometrical parameters of the pores.

Once the membrane is ready, $Fe_{28}Co_{67}Cu_5$ alloys were grown into the modulated pores of AAO templates at room temperature by electrodeposition using the electrolyte solution composed of the compounds shown in Table 5.2.1.

Table 5.2.1. Mols of the compounds involve in the solution for the electrodeposition process.

Mols (M)	Chemical compound
0.12	$CoSO_4$
0.05	$FeSO_4$
0.01	$CuSO_4$
0.16	H_3BO_3
0.06	$C_6H_8O_6$

The electrochemical deposition was carried out under potentiostatic conditions by applying -1.8V to the working electrode respect to the Ag/AgCl reference electrode, keeping the temperature of the electrolyte at 25°C and the pH value at about 3.0.

5.3 Isolated FeCoCu nanowires, structural and morphological properties

In order to obtain isolated FeCoCu NWs, the host membrane had to be removed. The first step is to dissolve the Au layer chemically by a mixed solution of iodine and potassium iodide, followed by the dissolution of the alumina membrane done using a mixed solution of CrO_3 and H_3PO_4. Then the nanowires were cleaned, immersed in the ethanol and dispersed on a holey-carbon grid of TEM or silicon substrate in order to perform TEM and MFM measurements.

Studies of the morphology of diameter-modulated (DM) FeCoCu NWs were performed by high-resolution TEM (HRTEM), using the Hitachi HF-3300 (I2TEM) microscope operated at 300 kV.

Bright-field TEM images displayed in Figure 5.2.3 illustrate the morphology of two representative DM NWs. Among the numerous NWs released on the TEM carbon grid, the longest ones (similar to the NW reported in Figure 5.2.3 a)) are about 13 μm long, although most of the NWs look similar to the wire in Figure 5.2.3 b) with intermediate lengths between 3 and 8 μm. These 1D nanostructures are formed by alternating segments of small diameter (SD, around 100 nm), and large diameter (LD, around 140-144 nm), with a smooth diameter-variation transition about 50nm of length. If we move from right to left side along the NW in Figure 5.2.3 a), we see that the length of the SD and LD segments is gradually reduced, with a more pronounced variation for the LD segments. The LD segments are around 1000 nm long at the right

end to nearly disappear at the left end. In the case of SD segments, their lengths are reduced from 430 to 300 nm (see Figure 5.2.3 c) and d), corresponding to the zoom of the marked areas in Figure 5.2.3 a)). This geometrical variation previously observed in DM Co NWs, also fabricated by electrodeposition in AAO templates, is attributed to plastic deformation and mechanical instabilities on the aluminium substrate [35]. Schwirn et al. [36] studied the hard anodization process to produce AAO templates. They found that small oscillations in the voltage during the anodization process are accompanied by an intense evolution of gas bubbles over the entire surface of the samples. The estimated pressure of typical bubbles with radii around 40 nm is high as 100 MPa, which is believed to be sufficient to cause plastic deformation of the pore walls in the AAO templates. They think that a periodic oscillation of the reaction rate could result in a periodic oscillation of the gas production rate, which in turn could lead to a periodic change of the compressive stress and a periodic modulation of the pore diameter. Finally, they found a range for the diameter pore size between 15 to 30 nm. Lee et al. [37] studied spontaneous current oscillations under potentiostatic conditions. They found that the amplitude and period of these current oscillations increase with the anodization time. As a consequence of the oscillatory behaviour, the resulting anodic alumina exhibits modulated pore structure, in which the diameter contrast and the length of pore modulation increase with the amplitude and the period of current oscillations, respectively. They studied several shapes of peaks for the current during the anodization process and found that the current peak profile determines the internal geometry of oxide nanopores. Finally, they conclude that the mechanism responsible for the oscillatory behaviour is assumed to be a diffusion-controlled anodic oxidation of aluminium. They observed a local oxide thickening at the central area and distorted pores at the bottom part. A large mechanical stress is associated with high current density.

From TEM observations presented Figure 5.2.3 a) and b), we deduce that NWs of intermediate lengths are actually pieces of longer ones which break during the extraction from the template.

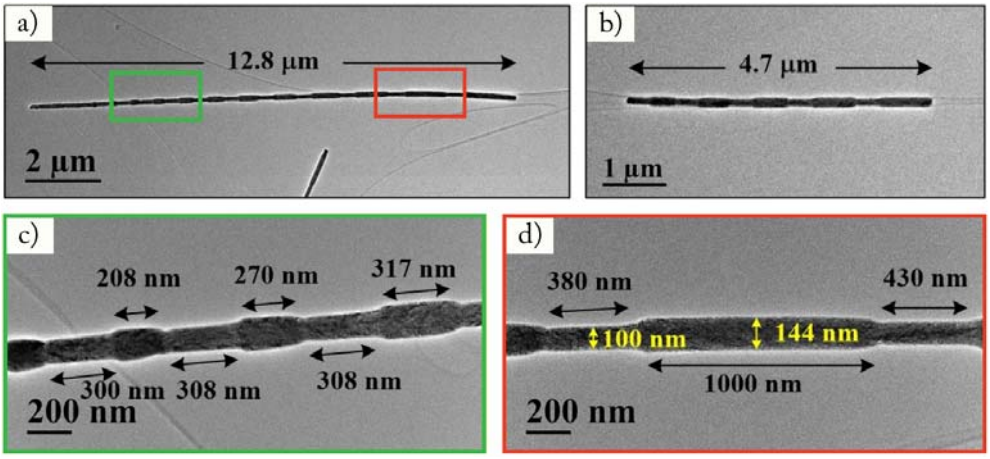

Figure 5.2.3. Bright-field TEM images of two representative DM FeCoCu NWs of a) 13 and b) 4.7 µm in length. The NW diameters and the segment lengths are measured from the high magnification TEM images corresponding to the areas enclosed in a) by c) yellow and d) red boxed. c) and d) illustrate the progressive change of the segments length.

Microstructural analysis of the wires was performed in high resolution TEM mode as reported in Figure 5.2.4. The micrographs do not reveal a clear single-crystal structure neither any texture over a long distance. Instead, the wires present a polycrystalline structure formed by nanocrystals of different sizes in the range of few nanometers. The fast Fourier transforms (FFTs) of the TEM images in Figure 5.2.4 present diffraction rings, which are the signatures of polycrystalline structures with randomly oriented grains. The indexation of the FFTs patterns agrees with the BCC structure of the FeCoCu for this composition [38]. In addition, the surface of the NWs is covered by an amorphous layer of 2-3 nm thick. This superficial amorphous layer formed by a surface oxidation process has been previously observed in FeCoCu NWs by Iglesias-Freire et al. [29]. The same oxidation layer has been confirmed by STEM-

EELS mapsin FeCoCu/Cu multilayered NWs by Palmero et al. [39]. They found a layer of about 9nm thick around the FeCoCu segments and 4 nm for the Cu layers.

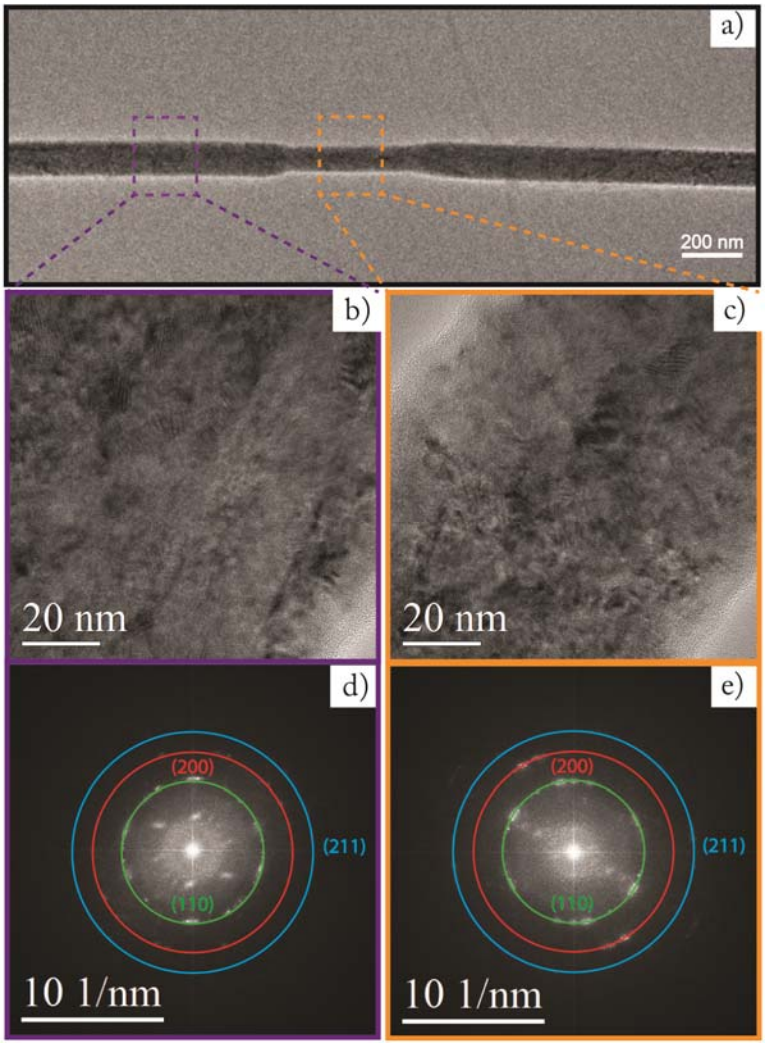

Figure 5.2.4. a) Bright-field at low magnification of an SD and LD segments. b) and c) High-resolution images for the LD and SD segments. d) and e) Fast Fourier transform performed on the high-resolution images showed in b) and c).

5.4 Magnetic remnant configuration of FeCoCu NWs

Electron holography (EH) experiments were carried out using the Hitachi HF-3300 described previously. In this study we have used the corrected Lorentz TL11

mode: the sample is inserted inside the normal stage of the I2TEM but the objective lens is switched off. The first transfer lens of the corrector (TL11) is used as an objective lens. The NWs are studied in a field-free condition that allows reaching a very large field of view up to 1.3 μm, with a fringe spacing of the holograms of 1.72 nm. In addition, the double-biprism configuration has been used to avoid the Fresnel fringes. Along this section, a comparative analysis between the EH results with MFM measurements will be done.

The MFM measurements and the growth of FeCoCu NWs were performed by the group of nanomagnetism and magnetization process lead by Professor Manuel Vazquez and Agustina Asenjo at the "Instituto de Ciencias de Materiales de Madrid, CSIC". They studied the remnant state of these isolated NWs by using MFM founding some bright and dark contrast. Figure 5.4.1 a) and b) displays topographic and magnetic images taken for an intermediate-length isolated NW. From the magnetic image Figure 5.4.1 b), a bright and dark contrast at the edge of this NW is observed. This contrast is expected for a near single-domain configuration (the so-called dipolar contrast). Moreover, the periodic bright and dark contrasts appear located in the diameter-variation crossover. The complex contrast in the MFM image therefore requires a careful non-trivial interpretation. The complementary study by EH associated with micromagnetic simulations will contribute to revealing the magnetic configuration as we will see in the next sections.

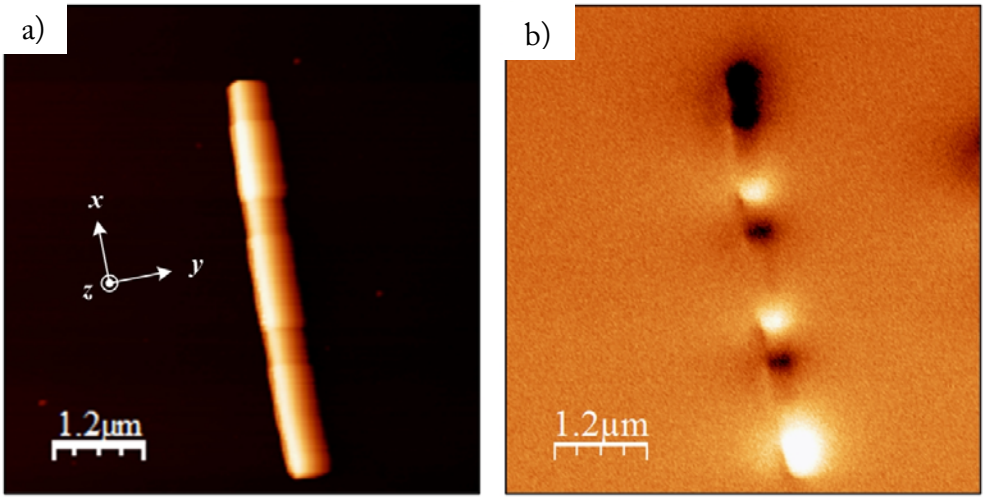

Figure 5.4.1. a) Topographic and b) MFM images for a DM FeCoCu NW of intermediate length.

For the EH experiments, amplitude and phase shift maps resulting from the holograms data treatment were studied. In order to separate the electrostatic and magnetic contributions to the phase shift, the sample was flipped and two different holograms for each orientation were acquired (up and down). In this way, as we discussed in chapter 3, we produce an equivalent time-reversal process of the electron beam, changing the sign of the magnetic phase shift contribution [40]. Figure 5.4.2 a) and b) displays EH images of the amplitude and magnetic phase shift map in an intermediate region of the NW reported in Figure 5.2.3. In addition, two magnetic flux images, $\Phi(x,y)$, are also presented in Figure 5.4.2 c) and d). These were obtained by the application of a cosine function on an amplified magnetic phase shift image [i.e. $\Phi(x,y) \sim \cos\left(n\phi_{MAG}(x,y)\right)$; n is an amplifier factor]. As observed in the amplitude image in Figure 5.4.2 a), the studied area contains a part of the wire composed by four repetitions of SD and LD segments with lengths ranging between 300-270 nm and 430-300 nm, respectively.

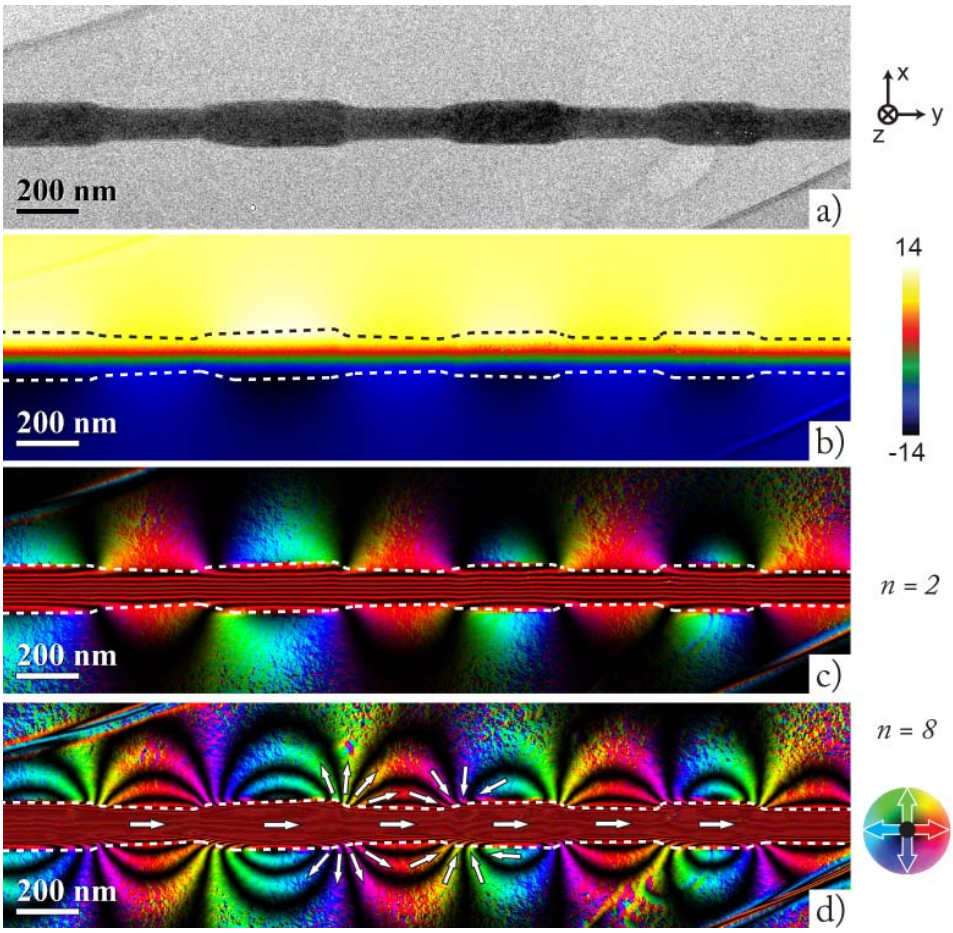

Figure 5.4.2. Experimental analysis of the magnetic phase shift of the electron produced by the magnetic induction of an isolated DM FeCoCu NW: a) amplitude, b) magnetic phase shift map reconstructed for a section of the NW, c) and d) magnetic flux images reconstructed from the magnetic phase shift images using as amplifier factor of n=2 and n=8 respectively. Colors in the magnetic flux images indicate only the magnetic induction direction according to the inserted color wheel beside d). The white arrows in d) are visual aids to visualize the local orientation of the in-plane projected magnetic induction inside and around the NW.

The magnetic phase shift image of Figure 5.4.2 b) presents a strong variation of the phase shift (strong change of color) inside the NW, along the X direction. As we discussed before, this change of phase shift along the X direction produces a magnetic induction oriented along the Y direction, in this case, the NW axis. This fact can be easily visualized in the magnetic flux image of Figure 5.4.2 c) where the direction of the flux lines into the nanowires seems to show a longitudinal alignment of the

magnetization. However, a small difference in the configuration of the flux lines is observed: inside SD segments the lines are perfectly parallel to the NW axis, while inside LD segments the lines are bent as they approach the lateral sides. This observation suggests that the longitudinal alignment of the magnetization varies in LD segments. A single-domain magnetization configuration is one of the expected remnant states in cylindrical nanowires due to the strong longitudinal shape anisotropy: this shape anisotropy is much stronger that the magnetocrystalline anisotropy and forces the magnetization to be oriented parallel to the longest dimension to minimize the magnetostatic energy.

5.4.1 Micromagnetic simulations in FeCoCu NWs

As EH only provides information of the integrated magnetic induction along the observation axis, a precise description of the 3D local spin configuration was carried out performing static micromagnetic simulations of the remnant state using OOMMF code [41]. The magnetization of saturation was determined as in the case of Co NWs (see chapter 3). The following magnetic parameters were used: saturation magnetization $M_s = 1060 \times 10^3$ A/m ($\mu_0 M_s \approx 1.33$T), exchange constant $A = 26 \times 10^{-12}$ J/m. As a good approximation, the anisotropy constant was neglected ($K = 0$) due to the polycrystalline character of the NWs. For these micromagnetic simulations, a representative 3D DM NW of 2.6 μm was built by stacking magnetic unit cell of $5 \times 5 \times 5$ nm^3. To simulate the stray fields surrounding the NW, the lateral dimensions (along the X and Y directions) where chosen larger than the diameter of the nanowire, leaving an empty space of about 100-200 nm between the NW surfaces and the universe frontiers. To perform the simulation calculations, the NW is set in an initial magnetization state where all spins are perfectly oriented along the Y-axis; the static

simulation then runs by using a second-order predictor corrector until the total energy of the system reaches a defined minimum.

The simulated remnant magnetic distribution of a DM FeCoCu NW was obtained on a wire of 2.6 μm length consisting of four repetitions of SD and LD segments to reduce the computational time. The diameter was set between 100 and 140 nm, the lengths of each type of segment were kept constant with values of 300 nm (SD segment) and 250 nm (LD segment), and a linear diameter-variation transition of 50 nm length. In addition, we have built the NW with ends of different diameter in order to evaluate their influence on the local magnetization orientation (one end has a SD modulation and the other one has the LD modulation). The geometrical parameters such as the size and shape of the DM NW, as well as the size of the simulated universe, are schematically illustrated in Figure 5.4.3.

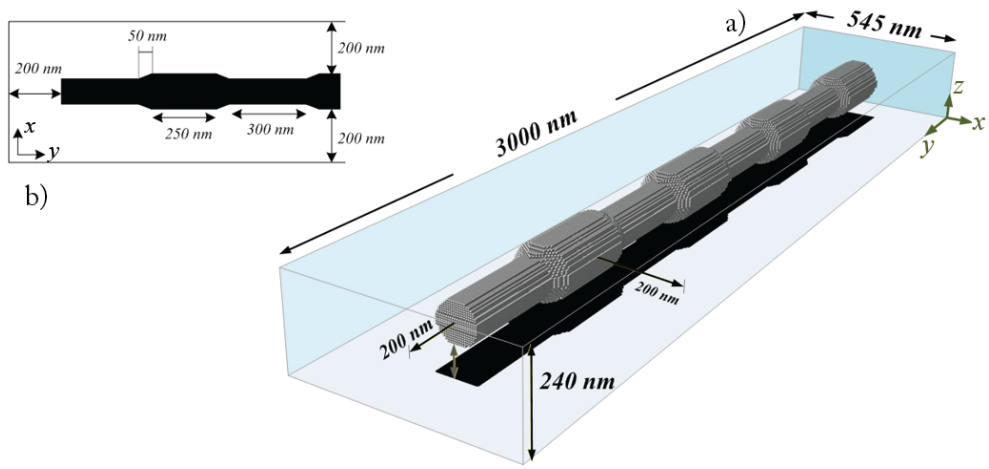

Figure 5.4.3. a) A perspective view of the 3D geometry used in the micromagnetic simulations. Grey region represents the magnetized body (NW) and the transparent box indicates the universe of the simulation. Black shadow corresponds to the XY plane projection of the NW. b) Zoom of a part of the black shadow to see the lateral dimension of the universe of the simulation at a half height (z=120 nm)

Figure 5.4.4 b) shows the simulated magnetic phase shift and Figure 5.4.4 c) and d) the magnetic flux images with the amplifier factor *n=2, n=8*. The optimization

of such experimental and simulation concordance was achieved by adjusting some of the magnetic parameters used in the micromagnetic simulation such as saturation magnetization M_s, and exchange constant A, and performing a quantitative comparison between experimental and simulated magnetic phase shift images through profiles traced perpendicular to the NW axis.

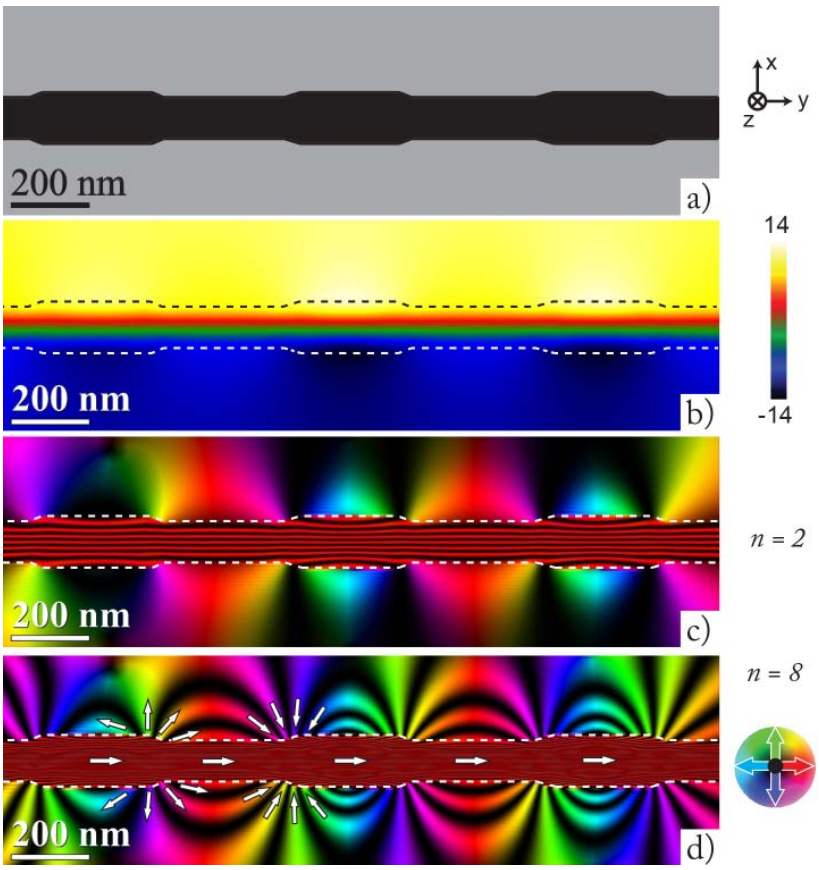

Figure 5.4.4. Simulation analysis of the magnetic phase shift of the electron produced by the magnetic induction of an isolated DM FeCoCu NW: a) amplitude, b) magnetic phase shift map reconstructed for a section of the NW, c) and d) magnetic flux images reconstructed from the magnetic phase shift images using as amplifier factor of n=2 and n=8 respectively. Colors in the magnetic flux images indicate only the magnetic induction direction according to the inserted color wheel beside d). The white arrows in d) are visual aids to visualize the local orientation of the in-plane projected magnetic induction inside and around the NW.

Figure 5.4.5 c) shows experimental and simulated magnetic phase shift profiles taken in the middle of an SD and LD segment. The best agreement for the magnetic

parameters is obtained by simulating the remnant magnetic state with the magnetic parameters mentioned above. These results correspond to the values reported for the $Fe_{30}Co_{70}$ [42], [43]. This value of magnetization of saturation is lower than the one measured by vibrating sample magnetometer (VSM) in FeCoCu NW arrays in an as-prepared condition (2.0 T) or after annealing the sample at 500 °C (1.7 T) [44]. As we know for VSM measurements you should know the exact volume of the material under study and it is difficult to determinate in some cases. Also, the estimation of the diameter, and the real shape of the NW segments is a problem for the quantitative calculation of the magnetization of saturation. As we discussed in chapter 3, we assume a perfect cylindrical shape to calculate of the magnetic induction. A few nanometers error in the estimation of the diameters can make the difference between the value for the magnetic induction reported here and the one reported by Bran et al. [44] for the same concentration of FeCoCu. Finally, the VSM measured the average saturation magnetization due to the contribution of a thousand of NWs.

The magnetic profiles of Figure 5.4.5 c) present a strong linear dependence inside the NW and small variations outside of it. Inside the wire, both profiles exhibit a similar positive slope due to the nearly single-domain structure of the NW. Outside the wire, a clear difference can be observed between the magnetic profiles in both segments: a positive variation occurs in the profile extracted from the outer part of the SD segment while a negative variation is obtained around the LD segment. The magnetic phase shift observed outside the NW is caused by the magnetic stray field spreading out of it, and the different variation of the phase shift along the X direction suggest a change of the local stray field orientation from SD segment to a LD segment. In order to map the in-plane projected stray field we reconstruct magnetic flux images using a higher amplifier factor of $n=8$ as we can see in the Figure 5.4.2 and Figure 5.4.4 d). We notice that the DM geometry of the FeCoCu NWs induces a complex

demagnetizing field configuration where the stray field emerges/enters to the wire in the transition regions where the diameter changes. This stray field configuration suggests that each diameter-variation crossover acts as a positive or negative magnetic charge that controls the local configuration of the demagnetizing field. According to the color map used in Figure 5.4.2 d), the positive and negative character of the magnetic charges changes alternately along the NW and the sign seems to be correlated to the flux direction of the magnetic induction inside the wire: if the field flows from a LD (SD) segment to a SD (LD) segment, the crossover between them behaves as a positive (negative) magnetic charge. As the magnetic induction inside the wire flows in the same direction, the remnant magnetic state of the DM NWs induces a sequence of alternately positive and negative magnetic charges.

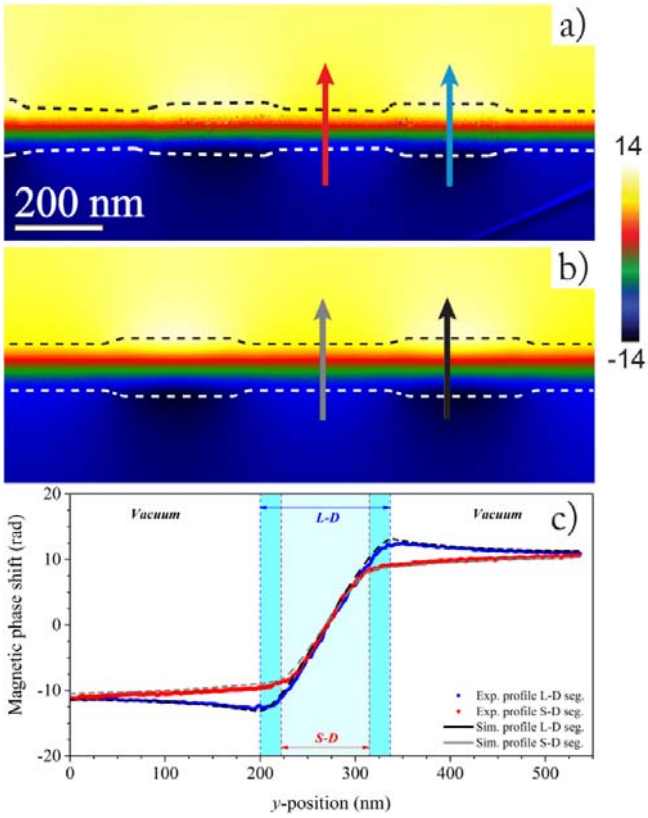

Figure 5.4.5. a) Experimental and b) simulated magnetic phase images. c) Profiles extracted from the magnetic phase images in the SD and LD segments where the arrows are drawn.

Making a local analysis, we found that this magnetic charge arrangement produces a flux-closure configuration of the demagnetizing field around LD segments. This remnant magnetic distribution resembles that observed by Lopatin et al. [45] and Ivanov et al. [46] in segmented Co/Ni NWs, where a compositional variation creates a modulation of the magnetization amplitude because the magnetic moment of the Co is 3 times larger than Ni and the magnetocrystalline anisotropy is oriented in different directions. Thus, this magnetization modulation promotes the formation of magnetic poles in the Co-Ni interfaces that act similarly as those of the DM FeCoCu NW.

To describe the overall remnant magnetic state of DM FeCoCu NWs, magnetic flux images around the ends of the wires were also reconstructed. Figure 5.4.6 displays magnetic flux images of two possible types of ends (SD and LD end). Additionally, magnetic flux images around the ends of the simulated DM NW were also represented (see Figure 5.4.6 b) and d)). As the shape of the ends in the real NWs is more irregular than the simulated one, the configuration of the magnetic flux lines are not perfectly comparable, but they have common features. In the thinner NW end, the parallel and longitudinal alignment of the magnetic flux observed close to the diameter-variation crossover (right-side of Figure 5.4.6 c) and d)) is slightly distorted by a progressive increase of the line spacing as they approach the lateral edge. In the thicker NW end (LD end), the magnetic flux is strongly modified at the lateral edge of the end, forming a type of C-shaped flux. Outside both ends, the stray field distribution resembles those found in 1D nanostructures with a uniaxial magnetic domain [47]. As a preliminary interpretation of the 2D projection of the magnetic induction inside the NW ends, we could conclude that the longitudinal spin alignment is only altered at the very end of the wires, being much stronger in the thicker ends.

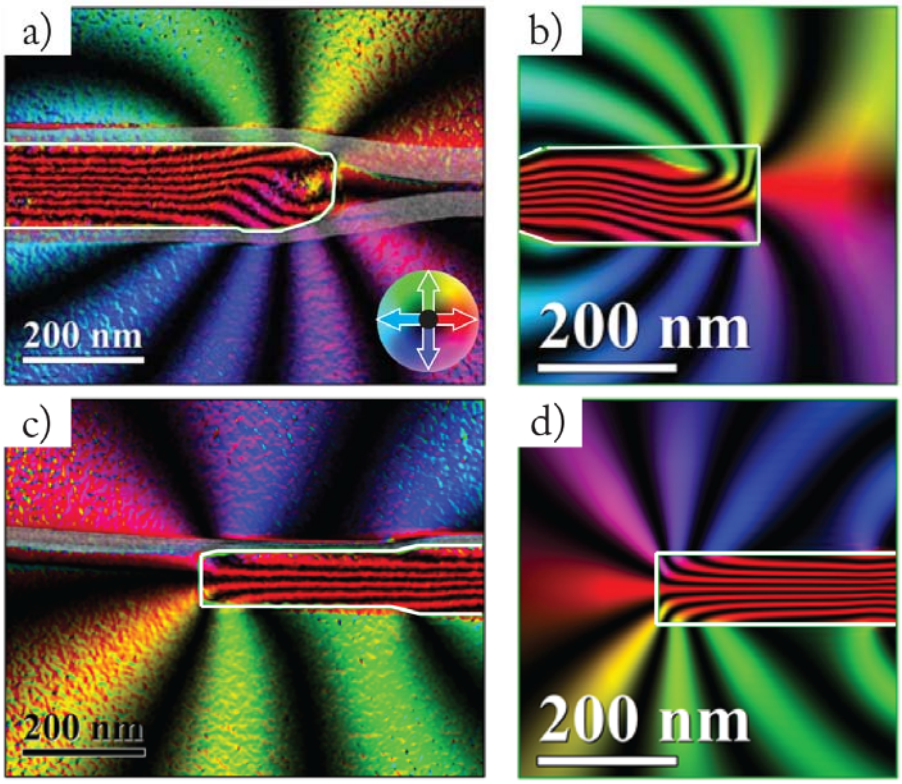

Figure 5.4.6. Magnetic flux images reconstructed around two NW ends with a) small c) large diameter. The correspondent calculated magnetic flux images for a b) SD and d) LD NW end. The color map represents the magnetic induction direction according to the color wheel into a). White contour lines and grey regions in a) and c) are artificially added to delineate the NW edges and to highlight the carbon TEM support, respectively.

Micromagnetic simulations made it possible to validate the interpretation of the magnetic distribution by EH, but also allowed going deeper in the full description of this remnant state thanks to the 3D capability to reconstruct the spin configuration and the demagnetizing field. A summary of 3D representations of the resulting simulated remnant state for the NW of Figure 5.4.3 is shown in Figure 5.4.7.

Figure 5.4.7 displays colormap representations of the *Y* and *X* component of the normalized magnetization, m_y and m_x respectively, for the spins located at the surface of the NW, and viewed from the +*Z* direction. Similar to that observed by EH experiments, a single color tone (red) in the m_y colormap reveals that the remnant state

of the NW tends to form a single-domain state with the spins mainly oriented along the +*Y* direction, except in the edges where a white color tone indicates that the averaged spin orientation is perpendicular to the NW axis. This fact is easily observed in the m_x colormap where an important contribution of this component is found in both NW ends, causing intense blue and red tones. In addition, the m_x colormap also reveals that the longitudinal alignment of the spins is also altered in the LD segments, where red and/or blue tones are also present. Figure 5.4.7 c) shows a cross section around the diameter variation. It was observed how these regions favour the formation of vortex-like structures, achieving to deviate the spin orientation up to 45° respect to the *Y* direction at the surface of the NW where the tilting effect is higher. In Figure 5.4.7 a) and c), it is clear that this curling state is extended only inside the LD segments and its effect is attenuated as it moves away to the diameter-variation crossover.

Similar to the magnetic charge sign, the chirality of these vortex structures changes consecutively along the wire and they seem to be correlated as each positive (negative) magnetic charge contains a clockwise (counter-clockwise) vortex-like chirality structure. This finding was also obtained by Iglesias-Freire et al. [29] in DM FeCoCu NWs with smaller diameters. Also, Bran [22], Berganza [48] and their teams found this kind of behaviour into bamboo-like FeCoCu NWs where the LD segment length is much shorter than the SD segment ones. It should be notice that this kind of magnetic structures also can be a result of artefacts of the micromagnetic simulations.

In our case, these vortex-like structures only extend along LD segments, and creates a kind of torsionally deformed longitudinal alignment of the spins due to the chirality difference of the vortex-like states present in their limits. The torsionally deformed structure of the spins causes the bending effect of the 2D projection flux lines inside the LD segments. A particular behaviour is observed in the LD segment beside

to the thin end where the vortex state is extended along all segment. This is produced by the two vortex structures with the same chirality around the LD segment. On the other hand, the SD segments are not affected by the vortex states, so that the spins are perfectly aligned along the NW axis as shown in Figure 5.4.7 c).

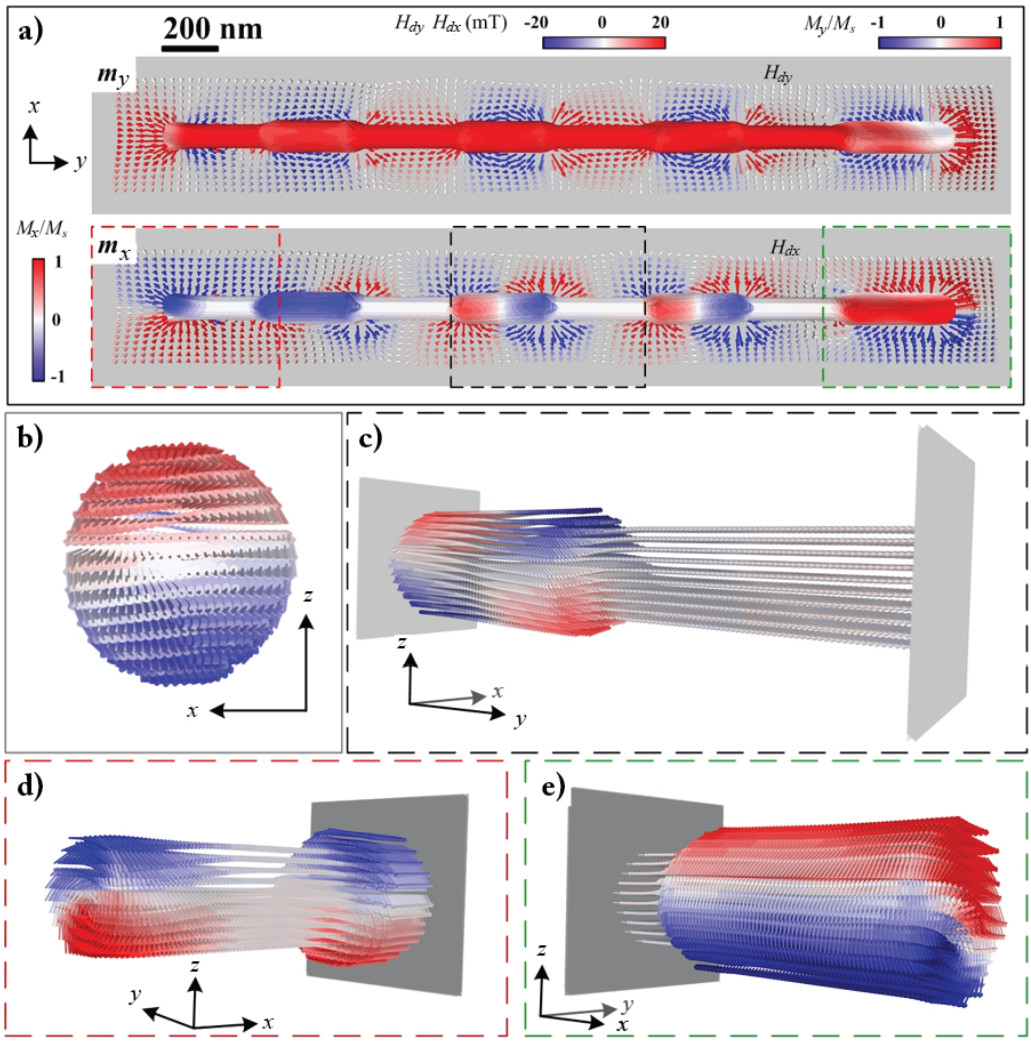

Figure 5.4.7. 3D representation of the simulated remanent magnetic state for the DM FeCoCu NW of Figure 5.4.3. Colors inside the NW indicate the orientation of the y- and x-component of the normalized magnetization (m_y and m_x, respectively). Colored arrows surrounding the NW represent the stray field (H_{dy} and H_{dx}) for an intermediate layer of the simulation (at a height of z = 120 nm). (b)-(e) A 3D perspective view of the remanent spin configuration for some sections of the simulated DM NW: (b) cross-section around a DM transition, (c) intermediate section (black dashed box in (a)) that covers one SD-LD segment, (c) SD NW end (red dashed box in (a)), (d) LD NW end (green dashed box in (a)). Colors in (b)-(e) represent the m_x magnitude.

Similar to the diameter-variation crossover, the ends of the wire also induce the formation of vortex-like structures in the lateral edges and it could extend along all the end (in the LD one). In the SD end, the vortex state is only formed in the edge and it disappears as the spins are further away from it, aligning parallel to the NW axis. Compared with those observed in the diameter-variation crossover, the vortex structure at the ends of the wire induce a curling state with spins highly tilted towards the perpendicular direction of the wire (up to 90° respect to the wire axis for spins at the NW surface), and this type of flux-closure magnetization states at the NW ends favors the minimization of magnetic charges.

The complexity of the magnetic charges in DM FeCoCu NWs also induces a non-intuitive behaviour in the demagnetizing field inside the wire. The alternating ordering of a positive and negative magnetic charges not only favours a parallel flux of the stray field to the magnetization around SD segments, they also create an internal demagnetizing field parallel to the magnetization.

This fact can be observed in Figure 5.4.8 a) where a 2D vector map of the demagnetizing field $\boldsymbol{H}_d$ for an intermediate XY plane is played. A reddish tone associated to the y component of $\boldsymbol{H}_d$ (H_{dy}) is observed inside the SD segments indicating that the internal dipolar field is parallel to the magnetization. The magnitude and variation of $\boldsymbol{H}_d$ at such XY plane can be observed in the profile shown in the Figure 5.4.8 b). In an intermediate section of the wire away from the ends, we see as the internal dipolar field is mainly aligned along the NW axis and its magnitude in the SD segments decreases dramatically as we move to the centre of the segment, passing from 96 mT (diameter-variation crossover) to 27 mT (centre of the SD segment); inside the LD segment, the dipolar field magnitude exhibit a sinusoidal-like behaviour with a

maximum value of 81 mT at the center of the segment and two minimum values of 49 mT in intermediate positions.

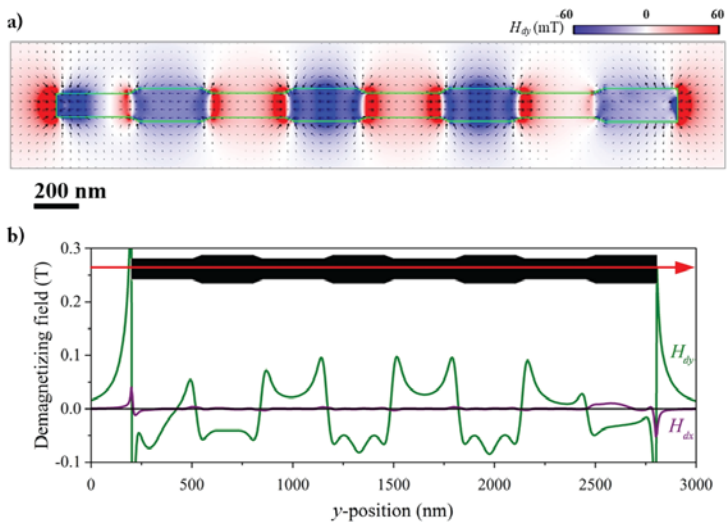

Figure 5.4.8. a) Colormap and arrows corresponding to the two-dimensional demagnetizing field [$\mathbf{H}_{dxy} = (H_{dx}, H_{dy})$] induced by the remnant magnetic state of the NW in an intermediate plane (z = 120 nm). Color scale represents the magnitude of H_{dy} and the green line delineates the NW contour. (b) H_{dx} and H_{dy} profiles taken along the red arrow.

The understanding of the magnetic distribution in DM FeCoCu NWs by EH experiments and micromagnetic simulations allows getting a better interpretation of the periodic magnetic contrast observed in MFM images. Figure 5.4.9 shows an illustrative scheme of the appearance of MFM magnetic contrast in DM NWs presented in Figure 5.4.1 b). The alternating bright and dark contrast pattern is a direct consequence of the way the diameter-variation crossovers act as alternating source and sinks of magnetic field even without the creation of any domain within the NW.

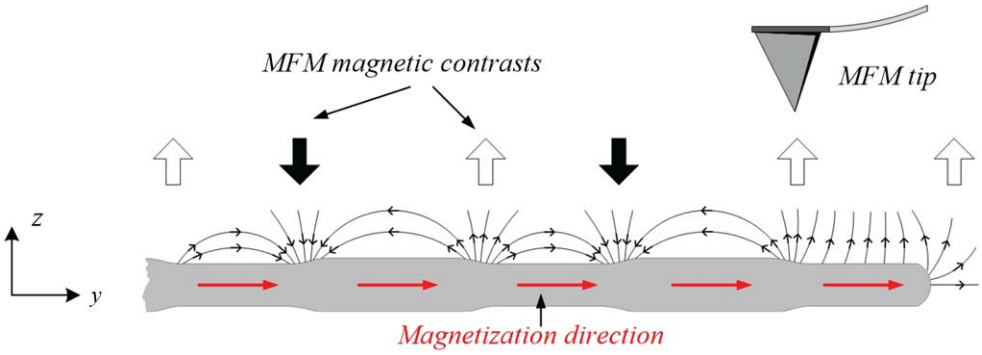

Figure 5.4.9. Schematic illustration to explain the origin of the bright and dark contrasts in MFM images.

Finally, we can conclude that the vortex-like structures play an important role in the spin configuration of LD segments because they provoke a torsionally deformed alignment of the spins in these thick segments. On the other hand, the induced magnetic charges control the local demagnetizing field of DM FeCoCu NWs where the magnetic interaction between neighbouring charges and the alternating positive/negative charge arrangement along the wire promote a flux-closure configuration around LD segments and an unexpected dipolar field that flow parallel to the magnetization both inside and around of SD segments. EH and micromagnetic simulations provide the answer to the bright and dark magnetic contrasts observed by MFM measurements which resemble DWs. These magnetic contrasts are produced by the outgoing/incoming stray field of the magnetic charges.

References

[1] D. A. Allwood, G. Xiong, C. C. Faulkner, D. Atkinson, D. Petit, and R. P. Cowburn, "Magnetic domain-wall logic," Science, vol. 309, no. 5741, pp. 1688–1692, 2005.

[2] D. A. Allwood, G. Xiong, and R. P. Cowburn, "Writing and erasing data in magnetic domain wall logic systems," J. Appl. Phys., vol. 100, no. 12, p. 123908, 2006.

[3] S. S. Parkin, M. Hayashi, and L. Thomas, "Magnetic domain-wall racetrack memory," Science, vol. 320, no. 5873, pp. 190–194, 2008.

[4] M. Hayashi, L. Thomas, R. Moriya, C. Rettner, and S. S. P. Parkin, "Current-Controlled Magnetic Domain-Wall Nanowire Shift Register," Science, vol. 320, no. 5873, pp. 209–211, Apr. 2008.

[5] H. Corte-León, P. Krzysteczko, H. W. Schumacher, A. Manzin, D. Cox, V. Antonov, and O. Kazakova, "Magnetic bead detection using domain wall-based nanosensor," J. Appl. Phys., vol. 117, no. 17, p. 17E313, May 2015.

[6] H. Corte-León, B. Gribkov, P. Krzysteczko, F. Marchi, J.-F. Motte, H. W. Schumacher, V. Antonov, and O. Kazakova, "Magnetic scanning gate microscopy of a domain wall nanosensor using microparticle probe," J. Magn. Magn. Mater., vol. 400, pp. 225–229, Feb. 2016.

[7] C. Bran, E. M. Palmero, R. P. del Real, and M. Vazquez, "CoFeCu electroplated nanowire arrays: Role of composition and annealing on structure and magnetic properties: CoFeCu electroplated nanowire arrays," Phys. Status Solidi A, vol. 211, no. 5, pp. 1076–1082, May 2014.

[8] Y. P. Ivanov, A. Alfadhel, M. Alnassar, J. E. Perez, M. Vazquez, A. Chuvilin, and J. Kosel, "Tunable magnetic nanowires for biomedical and harsh environment applications," Sci. Rep., vol. 6, p. 24189, Apr. 2016.

[9] Junyeon Kim, Myung-Hwa Jung, and Sug-Bong Choe, "Stability of Magnetic Domains With Notches in Permalloy Nanowires," IEEE Trans. Magn., vol. 45, no. 6, pp. 2481–2484, Jun. 2009.

[10] S. J. Noh, Y. Miyamoto, M. Okuda, N. Hayashi, and Y. Keun Kim, "Effects of notch shape on the magnetic domain wall motion in nanowires with in-plane or perpendicular magnetic anisotropy," J. Appl. Phys., vol. 111, no. 7, p. 07D123, 2012.

[11] L. A. Rodríguez, C. Magén, E. Snoeck, C. Gatel, L. Marín, L. Serrano-Ramón, J. L. Prieto, M. Muñoz, P. A. Algarabel, L. Morellon, J. M. De Teresa, and M. R. Ibarra, "Quantitative in situ magnetization reversal studies in Lorentz microscopy and electron holography," Ultramicroscopy, vol. 134, pp. 144–154, Nov. 2013.

[12] J. Brandão, R. L. Novak, H. Lozano, P. R. Soledade, A. Mello, F. Garcia, and L. C. Sampaio, "Control of the magnetic vortex chirality in Permalloy nanowires with asymmetric notches," J. Appl. Phys., vol. 116, no. 19, p. 193902, Nov. 2014.

[13] H. Y. Yuan and X. R. Wang, "Domain wall pinning in notched nanowires," Phys. Rev. B, vol. 89, no. 5, Feb. 2014.

[14] T.-C. Chen, C.-Y. Kuo, A. K. Mishra, B. Das, and J.-C. Wu, "Magnetic domain wall motion in notch patterned permalloy nanowire devices," Phys. B Condens. Matter, vol. 476, pp. 161–166, Nov. 2015.

[15] H. Y. Yuan and X. R. Wang, "Boosting domain wall propagation by notches," Phys. Rev. B, vol. 92, no. 5, Aug. 2015.

[16] K. He, D. J. Smith, and M. R. McCartney, "Observation of asymmetrical pinning of domain walls in notched Permalloy nanowires using electron holography," Appl. Phys. Lett., vol. 95, no. 18, p. 182507, 2009.

[17] S. Allende, D. Altbir, and K. Nielsch, "Magnetic cylindrical nanowires with single modulated diameter," Phys. Rev. B, vol. 80, no. 17, Nov. 2009.

[18] M. S. Salem, P. Sergelius, R. M. Corona, J. Escrig, D. Görlitz, and K. Nielsch, "Magnetic properties of cylindrical diameter modulated Ni80Fe20 nanowires: interaction and coercive fields," Nanoscale, vol. 5, no. 9, p. 3941, 2013.

[19] F. Tejo, N. Vidal-Silva, A. P. Espejo, and J. Escrig, "Angular dependence of the magnetic properties of cylindrical diameter modulated Ni80Fe20 nanowires," J. Appl. Phys., vol. 115, no. 17, p. 17D136, May 2014.

[20] D. W. Wong, M. Chandra Sekhar, W. L. Gan, I. Purnama, and W. S. Lew, "Dynamics of three-dimensional helical domain wall in cylindrical NiFe nanowires," J. Appl. Phys., vol. 117, no. 17, p. 17A747, May 2015.

[21] K. Pitzschel, J. Bachmann, S. Martens, J. M. Montero-Moreno, J. Kimling, G. Meier, J. Escrig, K. Nielsch, and D. Görlitz, "Magnetic reversal of cylindrical nickel nanowires with modulated diameters," J. Appl. Phys., vol. 109, no. 3, p. 33907, 2011.

[22] C. Bran, E. Berganza, E. M. Palmero, J. A. Fernandez-Roldan, R. P. Del Real, L. Aballe, M. Foerster, A. Asenjo, A. Fraile Rodríguez, and M. Vazquez, "Spin configuration of cylindrical bamboo-like magnetic nanowires," J Mater Chem C, vol. 4, no. 5, pp. 978–984, 2016.

[23] E. M. Palmero, C. Bran, R. P. del Real, and M. Vázquez, "Vortex domain wall propagation in periodically modulated diameter FeCoCu nanowire as determined by the magneto-optical Kerr effect," Nanotechnology, vol. 26, no. 46, p. 461001, Nov. 2015.

[24] W. Lee, R. Ji, U. Gösele, and K. Nielsch, "Fast fabrication of long-range ordered porous alumina membranes by hard anodization," Nat. Mater., vol. 5, no. 9, pp. 741–747, Sep. 2006.

[25] G. D. Sulka, A. Brzózka, and L. Liu, "Fabrication of diameter-modulated and ultrathin porous nanowires in anodic aluminum oxide templates," Electrochimica Acta, vol. 56, no. 14, pp. 4972–4979, May 2011.

[26] A. S. Esmaeily, M. Venkatesan, A. S. Razavian, and J. M. D. Coey, "Diameter-modulated ferromagnetic CoFe nanowires," J. Appl. Phys., vol. 113, no. 17, p. 17A327, 2013.

[27] V. M. Prida, J. García, B. Hernando, C. Bran, L. G. Vivas, and M. Vázquez, "Electrochemical synthesis of magnetic nanowires with controlled geometry and magnetic anisotropy," in Magnetic Nano- and Microwires, Elsevier, 2015, pp. 41–104.

[28] M. Yan, A. Kákay, S. Gliga, and R. Hertel, "Beating the Walker Limit with Massless Domain Walls in Cylindrical Nanowires," Phys. Rev. Lett., vol. 104, no. 5, Feb. 2010.

[29] Ó. Iglesias-Freire, C. Bran, E. Berganza, I. Mínguez-Bacho, C. Magén, M. Vázquez, and A. Asenjo, "Spin configuration in isolated FeCoCu nanowires modulated in diameter," Nanotechnology, vol. 26, no. 39, p. 395702, Oct. 2015.

[30] P. A. Midgley and R. E. Dunin-Borkowski, "Electron tomography and holography in materials science," Nat. Mater., vol. 8, no. 4, pp. 271–280, 2009.

[31] D. Wolf, A. Lubk, F. Röder, and H. Lichte, "Electron holographic tomography," Curr. Opin. Solid State Mater. Sci., vol. 17, no. 3, pp. 126–134, Jun. 2013.

[32] D. Wolf, L. A. Rodriguez, A. Béché, E. Javon, L. Serrano, C. Magen, C. Gatel, A. Lubk, H. Lichte, S. Bals, G. Van Tendeloo, A. Fernández-Pacheco, J. M. De Teresa, and E. Snoeck, "3D Magnetic Induction Maps of Nanoscale Materials Revealed by Electron Holographic Tomography," Chem. Mater., vol. 27, no. 19, pp. 6771–6778, Oct. 2015.

[33] N. Biziere, C. Gatel, R. Lassalle-Balier, M. C. Clochard, J. E. Wegrowe, and E. Snoeck, "Imaging the fine structure of a magnetic domain wall in a Ni nanocylinder," Nano Lett., vol. 13, no. 5, pp. 2053–2057, 2013.

[34] D. Reyes, N. Biziere, B. Warot-Fonrose, T. Wade, and C. Gatel, "Magnetic Configurations in Co/Cu Multilayered Nanowires: Evidence of Structural and Magnetic Interplay," Nano Lett., vol. 16, no. 2, pp. 1230–1236, Feb. 2016.

[35] F. Houdellier, L. de Knoop, C. Gatel, A. Masseboeuf, S. Mamishin, Y. Taniguchi, M. Delmas, M. Monthioux, M. J. Hÿtch, and E. Snoeck, "Development of TEM and SEM high brightness electron guns using cold-field emission from a carbon nanotip," Ultramicroscopy, vol. 151, pp. 107–115, Apr. 2015.

[36] I. Minguez-Bacho, S. Rodriguez-López, M. Vázquez, M. Hernández-Vélez, and K. Nielsch, "Electrochemical synthesis and magnetic characterization of periodically modulated Co nanowires," Nanotechnology, vol. 25, no. 14, p. 145301, Apr. 2014.

[37] K. Schwirn, W. Lee, R. Hillebrand, M. Steinhart, K. Nielsch, and U. Gösele, "Self-Ordered Anodic Aluminum Oxide Formed by H 2 SO 4 Hard Anodization," ACS Nano, vol. 2, no. 2, pp. 302–310, Feb. 2008.

[38] W. Lee, J.-C. Kim, and U. Gösele, "Spontaneous Current Oscillations during Hard Anodization of Aluminum under Potentiostatic Conditions," Adv. Funct. Mater., vol. 20, no. 1, pp. 21–27, Jan. 2010.

[39] B. Rodriguez-Gonzalez, C. Bran, T. Warnatz, J. Rivas, and M. Vazquez, "Structural and magnetic characterization of as-prepared and annealed FeCoCu nanowire arrays in ordered anodic aluminum oxide templates," J. Appl. Phys., vol. 115, no. 13, p. 133904, 2014.

[40] E. M. Palmero, C. Bran, P. Rafael, C. Magén, and M. Vázquez, "Structural and Magnetic Characterization of FeCoCu/Cu Multilayer Nanowire Arrays," IEEE Magn. Lett., vol. 5, pp. 1–4, 2014.

[41] A. Tonomura, T. Matsuda, J. Endo, T. Arii, and K. Mihama, "Holographic interference electron microscopy for determining specimen magnetic structure and thickness distribution," Phys. Rev. B, vol. 34, no. 5, p. 3397, 1986.

[42] M. J. Donahue and D. G. Porter, "OOMMF User's Guide, Version 1.0, Interagency Report NISTIR 6376." 1999.

[43] S. Vock, C. Hengst, M. Wolf, K. Tschulik, M. Uhlemann, Z. Sasvári, D. Makarov, O. G. Schmidt, L. Schultz, and V. Neu, "Magnetic vortex observation in FeCo nanowires by quantitative magnetic force microscopy," Appl. Phys. Lett., vol. 105, no. 17, p. 172409, Oct. 2014.

[44] S. L. Viñas, R. Salikhov, C. Bran, E. M. Palmero, M. Vazquez, B. Arvan, X. Yao, P. Toson, J. Fidler, M. Spasova, U. Wiedwald, and M. Farle, "Magnetic hardening of Fe 30 Co 70 nanowires," Nanotechnology, vol. 26, no. 41, p. 415704, Oct. 2015.

[45] C. Bran, Y. P. Ivanov, J. García, R. P. del Real, V. M. Prida, O. Chubykalo-Fesenko, and M. Vazquez, "Tuning the magnetization reversal process of FeCoCu nanowire arrays by thermal annealing," J. Appl. Phys., vol. 114, no. 4, p. 43908, 2013.

[46] S. Lopatin, Y. P. Ivanov, J. Kosel, and A. Chuvilin, "Multiscale differential phase contrast analysis with a unitary detector," Ultramicroscopy, vol. 162, pp. 74–81, Mar. 2016.

[47] Y. P. Ivanov, A. Chuvilin, S. Lopatin, and J. Kosel, "Modulated Magnetic Nanowires for Controlling Domain Wall Motion: Toward 3D Magnetic Memories," ACS Nano, vol. 10, no. 5, pp. 5326–5332, May 2016.

[48] R. Engel-Herbert and T. Hesjedal, "Calculation of the magnetic stray field of a uniaxial magnetic domain," J. Appl. Phys., vol. 97, no. 7, p. 74504, 2005.

[49] E. Berganza, C. Bran, M. Jaafar, M. Vázquez, and A. Asenjo, "Domain wall pinning in FeCoCu bamboo-like nanowires," Sci. Rep., vol. 6, p. 29702, Jul. 2016.

Conclusions and outlooks

The main objective of this thesis was the study of local magnetic states in Co-based nanowires at remnant state. Comparison between the state of the art electron holography measurements and micromagnetic simulations allowed for a quantitative and qualitative study of these magnetic states.

Co/Cu multilayered nanowires

Multilayered Co/Cu magnetic NWs have been grown by electrodeposition in polycarbonate membranes using the single bath technique. Different Co/Cu thicknesses were investigated: 25nm/15nm, 25nm/45nm, 50nm/50nm and 100nm/100nm. The NWs were firstly dissolved and an efficient cleaning process was carried out resulting in NWs with a minimum of contamination coming from the membrane and the electrode.

Special care has then been taken to locate and select the NWs onto the TEM grid to specify their orientation with respect to a defined axis on this grid. This allows in the first place to apply a magnetic field perpendicular (PP) and parallel (PL) to the wires axes. Then the perfect localization of the wires was used to perform EH experiments using the two PL and PP configurations. Finally, EFTEM and EELS experiments revealed the exact composition, thickness and shape of each Co/Cu layer in the very same NWs as the ones used for EH. This complete identification of the NWs has given a complete characterization of the NWs. For all the configurations a polycrystalline structure was found with a fcc structure for both elements. The chemical composition analysis showed the inclusion of at least 15% of Cu into the Co layers as a

result of the single bath technique. These impurities in the Co layer produce a decrease of the saturation magnetization compared with bulk Co. This was evidenced by EH experiments on a single Co NW grew in the same bath as the one used for multilayered NWs 1200×10^3 A/m ($\mu_0 M_s$ 1.5T).

EH experiments were performed in order to reveal the local magnetic states of the Co layers along the NWs. As EH results are the integration over the observation direction, micromagnetic simulations were carried out in order to complete the analysis of the magnetic states.

For the Co 25nm/Cu 15nm NW, the magnetic states found in most of the NWs were the magnetization oriented in the plane of the Co layer, antiparallel coupling (AP), vortex states and monodomain-like state. The magnetization in-plane (of the Co layer) is the most common in our wires (≈70%) this magnetization will remain in plane whatever the direction of the applied field with a preferred antiparallel coupling due to the dipolar interaction between Co layers. The transition between the AP and the vortex state when the field is applied PP and PL respectively appear for about 20% of the wires. The monodomain-like state was the obtained on a few wires NWs (≈ 10%) whatever the orientation of the applied magnetic field. Micromagnetic simulations including a uniaxial magnetocrystalline anisotropy were used to reproduce and to understand these magnetic states. Quantitative and qualitative agreements were then obtained between the simulated and the experimental results. All magnetic states for the Co 25nm/Cu 15nm configuration have been reproduced using an exchange constant $A = 22 \times 10^{-12}$ J/m and a magnetic anisotropy in the range of $100 - 280 \times 10^3$ J/m^3 randomly distributed in a cone of an aperture of 20-40° with respect to the wire axis.

When the thickness of the Cu layer increases (Co 25nm/Cu 45nm) the magnetic states remains the same no matter the direction of the magnetic field applied,

the state found were a mixture of AP coupling and vortices states. The vortices presented by this configuration shown tilted cores with respect to the wire axis, two different phase shift maps corresponds to these tilted vortices, the ones with the core tilted no more of 30° which was coupled with the adjacent layers and the ones with the core tilted ≥30° represented in the phase shift maps by circular features. These tilted vortices represent the weakening of the coupling of the adjacent layers. All these magnetic states were simulated with a magnetic anisotropy in the range of $100 - 130 \times 10^3\ \mathrm{J/m^3}$ and an aperture cone up to 30°.

Now if we increase the thickness of the Co (Co 50nm/Cu 50nm) the AP coupling disappears and only a wide range of vortices can be found. These vortices have the core tilted angles up to 90° (canted vortices) and can displays perfect circles at the phase shift maps due to their vortex body. This special configuration was displayed by the 45% of the wires. This configuration is possible for NWs with a diameter of 70-90 nm and magnetic anisotropies oriented in a cone of ≥45°. An interesting point about these magnetic canted vortices is the coupling between two or more adjacent vortices, which is under study and it will be developed as an outlook. On another hand the 55% of the remaining states presented coupled vortices with the core pointing almost parallel to the wire axis. These were obtained for smaller diameters than for the canted vortices (50-60nm) and also for Cu thickness below of the nominal value (≤50nm). The range of values for the magnetocrystalline anisotropy found to reproduce the canted and coupled vortices were $100 - 130 \times 10^3\ \mathrm{J/m^3}$ and $200 - 200 \times 10^3\ \mathrm{J/m^3}$ respectively. These anisotropies were lying in an aperture cones of ≥30° for canted vortices and 30° for coupled vortices with the core almost parallel to the wire axis.

Finally, if the Co and Cu thickness are increased until 100nm each one of them, the dipolar coupling is lost and is expected that each Co layer acts separately. Also, the

shape anisotropy is stronger along the wire axis than for previous configurations. About 80% of the wires presented the magnetization along the wire axis which can be considered as a monodomain-like and vortices states with the core pointing parallel to the wire axis. A quantitative analysis of the phase shift map with the help of micromagnetic simulations displayed that our magnetic states were vortices with the core tilted 0-30° with respect to the wire axis. Also, canted vortices were found in this configuration for larger diameters (>80nm) and Co thickness between 75-80nm. The canted vortices presented by the 20% of the NWs showed arc-shape or circular features depending on the tilted cores. The magnetic anisotropy used to reproduce these magnetic states was $130 \times 10^3\ \mathrm{J/m^3}$ with an aperture cone of 20°.

As a general point of view, the magnetic states are the result of the competition of the micromagnetic energies: the change in the layer thickness and diameter of the NW (shape anisotropy), the Cu thickness (dipolar coupling), the magnetic anisotropy, the magnetic field applied and the interaction of the spins produce specific magnetic states and thus, different magnetic properties for several applications or basic studies of interest. In this thesis, a quantitative and qualitative study of these local magnetic states was developed having a good agreement between the experimental results and micromagnetic calculations.

As a starting point to reveal the phase diagram of multilayered Co/Cu NWs, experimental results are analysed and compared with Co nanocylinders phase diagrams. The influence of the diameter and the thickness on the magnetic states after the application of a magnetic field was studied and the results showed an agreement with the experimental results for some configurations. As an outlook for these phase diagrams, micromagnetic simulations are planned to be performed in a Co/Cu multilayer for a wide range of magnetic anisotropies and different angles of aperture

cones. It will complete the results showed here showing the other possibilities of configurations and magnetic states.

Concerning to the Co/Cu NWs different outlooks can be proposed: one of the most interesting is the possibility to perform magnetoresistance measurements applying magnetic fields inside the microscope and perform EH experiments to observe the magnetic states obtained for each part of the magnetoresistance curve by EH. The idea is to choose the same NWs studied here and correlate the magnetic states previously observed with the ones produced during the magnetoresistance measurements.

The first part of this study can be implemented by applying an electrical current to an antiparallel coupling or a vortex state and observe if a magnetic switching can be possible and observe the resulting magnetic state. Also, the RF response can be measured for the different magnetic configurations obtained here.

The methodology exposed here, also, open the door to studies in several nanostructures as nanoparticles, thin layers, anti-dots, tracks and other shapes. Also, magnetic nanowires composed of other magnetic materials can be studied.

Last but not the least, the 3D identification of the magnetic structures by electron holographic tomography is an interesting outlook that can not be discarded. This experiments could solve some answers about the chirality of the coupled vortices with the core aligned along the wire axis and the magnetic coupling of the canted vortices.

FeCoCu diameter-modulated nanowires

A detailed quantitative and qualitative analysis of the magnetic configuration in FeCoCu diameter modulated NWs was done. The EH experiments and the micromagnetic simulations allowed for a detailed characterization of the local spin and

demagnetizing field configuration of cylindrical FeCoCu NWs with alternating modulation in diameter. At remnant state, the diameter modulated (DM) geometry of the wires altered the longitudinal alignment of the magnetization due to the formation of vortex-like states as well as magnetic charges, in regions where the diameter is varied. These vortex-like structures played an important role in the spin configuration of long diameter (LD) segments because they induced a torsionally deformed alignment of the spins in these thick segments. On the other hand, the induced magnetic charges controlled the local demagnetizing field of DM FeCoCu NWs where the magnetic interaction between neighbouring charges and the alternating positive/negative charge arrangement along the wire promote a flux-closure configuration around LD segments and an unexpected dipolar field that flow parallel to the magnetization both inside and around of the small diameter (SD) segments. The complete description of the remnant magnetic configuration carried out by EH and micromagnetic simulations allowed clarifying the origin of bright and dark magnetic contrast observed in MFM measurements that resemble domain walls (DWs). These magnetic contrasts are produced by the outgoing/incoming stray field of the magnetic charges.

This novel finding suggests that future studies for the control of the DW motion in DM cylindrical NWs will be focused on how the vortex-like structures and magnetic charges affect the magnetization reversal process. Ideally, we expect that both magnetic phenomena, or one of them, act as nucleation and pinning centres of DWs. As they are induced by the DM geometry of the wire, their optimization for handling DWs exclusively depends on the ability to grow nanowires with a specifically tailored modulation.

One of the outlooks for this system is to find the right distances between the SD and LD where the DM geometry can act as a domain wall pinning centres, and

study how the magnetic charges act for this configuration. On another hand, the study of the reversal process of these DM NWs is of special attention due to the behaviour of the magnetic charges at the interfaces where the modulation take place. It is expected that a change in the magnetic charges occurs.

The more interesting outlook for these FeCoCu DM NW is the possibility to inject current and observe the distribution of the magnetic charges. Also if an adequate geometry can be found to pin domain walls, it could be interesting to observe the movement of these DWs and observe the influence of the magnetic charges once these go through them. Also, the distribution of the stray field should be change if the modification of the magnetic charges is produced.

As a final outlook for this system, I think that it could be interesting to produce and study magnetic nanowires with modulations in diameter and composition at the same time to observe the changes that it produces on the magnetic charges and if the magnetic charges produce a change in the pinning sites due to the change of composition.

Growth of nanowires

The initial set-up to grow NWs was developed and tested with the production of Ni NWs, the protocol to perform a carefully cleaning process was obtained and implemented obtaining a good quality of the NWs almost free of membrane residues and gold pieces coming from the gold electrode deposited on the membrane. As an outlook, the next step is the growth of other systems of single or multilayered character and the improving of the deposition conditions. With this system of growth of nanowires and the methodology used for the analysis of magnetic nanowires, different magnetic systems of interest can be studied. Also, studies in NWs arrays using

techniques as XRD and VSM to compare with the TEM analysis are interesting. By last, the incorporation of membranes with different shapes opens a wide range of possibilities to study nanostructures of different shapes and properties.

Résumé étendu de la thèse

Introduction 238

Nanofils monoéléments 238

Nanofils multicouches 240

Objectifs et plan de la thèse 240

Techniques expérimentales 242

Croissance de nanofils 242

Imagerie de domaines magnétiques 244

Holographie électronique 247

Méthodologie 248

Synthèse des nanofils Co/Cu 248

Etude de la configuration magnétique des nanofils Co/Cu 251

Simulations micromagnétiques 254

Etude des nanofils multicouches Co/Cu 255

Analyse structurale et chimique d'un nanofil Co/Cu (25nm/15nm) 255

Configurations magnétiques expérimentales d'un nanofil Co/Cu (25nm/15nm) 256

Etude des nanofils FeCoCu à diamètre modulé 264

Analyse structurale et chimique des nanofils FeCoCu 265

Cartographie de l'aimantation par holographie électronique 267

Simulations micromagnétiques 269

Conclusion 275

Co/Cu nanofils multicouches 275

FeCoCu nanofils à diamètre modulé 277

Bibliographie 278

Introduction

La possibilité de déposer des couches minces dès le milieu du 20e siècle a permis de mettre en évidence de nouvelles propriétés en science des matériaux. Dans les films minces, les propriétés originales proviennent de leur faible épaisseur, d'un grand rapport surface-volume et de dimensions comparables à la longueur caractéristique (électronique, magnétique, ...). Des matériaux 1D (nanofils) et 0D (nanodots) ont également été synthétisés.

Les nanotubes de carbone sont l'exemple le plus fameux des matériaux à une dimension. Mais le développement de méthodes de synthèse a permis la croissance de nanofils de matériaux divers (semi-conducteurs[1,2], métal[3,4], oxydes[5,6,7] ...). Ces nanofils peuvent être soit mono élément soit inclure plusieurs matériaux. Ils peuvent être synthétisés par des méthodes physiques et chimiques telles que la méthode VLS (Vapor Liquid Synthesis)[8,9], l'évaporation thermique[10], une combinaison de processus de lift-off et de lithographie par faisceau d'électrons[11,12,13,14], un faisceau ionique focalisé (FIB)[15], en solution[16,17,18] ou dans une membrane poreuse[19,20,21], entre autres.

Au-delà de nanotubes de carbone, connus pour les propriétés mécaniques et électriques particulières[22,23,24], les applications de nanofils sont larges et peuvent être trouvées dans de nombreux domaines comme l'optique[25], l'électronique avec les transistors à émission de champ[26], les applications magnétiques avec le couplage de spin[27], le spin torque[28], et les déplacements de parois de domaines[29].

Nanofils monoéléments

Quelques exemples d'utilisation de nanofils monoéléments seront détaillés ci-dessous.

Les limites de circuits intégrés électroniques stimulent l'activité intense dans le domaine de la nanophotonique pour le développement de composants sur puce optiques[30]. Le traitement optique des données à l'échelle du nanomètre est prometteur pour surmonter ces limitations, mais nécessite le développement d'une boîte à outils des composants,

comme des émetteurs, des détecteurs, des modulateurs, des guides et des commutateurs d'ondes. Piccione et al.[25] ont démontré le principe d'une puce de commutation tout-optique utilisant des nanofils individuels de CdS. Un autre exemple de nanofils utilisés pour le champ de nanophotonique est les nanolasers[31]. Ces nanolasers ont émergé comme une nouvelle classe de lasers à semi-conducteurs miniaturisés qui sont potentiellement rentable et plus facile à intégrer.

Les nanofils de nickel sont utilisés pour sonder les forces de traction cellulaire[32]. Ils servent aussi d'outil pour la manipulation de cellules[33] et surpassent les nanoparticules magnétiques commerciales. M. Contreras et son équipe[34] également utilisé des nanofils Ni pour tuer les cellules cancéreuses. L'idée est d'exploiter un effet magnéto-mécanique, où les nanofils provoquent la mort cellulaire par vibration dans un champ magnétique de faible puissance.

Les nanofils monoéléments ont également trouvé diverses applications dans le magnétisme et sont étudiés pour les applications de stockage. Les origines de la limite de stockage ont évolué avec la technologie. Un premier rapport en 1997 sur le problème de la stabilité thermique des informations magnétiquement stockées[35] a estimé une limite supérieure d'environ 36 Gbit/in^2. Mais la technologie récente a déjà atteint des densités d'un ordre de grandeur supérieur à cette valeur. La différence entre les valeurs projetées et réelles pour la limite supérieure réside dans les avancées sur les aspects non-magnétiques de la technologie d'enregistrement tels que les systèmes d'actionneurs mécaniques utilisés pour positionner la lecture et l'écriture des capteurs. Une étude plus récente indique que la principale limitation est déterminée par le taux maximal tolérable d'erreur binaire et certains paramètres des matériaux, qui comprennent l'aimantation à saturation du support d'enregistrement. Elle montre que les densités de stockage seront limitées à 15 à 20 Tbit/in^2, sauf si la technologie peut aller au-delà des grandeurs disponibles actuellement sur la partie écriture[36]. En fait, certaines entreprises comme Sony et Fujifilm ont inscrit des données sur des bande de 148 et 154 Gb/in^2 [37,38].

Les réseaux de nanofils magnétiques monoéléments peuvent être utilisés dans des dispositifs de stockage magnétique ultra-haute densité. Dans ce cas, chaque nanofil peut

stocker un ou plusieurs bits d'information et, grâce à leur anisotropie inhérente, ils peuvent abaisser la limite où chaque taille de bit est limité par la taille du domaine magnétique unique. L'étude fondamentale de la paroi de domaine est donc d'un grand intérêt. Des simulations micromagnétiques ont été utilisées pour étudier le diagramme de phase pour des nanofils de permalloy où une paroi de domaine transversale (TDW) est formée dans les fils de rayons inférieurs à 20nm tandis que la paroi à point de Bloch (BPW) est favorisée dans les fils plus larges[39].

Nanofils multicouches

Les nanofils multicouches ont un intérêt particulier pour l'étude des phénomènes de GMR[40,41,42], qui consiste en une modification importante de la résistance électrique dans une structure composée d'une alternance de couches magnétiques/non magnétiques lorsqu'un champ magnétique est appliqué dans deux directions opposées. Les modifications peuvent atteindre 150% à partir de la résistance initiale lorsqu'un champ magnétique est appliqué à basse température et 15% pour les nanofils Co/Cu à température ambiante[43].

Les nanofils magnétiques permettent aussi d'envisager aussi une alternative à l'électronique à base de semi-conducteurs. Une architecture logique complète peut être construite en utilisant des nanofils magnétiques planaires avec des motifs géométriques simples. Ils peuvent être intégrés en un seul circuit.

Objectifs et plan de la thèse

Les nanofils magnétiques sont également particulièrement intéressants pour les études fondamentales des interactions magnétiques à l'échelle nanométrique et de très bons candidats pour produire des dispositifs à mémoire magnétique non volatiles ou des nano-oscillateurs à couplage de spin connectés en série pour augmenter la puissance radio-fréquence (RF) de sortie. Toutefois, les réalisations techniques en spintronique exigent une connaissance détaillée des états magnétiques dans chaque couche à l'état du reste.

L'objectif de cette thèse est le développement des études qualitatives et quantitatives des états magnétiques locaux de nanofils à base de Co tels que des nanofils multicouches Co/Cu et $Fe_{28}Co_{67}Cu_5$ (FeCoCu) de diamètre modulé par holographie électronique (EH). Pour le système de nanofils Co/Cu, un champ magnétique est appliqué perpendiculairement et parallèlement à l'axe du fil et l'état rémanent est cartographié quantitativement. Différentes épaisseurs de couches de Co et Cu sont proposées dans le but d'étudier les configurations magnétiques et l'effet du couplage dipolaire entre les couches. D'autre part, pour les nanofils FeCoCu modulés, la configuration magnétique est étudiée à la rémanence. Afin de révéler l'état magnétique 3D dans les deux systèmes, des simulations micromagnétiques sont effectuées et comparées qualitativement et quantitativement.

Ce travail de these, 5 chapitres sont proposés:

Dans le chapitre 1: "Propriétés magnétiques", les concepts de base en magnétisme sont décrits. L'origine microscopique du magnétisme et les propriétés ferromagnétiques des matériaux sont discutés. Une vue d'ensemble des énergies micromagnétiques qui contribuent au système ferromagnétique est suivie d'une discussion sur les états magnétiques dans des nanofils magnétiques. Enfin, je vais vous présenter l'importance d'effectuer des simulations micromagnétiques et le code utilisé lors de ce travail. *(ce chapitre ne sera pas repris dans le résumé)*

Dans le chapitre 2: "Techniques expérimentales ", je vais donner une description d'un large éventail de techniques pour élaborer des nanofils, avec un accent particulier sur la synthèse basée sur l'électrodéposition, utilisée pour fabriquer les nanofils étudiés dans ce travail. Ensuite, le chapitre sera consacré à l'introduction à la formation d'une image dans un et à l'observation des propriétés magnétiques par holographie électronique.

Le chapitre 3: «Méthodologie», présente les procédures et la méthodologie expérimentale suivie. La première partie est une description détaillée du processus d'élaboration de nanofils, puis la procédure pour effectuer l'holographie et le traitement

des données est proposée. La procédure pour effectuer des simulations micromagnétiques est également exposée.

Le chapitre 4: " Nanofils multicouches Co/Cu ", présente l'étude qualitative et quantitative de nanofils multicouches Co/Cu à l'état rémanent après l'application d'un champ magnétique perpendiculaire/parallèle à l'axe du fil. Cette étude réalisée par EH est confrontée à des simulations micromagnétiques. Les états magnétiques différents sont présentés et l'importance du rapport des épaisseurs couches/diamètre est discutée.

Pour le chapitre 5: "Nanofils de diamètre modulé FeCoCu", une description détaillée par EH et simulations micromagnétiques de l'état magnétique à l'intérieur et à l'extérieur des nanofils est effectuée. L'importance du champ de fuite généré par ce segment est représentée et l'influence de la taille des diamètres est discutée.

Techniques expérimentales

Croissance de nanofils

Il existe de nombreuses méthodes pour réaliser la croissance de nanofils comme la méthode VLS (vapeur-liquide-solide), l'ablation laser, l'évaporation, la lithographie à partir de films minces ou encore les croissances en solution.

L'électrodéposition a été choisie pour déposer les nanofils au cours de cette thèse. Elle permet de faire croître des fils dans un « template », moule formé de nanopores allongés.

Le dépôt électrolytique de métaux purs et alliages implique la réduction de cations par le gain d'électrons. Ce procédé est effectué sur la surface de l'électrode dite électrode de travail. Le matériau désiré est déposé sur cette électrode. La réaction électrochimique ne peut avoir lieu que s'il y a une réaction d'oxydation qui donne les électrons nécessaires. Pour le système d'électrodéposition de base, trois électrodes sont nécessaires: l'anode, la cathode et l'électrode de référence. Les trois électrodes sont immergées dans la solution que l'on appelle l'électrolyte. Normalement, l'électrode de travail (anode) est fabriquée à partir d'un matériau non réactif ou un matériau dont les ions sont déjà dans la

solution[44]. L'électrode de référence est utilisée pour mesurer la caractéristique de réponse en courant et en tension de la cathode. Ces électrodes sont commandées par un circuit appelé potentiostat ou galvanostat externe. Le potentiostat contrôle le potentiel entre la cathode et l'électrode de référence. Il permet également de maintenir le potentiel entre les électrodes en fournissant le courant électrique nécessaire. Dans la figure 1, le schéma de l'installation d'électrodéposition est représenté.

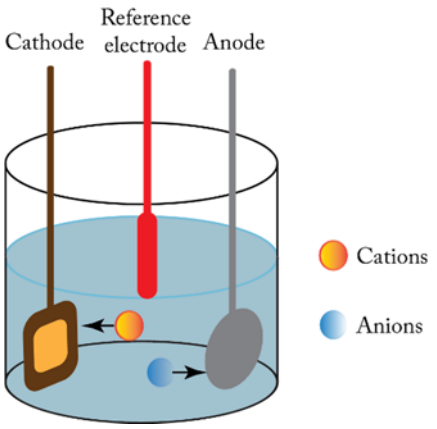

Figure 1 Schéma de principe d'une cellule d'électrodéposition

Au cours du processus d'électrodéposition, deux processus principaux sont impliqués, et ils se produisent en continu et simultanément: le transport de masse et le transfert d'électrons. Le processus le plus lent est le processus de limitation.

Au cours du processus d'électrodéposition, nous devons tenir compte de plusieurs paramètres qui affectent le processus et influencent les propriétés de l'échantillon résultant:

• *La température*: elle a une grande influence sur la diffusion ionique ainsi que sur les atomes déjà déposés. Les hautes températures donnent une solubilité et une conductivité électrique améliorées mais tend à accélérer les processus d'évaporation. Il y a aussi une influence sur le rendement: une augmentation de température de 1 ° C entraîne une augmentation de 10% du taux des processus électrochimiques et une amélioration du taux de transfert de masse de 2%.

• *L'agitation de la solution*: améliore le transport d'ions vers le substrat et réduit l'épaisseur de la couche de diffusion.

• *Le pH de la solution*: c'est un paramètre très important qui va influencer les propriétés des métaux déposés. Si le pH est trop élevé, la présence d'ions hydroxyde qui entourent les ions métalliques peut affecter le dépôt. Et si le pH est trop bas, la perte au niveau de la cathode peut être considérable[45].

• *le potentiel de la cathode*: il permet de choisir le métal déposé lorsque le bain de dépôt électrolytique contient deux ou plusieurs matériaux. Sa stabilité peut affecter l'homogénéité de la composition le long du processus.

Le processus d'électrodéposition est une technique polyvalente qui permet nanofils de plus en plus d'une manière relativement facile, même s'il y a beaucoup de paramètres qui interviennent au cours du processus de croissance. Les taux de croissance moyens dans certains cas, se situent entre 10 µm/h à une température de dépôt de 0°C et 2682 µm/h pour 60°C[46,47,48]. Nous avons utilisé cette technique pour la croissance des nanofils multicouches dans des membranes de polycarbonate composé de pores de taille nanométrique. Dans le chapitre des résultats, les détails sur le processus spécifique sont présentés.

Imagerie de domaines magnétiques

L'étude des propriétés magnétiques des matériaux ferromagnétiques nanométriques nécessite la combinaison de techniques de caractérisation macroscopiques qui fournissent des informations magnétiques moyennes sur de grandes échelles de longueur avec des techniques locales capables de sonder les propriétés magnétiques à haute résolution spatiale et la sensibilité. Parmi ces derniers, les techniques d'imagerie magnétique permettent une étude directe des configurations magnétiques et en particulier des structures de domaine magnétiques à l'échelle submicronique. La possibilité d'imagerie magnétique à haute résolution et l'amélioration du temps de calcul des simulations micromagnétiques ont contribué de manière significative à la

compréhension des phénomènes magnétiques à l'échelle locale, permettant des avancées technologiques dans le domaine de nanomagnétisme et spintronique[49,50,51].

Aujourd'hui, on dénombre de multiples techniques d'imagerie magnétique. Parmi elles, on peut citer la microscopie Kerr, sur la base de l'effet Kerr magnéto-optique (MOKE) [52,53,54]; la microscopie électronique à balayage avec analyse de polarisation (SEMPA)[55,56,57]; la microscopie électronique polarisée en spin à basse énergie (SPLEEM);les techniques à base de rayonnement synchrotron telles que le dichroïsme circulaire magnétique, la microscopie d'émission de photoélectrons (XMCD-PEEM)[58,59] et la microscopie à rayons X magnétique en transmission (M-XTM); les techniques de sonde à balayage telles que la microscopie à force magnétique (MFM)[60,61] et la microscopie à effet tunnel polarisée en spin (SP-STM)[62]; et dans un microscope en transmission, la microscopie de Lorentz (LM) et l'holographie d'électron (EH)[63,64,65]. Toutes ces méthodes expérimentales offrent un large éventail de possibilités pour étudier les phénomènes micromagnétiques dans différentes configurations comme on peut le voir dans la liste comparative de leurs principales caractéristiques présentées dans le tableau ci-dessous. Au total, ils fournissent une résolution spatiale allant de quelques microns à quelques angströms, une sensibilité élevée pour détecter des petits changements de l'aimantation locale, sonder la surface ou les propriétés de volume et une polyvalence suffisante pour permettre l'application de multiples stimuli externes (température, champs électromagnétiques, etc. .). Aucune de ces techniques ne couvre toutes les possibilités, et elles sont donc complémentaires.

Technique	Meilleure résolution spatiale (nm)	Profondeur information (nm)	Temps d'acquisition (s)	Quantitatif	Type de l'information profondeur	Type d'imagerie
XMCD–PEEM	20	2-20	0.03-10	Oui	Surface	Parallèle
M-XTM	20	Épaisseur de l'échantillon	3	Oui	Volume	Parallèle-balayage
Kerr Microscopy	200	20	10^{-8} to 1	Oui	Surface	Parallèle-balayage
MFM	30	200-500	300 to 1800	Non	Surface	Balayage
SEMPA	10	2	60-6000	Oui	Surface	Balayage
SPLEEM	20	1	1	Oui	Surface	Parallèle
DPC	2	Épaisseur de l'échantillon	5-50	Oui	Volume	Parallèle-balayage
Lorentz Microscopy	10	Épaisseur de l'échantillon	0.04-30	Oui	Volume	Parallèle
Electron Holography	2	Épaisseur de l'échantillon	0.03-10	Oui	Volume	Parallèle
SP-STM	0.02	0.2	30-1800	Oui	Surface	Balayage

Pour l'étude des états magnétiques locaux, la résolution spatiale est un critère déterminant. Cela rend les techniques à base de MET très pertinentes, elles fournissent des informations magnétiques quantitatives sur le volume de l'échantillon avec la possibilité d'appliquer des stimuli externes (champs magnétiques et électriques, injection du courant électrique, changements de température, contrainte, lumière, etc.) avec une résolution spatiale allant vers l'échelle atomique.

Holographie électronique

Historiquement, les premières tentatives pour étudier les matériaux magnétiques par MET sont en corrélation avec la configuration de domaine magnétique mesuré par d'autres techniques. Mayer[66] a établi la première méthode pour observer le magnétisme en adaptant un microscope électronique à miroir. En 1959, Hale et al.[68] ont développé les premières méthodes d'imagerie de domaines dans des films minces ferromagnétiques grâce au MET défocalisé et à l'utilisation d'un diaphragme objectif décentré[69]. Ils ont établi respectivement la base de la microscopie de Lorentz en mode Fresnel et Foucault. Dans les années 1970 et 1980, d'autres techniques magnétiques à base MET telles que la microscopie en contraste de phase[70,71,72,73] et l'holographie électronique off-axis[74,75] ont été développées. En EH, l'information magnétique est obtenue par la récupération de la phase de l'onde électronique. Le principe de EH a été proposé par Gabor[76,77], en 1949, pour surmonter l'aberration sphérique limitant la résolution de l'objectif. L'holographie électronique off axis est basé sur une expérience interférométrique dans un MET en superposant un faisceau d'électrons qui interagit avec l'objet avec un faisceau électronique non perturbé qui passe entièrement à travers le vide (onde de référence), ce qui permet l'extraction de l'information complète du faisceau électronique de sortie (amplitude et phase).

L'hologramme résultant est un ensemble de franges avec des variations de périodicité locales liées à la différence relative de la phase de l'onde objet et l'onde de référence. L'intensité de l'hologramme et le contraste est liée à l'amplitude de l'onde objet[78] et sa stabilité pendant le temps d'exposition. Pour mettre en oeuvre cette technique, le microscope électronique doit présenter une source d'électrons très cohérente associée à un biprisme à électrons pour créer la superposition des deux faisceaux[79,80]. Dans les dernières décennies, la généralisation d'une nouvelle génération d'instruments avec des sources d'électrons à haute luminosité cohérentes et stables tels que les canons Schottky ou à émission de champ froide (S-FEG et C-FEG) ont permis d'atteindre les cohérences nécessaires. Le biprisme électronique est généralement une fibre de verre

recouverte de Pt[81]. La superposition des ondes de référence et objet est obtenue par l'application d'une tension positive sur le biprisme.

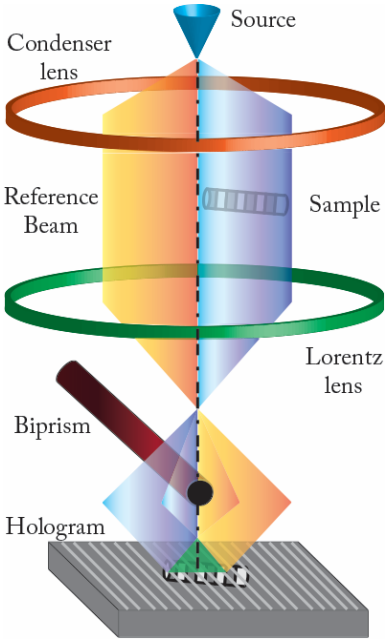

Figure 2 Configuration expérimentale en holographie électronique off axis

Méthodologie

Ce chapitre est consacré à la description détaillée de la méthodologie utilisée au cours de ce travail. La première partie de ce chapitre donne le processus détaillé d'élaboration de nanofils multicouches Co/Cu au LSI-Palaiseau. La seconde partie montre le processus pour effectuer holographie électronique (EH) et le traitement de l'hologramme pour obtenir les images de phase magnétiques. Enfin, le processus de simulations micromagnétiques est détaillé.

Synthèse des nanofils Co/Cu

Pour cette étude, les nanofils multicouches Co/Cu ont été élaborés par synthèse dans un template, en utilisant la technique de dépôt électrolytique par impulsions.

Le principe du montage est présenté sur la figure 3. L'objet dans lequel le dépôt aura lieu (membrane) est immergé dans un récipient contenant de l'électrolyte (solution aqueuse) et une contre-électrode, et la liaison des deux électrodes à une source d'alimentation externe permet de faire circuler le courant (potentiostat). L'objet à remplir est relié à une borne négative de l'alimentation électrique, de telle sorte que les ions métalliques sont réduits en atomes métalliques et déposés dans le template. Une électrode de référence est ajoutée à mesurer la tension réelle entre la contre-électrode et la membrane (Ag/AgCl).

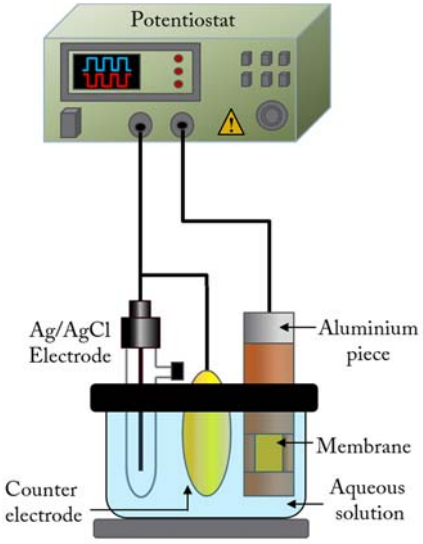

Figure 3 Montage permettant le dépôt des nanofils Co/Cu

Cu est l'élément le plus noble donc le plus facile à déposer et la plage de tension utilisée pour déposer le Cu se chevauche avec la tension à laquelle le Co est déposé. On obtient ainsi un dépôt simultané des deux métaux au cours du dépôt de Co. Afin de minimiser ce problème, la concentration de Cu dans la solution doit être très faible par rapport à la concentration de Co (moins de 3 % de la concentration en Co dans ce cas).

Des membranes de polycarbonate (fabrication commerciale, LLC) avec une taille de pores de 30 nm ont été utilisées pour le procédé de dépôt. Pour créer un contact électrique avec le substrat pour le dépôt des nanofils, une couche mince d'or de 100 nm d'épaisseur a été déposée par pulvérisation cathodique sur une face de la membrane comme représenté sur la figure 4.

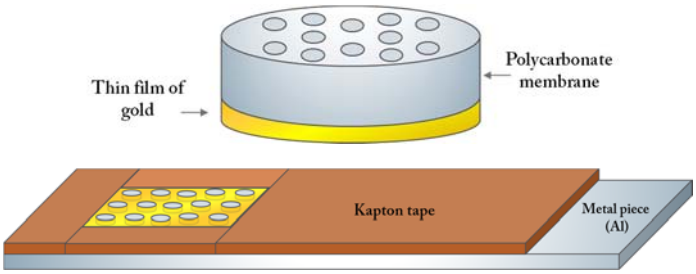

Figure 4 Schéma de la membrane de polycarbonate avec la couche mince d'or

Différentes épaisseurs de Co et de Cu ont été déposées en faisant varier la durée des impulsions. Sur la figure 5 la durée de chaque impulsion et l'épaisseur nominale est donnée.

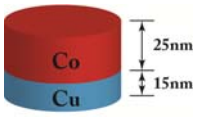

Échantillon M1	Co	Cu
Temps (s)	1.00	10.00
Épaisseur (nm)	25	15

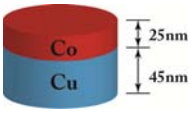

Échantillon M2	Co	Cu
Temps (s)	1.00	30.00
Thickness (nm)	25	45

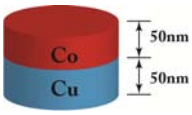

Échantillon M3	Co	Cu
Time (s)	2.00	35.00
Épaisseur (nm)	50	50

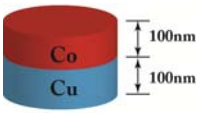

Échantillon M4	Co	Cu
Temps (s)	4.00	70.00
Thickness (nm)	100	100

Échantillon M5	Co	Cu
Temps (s)	300.00	0.00
Thickness (nm)	7500	

Figure 5 Liste des échantillons multicouches Co/Cu déposés

Etude de la configuration magnétique des nanofils Co/Cu

Le but de cette thèse est d'explorer les configurations magnétiques dans des nanofils magnétiques, principalement Co/Cu, à l'état rémanent à partir de deux directions de saturation de l'aimantation. Les fils ont ainsi été saturés selon l'axe du fil dans un premier temps, puis selon l'axe perpendiculaire au fil. L'application du champ selon les deux directions a nécessité un travail important de repérage des fils sur la grille de microscopie pour connaître leur alignement par rapport aux barreaux de grille et avoir un repère macroscopique avant l'application du champ.

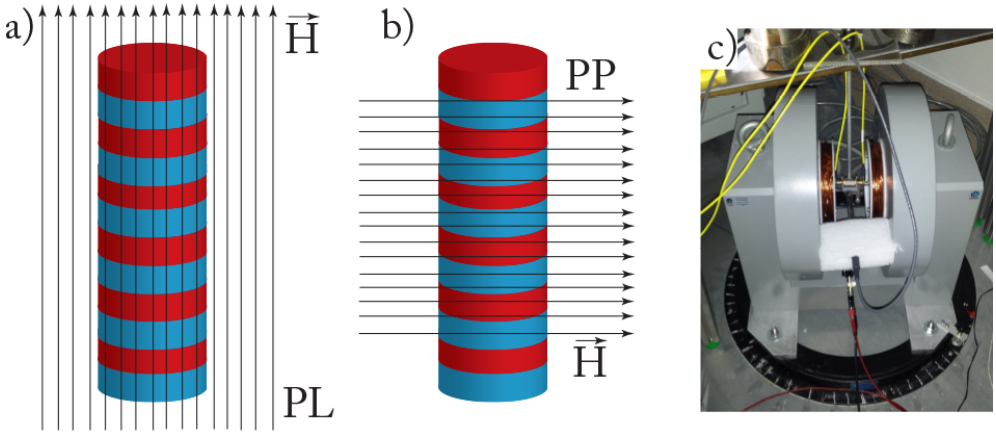

Figure 6 Schéma expliquant l'application du champ magnétique de saturation: a) parallèle (PL) and b) perpendiculaire (PP) par rapport au fil. c) électroaimant utilisé pour l'application du champ.

Les expériences d'holographie électronique off axis ont été effectuées sur le HF3300C (I2TEM) équipé d'un canon à émission froide pour atteindre une sensibilité de gradient de phase élevée et permettant de travailler en mode Lorentz corrigé pour atteindre une résolution spatiale sans précédent de 0,5 nm. Ce microscope comporte deux modes: un mode normal, où l'échantillon est placé entre les pièces polaires de l'objectif , et un mode Lorentz qui offre un environnement sans champ magnétique au niveau de l'échantillon tout en gardant l' objectif allumé.

Plusieurs fils de longueur micrométriques ont été étudiés pour chacune des configurations d'épaisseur de Co/Cu. Par exemple, une configuration magnétique de 20 nanofils a été étudiée à partir des 85 sélectionnés à l'aide d'observations classiques.

Un exemple d'hologramme enregistré sur un fil est proposé en figure 7. A partir de l'hologramme, un processus d'extraction de la phase magnétique est nécessaire. Il s'effectue en plusieurs étapes qui comprennent :

- l'utilisation de deux images de référence pour s'affranchir des distorsions liées au microscope et aux artefacts liés à l'erreur sur le choix de la fréquence spatiale liée à la périodicité des franges

- la séparation des contributions des phases électrostatiques et magnétiques.

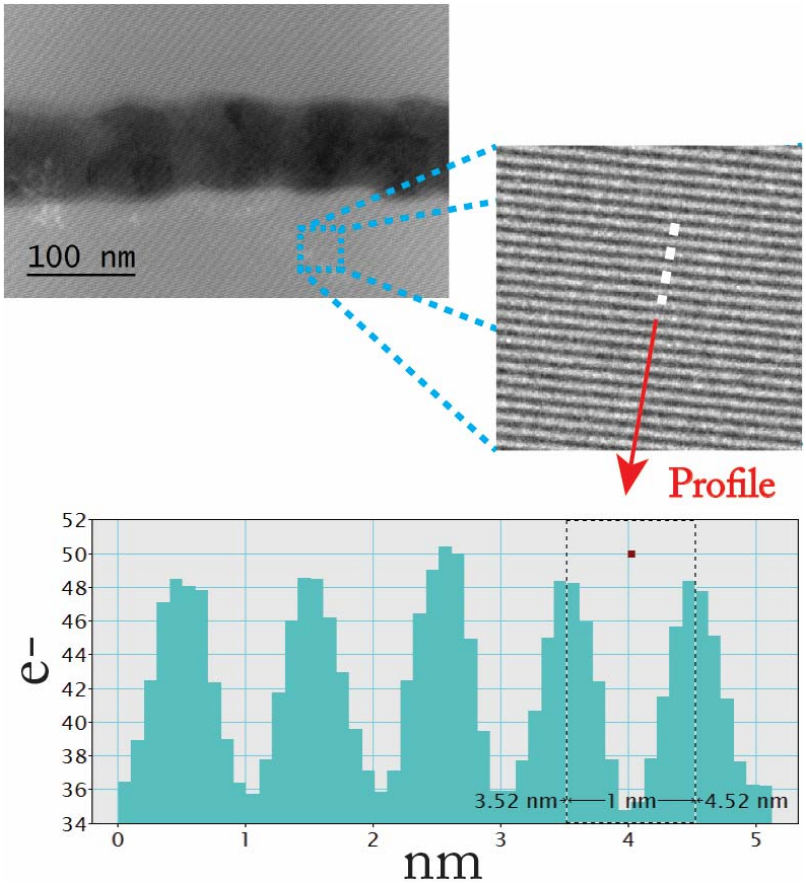

Figure 7 Hologramme obtenu sur un nanofil Co/Cu. Les franges d'interférences sont espacées de 1nm environ

Une fois le traitement effectué, il est possible à partir de l'image de phase de remonter à l'induction dans la couche, puisque :

$$\phi_{MAG}(x) = -\frac{e}{\hbar}\int_{-\infty}^{+\infty}\int_{-\infty}^{x} B_y(x',z)dx'dz$$

et en prenant le gradient

$$\frac{d\phi_{MAG}}{dx}(x) = -\frac{e}{\hbar}\int B_y(x,z)dz$$

Il est donc possible d'avoir accès à l'induction dans le plan d'observation, en gardant en tête que l'image de phase obtenue est la projection de la configuration magnétique le long de la trajectoire des électrons. Elle comprend donc les champs de suite situés au dessus et en dessous de l'échantillon et toute l'information magnétique contenue dans l'épaisseur du nanofil. Il en résulte deux points importants

- la mesure de l'induction peut être reliée à l'aimantation dans le fil si les champs de fuite sont négligeables

- différentes configurations magnétiques volumiques peuvent donner la même projection et la comparaison avec des simulations micromagnétiques est indispensable. Il est nécessaire de comparer qualitativement et quantitativement les profils de déphasage obtenus sur les nanofils.

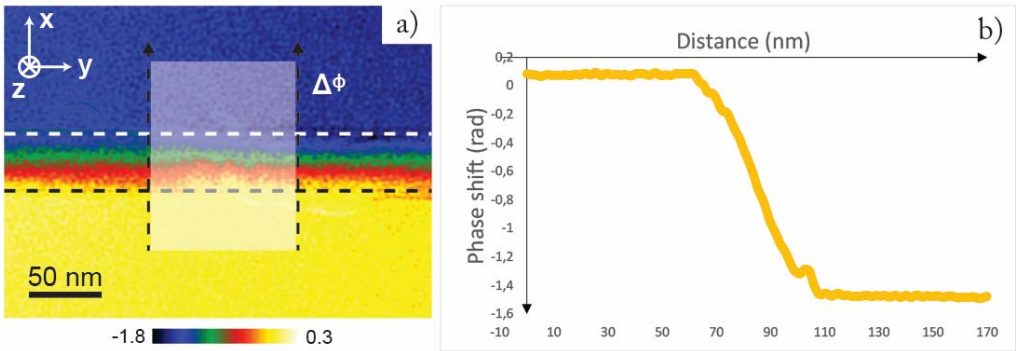

Figure 8 a) image de phase obtenue dans un nanofil après le processus de traitement et b) profil du déphasage – ces images expérimentales seront comparées à des simulations micromagnétiques.

Simulations micromagnétiques

Pour analyser plus profondément les résultats expérimentaux, les états magnétiques résiduels 3D et des champs parasites de 20 bicouches de Co/Cu ont été calculés simulé à l'aide du freeware 3D OOMMF[82] dans un univers de 1000 × 500 × 500 nm3 avec une taille de cellule de 2nm correspondant à la résolution spatiale des images magnétiques en phase expérimentale. Le champ de saturation est appliqué à 10 ° par rapport à l'axe Y ou X pour reproduire l'incertitude des conditions expérimentales.

Les paramètres géométriques obtenus à partir des études structurales et chimiques sont mises en oeuvre dans les calculs en 3D (moyenne angle de couches, l'épaisseur et le diamètre basculés). La caractérisation complète des nanofils d'un point de vue structural et chimique est donc primordiale.

L'aimantation des couches Co a été fixé à 1200 × 10^3A/m, qui est la valeur moyenne déterminée à partir des expériences d'holographie électronique sur des nanofils de Co simples issues du même bain électrochimique. Enfin, les paramètres magnétiques réglables dans les simulations sont la direction et l'amplitude de la constante d'anisotropie magnétocristalline, ainsi que la valeur d'échange A. Pour tenir compte de la nature polycristalline des couches Co, nous choisissons de définir un modèle simple avec une anisotropie magnétocristalline uniaxiale, qui est distribuée au hasard d' une couche à l'autre, au lieu d'une anisotropie cubique que pour les matériaux fcc.

La simulation donne accès à la configuration magnétique 3D comme indiqué sur la figure 9.

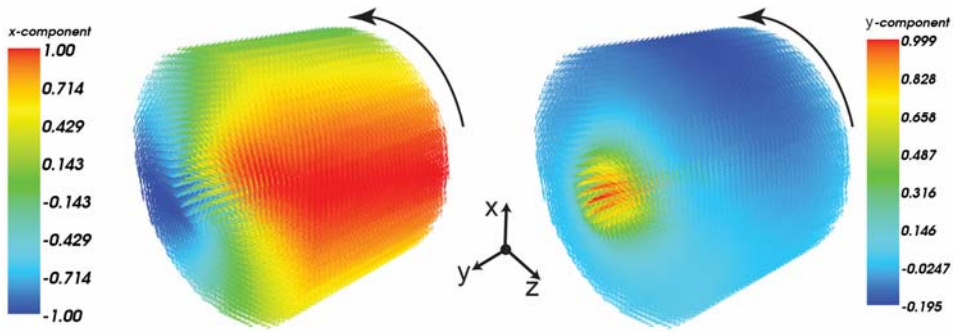

Figure 9 Composante x et z de l'aimantation d'un fil de cobalt.

Etude des nanofils multicouches Co/Cu

Comme présenté dans la partie méthodologie, plusieurs périodes de nanofils ont été étudiées. Dans ce résumé, seule une configuration (25/15) sera présentée

Analyse structurale et chimique d'un nanofil Co/Cu (25nm/15nm)

Une image en champ clair (BF) d'un nanofil Co/Cu (25nm/15nm) d'épaisseur nominale est présentée sur la figure 10. Le NW présente un diamètre moyen de 64 ± 4 nm. Le caractère polycristallin des couches de Co et Cu est montré par le diagramme de diffraction en aire sélectionnée (SADP). L'analyse des anneaux et l'espacement indiquent une structure fcc des phases polycristallines pour Co et Cu comme prévu lorsque du cuivre est inséré dans la couche de Co[83]. L'image haute résolution (HR) images confirment la structure polycristalline de Co et Cu avec des grains orientés aléatoirement de tailles de 7nm ± 2 (Figure 10b).

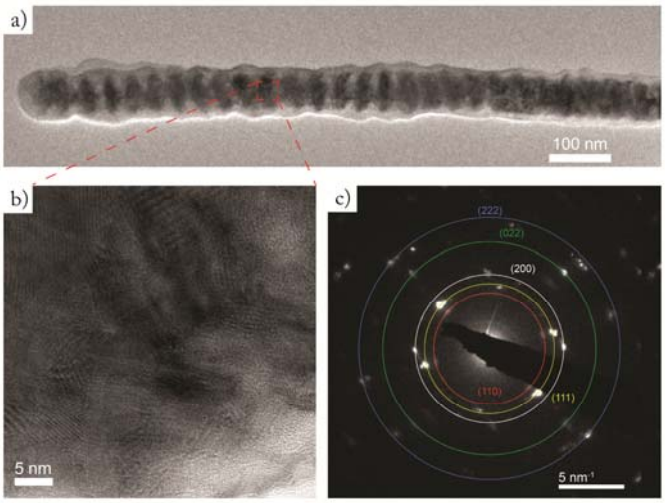

Figure 10 a) Image en champ clair d'un nanofileCo/ Cu (25nm/15nm), b) image MET haute résolution, c) cliché de diffraction d'une zone de cobalt

Le contraste entre les deux espèces chimiques de Z proche est faible et pour identifier clairement les couches de cobalt et de cuivre une analyse par imagerie filtrée en énergie (EFTEM) a complété les observations MET. Basée sur la spectroscopie de pertes d'énergie des électrons, le mode EFTEM permet d'obtenir des images des espèces chimiques présentes dans l'objet.

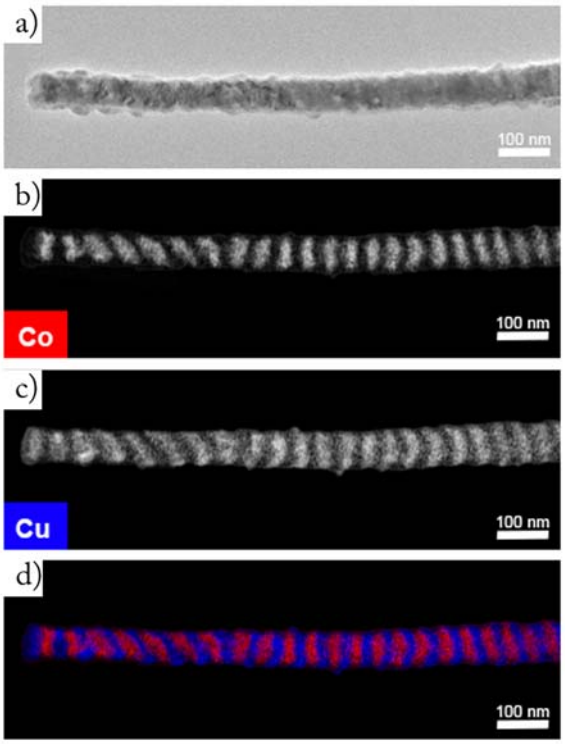

Figure 11 a) Image en champ clair d'un nanofileCo/ Cu (25nm/15nm), b) cartographie du cobalt, c) cartographie du cuivre, d) superposition des deux cartographies

Configurations magnétiques expérimentales d'un nanofil Co/Cu (25nm/15nm)

Comme discuté précédemment, 20 nanofils ont été étudiés, plusieurs configurations magnétiques ont été identifiées pour ces fils de même épaisseur nominale en cobalt et en cuivre.

Dans tous les cas, la même démarche a été suivie :

- image de microscopie en champ clair

- image filtrée en énergie avec le cobalt et le cuivre

- mesures en holographie électronique des déphasages magnétiques à l'état rémanent pour les 2 directions de saturation.

- simulations micromagnétiques pour expliquer l'image de phase expérimentale.

La figure 12 présente les résultats sur une portion de fil de 64 ± 2nm de diamètre. Les figure 12a) et figure 12b) montrent l'hologramme et la cartographie chimique. Les déphasages obtenus à partir des hologrammes sont présentés en figure 12c) et figure 12d). Elles correspondent respectivement aux états magnétiques rémanents des mêmes couches, pour un champ appliqué perpendiculairement (définie comme étant la direction X) et parallèle (direction Y) par rapport à l'axe du fil. Les positions des couches Co et Cu déduites des cartes chimiques EFTEM ont été ajoutées pour plus de clarté sur chaque figure. On peut observer clairement que les deux états rémanents expérimentaux sont différents en fonction de la direction du champ appliqué. La figure 12c) montre une alternance de contraste correspondant à l'aimantation dans des directions opposées X d'une couche de Co à l'autre. Sur la figure 12 d), les lignes d'isophases sont parallèles à la direction Y et reflètent une induction intégrée alignée selon l'axe du fil.

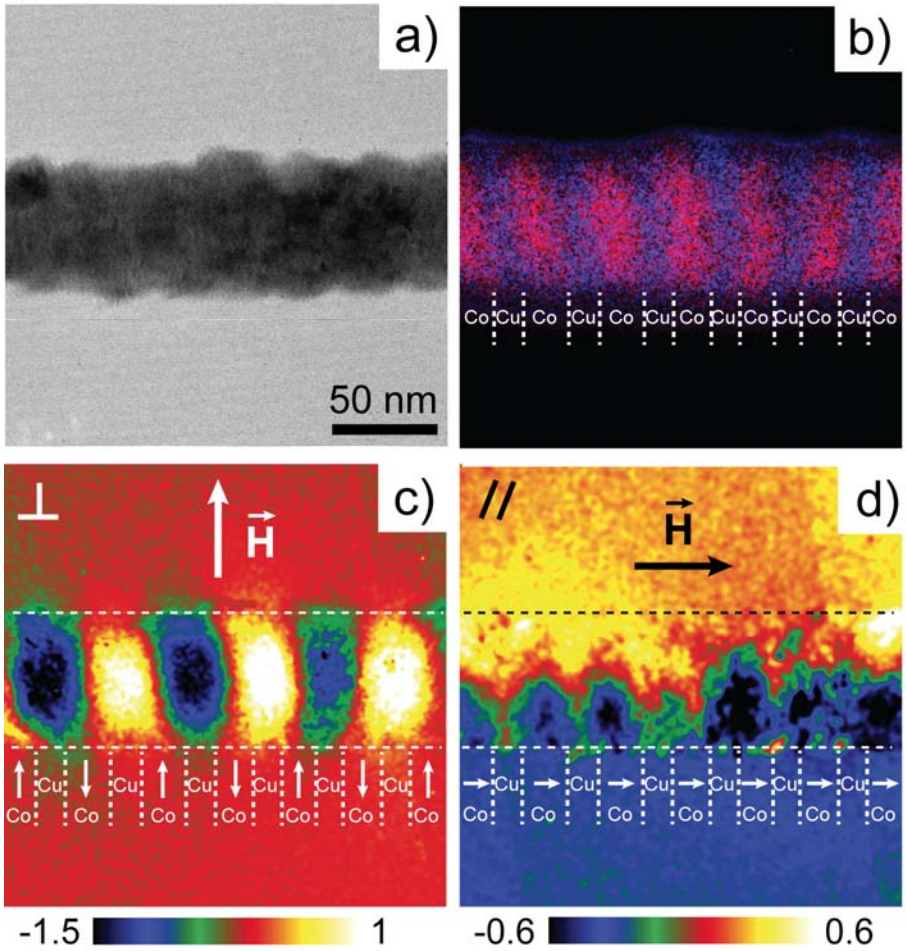

Figure12 Nanofil Co/Cu (25nm/15nm) : a) Hologramme du fil observé. b) image EFTEM de la même zone pour distinguer le cuivre (bleu) et le cobalt (rouge). c) image de phase magnétique obtenue après l'application du champ de saturation perpendiculaire par rapport à l'axe du fil. d) image de phase magnétique obtenue après l'application du champ de saturation parallèle à l'axe du fil.

Sur les figures 13 et 14, les résultats des simulations micromagnétiques appliquées à la partie en cours d'étude pour la configuration PL et PP sont présentés. Nous avons comparé l'amplitude de déphasage et non l'induction magnétique à cause du problème d'intégration. L'état rémanent dans la figure 13 correspond à un couplage antiparallèle des aimantations dans les couches de Co. La variation du déphasage est située dans les couches de Co et reste le même dans les couches de Cu où aucun signal magnétique est présent. Il est intéressant de noter que l'amplitude varie d'une couche à l'autre. La direction d'aimantation dans chaque couche individuelle Co est légèrement différente

en raison de la direction d'anisotropie répartie de façon aléatoire dans chaque couche. Ici, ce paramètre a été ajusté avec succès pour quelques couches pour s'accorder à l'expérience. Enfin, la figure 13d) montre la configuration 3D pour l'aimantation résultant des simulations micromagnétiques. L'échelle de couleur représente la composante de l'aimantation le long de l'axe X.

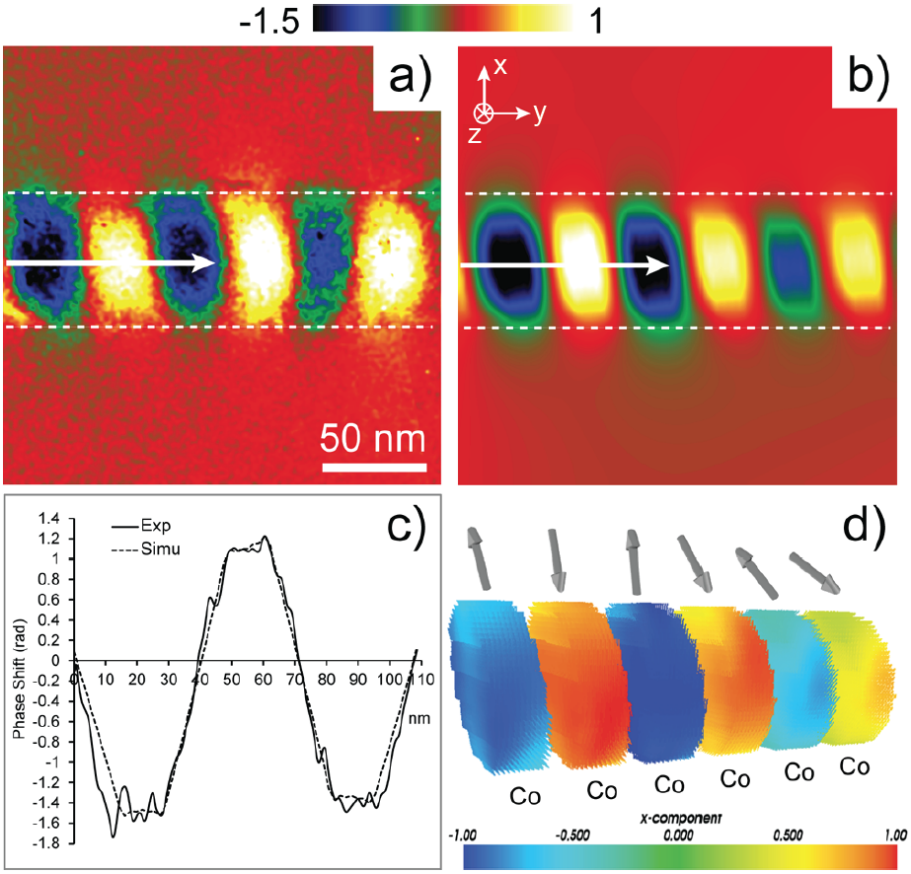

Figure 13. Configuration magnétique pour le nanofil Co/Cu (25nm / 15n) : a) image de phase magnétique expérimentale extraite des hologrammes , b) image de phase simulée, c) comparaison des profils expérimentaux et simulés de l' image de phase magnétique obtenu le long de la flèche blanche en a), d) configuration magnétique 3D des couches de cobalt correspondant à l'image b)

L'état rémanent dans la figure 14 correspond à un vortex magnétique dans chaque couche de cobalt, avec les cœurs de vortex pointant le long de l'axe du fil (figure 14d). L'intégration de l'aimantation sur l'axe d'observation permet d'observer seulement le cœur de ces vortex car les autres composantes du vortex sont compensées. Au sujet des

simulations micromagnétiques de la figure 14d), il convient de mentionner que les vortex montrent souvent une orientation alternativement droite et gauche en raison du couplage intercouche initial. Il convient également de noter que la polarité des vortex est dirigée vers le haut (si l'on définit comme quand il est orienté dans la direction + Y et vers le bas dans la direction -Y) . Cependant, dans les images de déphasage expérimentales, il est impossible de discerner entre ces orientations.

Ces résultats sont directement basés sur la comparaison quantitative des images et profils de déphasage entre les images d'holographie électronique et les simulations micromagnétiques.

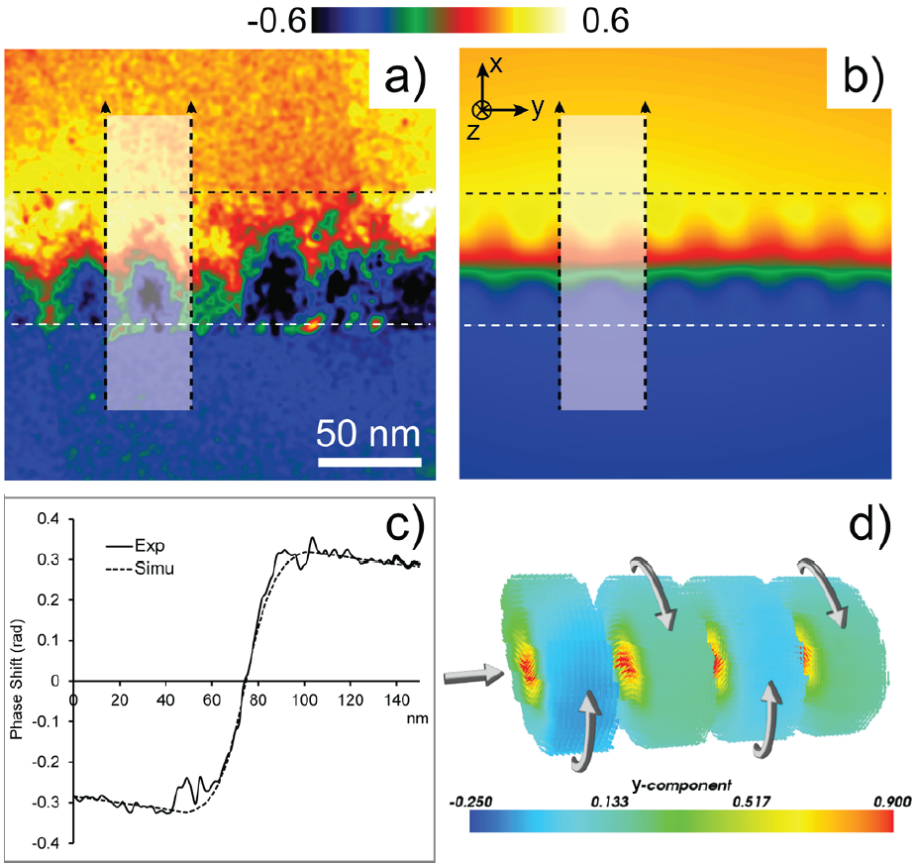

Figure 14. Configuration magnétique pour le nanofil Co/Cu (25nm / 15nm) : a) image de phase magnétique expérimentale extraite des hologrammes. b) image de phase simulée. c) comparaison des profils expérimentaux et simulés du déphasage magnétique obtenu le long de la flèche blanche en a) . d) configuration magnétique 3D des couches de cobalt correspondant à l'image b)

Pour obtenir un tel accord quantitatif dans les deux configurations (état antiparallèle et vortex), la constante d'échange A a été fixée à 22×10^{-12} J/m. Cette valeur d'échange est particulièrement importante car elle définit (également avec la constante d'anisotropie, mais dans une bien moindre mesure) la taille du coeur du vortex. Comme la composante de l'aimantation alignée dans la direction Y définit l'amplitude du déphasage, une corrélation directe entre l'amplitude de déphasage et la constante d'échange à l'état vortex peut être établie. Pour reproduire la transition entre l'état antiparallèle et vortex couplés, la constante d'anisotropie a été réglée sur 100×10^{3}J/m^{3}, et la direction de l'anisotropie a été distribuée au hasard d'une couche à l'autre dans un cône avec un angle d'ouverture de 20 ° de la normale des couches.

Le couplage antiparallèle est la configuration la plus difficile à obtenir (Figure 13). En effet, si la distribution aléatoire de l'axe d'anisotropie a un petit effet sur l'amplitude des vortex, son impact sur l'orientation de l'aimantation dans l'état antiparallèle, et donc sur le déphasage lié, est important. En effet, l'amplitude de déphasage sera maximale (respectivement minimale) si l'aimantation est alignée avec la direction X (respectivement Z). Ceci peut être expliqué par le fait que l'EH n'est sensible qu'aux composantes dans le plan de l'aimantation. Alors que le comportement global des nombreuses couches est reproduit fidèlement, il est très difficile de récupérer les directions d'anisotropie de toutes les couches en ajustant quantitativement le signal expérimental. Cependant, nous montrons que notre méthode est assez puissante pour récupérer les paramètres magnétiques des différentes couches.

Comme déjà mentionné dans la partie Méthodologie, notre modèle pour les simulations micromagnétiques est simplifié pour tenir compte de la polycristallinité des couches (anisotropie uniaxiale au lieu de cubique pour les matériaux cfc). Alors que la diminution de l'aimantation peut être expliquée par des impuretés de Cu dans le Co, les valeurs inférieures des constantes d'échange et anisotropie ont été observées dans d'autres études [84,85,86,87]. Par exemple, Henry et al.[84] ont trouvé que l'axe d'anisotropie d'un nanocylindre de Co hcp passe de perpendiculaire à parallèle à l'axe du fil pour une valeur de diamètre critique d'environ 60 nm, ce qui conduit à une diminution de la constante d'anisotropie

mesurée jusqu'à 200 x 10^3J/m à la transition du fait de la distribution aléatoire des grains. Dans notre étude, nous croyons que nous rencontrons une situation similaire. Il convient de rappeler que les paramètres d'échange et d'anisotropie que nous déduisons ici reposent sur la valeur d'aimantation moyenne de 1200 × 10^3 A/m fixée pour les simulations. Pour un autre ensemble de paramètres, on peut obtenir des valeurs légèrement différentes.

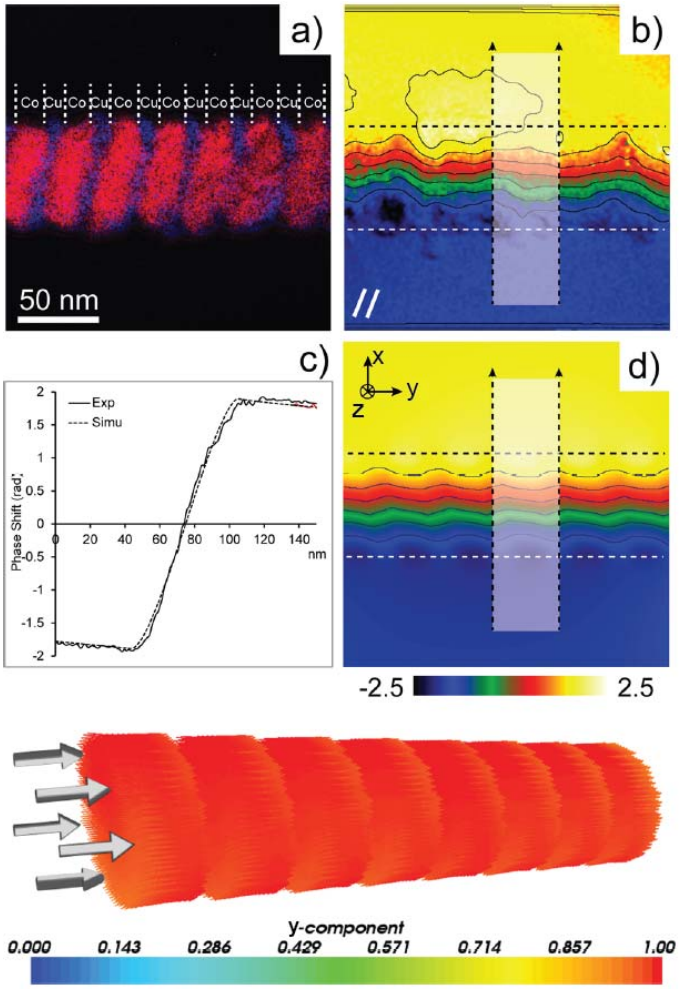

Figure 15. Configuration magnétique pour le nanofil Co/Cu 25nm / 15nm): a) image EFTEM du fil étudié . b) image de phase magnétique expérimentale avec les lignes d'induction correspondant (en noir) c) comparaison des profils expérimentaux et simulés du déphasage obtenu pour les rectangles dessinés en b) et d) . d) image de phase simulée du déphasage avec les lignes d'induction correspondant (en noir). e) configuration magnétique 3D des couches de cobalt correspondant à l'image de phase simulée d).

En reproduisant notre méthodologie pour les 20 fils différents, nous démontrons qu'un autre état magnétique peut apparaître dans d'autres nanofils pour cette configuration Co/Cu de 25nm/15nm. En plus des configurations antiparallèles et vortex présentées précédemment, nous avons également observé un état monodomaine-like pour lequel toutes les aimantations des couches Co sont orientées uniformément dans la direction de l'axe du fil (Figure 15). L'image de phase présente des caractéristiques similaires à celles des vortex couplés, mais l'amplitude du déphasage extrait sur la période Co/Cu est ici environ trois fois plus élevé. Ensuite, il est intéressant de noter que discrétisation entre vortex et états monodomaines ne peut se faire que par la comparaison quantitative des profils de décalage des phases calculées et mesurées.

Enfin, nous pouvons également faire des statistiques sur les différents états magnétiques dans cette configuration Co/Cu (25nm/15nm) en fonction de la direction du champ de saturation. Tout d'abord, si la direction d'anisotropie moyenne dans les couches de Co est essentiellement dans le plan, les aimantations resteront dans le plan quelle que soit la direction du champ appliqué avec un couplage antiparallèle préféré en raison de l'interaction dipolaire entre des couches de Co. Cette configuration est la plus commune dans nos fils (≈70%). Si la direction d'anisotropie est principalement orientée autour de la normale des couches, plusieurs configurations peuvent se présenter. Si l'effet combiné de l'anisotropie magnétocristalline et du couplage dipolaire entre les couches est suffisant pour contrebalancer l'anisotropie de forme, les aimantations présentent un comportement monodomaine. Cette configuration a été obtenue en quelques fils (≈10%) et a été reproduite dans les simulations (comme par exemple dans la figure 15e) pour une constante d'anisotropie supérieure à 200×10^3 J/m et une direction orientée aléatoirement autour de la normale des couches de Co dans un cône ayant un angle d'ouverture allant jusqu'à 20°. Il est intéressant de noter que de telles valeurs d'anisotropie et de direction sont similaires à celles observées pour du cobalt hcp électrodéposé. En général, dans les nanofils avec une texture polycristalline, le cobalt présente de nombreux défauts structuraux comme des fautes d'empilement. Il peut devenir difficile de faire la différence entre les structures hcp et fcc: il est alors possible d'obtenir du cobalt polycristallin avec des propriétés structurelles essentiellement

similaires à fcc mais avec quelques caractéristiques magnétiques correspondant à une structure hcp. Pour des valeurs inférieures de la constante d'anisotropie, l'anisotropie magnétocristalline aura toujours tendance à garder l'aimantation hors du plan, mais l'anisotropie de forme va pousser la rotation perpendiculairement à l'axe du fil. Cela conduit à la transition entre les vortex lorsque le champ est parallèle à l'axe du fil à un couplage antiparallèle pour le champ perpendiculaire. Cette configuration apparaît pour environ 20% des fils. Typiquement, de telles transitions magnétiques apparaissent si la constante d'anisotropie est inférieure à 180×10^3 J/m et si l'anisotropie est distribuée avec une ouverture de 40° du cône.

Etude des nanofils FeCoCu à diamètre modulé

Un intérêt croissant se développe ces dernières années pour la recherche de nouveaux nano-objets magnétiques permettant le contrôle de mouvement des parois de domaines magnétiques. Des nanostructures unidimensionnelles telles que les nanofils ferromagnétiques isolés ou des nanostripes sont utilisées pour obtenir une manipulation précise des parois de domaine, soit par l'application de champs magnétiques ou par l'injection de courant électrique. La modulation de diamètre de nanofils cylindriques devrait être efficace pour contrôler la propagation des parois. Des simulations micromagnétiques et Monte Carlo[88,89,90,91] ont montré que cette modulation du diamètre peut en effet bloquer la propagation.

Dans ce chapitre, nous avons exploité le potentiel de l'holographie électronique off-axis et des simulations micromagnétiques pour effectuer une caractérisation magnétique quantitative à haute résolution de nanofils cylindriques de FeCoCu NFs à diamètre modulé. La possibilité de reconstruire la distribution de l'induction à l'intérieur (aimantation) et à l'extérieur (champs parasites) du nanofil permet une compréhension plus profonde des caractéristiques géométriques optimales pour obtenir une propagation de parois de domaines contrôlée.

Analyse structurale et chimique des nanofils FeCoCu

Les études de la morphologie du fils à diamètre modulé ont été réalisées par MET haute résolution (HRTEM), grâce au microscope Hitachi HF-3300 (I2TEM).

Les images MET en champ clair de la figure 16 illustrent la morphologie des deux fils caractéristiques. Parmi les nombreux nanofils déposés sur la grille MET de carbone, les plus longs (un exemple est proposé sur la figure16a) sont d'environ 13µm de long, mais la plupart des nanofils ressemblent au fil de figure16b) avec des longueurs intermédiaires entre 3 et 8µm. Ces nanostructures 1D sont formées par des segments de petit diamètre (SD, environ 100 nm) et de grand diamètre (LD, environ 140-144 nm) en alternance, avec une variation de diamètre progressive. Si nous passons de droite à gauche le long du nanofil sur la figure16a), nous voyons que la longueur des SD et LD segments est progressivement réduite, avec une variation plus marquée pour les segments LD. Cette variation géométrique précédemment observée dans les nanofils de Co de diamètre modulé, également fabriqué par dépôt électrolytique dans les modèles AAO, est attribuée à une déformation plastique et aux instabilités mécaniques sur le substrat d'aluminium[92].

A partir des observations présentées en figure 16 a) et b), on en déduit que les nanofils de longueur intermédiaire sont en fait des morceaux plus longs qui sont sectionnés lors de l'extraction de la membrane.

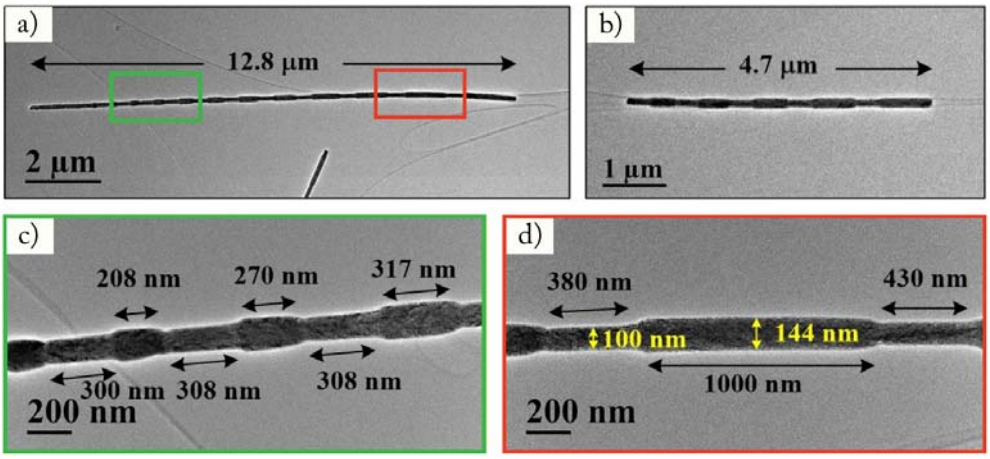

Figure 16. Images MET champ clair de deux fils FeCoCu à diamètre modulé de a) 13 µm et b) de 4,7 µm de longueur . Les diamètres des nanofils et les longueurs de segments sont mesurés à partir des images à fort grandissement en MET correspondant aux zones rectangulaires en a). c) et d) illustrent le changement progressif de la longueur des segments.

L'analyse de la microstructure des fils a été effectuée en mode MET haute résolution comme indiqué sur la figure 17. Les micrographies ne révèlent pas une structure monocristalline claire ni aucune texture sur une longue distance. Au lieu de cela, les fils présentent une structure polycristalline formée par des nanocristaux de différentes tailles dans la gamme de quelques nanomètres. Les transformées rapides de Fourier (FFT) des images de de la Figure 17 présentent des anneaux de diffraction, qui sont les signatures des structures polycristallines à grains orientés de façon aléatoire. L'indexation des spots dans la FFT est en accord avec la structure bcc du FeCoCu pour cette composition[93]. En outre, la surface des nanofils est recouverte d'une couche d'amorphe de 2 à 3 nm d'épaisseur. Cette couche amorphe superficielle formée par un procédé d'oxydation de surface a été observée précédemment dans des nanofils FeCoCu par Iglesias-Freire et al.[94]. La même couche d'oxydation a été confirmée par STEM-EELS sur des fils multicouches FeCoCu/Cu NFs par Palmero et al.[95]. Ils ont trouvé une couche d'environ 9 nm d'épaisseur autour des segments FeCoCu et 4 nm pour les couches de Cu.

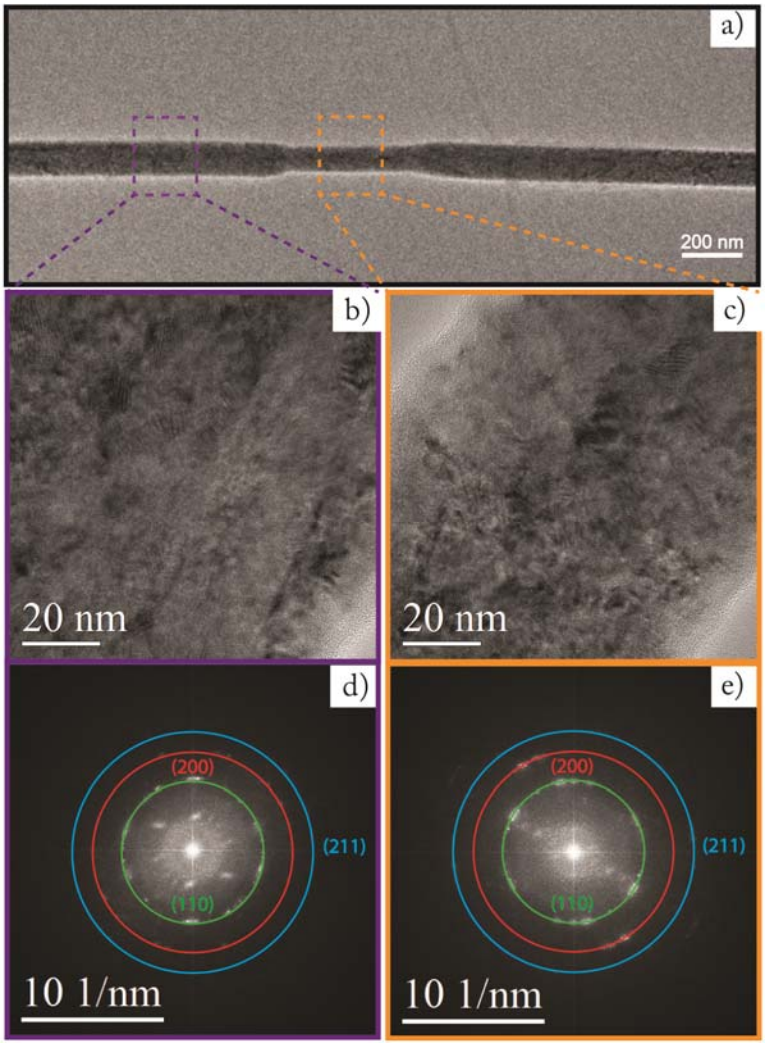

Figure 17 a) Image en champ clair à faible grandissement de carte segments SD et LD. b)et c) images en mode haute résolution de zones LD et SD respectivement. d) et e) Transformées de Fourier des images b) et c)

Cartographie de l'aimantation par holographie électronique

Les expériences d'holographie électronique (EH) ont été réalisées en utilisant le Hitachi HF-3300 décrit précédemment. Dans cette étude, nous avons utilisé le mode Lorentz TL11 corrigé: l'échantillon est introduit à l'intérieur de la gonio normale de l'I2TEM, mais l'objectif est éteint. La première lentille de transfert du correcteur (TL11) est utilisée comme lentille objectif. Les nanofils sont étudiés sans champ, ce qui permet d'atteindre un très grand champ de vue allant jusqu'à 1,3 µm, avec un espacement de

franges des hologrammes de 1,72 nm. En outre, la configuration à double biprisme a été utilisée pour éviter les franges de Fresnel.

La figure 18a) et b) montre des images d'amplitude et de phase magnétique dans une région intermédiaire du nanofil de la figure 17. En outre, les deux images de flux magnétique, ⊠(x, y), sont également présentés à la figure 18c) et d). Comme observé dans l'image d'amplitude dans la figure 18a), la zone étudiée contient une partie du fil composé par quatre répétitions de SD et LD segments avec des longueurs comprises entre 300-270 nm et 430-300 nm, respectivement.

L'image de phase magnétique de la figure 18b) présente une forte variation (forte de changement de couleur) dans le nanofil, le long de la direction Y. Comme nous l'avons déjà dit, ce changement de déphasage le long de la direction Y implique une induction magnétique orientée selon la direction X, dans ce cas, l'axe du nanofil. Ce fait peut être facilement visualisé dans l'image de flux magnétique de la figure 18c) où la direction des lignes de flux dans les nanofils semble montrer un alignement longitudinal de l'aimantation. Cependant, il existe une légère différence dans la configuration des lignes de flux: à l'intérieur des segments SD, les lignes sont parfaitement parallèles à l'axe du nanofil, tandis qu'à l'intérieur des segments LD elles sont tordues à mesure que l'on s'approche des bords. Cette observation suggère que l'alignement longitudinal de l'aimantation varie dans les segments LD. Une configuration d'aimantation monodomaine est l'un des états rémanents attendus dans des nanofils cylindriques en raison de la forte anisotropie de forme longitudinale: cette anisotropie de forme est beaucoup plus forte que l'anisotropie magnétocristalline et force l'aimantation à être orientée parallèlement à la dimension la plus longue pour réduire l'énergie magnétostatique.

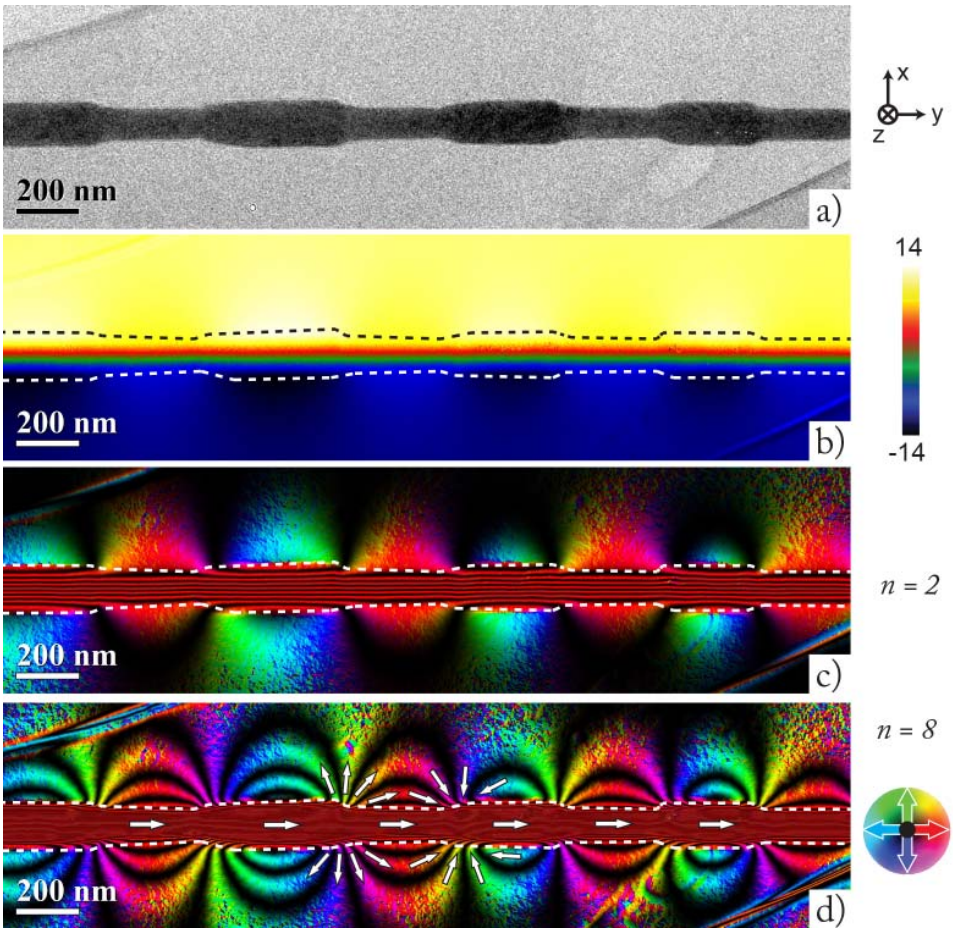

Figure18 Analyse expérimentale du déphasage magnétique produit par l'induction magnétique d'un nanofil isolé de FeCoCu de diamètre modulé: a) image d'amplitude , b) cartographie de la phase magnétique reconstruite pour une section du nanofil , c) et d) images de flux magnétique reconstruits à partir des images de phase magnétique, en utilisant comme facteur d'amplification , respectivement de n = 2 et n = 8 . Les couleurs dans les images de flux magnétique indiquent la direction de l'induction magnétique en fonction de la roue de couleur insérée à côté de d) . Les flèches blanches sur d) sont des guides pour visualiser l'orientation locale de l'induction magnétique dans le plan prévu à l'intérieur et autour du NW.

Simulations micromagnétiques

Comme les expériences d'holographie électronique ne fournissent que des informations sur l'induction magnétique intégrée le long de l'axe d'observation, une description précise de la configuration 3D de spin local a été réalisée grâce des simulations micromagnétiques statiques en utilisant le code OOMMF. Les paramètres magnétiques

suivants ont été utilisés: l'aimantation à saturation M_s = 1060x10^3 A/m ($\mu_0 M_S \approx 1.33T$), la constante d'échange A = 26 × 10^{-12}J/m. La constante d'anisotropie a été négligée (K = 0) en raison du caractère polycristallin des nanofils. Pour ces simulations micromagnétiques, un modèle 3D d'un nanofil de 2,6 µm a été construit par empilement de cellules d'unité magnétique de 5 × 5 × 5nm^3. Pour simuler les champs parasites entourant le nanofil, les dimensions latérales (selon les directions X et Y) ont été choisies plus grandes que le diamètre du nanofil, laissant un espace vide d'environ 100-200 nm entre les surfaces du nanofil et les frontières de l'univers. Pour effectuer les calculs de simulation, le nanofil se trouve dans un état d'aimantation initiale où tous les spins sont parfaitement orientés selon l'axe Y; la simulation statique s'exécute ensuite à l'aide d'un correcteur de prédiction du second ordre jusqu'à ce que l'énergie totale du système atteigne un minimum défini.

La configuration magnétique a été obtenu sur un fil de 2,6 µm de longueur composé de quatre répétitions de segments SD et LD pour réduire le temps de calcul. Le diamètre varie entre 100 et 140 nm, et la longueur de chaque type de segment a été maintenue constante avec des valeurs de 300 nm (segment SD) et 250 nm (segment LD), et une variation linéaire de diamètre de 50nm. En outre, nous avons construit le nanofil avec des extrémités de diamètre différent afin d'évaluer leur influence sur l'orientation de l'aimantation locale. Les paramètres géométriques tels que la taille et la forme du nanofil, ainsi que la taille de l'univers simulé, sont schématiquement illustrés sur la figure 19.

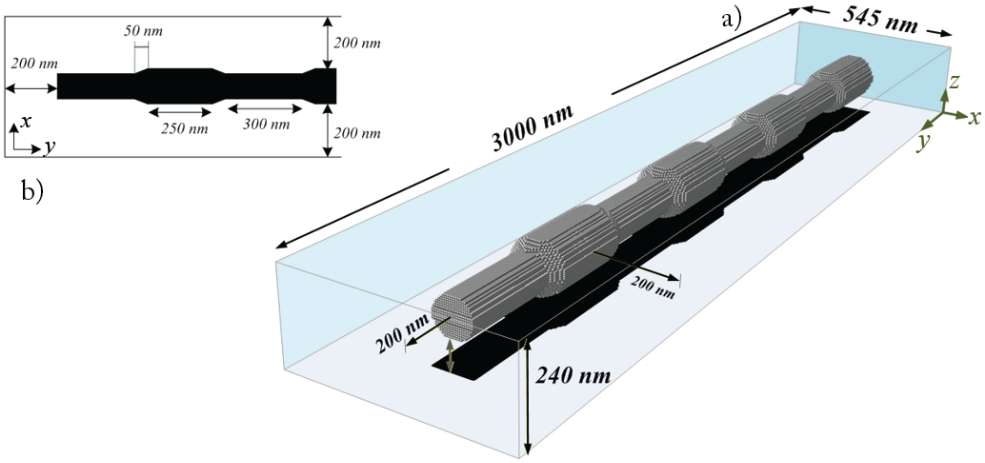

Figure 19 a) vue en perspective de la géométrie 3D utilisée dans les simulations micromagnétiques. La région grise représente le corps aimanté (nanofil) et la boîte transparente indique l'univers de la simulation. L'ombre noire correspond au plan de projection XY du nanofil. b) Zoom d'une partie de l'ombre noire pour voir la dimension latérale de l'univers de la simulation à mi-hauteur (z = 120 nm)

La figure 20b) montre le déphasage simulé magnétique et la figure 20c) et d) les images du flux magnétique avec le facteur d'amplification n = 2, n = 8. L'optimisation de l'adéquation entre expérience et simulation a été obtenue en ajustant certains des paramètres magnétiques utilisés dans la simulation micromagnétique tels que M_s l'aimantation à saturation, et la constante d'échange A, et en effectuant une comparaison quantitative entre les images expérimentales et simulées du déphasage magnétique à travers des profils tracés perpendiculairement à l'axe du nanofil .

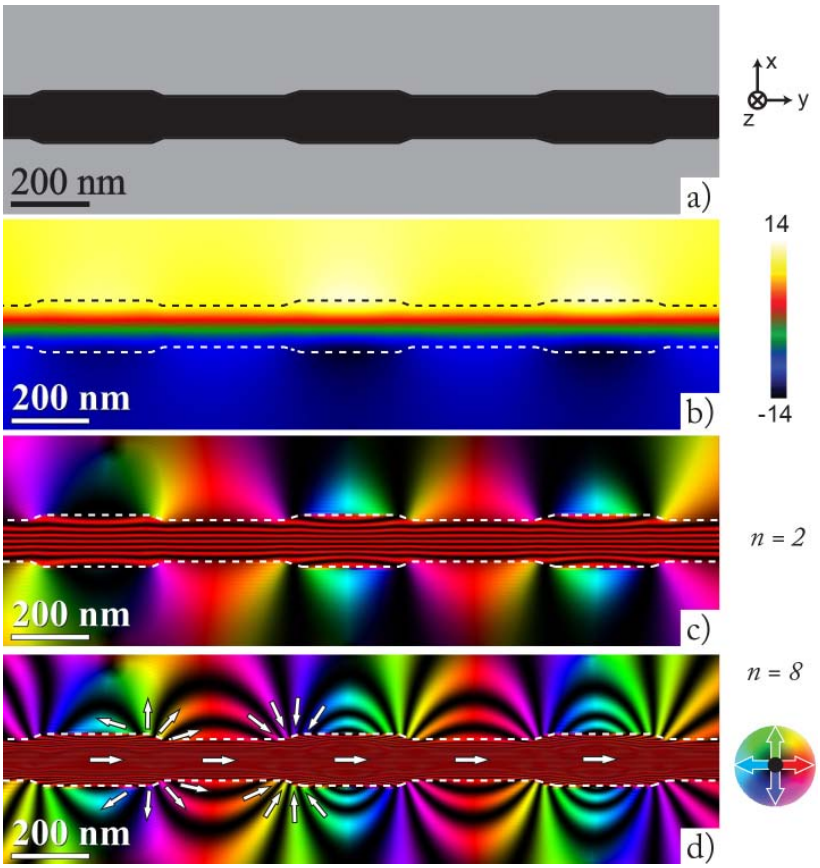

Figure 20 a) image d' amplitude obtenue à partir de la simulation micromagnétique , b) carte du déphasage pour une section du NW , c) et d) images de flux magnétiques reconstruits à partir des images de déphasage magnétique, en utilisant comme facteur d'amplification , respectivement de n = 2 et n = 8 . Les couleurs dans les images de flux magnétique indiquent que la direction de l'induction magnétique en fonction de la roue de couleur insérée à côté à d) . Les flèches blanches à d) sont des guides pour visualiser l'orientation locale de l'induction magnétique dans le plan prévu à l'intérieur et autour du NW .

La figure 21c) montre des profils de déphasage magnétique expérimental et simulé pris au milieu d'un segment SD et LD. Le meilleur accord pour les paramètres magnétiques est obtenu en simulant l'état magnétique rémanent avec les paramètres magnétiques mentionnés précédemment. Ces résultats correspondent aux valeurs rapportées pour le Fe30Co70[96,97]. Cette valeur de l'aimantation de saturation est inférieure à celle mesurée par VSM dans des réseaux de nanofils FeCoCu[98]. Cette valeur inférieure peut être attribuée en partie à la concentration particulière de Cu dans cette étude. Par ailleurs l'estimation du diamètre et de la forme réelle des segments est un problème pour le calcul

quantitatif de l'aimantation à saturation. Nous supposons en effet une forme cylindrique parfaite pour le calcul de l'induction magnétique. Quelques nanomètres dans l'estimation du diamètre peuvent faire la différence entre la valeur de l'induction magnétique rapportée ici et celle rapportée par Bran et al.[98] pour la même concentration de FeCoCu. Enfin, le VSM mesure l'aimantation moyenne à saturation due à la contribution d'un millier de nanofils.

Les profils magnétiques de la figure 21c) présentent une forte dépendance linéaire à l'intérieur du nanofil et de petites variations en dehors de celui-ci. A l'intérieur du fil, les deux profils présentent une pente positive similaire en raison de la structure presque monodomaine du nanofil. En dehors du fil, une nette différence peut être observée entre les profils magnétiques dans les deux segments: une variation positive se produit dans le profil extrait de la partie extérieure du segment SD tandis qu'une variation négative est obtenue autour du segment de LD. Le déphasage magnétique observé en dehors du nanofil est causée par le champ magnétique parasite présent autour de lui, et les différentes variations du déphasage le long de la direction Y suggèrent un changement de l'orientation du champ de fuite local du secteur SD à un segment de LD. Pour cartographier le champ de dispersion dans le plan projeté nous reconstruisons des images de flux magnétique en utilisant un facteur d'amplification plus élevé de n = 8, comme on peut le voir dans la Figure 18 et Figure 20d). Nous remarquons que la géométrie de diamètre modulé induit une configuration complexe de champ démagnétisant où le champ parasite émerge/pénètre sur le fil dans les zones de changements les diamètres. Cette configuration de champ parasite suggère que chaque variation de diamètre agit comme une charge magnétique positive ou négative, qui contrôle la configuration locale du champ démagnétisant.

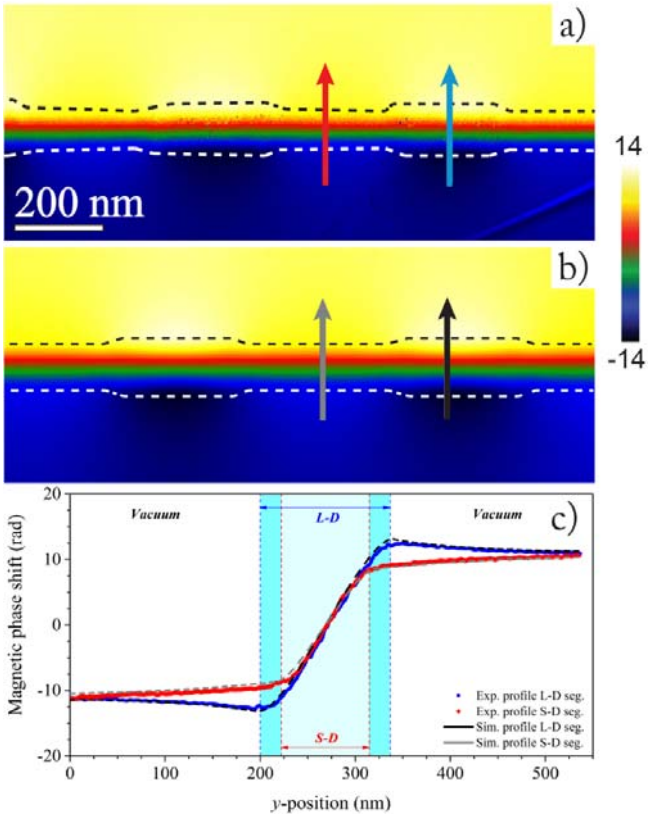

Figure 21 a) image expérimentale et b) et simulée de la phase magnétique. c) Profils extraits des images de phase magnétiques dans les SD et LD segments où les flèches sont tirées.

Grâce à une analyse locale, nous avons trouvé que cet arrangement de charge magnétique produit une configuration de flux de fermeture du champ démagnétisant autour des segments LD. Cette distribution magnétique reste ressemble à celle observée par Lopatin et al.[98] et Ivanov et al.[100] dans fils segmentés Co/Ni NFs, où une variation de composition crée une modulation de l'amplitude d'aimantation. Deux raisons sont évoquées : le moment magnétique de Co est de 3 fois supérieure à celle de Ni et l'anisotropie magnétocristalline est orientée dans des directions différentes. Ainsi, cette modulation d'aimantatio favorise la formation de pôles magnétiques dans les interfaces de Co-Ni qui agissent de manière similaire à celles du diamètre modulé dans les nanofils FeCoCu.

Conclusion

L'objectif principal de cette thèse est l'étude des états magnétiques locaux dans des nanofils à base de cobalt à l'état rémanent. La comparaison entre les mesures d'holographie électroniques et les simulations micromagnétiques ont permis une étude quantitative et qualitative de ces états magnétiques.

Co/Cu nanofils multicouches

Les nanofils magnétiques multicouches Co/Cu ont été synthétisés par dépôt électrolytique dans des membranes en polycarbonate. Différentes épaisseurs Co/Cu ont été étudiées: 25nm/15nm, 25nm/45nm, 50nm/50nm et 100nm/100nm.

Un soin particulier a ensuite été apporté pour localiser et sélectionner les nanofils sur la grille de MET afin de préciser leur orientation par rapport à un axe défini sur cette grille. Ceci permet en premier lieu d'appliquer un champ magnétique perpendiculaire (PP) et parallèle (PL) aux axes des fils. Des expériences en champ clair, EFTEM et EELS ont révélé la composition exacte, l'épaisseur et la forme de chaque couche dans les mêmes nanofils que ceux utilisés pour EH. Pour toutes les configurations une structure polycristalline a été observée avec une structure fcc pour les deux éléments. L'analyse de la composition chimique a montré l'inclusion d'au moins 15% de Cu dans les couches de Co, liée à l'utilisation d'un bain unique lors de l'électrodéposition. Ces impuretés dans la couche de Co produisent une diminution de l'aimantation à saturation par rapport Co pur. Des expériences d'holographie électronique ont été réalisées dans le but de révéler les états magnétiques locaux des couches de Co. Comme les résultats d'holographie correspondent à l'intégration du signal magnétique selon la direction d'observation, les simulations micromagnétiques ont été effectuées afin de compléter l'analyse des états magnétiques.

Pour la configuration Co(25nm)/Cu(15nm), les états magnétiques observés dans la plupart des nanofils correspondent à une aimantation orientée dans le plan de la couche de Co, un couplage antiparallèle (AP), des états de vortex ou un état monodomaine.

Si l'on augmente les épaisseurs à Co(50nm)/Cu(50nm), le couplage AP disparaît et seulement une large gamme de vortex peut être observée. Enfin, si les épaisseurs de Co et Cu sont de 100 nm chacune, le couplage dipolaire disparaît et il est prévu que chaque couche de Co soit indépendante. L'anisotropie de forme est également plus forte le long de l'axe du fil que pour les configurations précédentes.

D'un point de vue général, les états magnétiques sont le résultat de la concurrence de plusieurs effets : la variation de l'épaisseur de la couche et du diamètre du nanofil (anisotropie de forme), l'épaisseur de Cu (couplage dipolaire), l'anisotropie magnétique, le champ magnétique appliqué. Dans cette thèse, une étude quantitative et qualitative de ces états magnétiques locaux a été développée pour aboutir à un bon accord entre les résultats expérimentaux et les calculs micromagnétiques.

Comme point de départ pour calculer le diagramme de phase de nanofils multicouches Co/Cu, les résultats expérimentaux sont analysés et comparés avec les diagrammes de phase de nanocylindres de cobalt pur. L'influence du diamètre et de l'épaisseur après l'application d'un champ magnétique sur les états magnétiques a été étudiée et les résultats ont montré une concordance avec les résultats expérimentaux pour certaines configurations.

Différentes perspectives sur les nanofils Co/Cu peuvent être proposées: l'une des plus intéressantes est la possibilité d'effectuer des mesures de magnétorésistance en appliquant des champs magnétiques à l'intérieur du microscope et de réaliser des expériences d'holographie pour observer les états magnétiques obtenus pour chaque partie de la courbe de magnétorésistance.

Une étude peut être réalisée en appliquant un courant électrique à un couplage antiparallèle ou un état de vortex et en observant si une commutation magnétique peut être possible. En outre, la réponse RF peut être mesurée pour les différentes configurations magnétiques obtenues ici.

L'identification 3D des structures magnétiques par tomographie holographique est une perspective intéressante qui devra être considérée. Cette expérience pourrait apporter quelques réponses au sujet de la chiralité des vortex couplés avec le cœur aligné le long de l'axe du fil.

FeCoCu nanofils à diamètre modulé

Une analyse quantitative et qualitative détaillée de la configuration magnétique de nanofils FeCoCu à diamètre modulé a été faite. Les expériences d'holographie électronique et les simulations micromagnétiques ont permis une caractérisation détaillée du spin local et de configuration du champ démagnétisant. A l'état rémanent, la géométrie des fils modifie l'alignement longitudinal de l'aimantation due à la formation d'états de vortex et induit des charges magnétiques dans les régions où le diamètre varie. Ces structures vortex jouent un rôle important dans la configuration de spin dans les segments de grand diamètre (LD) parce qu'ils induisent une déformation en torsion de l'alignement des spins.

La description complète de la configuration magnétique reste réalisée par holographie électronique et les simulations micromagnétiques ont permis de clarifier l'origine du contraste magnétique clair et sombre observé dans les mesures de MFM qui ressemblent à des parois de domaines. Ces contrastes magnétiques sont produits par le nouveau champ sortant/parasite des charges magnétiques.

Cette nouvelle découverte suggère que les futures études pour le contrôle du mouvement des parois de domaines dans les nanofils cylindriques doivent se concentrer sur la façon dont les structures vortex et les charges magnétiques influent sur le processus de retournement de l'aimantation. Idéalement, nous nous attendons à ce que les deux phénomènes magnétiques, ou l'un d'eux, agissent comme lieux de nucléation et d'épinglage des parois de domaines.

Les perspectives plus intéressantes concernent la possibilité d'injecter du courant et d'observer la répartition des charges magnétiques. Aussi, si une géométrie adéquate peut être trouvée pour épingler les parois de domaines, il pourrait être intéressant d'observer

le mouvement de ces parois et observer l'influence des charges magnétiques, une fois que les parois passent à proximité.

Bibliographie

1 C. M. Lieber, "Semiconductor nanowires: A platform for nanoscience and nanotechnology," MRS Bull., vol. 36, no. 12, pp. 1052–1063, Dec. 2011.

2 L. Chen, W. Lu, and C. M. Lieber, "Chapter 1. Semiconductor Nanowire Growth and Integration," in RSC Smart Materials, W. Lu and J. Xiang, Eds. Cambridge: Royal Society of Chemistry, 2014, pp. 1–53.

3 P.-C. Hsu, S. Wang, H. Wu, V. K. Narasimhan, D. Kong, H. Ryoung Lee, and Y. Cui, "Performance enhancement of metal nanowire transparent conducting electrodes by mesoscale metal wires," Nat. Commun., vol. 4, Sep. 2013.

4 J.-Y. Lee, S. T. Connor, Y. Cui, and P. Peumans, "Solution-Processed Metal Nanowire Mesh Transparent Electrodes," Nano Lett., vol. 8, no. 2, pp. 689–692, Feb. 2008.

5 E. Comini and G. Sberveglieri, "Metal oxide nanowires as chemical sensors," Mater. Today, vol. 13, no. 7, pp. 36–44, 2010.

6 J. Cui, "Zinc oxide nanowires," Mater. Charact., vol. 64, pp. 43–52, Feb. 2012.

7 D. Han, X. Zhang, Z. Wu, Z. Hua, Z. Wang, and S. Yang, "Synthesis and magnetic properties of complex oxides La0.67Sr0.33MnO3 nanowire arrays," Ceram. Int., Jul. 2016.

8 R. S. Wagner and W. C. Ellis, "VAPOR-LIQUID-SOLID MECHANISM OF SINGLE CRYSTAL GROWTH," Appl. Phys. Lett., vol. 4, no. 5, p. 89, 1964.

9 Y. Li, Y. Wang, S. Ryu, A. F. Marshall, W. Cai, and P. C. McIntyre, "Spontaneous, Defect-Free Kinking via Capillary Instability during Vapor–Liquid–Solid Nanowire Growth," Nano Lett., vol. 16, no. 3, pp. 1713–1718, Mar. 2016.

10 Z. R. Dai, Z. W. Pan, and Z. L. Wang, "Novel nanostructures of functional oxides synthesized by thermal evaporation," Adv. Funct. Mater., vol. 13, no. 1, pp. 9–24, 2003.

11 A. Pierret, M. Hocevar, S. L. Diedenhofen, R. E. Algra, E. Vlieg, E. C. Timmering, M. A. Verschuuren, G. W. G. Immink, M. A. Verheijen, and E. P. A. M. Bakkers, "Generic nano-imprint process for fabrication of nanowire arrays," Nanotechnology, vol. 21, no. 6, p. 65305, Feb. 2010.

[12] R.-H. Horng, H.-I. Lin, and D.-S. Wuu, "ZnO nanowires lift-off from silicon substrate embedded in flexible films," in Nanoelectronics Conference (INEC), 2013 IEEE 5th International, 2013, pp. 1–3.

[13] P. Mohan, J. Motohisa, and T. Fukui, "Controlled growth of highly uniform, axial/radial direction-defined, individually addressable InP nanowire arrays," Nanotechnology, vol. 16, no. 12, pp. 2903–2907, Dec. 2005.

[14] S. F. A. Rahman, U. Hashim, M. N. M. Nor, A. M. M. Nuri, M. E. A. Shohini, S. Salleh, M. Rusop, and T. Soga, "Nanowire Formation Using Electron Beam Lithography," 2009, pp. 504–508.

[15] A. Fernández-Pacheco, L. Serrano-Ramón, J. M. Michalik, M. R. Ibarra, J. M. De Teresa, L. O'Brien, D. Petit, J. Lee, and R. P. Cowburn, "Three dimensional magnetic nanowires grown by focused electron-beam induced deposition," Sci. Rep., vol. 3, Mar. 2013.

[16] L.-M. Lacroix, R. Arenal, and G. Viau, "Dynamic HAADF-STEM Observation of a Single-Atom Chain as the Transient State of Gold Ultrathin Nanowire Breakdown," J. Am. Chem. Soc., vol. 136, no. 38, pp. 13075–13077, Sep. 2014.

[17] A. Loubat, L.-M. Lacroix, A. Robert, M. Impéror-Clerc, R. Poteau, L. Maron, R. Arenal, B. Pansu, and G. Viau, "Ultrathin Gold Nanowires: Soft-Templating versus Liquid Phase Synthesis, a Quantitative Study," J. Phys. Chem. C, vol. 119, no. 8, pp. 4422–4430, Feb. 2015.

[18] F. Ott, I. Panagiotopoulos, E. Anagnostopoulou, M. Pousthomis, L.-M. Lacroix, G. Viau, and J.-Y. Piquemal, "Soft chemistry nanowires for permanent magnet fabrication," in Magnetic Nano- and Microwires, Elsevier, 2015, pp. 629–651.

[19] T. L. Wade and J.-E. Wegrowe, "Template synthesis of nanomaterials," Eur. Phys. J. Appl. Phys., vol. 29, no. 1, pp. 3–22, Jan. 2005.

[20] M. Vázquez, M. Hernández-Vélez, K. Pirota, A. Asenjo, D. Navas, J. Velázquez, P. Vargas, and C. Ramos, "Arrays of Ni nanowires in alumina membranes: magnetic properties and spatial ordering," Eur. Phys. J. B, vol. 40, no. 4, pp. 489–497, Aug. 2004.

[21] D. L. Zagorskiy, V. V. Korotkov, K. V. Frolov, S. N. Sulyanov, V. N. Kudryavtsev, S. S. Kruglikov, and S. A. Bedin, "Track Pore Matrixes for the Preparation of Co, Ni and Fe Nanowires: Electrodeposition and their Properties," Phys. Procedia, vol. 80, pp. 144–147, 2015.

[22] H. Dai, "Carbon Nanotubes: Synthesis, Integration, and Properties," Acc. Chem. Res., vol. 35, no. 12, pp. 1035–1044, Dec. 2002.

[23] M. M. J. Treacy, T. W. Ebbesen, and J. M. Gibson, "Exceptionally high Young's modulus observed for individual carbon nanotubes," Nature, vol. 381, no. 6584, pp. 678–680, Jun. 1996.

[24] P. R. Bandaru, "Electrical Properties and Applications of Carbon Nanotube Structures," J. Nanosci. Nanotechnol., vol. 7, no. 4, pp. 1239–1267, Apr. 2007.

[25] B. Piccione, C.-H. Cho, L. K. van Vugt, and R. Agarwal, "All-optical active switching in individual semiconductor nanowires," Nat. Nanotechnol., vol. 7, no. 10, pp. 640–645, Sep. 2012.

[26] G.-C. Yi, Ed., Semiconductor Nanostructures for Optoelectronic Devices. Berlin, Heidelberg: Springer Berlin Heidelberg, 2012.

[27] J.-V. Kim, "Spin-Torque Oscillators," in Solid State Physics, vol. 63, Elsevier, 2012, pp. 217–294.

[28] T. Valet and A. Fert, "Theory of the perpendicular magnetoresistance in magnetic multilayers," Phys. Rev. B, vol. 48, no. 10, p. 7099, 1993.

[29] L. O'Brien, D. Petit, E. R. Lewis, R. P. Cowburn, D. E. Read, J. Sampaio, H. T. Zeng, and A.-V. Jausovec, "Tunable Remote Pinning of Domain Walls in Magnetic Nanowires," Phys. Rev. Lett., vol. 106, no. 8, Feb. 2011.

[30] R. Kirchain and L. Kimerling, "A roadmap for nanophotonics," Nat Photon, vol. 1, no. 6, pp. 303–305, Jun. 2007.

[31] C. Couteau, A. Larrue, C. Wilhelm, and C. Soci, "Nanowire Lasers," Nanophotonics, vol. 4, no. 1, Jan. 2015.

[32] Y.-C. Lin, C. M. Kramer, C. S. Chen, and D. H. Reich, "Probing cellular traction forces with magnetic nanowires and microfabricated force sensor arrays," Nanotechnology, vol. 23, no. 7, p. 75101, Feb. 2012.

[33] A. Hultgren, M. Tanase, C. S. Chen, G. J. Meyer, and D. H. Reich, "Cell manipulation using magnetic nanowires," J. Appl. Phys., vol. 93, no. 10, p. 7554, 2003.

[34] M. Contreras, R. Sougrat, A. Zaher, T. Ravasi, and J. Kosel, "Non-chemotoxic induction of cancer cell death using magnetic nanowires," Int. J. Nanomedicine, p. 2141, Mar. 2015.

[35] S. H. Charap, P.-L. Lu, and Y. He, "Thermal stability of recorded information at high densities," Magn. IEEE Trans. On, vol. 33, no. 1, pp. 978–983, 1997.

[36] R. F. L. Evans, R. W. Chantrell, U. Nowak, A. Lyberatos, and H.-J. Richter, "Thermally induced error: Density limit for magnetic data storage," Appl. Phys. Lett., vol. 100, no. 10, p. 102402, 2012.

[37] "FujiFilm achieves 154TB data storage record on Tape," StorageServers, 20-May-2014. .

[38] "Sony creates an 185TB tape cartridge!," StorageServers, 01-May-2014. .

[39] C. A. Ferguson, D. A. MacLaren, and S. McVitie, "Metastable magnetic domain walls in cylindrical nanowires," J. Magn. Magn. Mater., vol. 381, pp. 457–462, May 2015.

[40] M. N. Baibich, J. M. Broto, A. Fert, F. N. Van Dau, F. Petroff, P. Etienne, G. Creuzet, A. Friederich, and J. Chazelas, "Giant Magnetoresistance of (001)Fe/(001)Cr Magnetic Superlattices," Phys. Rev. Lett., vol. 61, no. 21, pp. 2472–2475, Nov. 1988.

[41] G. Binasch, P. Grünberg, F. Saurenbach, and W. Zinn, "Enhanced magnetoresistance in layered magnetic structures with antiferromagnetic interlayer exchange," Phys. Rev. B, vol. 39, no. 7, p. 4828, 1989.

[42] A. Fert, "Nobel Lecture: Origin, development, and future of spintronics," Rev. Mod. Phys., vol. 80, no. 4, pp. 1517–1530, Dec. 2008.

[43] L. Piraux, J. M. George, J. F. Despres, C. Leroy, E. Ferain, R. Legras, K. Ounadjela, and A. Fert, "Giant magnetoresistance in magnetic multilayered nanowires," Appl. Phys. Lett., vol. 65, no. 19, p. 2484, 1994.

[44] S.-I. Pyun, H.-C. Shin, J.-W. Lee, and J.-Y. Go, "Electrochemical Methods," in *Electrochemistry of Insertion Materials for Hydrogen and Lithium*, Berlin, Heidelberg: Springer Berlin Heidelberg, 2012, pp. 11–32.

[45] Y. D. Gamburg and G. Zangari, Theory and Practice of Metal Electrodeposition. New York, NY: Springer New York, 2011.

[46] S. Shin, B. H. Kong, B. S. Kim, K. M. Kim, H. K. Cho, and H. H. Cho, "Over 95% of large-scale length uniformity in template-assisted electrodeposited nanowires by subzero-temperature electrodeposition," Nanoscale Res. Lett., vol. 6, no. 1, p. 1, 2011.

[47] Giray Kartopu and Orhan Yalçın, Fabrication and Applications of Metal Nanowire Arrays Electrodeposited in Ordered Porous Templates. INTECH Open Access Publisher, 2010.

[48] X. Dou, G. Li, H. Lei, X. Huang, L. Li, and I. W. Boyd, "Template Epitaxial Growth of Thermoelectric Bi/BiSb Superlattice Nanowires by Charge-Controlled Pulse Electrodeposition," J. Electrochem. Soc., vol. 156, no. 9, p. K149, 2009.

[49] F. Nasirpouri and A. Nogaret, Eds., Nanomagnetism and spintronics: fabrication, materials, characterization and applications. Singapore: World Scientific, 2011.

[50] J. Kim, Advances in Nanotechnology and the Environment. CRC Press, 2011.

[51] T. Shinjō, Ed., Nanomagnetism and spintronics. Amsterdam; New York: Elsevier, 2009.

[52] J. McCord, "Progress in magnetic domain observation by advanced magneto-optical microscopy," J. Phys. Appl. Phys., vol. 48, no. 33, p. 333001, Aug. 2015.

[53] B. Mozooni and J. McCord, "Direct observation of closure domain wall mediated spin waves," Appl. Phys. Lett., vol. 107, no. 4, p. 42402, Jul. 2015.

[54] E. Nikulina, O. Idigoras, P. Vavassori, A. Chuvilin, and A. Berger, "Magneto-optical magnetometry of individual 30 nm cobalt nanowires grown by electron beam induced deposition," Appl. Phys. Lett., vol. 100, no. 14, p. 142401, 2012.

[55] W. Kuch, "Magnetic imaging," in Magnetism: A Synchrotron Radiation Approach, Springer, 2006, pp. 275–320.

[56] S. A. Gusev, V. N. Petrov, and E. V. Skorokhodov, "Problems of implementing SEMPA in experiments," J. Surf. Investig. X-Ray Synchrotron Neutron Tech., vol. 4, no. 4, pp. 582–587, Aug. 2010.

[57] T. Kohashi and K. Koike, "A spin-polarized scanning electron microscope with 5-nm resolution," Jpn. J. Appl. Phys., vol. 40, no. 11B, p. L1264, 2001.

[58] O. Boulle, J. Vogel, H. Yang, S. Pizzini, D. de Souza Chaves, A. Locatelli, T. O. Menteş, A. Sala, L. D. Buda-Prejbeanu, O. Klein, M. Belmeguenai, Y. Roussigné, A. Stashkevich, S. M. Chérif, L. Aballe, M. Foerster, M. Chshiev, S. Auffret, I. M. Miron, and G. Gaudin, "Room-temperature chiral magnetic skyrmions in ultrathin magnetic nanostructures," Nat. Nanotechnol., Jan. 2016.

[59] J. Vogel, W. Kuch, M. Bonfim, J. Camarero, Y. Pennec, F. Offi, K. Fukumoto, J. Kirschner, A. Fontaine, and S. Pizzini, "Time-resolved magnetic domain imaging by x-ray photoemission electron microscopy," Appl. Phys. Lett., vol. 82, no. 14, p. 2299, 2003.

[60] L. Abelmann, S. Porthun, M. Haast, C. Lodder, A. Moser, M. E. Best, P. J. van Schendel, B. Stiefel, H. J. Hug, G. P. Heydon, and others, "Comparing the resolution of magnetic force microscopes using the CAMST reference samples," J. Magn. Magn. Mater., vol. 190, no. 1, pp. 135–147, 1998.

[61] M. R. Koblischka and U. Hartmann, "Recent advances in magnetic force microscopy," Ultramicroscopy, vol. 97, no. 1–4, pp. 103–112, Oct. 2003.

[62] R. Wiesendanger, "Spin mapping at the nanoscale and atomic scale," Rev. Mod. Phys., vol. 81, no. 4, pp. 1495–1550, Nov. 2009.

[63] H. Hopster and H. P. Oepen, Eds., Magnetic microscopy of nanostructures, 1st ed. Berlin; New York: Springer, 2004.

[64] Y. Zhu, Ed., Modern techniques for characterizing magnetic materials. Boston: Kluwer Academic Publishers, 2005.

[65] R. J. Celotta, J. Unguris, M. H. Kelley, and D. T. Pierce, "Techniques to measure magnetic domain structures," Charact. Mater., 1999.

[67] L. Mayer, "Electron Mirror Microscopy of Magnetic Domains," J. Appl. Phys., vol. 28, no. 9, p. 975, 1957.

[68] M. E. Hale, H. W. Fuller, and H. Rubinstein, "Magnetic Domain Observations by Electron Microscopy," J. Appl. Phys., vol. 30, no. 5, p. 789, 1959.

[69] H. W. Fuller and M. E. Hale, "Domains in Thin Magnetic Films Observed by Electron Microscopy," J. Appl. Phys., vol. 31, no. 10, p. 1699, 1960.

[70] J. N. Chapman, P. E. Batson, E. M. Waddell, and R. P. Ferrier, "The direct determination of magnetic domain wall profiles by differential phase contrast electron microscopy," Ultramicroscopy, vol. 3, pp. 203–214, 1978.

[71] E. M. Waddell and J. N. Chapman, "Linear imaging of strong phase objects using asymmetrical detectors in STEM," Opt. Stuttg, vol. 54, pp. 83–96, 1979.

[72] J. N. Chapman, "The investigation of magnetic domain structures in thin foils by electron microscopy," J. Phys. Appl. Phys., vol. 17, no. 4, p. 623, 1984.

[73] J. N. Chapman, I. R. McFadyen, and S. McVitie, "Modified differential phase contrast Lorentz microscopy for improved imaging of magnetic structures," Magn. IEEE Trans. On, vol. 26, no. 5, pp. 1506–1511, 1990.

[74] A. Tonomura, T. Matsuda, J. Endo, T. Arii, and K. Mihama, "Direct Observation of Fine Structure of Magnetic Domain Walls by Electron Holography," Phys Rev Lett, vol. 44, no. 21, pp. 1430–1433, May 1980.

[75] A. Tonomura, "Applications of electron holography," Rev. Mod. Phys., vol. 59, no. 3, p. 639, 1987.

[76] D. Gabor, "A New Microscopic Principle," \nat, vol. 161, pp. 777–778, May 1948.

[77] D. Gabor, "Microscopy by Reconstructed Wave-Fronts," Proc. R. Soc. Math. Phys. Eng. Sci., vol. 197, no. 1051, pp. 454–487, Jul. 1949.

[78] A. Tonomura, "Electron-holographic interference microscopy," Adv. Phys., vol. 41, no. 1, pp. 59–103, Feb. 1992.

[79] H. Lichte, "Parameters for high-resolution electron holography," Ultramicroscopy, vol. 51, no. 1, pp. 15–20, 1993.

[80] H. Lichte, "Gottfried Möllenstedt and his electron biprism: four decades of challenging and exciting electron physics," J. Electron Microsc. (Tokyo), vol. 47, no. 5, pp. 387–394, 1998.

[81] R. E. Dunin-Borkowski, T. Kasama, M. Beleggia, and G. Pozzi, "Lorentz Microscopy and Electron Holography of Magnetic Materials," in Handbook of Nanoscopy, vol. 1&2, Wiley-VCH, 2012, pp. 221–251.

[82] M. J. Donahue and D. G. Porter, "OOMMF User's Guide, Version 1.0, Interagency Report NISTIR 6376." 1999.

[83] J.-L. Maurice, D. Imhoff, P. Etienne, O. Durand, S. Dubois, L. Piraux, J.-M. George, P. Galtier, and A. Fert, "Microstructure of magnetic metallic superlattices grown by

electrodeposition in membrane nanopores," J. Magn. Magn. Mater., vol. 184, no. 1, pp. 1–18, 1998.

[84] Y. Henry, K. Ounadjela, L. Piraux, S. Dubois, J.-M. George, and J.-L. Duvail, "Magnetic anisotropy and domain patterns in electrodeposited cobalt nanowires," Eur. Phys. J. B-Condens. Matter Complex Syst., vol. 20, no. 1, pp. 35–54, 2001.

[85] M. Rivera, C. H. Rios-Reyes, and L. H. Mendoza-Huizar, "Magnetic transition phase diagram of cobalt clusters electrodeposited on HOPG: Experimental and micromagnetic modelling study," J. Magn. Magn. Mater., vol. 323, no. 7, pp. 997–1000, Apr. 2011.

[86] F. Dumas-Bouchiat, H. S. Nagaraja, F. Rossignol, C. Champeaux, G. Trolliard, A. Catherinot, and D. Givord, "Cobalt cluster-assembled thin films deposited by low energy cluster beam deposition: Structural and magnetic investigations of deposited layers," J. Appl. Phys., vol. 100, no. 6, p. 64304, 2006.

[87] D. Grujicic and B. Pesic, "Micromagnetic studies of cobalt microbars fabricated by nanoimprint lithography and electrodeposition," J. Magn. Magn. Mater., vol. 285, no. 3, pp. 303–313, Jan. 2005.

[88] S. Allende, D. Altbir, and K. Nielsch, "Magnetic cylindrical nanowires with single modulated diameter," Phys. Rev. B, vol. 80, no. 17, Nov. 2009.

[89] M. S. Salem, P. Sergelius, R. M. Corona, J. Escrig, D. Görlitz, and K. Nielsch, "Magnetic properties of cylindrical diameter modulated Ni80Fe20 nanowires: interaction and coercive fields," Nanoscale, vol. 5, no. 9, p. 3941, 2013.

[90] F. Tejo, N. Vidal-Silva, A. P. Espejo, and J. Escrig, "Angular dependence of the magnetic properties of cylindrical diameter modulated Ni80Fe20 nanowires," J. Appl. Phys., vol. 115, no. 17, p. 17D136, May 2014.

[91] D. W. Wong, M. Chandra Sekhar, W. L. Gan, I. Purnama, and W. S. Lew, "Dynamics of three-dimensional helical domain wall in cylindrical NiFe nanowires," J. Appl. Phys., vol. 117, no. 17, p. 17A747, May 2015.

[92] I. Minguez-Bacho, S. Rodriguez-López, M. Vázquez, M. Hernández-Vélez, and K. Nielsch, "Electrochemical synthesis and magnetic characterization of periodically modulated Co nanowires," Nanotechnology, vol. 25, no. 14, p. 145301, Apr. 2014.

[93] B. Rodriguez-Gonzalez, C. Bran, T. Warnatz, J. Rivas, and M. Vazquez, "Structural and magnetic characterization of as-prepared and annealed FeCoCu nanowire arrays in ordered anodic aluminum oxide templates," J. Appl. Phys., vol. 115, no. 13, p. 133904, 2014.

[94] Ó. Iglesias-Freire, C. Bran, E. Berganza, I. Mínguez-Bacho, C. Magén, M. Vázquez, and A. Asenjo, "Spin configuration in isolated FeCoCu nanowires modulated in diameter," Nanotechnology, vol. 26, no. 39, p. 395702, Oct. 2015.

[95] E. M. Palmero, C. Bran, P. Rafael, C. Magén, and M. Vázquez, "Structural and Magnetic Characterization of FeCoCu/Cu Multilayer Nanowire Arrays," IEEE Magn. Lett., vol. 5, pp. 1–4, 2014.

[96] S. Vock, C. Hengst, M. Wolf, K. Tschulik, M. Uhlemann, Z. Sasvári, D. Makarov, O. G. Schmidt, L. Schultz, and V. Neu, "Magnetic vortex observation in FeCo nanowires by quantitative magnetic force microscopy," Appl. Phys. Lett., vol. 105, no. 17, p. 172409, Oct. 2014.

[97] S. L. Viñas, R. Salikhov, C. Bran, E. M. Palmero, M. Vazquez, B. Arvan, X. Yao, P. Toson, J. Fidler, M. Spasova, U. Wiedwald, and M. Farle, "Magnetic hardening of Fe 30 Co 70 nanowires," Nanotechnology, vol. 26, no. 41, p. 415704, Oct. 2015.

[98] C. Bran, Y. P. Ivanov, J. García, R. P. del Real, V. M. Prida, O. Chubykalo-Fesenko, and M. Vazquez, "Tuning the magnetization reversal process of FeCoCu nanowire arrays by thermal annealing," J. Appl. Phys., vol. 114, no. 4, p. 43908, 2013.

[99] S. Lopatin, Y. P. Ivanov, J. Kosel, and A. Chuvilin, "Multiscale differential phase contrast analysis with a unitary detector," Ultramicroscopy, vol. 162, pp. 74–81, Mar. 2016.

[100] Y. P. Ivanov, A. Chuvilin, S. Lopatin, and J. Kosel, "Modulated Magnetic Nanowires for Controlling Domain Wall Motion: Toward 3D Magnetic Memories," ACS Nano, vol. 10, no. 5, pp. 5326–5332, May 2016.